Chemoproteomic Profiling Studies of Compound Selectivity and Target Protein Ligandability



Elisabeth Mira Rothweiler

Wolfson College

University of Oxford

Supervised by

Prof Paul Brennan

Dr Kilian Huber

Submitted Trinity Term, October 05, 2023

This Thesis is submitted to the Nuffield Department of Medicine as a requirement for the Degree of Doctor of Philosophy in Clinical Medicine.

Declaration

I declare that this thesis is entirely my own work and research, except where otherwise stated.

Elisabeth Mira Rothweiler, Wolfson College

Acknowledgements

Firstly, I would like to thank and express greatest gratitude to my supervisors Paul Brennan and Kilian Huber for excellent scientific guidance and fruitful project discussions. I feel very fortunate to have had the honour to work with both their wonderful groups in the TDI and the ODDI and am grateful for their support and mentorship. The CMD provided me with excellent facilities and learning opportunities amongst exceptional co-workers. Thus, I would like to thank Jennifer Ward and Jakub Stefaniak for sharing their expertise in chemical biology, and Catherine Rogers and Paul Smith for teaching me to work with cell-based assays. Many thanks to Oleg Fedorov, James Bennett and Charline Giroud, for passing on their knowledge in biochemical assays. Many thanks to Usha Singh for support in the tissue culture and Esra Balikci for crystal structure analyses. I would like to thank Jeppe Tranberg-Jensen for creating ProteomeLabeller and collaborating on bioinformatic analyses and Martin Buttenschön for performing statistic analyses on the MS data. I would like to thank Tryfon Zarganis-Tzitzikas, Thomas Grimes and Mia Callens for insightful chemistry discussions. I would like to thank Benedikt Kessler and Mike Willis for great input and guidance as my Thesis Committee. Many thanks to Iolanda Vendrell and Svenja Hester for running MS samples, and to our laboratory managers Christopher Dodd and Zuzana Benokova for our well organised lab. I would like to thank our IT technician Christopher Sluman, who helped me with any technical issue. I would like to thank the Bayer Pharma AG for funding of the Lambert Russell studentship and Philipp Cromm and Volker Badock, who provided valuable scientific discussions. Lastly, I would like to thank all my wonderful friends and my supportive, loving family, especially my parents, and my dear sister Jasmin.

Abstract

Chemical probes are valuable tools to study compound selectivity and target engagement. These qualities are immensely important for drug discovery, as compounds lacking efficacy and safety are a major reason for phase II failures in clinical trials. It is highly important to study lead compounds, not only in biophysical and biochemical assays but also in the cellular context, revealing selectivity as well as potential unwanted off-targets. In cells, the protein is preserved in its native form and environment, which allows for the consideration of physiological co-factor effects and post-translational modifications, which may be absent in assays performed with recombinant protein. The chemoproteomic techniques referred to within this work thus present a useful example of deconvoluting the targets of small bioactive molecules in the cellular proteome that can enable and simultaneously help de-risk drug discovery projects.

The introduction describes chemoproteomic techniques coupled to mass spectrometry as well as complementary techniques for studying target engagement *in cellulo*. The second chapter delves into the family of E3 ligases and their role as tools in targeted protein degradation. It presents a bioinformatic analysis and a compound library selection to maximise the number of ligandable E3 ligases. The third chapter reports how an isoTOP ABPP screening platform was established and optimised to enable the creation of an E3-ligase-centric druggability map by profiling covalent fragments. Followingly, the fourth chapter describes utilising the isoTOP ABPP for profiling not only fragments but also lead compounds and

chemical probes for KEAP1 and NUDT7. The fifth chapter characterises the clinical compound GSK3326595 using mass spectrometry-based proteomic methods supplemented by a newly developed cellular NanoBRET assay. In the sixth chapter, a NanoBRET PPI assay is introduced to evaluate fragments as pharmacological modulators of the DENND1A and RAB35 interactions.

Table of Figures

Figure 1: NanoBRET principle and commonly used fluorophores....28
Figure 2: Schematic of a compound-centric pulldown based on an affinity-matrix....34
Figure 3: isoTOP-ABPP as schematic workflow....39
Figure 4: Ubiquitin and it's relevant residues for ubiquitination....49
Figure 5: Ubiquitin-proteasome pathway....52
Figure 6: Targeted protein degradation strategies....55
Figure 7: Covalent TPD and TPS recruiters targeting E3 ligases and DUBs....59
Figure 8: Results of the Kinaseblender analysis....65
Figure 9: Venn diagrams depicting E3 ligase overlap between cell lines....66
Figure 10: Waterfall plots depicting proteins identified in total proteome data....67
Figure 11: Reactive probe and competitor libraries....71
Figure 12: Detection of probe 1 labelling in K562 lysates in in-gel fluorescence....73
Figure 13: Survey of probe reactivity at 100 µM incubated for 1 h at RT....76
Figure 14: Coomassie stains and western blot detection with IRDye 800 CW streptavidin....78
Figure 15: Test of cell viability in CellTiterGlo assay....79
Figure 16: Optimisation steps conducted inhouse....85
Figure 17: Sonication test of different sonication conditions in K562 lysates....86
Figure 18: MS^2 charge distribution depicted in RawMeat software....87
Figure 19: Method comparison on QExactive....88
Figure 20: Performance of re-suspension buffers....90
Figure 21: Performance of biological and technical replicates....90
Figure 22: Comparison of QExactive 120 min to TimsTOF 21 min method....92
Figure 23: Visualisation of closed search and open search in FragPipe....93
Figure 24: Summary of the non-competitive screening of eight probes....97
Figure 25: Venn diagrams depicting performance of probes on protein level....99
Figure 26: Venn diagrams depicting performance of probes on modified site level....100
Figure 27: Literature comparison of protein labelling....103
Figure 28: E3 ligases detected in the non-competition dataset....105
Figure 29: Summary of the competitive screening of probe set in four cell lines....108
Figure 30: E3 ligases detected in the competition dataset....110
Figure 31: Comparison of data in K562 intact cell/lysate and DDA/DIA mode....115
Figure 32: Organisation and binding regions of human KEAP1....122
Figure 33: Waterfall plots of isoTOP ABPP screening for KEAP1....124
Figure 34: Sequence for NUDT7....126
Figure 35: Waterfall plots for competitive isoTOP ABPP for NUDT7....128
Figure 36: Schematic of tripartite protein NLRP3....130
Figure 37: NLRP3 speck-formation assay....133
Figure 38: Speck formation assay results for covalent fragment screening....134
Figure 39: Speck formation (SPECK) and cell death (PYRO)....136
Figure 40: STRING analysis of proteins which were competed with R > 3....137
Figure 41: Determination of effect of 1c on NCIH226 thermal profile....140
Figure 42: Determination of effect of 9c on NCIH226 thermal profile....141
Figure 43: FRAP assay results....144
Figure 44: Intact MS performed on KEAP1 recombinant protein using 1c....146

Figure 45: Intact MS performed on KEAP1 recombinant protein using 9c.....147
Figure 46: Schematic of PRMT5 and produced methylation patterns.....154
Figure 47: Compounds used in the NanoBRET study.....155
Figure 48: PRMT5 NanoBRET assay and ETP probe development.....156
Figure 49: Subcellular localization and co-localization of endogenous PRMT5 and NL-PRMT5.....157
Figure 50: Optimisation of ETP concentration and evaluation of PRMT5 inhibitors in a cell-based NanoBRET assay using CBH-002.....159
Figure 51: Comparison of inhibitor EC_{50}.....160
Figure 52: Effect of SAM levels on cellular EC_{50} values of PRMT5 inhibitors.....163
Figure 53: Co-crystal structures indicate mutually exclusive binding of SAM, LLY-283 and GSK3235025 (EPZ015666).....164
Figure 54: Proteome-wide specificity of GSK3326595 as determined by chemical proteomics.....167
Figure 55: 2D thermal profiling results for GSK3326595.....168
Figure 56: Views of DENND1A and Rab35 based on co-crystal structure.....177
Figure 57:Scatter plots showing 10 plates of NanoBRET PPI.....179
Figure 58: Selection of best 26 fragments from dose-response experiments.....181
Figure 59: NanoBRET DENND1A-NL and HT-RAB35.....184
Figure 60: Evaluation of six fragments in NanoBRET using DENND1A V2-NL and in counter screen assay using BRD9 BD-NL and H3.3.....186
Figure 61: Gels of the purification of RAB35a-c002.....188
Figure 62: Formation of covalent mass adducts.....189
Figure 63: Incubation of RAB35 (2 µM) with fragment Z1151194523.....191
Figure 64: Competition experiment using fragment Z1151194523 and IA.....192
Figure 65: PEAKS software view of trypsin digest of RAB35.....193
Figure 66: PEAKS software view of GluC digest.....194
Figure 67: Principle of GEF-activity assay and results for DENND1A and RAB35.....195

Table of Tables

Table 1: Criteria proposed for reversible, covalent and degrader chemical probes.....26
Table 2: Advantages and disadvantages of covalent ligands listed. 42
Table 3: TPD/TPS targets addressed with covalent recruiters.....62
Table 4: Tabular view of top 10 identified E3 ligases in total proteome dataset.....69
Table 5: Masses of modification for each light (L) and heavy (H) modified peptides...94
Table 6: Table showing the probes and cell line coverage of E3 ligases.....106
Table 7: Table showing E3 ligases, modified residue numbers and amino acid 112
Table 8: Tables showing competition for NUDIX family 129
Table 9: Table showing results of dose-response screen of 16 fragments.....136
Table 10: Table showing cell line NCIH226, and cysteine reactive sites on TRIM28 identified with probe 1 and competitor 1c 139
Table 11: Comparison of literature data and NanoBRET TE assay results.....161

List of Abbreviations

ABPP	Activity-based protein profiling
ACAT	Acyl-coenzyme A, cholesterol acyltransferase
ACN	Acetonitrile
AF	AlphaFold
AI	Artificial intelligence
ASC	Apoptosis-associated speck-like protein containing a CARD
BODIPY	Boron dipyrromethene
BRD	Bromodomain
BRET	Bioluminescence Resonance Energy Transfer
C	Cys, cysteine
CCLE	Cancer cell line encyclopaedia
CDDO	Bardoxolone methyl
CETSA	Cellular Thermal Shift Assay
CRBN	Cereblon
CRISPR	Clustered Regularly Interspaced Short Palindromic Repeats
CRL	Cullin/RING ubiquitin ligases
CuAAC	Copper(I)-catalysed azide-alkyne cycloaddition
D	Asn, aspartic acid
DBIA	desthiobiotin iodoacetamide
DD	Drug discovery
DDA	Data-dependent acquisition
DDB1	Damaged DNA binding protein 1
DDM	N-dodecyl β-D-maltoside
DENND1A	DENN Domain Containing 1A
DIA	Data-independent acquisition
DMSO	Dimethyl sulfoxide
DSF	Differential scanning fluorimetry
DTB	Desthiobiotin
DTT	Dithiothreitol
DUB	Deubiquitinase
DUBTAC	Deubiquitinase-targeting chimeras
E	Glu, glutamic acid
ELISA	Enzyme-Linked Immunosorbent Assay
ETP	Energy-transfer probe
EubOPEN	Enable and Unlock biology in the open
FA	Formic acid
FAAH	Fatty acid amide hydrolase
FAIMS	Field asymmetric waveform ion mobility spectrometry
FDA	Food and Drug Administration

flupol	Fluorescence polarization
FRAP	Fluorescence recovery after photobleaching
FRET	Fluorescence resonance energy transfer
GFP	Green fluorescent protein
HCV	Hepatitis C virus
HECT	Homologous to E6-AP carboxy terminus
HT	Halo-tag
HTS	High throughput screening
IAA	Iodoacetamide-alkyne
IBR	in-between-RING
ICAT	Isotope-coded affinity tag
ID	Identifier
IMIDs	Immunomodulatory drugs
isoDTB	isotopically differentiated desthiobiotin
isoTOP	isotopically differentiated tandem-orthogonal proteolysis
K	Lys, lysine
KDM	Lysine demethylase
KEAP1	Kelch-like ECH-associated protein 1
M	Met, methionine
MG	Molecular glue
MoA	Mechanism of action
MS	Mass spectrometry
NCI	National Cancer Institute
NHS	N-Hydroxysuccinimide
NLRP3	NACHT, LRR and PYD domains-containing protein 3
NLuc	Nano Luciferase
NME	New molecular entity
NP-40	Nonidet P-40
NUDT7	Nudix Hydrolase 7
ODDI	Oxford Drug Discovery Institute
PAINS	Pan-assay interfering compounds
PARP	Putative poly-ADP ribose polymerase
PCOS	Polycystic Ovary Syndrome
PDB	Protein data bank
POI	Protein of interest
PPI	Protein-protein interaction
pPSE	Prediction-aware part-sphere exposure
PRMT5	Protein arginine methyl transferase 5
PROTAC	Proteolysis targeting chimeras
PTM	Post-translational modification
R	Arg, arginine

R&D	Research and development
RAB35	Ras-related protein Rab-35
RBR	RING-between-RING
RFA	Rhodamine-conjugated F-amidine
RING	Really interesting new gene
RLuc	Renilla Luciferase
S	Ser, serine
SAR	Structure-activity-relationship
SASA	Solvent accessible surface area
SDS-Page	Sodium dodecyl-sulfate polyacrylamide gel electrophoresis
SF	Sulfonyl fluoride
SGC	Structural Genomics Consortium
SILAC	Stable isotope labelling by amino acids in cell culture
SLC-ABPP	Streamlined cysteine activity-based protein profiling
SOCS2	Suppressor of cytokine signalling 2
SuTEX	Sulphur triazole
T	Thr, threonine
TAMRA	Tetramethyl rhodamine
TE	Target engagement
TEV	Tobacco etch virus
TFA	Trifluoro acetic acid
TMT	Tandem mass tag
TPD	Targeted protein degradation
TPS	Targeted protein stabilisation
TRIM28	KAP1, Krüppel-associated box associated protein 1
Ub	Ubiquitin
UPS	Ubiquitin-proteasome pathway
VDAC	Voltage-dependent anion channels
VHL	Van Hippel Lindau
VS	Vinyl sulfone
WB	Western Blot
WT	Wildtype
Y	Tyr, tyrosine
YFP	Yellow fluorescent protein
ZNF	Zinc-finger protein

Table of Contents

1. Introduction 14

1.1 Chemical biology methods to support drug development 14
1.1.1 Relevance of target engagement in cellular and phenotypic context 17
1.1.2 Chemoproteomics and chemical probes in drug discovery 20
1.1.3 Target 2035 24
1.2 Non-proteomic methods for evaluation of target engagement in cellulo 27
1.2.1 NanoBRET 27
1.2.2 Cellular Thermal Shift Assay 29
1.2.3 Fluorescence Recovery After Photobleaching 31
1.3 Chemoproteomic methods enabling drug discovery 32
1.3.1 Compound-centric pulldown (affinity-enrichment) 33
1.3.2 Activity-based Protein Profiling and isoTOP ABPP (activity-enrichment) 35
1.3.3 Covalent fragment screening 41
1.4 Aims of the project 44

2. Chemical modulation of protein homeostasis 47

2.1 Proteostasis: the ubiquitin proteasome pathway 48
2.1.1 E3 ligases and their role in cellular homeostasis 51
2.1.2 The therapeutic means PROTACs and DUBTACs 54
2.1.3 Covalent E3 ligase recruiters 57
2.2 Generating a E3 ligase druggability map 63
2.2.1 Bioinformatic analysis of a proteomic and transcriptomic dataset 63
2.2.2 Total proteome validation in-house 66
2.3 Selection of a covalent probe library 70
2.3.1 Reactive probes and competitors addressing distinct amino acids 70
2.3.2 Reactivity survey of the probe library 72
2.4 Summary 80

3. Profiling of E3 ligases on proteome-wide scale 83

3.1 isoTOP ABPP optimisation 83
3.1.1 Sonication, digest and re-suspension buffer optimisation 86
3.1.2 Instrument and gradient performance 91
3.1.3 Data analysis tools 93
3.1.3.1 FragPipe software 93
3.1.3.2 R script and ProteomeLabeller 95
3.2 isoTOP ABPP: uncompetitive determination of ligandable sites 96
3.2.1 Non-competitive results for cell lines K562, DU145, NCIH226 and U251 96
3.2.2 Enriched E3 ligases 104
3.3 isoTOP ABPP: competitive distinction of druggable binding sites 106
3.3.1 Competition results for cell lines 107
3.3.2 Competed E3 ligases 109
3.3.3. Further optimisation of data acquisition mode 113
3.4 Summary and outlook 116

4. Target evaluation of chemical probes and fragments using isoTOP ABPP 121

4.1 E3 LIGASE KEAP1 AND A SELECTIVE CHEMICAL PROBE 122
4.1.1 ISOTOP ABPP OF CHEMICAL PROBE S213726 123
4.2. EVALUATION OF A CHEMICAL PROBE FOR NUDIX-FAMILY MEMBER NUDT7 125
4.2.1 ISOTOP ABPP OF CHEMICAL PROBE NU074516A 126
4.3 NLRP3 INFLAMMASOME AND NEURODEGENERATION 130
4.3.1 SCREENING OF COVALENT FRAGMENT LIBRARY IN SPECK-FORMATION ASSAY 132
4.3.1.1 Fragment screening campaign 133
4.3.1.2 isoTOP for fragment target identification 137
4.4 FRAGMENT BINDING VALIDATION USING ORTHOGONAL METHODS 138
4.4.1 EVALUATION OF COVALENT FRAGMENTS IN CETSA 138
4.4.3 INTACT MS STUDIES WITH KEAP1 145
4.5 SUMMARY AND OUTLOOK 149

5. Characterisation of selectivity of GSK3326595 152

5.1 ROLE OF PRMT5 AS METHYLTRANSFERASE 152
5.1.1 PRMT5 INHIBITOR CLASSES 154
5.1.2 FIRST IN CLASS STUDY OF PRMT5 CELLULAR TARGET ENGAGEMENT VIA NANOBRET . 156
5.2 VALIDATION OF GSK3326595 SELECTIVITY 157
5.2.1 ESTABLISHMENT OF NANOBRET TE-ASSAY WITH CBH-002 157
5.2.1.1 MEASUREMENT OF EC_{50} VALUES IN CELLS 159
5.2.2. CHEMOPROTEOMIC PULLDOWN AND ORTHOGONAL TARGET VALIDATION 165
5.3 SUMMARY AND OUTLOOK 169

6. Evaluation of covalent fragments as interrupters of protein-protein interactions 175

6.1 POLYCYSTIC OVARY SYNDROME: DENND1A AND RAB35 176
6.2 EVALUATION OF FRAGMENTS AS INTERRUPTERS OF PPI 178
6.2.1 NANOBRET PPI ASSAY DENND1A AND RAB35 178
6.2.2 EXPRESSION AND PURIFICATION OF RAB35-C002 187
6.2.3 INTACT MS FOR BINDING VALIDATION 189
6.2.4 FASP PROTEIN DIGEST FOR MAPPING OF BINDING SITE 192
6.2.5 GEF-ACTIVITY ASSAY 194
6.3 SUMMARY AND OUTLOOK 196

7. Closing Remarks 201

8. Methods 205

9. References 244

10. Appendix 275

1. Introduction

Parts of this introduction have been published in a first-author review by Rothweiler et al. about covalent fragment-based ligand screening and ubiquitin proteasome modulators [1].

1.1 Chemical biology methods to support drug development

In the past decade, the Food and Drug Administration (FDA) approved 378 novel molecular entities (NMEs), which marks an increase of 60 % in comparison to approvals in 2000 – 2009 [2]. However, in the year 2022, only 37 NMEs were approved, which was the fewest number since 2016. This marked a drop from the previous five-year high, with 18 approved small molecules in comparison to 28 in the year 2021 [3]. Despite increased investment in research and development (R&D), the attrition rate of NMEs in clinical trials is still high. Depending on the therapeutic area, only around 10-20% of drugs that enter clinical trials will eventually get FDA approval, a trend which has not changed over the past decades [4]. A analysis of successful candidate compounds in Phase I clinical trials indicated the success rate was around 60 %, whereas in Phase II clinical trial success was substantially lower with around 30 % [5]. Phase III success rates were approximately 60 %, and 85 % during the regulatory review process [6]. Notably, the majority of failures in clinical trials in Phase II/III were due to compound efficacy (52 %) and safety (25 %) [7].

Due to advances in modern genomic sequencing, the decoding of the human genome, and the development of efficient high-throughput screening (HTS) techniques, target-based drug discovery approaches are nowadays a default approach for the discovery of NMEs [8]. In a typical pipeline, genetic, target-based experiments (such as RNA interference or CRISPR) are combined with subsequent biophysical screenings of millions of compounds

against the target to identify lead compound structures. These HTS screenings often utilise recombinant protein, which allows for fast screenings against vast compound libraries, assuming the protein is available for expression and purification. In addition, artificial intelligence (AI) is becoming increasingly relevant in modern drug discovery as it may be applied to drug design (e.g. protein structure prediction, *de novo* drug design) or drug screening (e.g. bioactivity or toxicity predictions) [9]. Yet, despite these advances, the field has not yielded a corresponding increase in NMEs and successful clinical candidates [10]. As the process of developing a new drug can take 12 – 15 years, with costs often exceeding one billion dollars [11], there is an urgent need to review causes and understand the underlying mechanisms of why around 90 % of the drugs entering clinical trials are failing [12]. AstraZeneca revised its R&D strategy in 2010 and proposed the 5 R framework. The authors identified five key factors leading to project failures, which were: the right target, the right tissue (target engagement), the right safety, the right patient, and the right commercial potential [13]. Likewise, in a study conducted by Pfizer reviewing their clinical drug development pipeline, exposure to the site of action/target and demonstration of target engagement were also identified as major factors contributing to Phase II clinical candidate's success. Thus, the three "pillars of survival" have been proposed: sufficient exposure at the site of action, demonstration of target engagement, expression of functional pharmacological activity; and as an additional pillar, the proof of phenotype perturbation [14].

Moellering and Cravatt proposed that the gap between early, rather genetics-focused, and late, more pharmacology-focused drug discovery stages can affect the development of drug candidates and their overall success in clinical trials [15]. While in pharmacology-based studies the emphasis lies on the compound and its phenotypic effect in cell or

animal models, in modern target-based studies this approach has largely been displaced by technically simpler molecular biology and genetic studies centred around a target protein. There is a consensus that robust studies to both "know your target" and to "know your molecule" are key for drug discovery, and Bunnage et al. suggest that important concepts for target identification and validation include: choosing a relevant cell line and disease phenotype for screening, using complementary genetic techniques (e.g. knockout, knockdown), generating cell lines expressing mutant target protein, and target deconvolution of hits to reveal their molecular target and MoA [16]. Ideally, a suite of orthogonal biophysical, biochemical, genetic, and chemical proteomic assays should be combined to demonstrate target engagement.

There are several examples of why it is crucial to confirm the target protein and validate target engagement in the early drug development process. For instance, iniparib, a putative poly-ADP ribose polymerase (PARP)-inhibitor, failed in Phase III clinical trials for breast cancer after successful Phase II trials [17]. The principle of clinical PARP inhibitors, such as olaparib, is based on the increased susceptibility of cells to DNA damage, e.g. cancers exhibiting impaired DNA repair pathways are particularly sensitive to PARP inhibition [18]. Subsequent investigations of iniparib on cancer cell growth did show no signs of PARP inhibition, and iniparib was questioned to be classified as a PARP-inhibitor, presumably exerting effects through other mechanisms [19]. Another example is the fatty acid amide hydrolase (FAAH) inhibitor BIA 10-2474, which was abruptly halted in Phase I clinical trials after several patients suffered serious adverse neurological events after administration of the drug, with one fatality [20]. Subsequent chemoproteomic studies of the compound confirmed binding to FAAH but revealed numerous off-targets [21], such as ALDH2, an aldehyde dehydrogenase responsible for

protecting the brain from oxidative stress damage, which was found to be covalently bound by a metabolite of BIA 10-2474 [22]. Thalidomide was famously withdrawn from the market after demonstrating severe teratogenic effects when it was administered for morning sickness in pregnant women [23]. More recently, in an affinity purification in human HeLa cell extracts, CRBN was identified as a thalidomide-binding protein [24]. Ito et al. showed that CRBN forms an E3 ligase complex with its adaptor, damaged DNA binding protein 1 (DDB1) and CUL4A, which is involved in limb growth in zebra fish, Impact on limb growth had previously not been observed in mouse models. Lenalidomide, a derivative of thalidomide, has since been re-purposed as a drug for multiple myeloma as it was shown to degrade IKZF1 and IKZF3 [25, 26].

1.1.1 Relevance of target engagement in cellular and phenotypic context

Confirmation and quantification of cell-based target engagement complement biochemical (usually acellular) HTS assays in early lead optimisation stages by evaluating compounds in a complex, physiologically relevant environment [13, 14]. As such, the relevance of phenotypic methods in DD should not be overlooked. According to an analysis by Swinney and Anthony of FDA-approved NMEs between 1999-2008, the first-in-class small molecules discovered in phenotypic screenings exceeded the number stemming from target-based approaches [27]. Lower NME numbers are reported by Eder et al. for the same decade; however they acknowledge that these screenings offer important pharmacological tools to study new biology [28]. Historically, phenotypic screenings have been effective, for example, leading to the discovery of the first blockbuster drug, salvarsan, by Paul Ehrlich. Ehrlich had screened chemical dyes in rabbit and mouse models as syphillis could not be cultured in dishes [29].

Modern phenotypic assays should allow for the evaluation of complex biological systems and should be conducted in relevant cell or tissue types, capturing cellular interactions or signal transduction pathways and offering a functional readout for the mechanism of action [30]. The phenotypic drug discovery approach is defined as unbiased and mechanism-agnostic, and relies on relevant disease models to ensure the translation of hits from assays into clinical candidates [31]. Thus, the advantage of phenotypic screens is that they tend to deliver a cell-active, phenotype-modulating compound as a starting point without concern for low target relevance to the disease, which is emblematic of target-based DD. By contrast, the throughput of phenotypic screens is generally lower, and costs may be higher, in comparison to HTS [32]. Yet, the elevated complexity in cells, in comparison to biochemical assays using purified proteins, provides insight into the physiological effects of pharmacologic modulation of the target of interest. This accounts not only for the influence of posttranslational modifications and varying metabolite levels but also for protein-protein interactions, all of which can be critical for compound efficacy, biomarker identification, and patient stratification [33].

Phenotypic assays can be classified as either cell-, tissue-, or organism-based. In the context of cell-based assays, tumour-derived cells can often display abnormalities, thus assays utilising more native cells, such as induced pluripotent stem cells or human primary cells, can be advantageous [34]. Conversely, three-dimensional culture systems of patient-derived stem cells can be more relevant as disease models [35]. In general, the use of human cells and tissues, if available, should be preferred over rodent samples, as identical genetic mutations may not lead to inconsistent phenotypes in vivo [36]. Examples of medicines with novel mechanisms derived from cellular phenotypic screens comprise of disease areas spanning spinal muscular atrophy, cystic fibrosis, and hepatitis C [37, 38].

Ivacaftor, a potentiator of the CFTR-mediated chloride-ion transporter, was discovered in a gain-of-function assay in NIH/3T3 cells using a CFTR mutant, rescuing epithelial cell function in cystic fibrosis [39]. Secondly, an orally available inhibitor of the hepatitis C virus (HCV) protein NS5A was identified in an HCV replicon phenotypic screening hindering the replication of the virus directly [40]. Another example, risdiplam (used for treatment of spinal muscular atrophy), was found to modulate splicing and restore a missing exon in SMN2 mRNA in a screen monitoring survival in rat primary motor neurons [41]. In the context of animal model-based phenotypic screening, lacosamide was found to enhance sodium ion channel slow inactivation in an in vivo screening in rodent epilepsy models [42].

The libraries used for target-based and phenotypic-based drug discovery approaches differ due to the differences in experimental design and assay objectives. While target-based libraries are built around a known target with pharmacophores and scaffolds derived from screenings (in vitro or in silico), phenotypic-based libraries are maximally diverse in a biological and chemical sense to cover various new drug scaffolds and target proteins as starting points [43]. Ideally, compounds for phenotypic screens should have good solubility and cell permeability [43]. The aforementioned differences in library design are reflected in the type of hits each assay produces: while target-based screenings identify small molecules as direct binders of the target or interaction site, the hits from phenotypic screens require target deconvolution and mechanistic studies to identify the MoA of the hit compound. Chemoproteomic methods are thus suitable to examine compound effects and target engagement *in cellulo*.

1.1.2 Chemoproteomics and chemical probes in drug discovery

Chemoproteomics has recently emerged as a field at the interface of chemistry, biochemistry, and cell biology and is a powerful means to study target engagement and molecular mechanisms of small molecules [44]. Chemoproteomic techniques can provide phenotypic or cell-based platforms for both screening and optimisation of compounds and compound libraries against targets for which no biochemical assay is available or where the proteins are difficult to express and purify, as well as platforms for identification of the target of bioactive small molecules. For the latter, the power of chemoproteomics lies in the ability to identify both targets and off-targets of molecules, taking protein-protein interactions (PPIs), post-translational modifications (PTMs) or co-factors into account. Chemoproteomics can also be used to re-assess compounds with known targets, as described for the PRMT5 inhibitor GSK3326595 in chapter 5.

Additionally, chemoproteomics can be utilised to assess proteins and pathways which have previously been considered as difficult-to-drug, such as RAS or WNT/β-catenin pathways [15]. The overactive WNT pathway was found to cause β-catenin accumulation and cell proliferation and has thus been implicated in numerous cancers [45]. Compound XAV939 was found to inhibit the WNT pathway by increasing axin levels, which in turn stabilise the β-catenin destruction complex, leading to the degradation and proteolysis of β-catenin [46]. A subsequent affinity-based chemoproteomic study using an XAV939-analogue in an experiment revealed that two protein isoforms were inhibited, tankyrase 1 and tankyrase 2, which prevented axin degradation stabilising the destruction complex. Another useful example to consider is the identification of voltage-dependent anion channels (VDACs) as targets of erastin, a ferroptosis stimulator. VDACs are located in

the mitochondrial membrane and have been shown to have a gatekeeper function in the regulation of metabolism and apoptosis [47]. Using an analogue of the compound erastin immobilised on solid-phase beads, a chemoproteomics study reported VDAC1, VDAC2, and VDAC3 as novel targets [48]. These channels have been linked to oxidative cell death via the RAS-RAF-MEK-axis, and interestingly the compound lethality was found to be greater in KRAS-mutated cancer cells. Both VDAC2 and VDAC3 have been indicated as essential for erastin's effect in cancer cells [49]. These examples underline that cell-active compounds may be found to act through more than one target protein.

Phenotypic- or cell-based assays are furthermore excellent systems to study small molecule tool compounds which aim to elucidate the functional role of targeted proteins in physiologically relevant environments. These so-called chemical probes serve as research tools to interrogate target proteins and their functions, and they can serve as starting points for the development of new therapeutic modalities. While an FDA approved drug primarily must be safe and effective, it may still have an undefined MoA. In fact, the drug aspirin widely-used for fever and pains was only in 1971 classified as a non-selective cyclooxygenase inhibitor [50]. Concomitantly, lithium, which is used to treat bipolar disorders as a mood stabiliser, to this day has a largely undefined MoA [51]. By contrast, for a chemical probe, a defined MoA is required, and selectivity must be demonstrated. Furthermore, these probes are often made freely available for the research community to enhance the functional annotation of the human genome [52]. In order for these tool compounds to deliver robust, reliable and biologically relevant data, criteria for chemical probes have been developed [53]. The Structural Genomics Consortium (SGC), a collaboration of academic and industry partners has defined that chemical probes for epigenetics targets are required to display an in vitro potency at the target protein < 100

nM with a selectivity > 30-fold over proteins in the same family, they need to be profiled against a panel of pharmacologically relevant off-targets and should achieve on-target effects in cells < 1 μM [1]. The use of a structurally related, negative control is crucial to provide evidence that the effect observed in a phenotypic-screen is caused by the target engagement of the active chemical probe [54].

While there exist well-characterised chemical probes, certain other inhibitors are not characterised according to the standards mentioned above and therefore might be prone for unwanted off-target binding. An example is staurosporine, which was first described as an inhibitor of protein kinase C [55], but was later found to be a pan-kinase inhibitor instead and was described as unsuitable as a chemical probe [2], as it was addressing 395 targets [56]. Especially compounds containing pan-assay interfering compound (PAINS) motifs often create artifacts in assays as they react promiscuously and then produce misleading readouts [57]. PAINS might interfere with an assay by inherent colouring or fluorescence, or they can introduce trapped metal ions from the synthesis into the assay leading to false positive signals. As of their high reactivity, they mostly do not bind into classical binding-pockets and are likely to react with multiple proteins or form aggregates [58]. Common PAINS are flavones and polyhydroxylated natural products, such as resveratrol. Resveratrol was thought to address sirutin directly, however it was shown that the compound only affected SIRT1 deacetylating activity in presence of a TAMRA-labelled peptide substrate and was found to require the fluorophore for its exerted effect [59]. The same study showed multiple off-targets for resveratrol and therefore it is sought not to be a suitable tool compound for the studying of sirutin and related pathways. A

[1] https://www.thesgc.org
[2] https://www.chemicalprobes.org/unsuitables/Staurosporine

flavonol, epigallocatechin-gallate, was identified as a DYRK1A kinase inhibitor effective in transgenic mouse models overexpressing the kinase [60]. Epigallocatechin-gallate contains a highly-promiscuous PAINS motif, catechol, a known redox cycler, which can lead to the formation of reactive chelators and orthoquinones that can bind to proteins, lipids and nucleic acids leading to assay interference [61]. In order to reduce the preponderance of PAINs as hits in high-throughput screens, electronic filters have been developed to evaluate screening libraries and improve the recognition of PAINs motifs [62].

A huge landmark in the development of chemical probes was the discovery of the bromodomain inhibitors JQ1 [63] and I-BET [64]. The compounds were initially found to regulate gene expression by inhibiting PPI between BET bromodomains and lysine residues on histones. With these tool compounds in hand, inhibitors of other bromodomains were able to be evaluated for their ability to suppress tumour cell proliferation. Interestingly, JQ1 itself was validated through a combination of a cell-based and a phenotypic assay; a fluorescence recovery after photobleaching (FRAP) assay using GFP-tagged BRD4 was conducted to demonstrate the inhibited binding of the bromodomain to chromatin, and patient-derived NUT midline carcinoma cells were used to demonstrate inhibition of growth and cell cycle progression in a highly clinically relevant model [63]. Nowadays, there are a number of well-characterised chemical probes for an array of protein families, among them kinases, hydrolases, methyltransferases, transcription factors, ion channels, or bromodomains [65]. To study chemical probes, tool compounds and analogues can be functionalised for chemoproteomic experiments e.g. with an amine affinity handle for immobilisation on beads or with an alkyne-tail for click-reactions with reporter-tags for visualisation in WB, or with biotin-tags for enrichment studies. For instance, with the hepatitis C virus-encoded protein NS5A, an azide-

containing clickable compound was used to elucidate subcellular co-localisation of the target (note that, interestingly, larger BODIPY-containing reporter molecules had failed to do so) [66]. In another example of i*n vivo* chemoproteomics, a clickable analogue of chemical probe PF-04457845 was administered to mice orally, followed by tissue biopsy, in-lysate click reaction with a rhodamine-azide fluorophore, and subsequent in-gel visualisation to demonstrate both target engagement and high selectivity for FAAH [67].

1.1.3 Target 2035

Target 2035 is a worldwide science endeavour to help develop pharmacological modulators for every protein in the human genome by the year 2035 [68]. The aim is to provide chemical and biological tool compounds to annotate and interrogate functions and disease-relevance of the entirety of the human proteome. The project has two main phases [3], of which we are currently in phase I, where the focus lies on the creation of a roadmap to characterise and collect existing pharmacological modulators and create novel ones for protein candidates from all protein families, as well as on development of a centralised data hub and core facilities for biochemical and cell-based assays and profiling studies [69]. Phase II, starting in 2025, will be primarily focussing on completing the set of chemical probes for all proteins; arising therapeutic modalities, such as PPI interrupters or PROTACs are also of interest as they can enable the creation of novel pharmacological modulators. In addition to Target 2035, the EUbOPEN partnership of excellence (Enable and Unlock biology in the OPEN) [4] aims to generate a large number of novel chemical probes for example for E3 ligases by using biochemical and cell-based, chemoproteomic

[3] https://www.target2035.net/target2035-phases
[4] http://www.eubopen.org/

techniques for their characterisation. As of the time of writing, 206 validated chemical probes exist for a variety of targets [5].

Building on existing criteria for chemical probes, quality criteria for reversible and irreversible covalent as well as degrader chemical probes have been proposed [70]. With respect to target-related criteria, the authors propose assessment of biochemical and cell-based potency, selectivity within a family, and biophysical proof of target engagement (Table 1). As the inhibitory effect of covalent probes is time-dependent, biochemically derived IC_{50} values approximate compound potency and serve as a surrogate for more precise studies of inactivation rate and target affinity (K_{intact}/K_i) [71]. For covalent chemical probes, the site of covalent labelling should be reported, and for degraders, both on-target binding of POI and E3 ligase should be evaluated. Selectivity studies with covalent probes can be supported by ABPP and pulldown studies using biotinylated analogues for on-bead enrichment. With respect to the chemical matter, PAINS motifs should be excluded to avoid promiscuity, suitable inactive controls should be introduced, and the stability and solubility of compounds in aqueous or organic solvents should be ensured.

[5] https://www.thesgc.org

Quality criteria	Reversible CP	Covalent CP	Degrader CP
Potency	Biochemical < 100 nm, cellular < 1 µM	Provide K_{intact}/K_i, cellular < 1 µM	DC_{50} < 1 µM, Dmax > 80%
Selectivity	> 30-fold within family	> 30-fold to neighbours + unbiased proteomics	> 30-fold to neighbours + unbiased proteomics
Target engagement	Biophysical proof of on-target activity	Site of covalent labelling	Proof of on-target POI and E3 activity
Chemical matter	Derisk promiscuous and PAINS compounds		
Controls	> 100-fold weaker on target	Intact warhead, > 100-fold weaker	Intact binder, > 100-fold weaker
Stability/reactivity	Stability in media	Avoid excess reactivity	Avoid deterioration of structural integrity

Table 1: Criteria proposed for reversible, covalent and degrader chemical probes (CP). Table adapted from Hartung et al. [70]

1.2 Non-proteomic methods for evaluation of target engagement in cellulo

1.2.1 NanoBRET

For the quantification of target engagement and the formation of compound-target complexes, Bioluminescence Resonance Energy Transfer (BRET) provides a robust method for profiling in live cells [72]. In a typical BRET experiment, energy is transferred from a donor to an acceptor molecule by Förster transfer (Figure 1A), with BRET partners needing to be within close proximity (< 10 nm) for the transfer to occur [73]. A typical acceptor is a small molecule conjugated to a fluorophore, referred to hereafter as an energy transfer probe (ETP). The fluorophore moiety is often either boron dipyrromethene (BODIPY) or tetramethyl rhodamine (TAMRA) which differ in their excitation and emission wavelengths (Figure 1B). By contrast, the donor is usually a luciferase conjugate of the target protein, expressed either transiently or stably within the cell. There are three important requirements for a functional BRET assay: first of all, both fusion protein and ETP should be labelled with luciferase and fluorophore, respectively, without disturbing their function. Moreover, they should be configured and localised appropriately within the experimental setup, and lastly the energy transfer needs to be monitored in a suitable microplate reader in real-time [74].

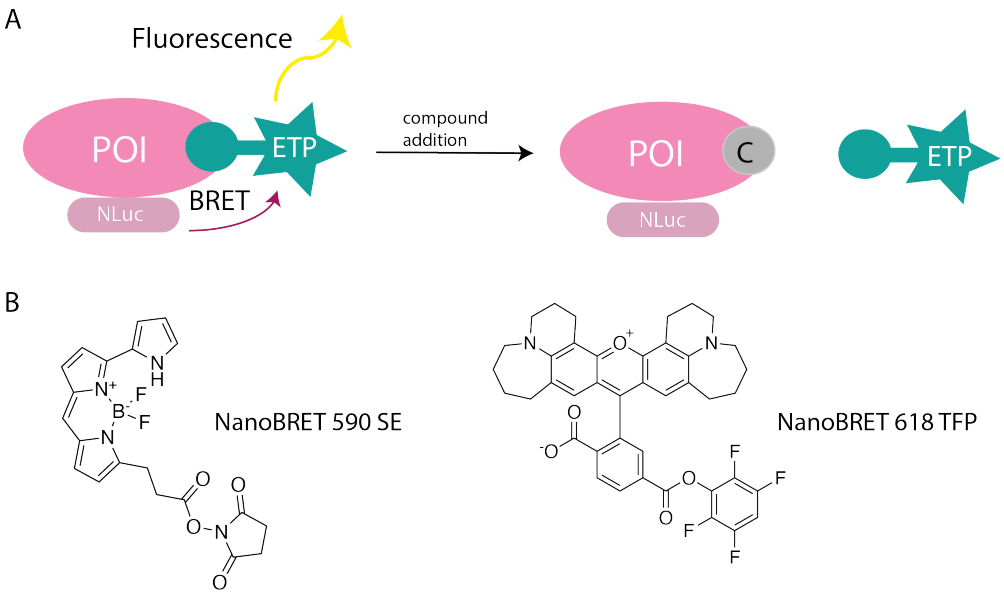


Figure 1: NanoBRET principle and commonly used fluorophores. A)NanoBRET TE assay principle: The NanoLuciferase (NLuc) is fused to the POI and can excite the fluorophore of the energy transfer probe (ETP) through BRET. If a compound (C) outcompetes the ETP, the signal is interrupted. B) Commonly used fluorophores developed by Promega Corporation.

The BRET method was first established in 1999 when Xu et al. studied circadian clock proteins in cyanobacteria using Renilla Luciferase (RLuc) as an energy donor consuming coelenterazine and yellow fluorescent protein as an acceptor [75]. This system soon became known as BRET1, and later other systems, such as BRET2 or NanoBRET, have been developed aiming to optimise the spectral separation of donor and acceptor to reduce background signal and increase sensitivity. NanoBRET utilises NLuc [76], a small engineered protein of 19 kDa which uses furimazine, a derivative of coelenterazine, as a substrate and has been shown to produce sustained luminescence with high intensity [77]. The study also focused on optimising the acceptor fluorophore and found a nonchloro-TOM ligand to yield the greatest signal with no toxicity as well as rapid saturation. As an alternative to ETP, a HaloTag-fusion protein was used, which readily incorporates fluorophores and, together with NLuc, allows for the use of NanoBRET to study PPIs. Dixon et al. developed a NLuc-derived split luciferase reporter system named NanoBiT

[78], inspired by protein-fragment complementation assays. NanoBiT consists of a large 18 kDa NLuc fragment (LgBiT) and a small 1.3 kDa fragment (SmBiT). SmBiT has been optimised to exert low intrinsic affinity to the complementary LgBiT enabling the system to measure weak PPIs and was used to study, e.g. GPCRs [79].

Fluorescence resonance energy transfer (FRET) is an alternative to BRET that can be used in cells, lysates or on purified proteins [80]. However, FRET requires two fluorophores, and one must be excited by an external light source for the energy transfer to happen. By contrast, BRET is independent from an external excitation as the emission of light occurs internally due to luminescence, where energy is provided by substrate consumption. BRET circumvents common problems in FRET assays, such as photobleaching, autofluorescence or undesired excitation of both fluorophores simultaneously [74]. On the other hand, a disadvantage of BRET is that it needs at least one luciferase fusion protein whereas FRET can rely on fusion antibodies alone. Several studies involving kinases and even PROTACs have shown that NanoBRET is a powerful platform to study direct compound-target interactions in a quantitative manner [81-83].

1.2.2 Cellular Thermal Shift Assay

Cellular Thermal Shift Assay (CETSA) has emerged as a powerful technique to directly evaluate TE in cells by monitoring ligand-induced thermal stabilisation of proteins. In a CETSA assay, the cellular TE is determined by the local compound concentration and the binding affinity of the compound. In turn, the compound levels within the cell are dependent on permeability and, in a broader, more systemic sense, are determined by absorption, distribution, metabolism, and excretion. The affinity of a compound is

affected by the state of the protein within the cell, as it might bear PTMs, such as phosphorylation regulating its activity, or form PPI complexes, which might impede compound binding [84]. In a typical CETSA experiment, thermal melting curves can be derived from the soluble fraction of proteins in heated cell lysates, similar to differential scanning fluorimetry (DSF) experiments using purified proteins. Thermal shifts obtained from such experiments are useful surrogates for compound activity and have been shown to correlate with the IC_{50} at high compound concentrations [85]. Note that in a DSF experiment, the detection of thermal shifts relies on a fluorescent dye which binds to unfolded protein surface indicating the protein melting point [86], whereas in CETSA, the unfolded protein fraction is removed by centrifugation and native protein levels are measured via immunoassay or mass spectrometry. Conceptually, CETSA comprises the following steps: compound treatment (lysates, cells or tissue), sample exposure to a heat gradient to thermally denature and precipitate unstabilised proteins, cooling and lysis (if applicable), extraction of the soluble fraction and detection of the contained proteins [87]. CETSA can be conducted in variations such as Western blot-CETSA for validation of compound binding to the target or MS-based CETSA for target deconvolution and evaluation of on- and off-targets on a proteome-wide scale [88]. CETSA has found use as a powerful technique to validate clinical drug candidates. For instance, it was used to evaluate PARP1 inhibitors in cells: whilst olaparib, a validated PARP1 inhibitor, displayed a thermal shift, iniparib, a candidate that failed clinical trials, interestingly did not [84].

1.2.3 Fluorescence Recovery After Photobleaching

FRAP stands for Fluorescence Recovery After Photobleaching and is a microscopy technique which allows for quantitative observation of protein mobility within cells. A selected region of interest in the cell containing fluorescent protein (e.g. GFP-tagged) is irradiated with a laser beam, which induces photobleaching (i.e. the fluorophore irreversibly loses the ability to fluorescence due to photon-induced damages to its chemical structure) and the recovery time of fluorescence intensity within the area can be recorded [89]. The recovery time depends on the dynamic protein re-distribution, binding, and mobility (due to Brownian motion), which can be influenced by inhibitory compounds. The photostable GFP-tag is widely used in FRAP to study the function and localisation of tagged proteins in live cells [90]. Note that the fluorescent-tag should be bright and photostable and react to photobleaching instantly without harmful side effects and should not affect protein function.

Generally, a FRAP workflow depends on the unique protein studied, its localisation, the used cell line, and the available microscope [91]. Common steps include tuning the acquisition settings to allow for optimal data collection, bleaching the region of interest with a pulsed laser beam, and the time-lapsed acquisition of the fluorescence recovery followed by data analysis to identify half-time of recovery and percentage of immobile fraction [92]. FRAP is a versatile technique: it has been used to study membrane proteins [93], as well as subcellular regions such as the endoplasmatic reticulum [94] or mitochondria [95], and nuclear proteins such as transcription factors (e.g. SOX9 [96]). Moreover, nuclear proteins can be monitored in terms of their mobility within the nucleus and their interactions with the immobile DNA [97]. FRAP was shown to be a viable assay for

screening bromodomain-containing proteins *in vivo*, contributing to the development of chemical probes: Philpott et al. studied a set of 11 bromodomain-containing proteins using FRAP for monitoring binding of the BRD to chromatin directly [98]. Proteins with a mutated acetyl-lysine binding pocket served as a viable negative control for ablating chromatin binding and supported testing of the cell permeability and efficacy of these BRD-inhibitors.

1.3 Chemoproteomic methods enabling drug discovery

Chemoproteomic techniques can be divided into experiments on a global, proteome-wide scale, which monitor the cell-wide effects of a compound under physiological conditions (e.g. with respect to PPIs, PTMs, co-factors, localisation and abundance), and targeted experiments, which are compound-centric and focus on affinity- or activity-enrichment techniques to investigate the on- and off-targets of a given compound [44]. Global experiments usually involve the treatment of cells with compound and DMSO vehicle control to monitor proteome-wide changes when the system is exposed to the compound. The sheer number of proteins in these sample types often limits the analytical depth of the data, as the detection of changes on proteome-level is biased towards more abundant proteins. Detected changes in protein levels might account for housekeeping or stress response genes rather than true targets [99].

Typically, as no target enrichment is performed, the changes within the proteome are challenging to detect, therefore a good separation of peptides or proteins contained in the sample is desirable to increase the resolution. In the past, 2-dimensional gel electrophoresis with fluorescent-tags was commonly used to evaluate compound effects

[100]. These gels allow for simultaneous evaluation of hundreds of proteins, however there are limitations with regard to the resolution of membrane proteins, very basic/acidic proteins or very small/large proteins [101]. Nowadays, with the advance of MS machine development, the introduction of tags, efficient separation techniques such as pre-fractionation and sensitive detectors, peptide identification and quantification has enabled the evaluation of thousands of proteins in one sample [102, 103]. In turn, differential stable isotope labelling techniques have facilitated the quantification of differences in two biological samples on a global scale; these techniques comprise, e.g. stable isotope labelling by amino acids in cell culture (SILAC) [104] or isotope-coded affinity tag (ICAT) [105]. Quantification can also be achieved through chemical labels, such as tandem mass tags (TMT) [106], or in a label-free fashion, which requires no tag [107]. Compound-centric, affinity-enrichment pulldowns represent a label-free method where the enriched targets of two differently treated samples are compared.

1.3.1 Compound-centric pulldown (affinity-enrichment)

Compound-centric pulldowns are valuable tools to demonstrate a compound's global target engagement and selectivity. In principle, a bioactive compound is immobilised on beads as a bait for proteins (Figure 2) This is usually done by installation of an amide-linker in a position, which does not affect compound binding and thus requires extensive structure-activity-relationship (SAR) studies to investigate where the linker can be attached. The linker a can be reacted with free NHS-esters on agarose or sepharose beads to create an affinity matrix. Cells or lysates are pre-treated with either parent compound or DMSO vehicle control, in the compound-treated sample the binding partners will be occupied, whereas in the control sample these proteins and binding sites remain free.

Subsequently, the pre-treated lysates are combined with the affinity matrix for enrichment, where the free proteins in the control sample can bind to the bait. In contrast, the proteins treated with the parent compound are pre-occupied and do not bind. The enriched proteins are washed and eluted from the beads before tryptic digestion and analysis via MS. Bantscheff et al. highlight several considerations for affinity-enrichment [108]. For example, the installation of the linker should not interfere with the compound's bioactivity. Furthermore, the lysis should be performed in non-denaturing conditions to ensure protein folding, solubility, and preservation of PPI; in turn this likely affects the detection of membrane proteins, which require harsher lysis methods. The enrichment at the bait is affected by the abundance of the proteins and their binding affinity to the compound, thus appropriate negative controls (inactive compounds) should be included in the analysis.

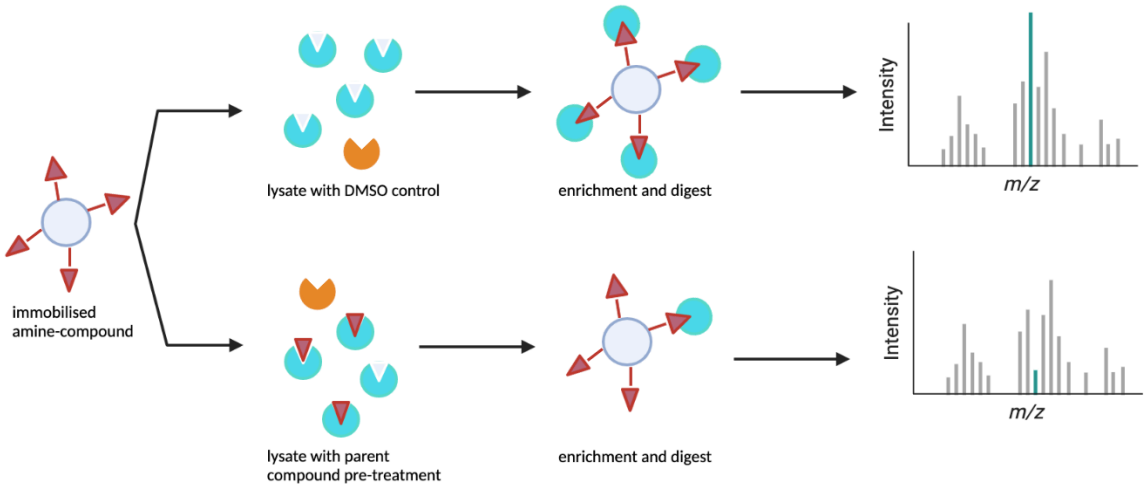


Figure 2: Schematic of a compound-centric pulldown based on an affinity-matrix. After immobilising an amine-compound on NHS-activated sepharose beads, the remainder of the reactive groups is blocked using ethanolamine. Lysates can either be pre-incubated with competitor or DMSO before enrichment and digest of enriched proteins, followed by submission to MS. Schematic was drawn with Biorender.

As discussed earlier, affinity-enrichment-based chemoproteomic techniques have been of great benefit to drug development, as they allowed to refute iniparib as a PARP-inhibitor, off-targets of an FAAH inhibitor were revealed, and CRBN was identified as the target of thalidomide. Compound-centric pull-down experiments have been widely applied in the field of kinases: Brehmer et al. profiled immobilised analogue of kinase inhibitor gefitinib in HeLa lysates and found serine/threonine kinase GAK as a target [109]. Similarly, Godl et al. investigated inhibitor SU6668 and revealed Aurora kinases and TANK-binding kinase 1 as unexpected targets [110]. As a result, the idea of combining known kinase inhibitors as bait on beads led to the development of kinobeads matrix. which provides a highly efficient profiling platform for around 200 kinases [111]. On the one hand, this approach allowed for profiling of targets of the immobilised, unselective inhibitors which did reveal new targets [112] and on the other hand, this approach was further developed as a screening platform for competitive experiments to profile free competitors against the kinobeads matrix to reveal target selectivity of the competitor [113]. While affinity-enrichment is used for non-covalent compounds, activity-enrichment is applied to covalent binders.

1.3.2 Activity-based Protein Profiling and isoTOP ABPP (activity-enrichment)

The most prominent example of activity-enrichment is Activity-based Protein Profiling (ABPP). The method pioneered by Benjamin Cravatt [114] uses covalent active site-directed probes, known as reactive probes, to profile catalytic sites and amino acid residues in functional hotspots or protein surface areas [1, 115]. In ABPP assays, function and ligandability of proteins, as well as exact compound binding sites can be investigated. Conceptually, reactive probes contain an electrophilic, promiscuous warhead linked to an

analytical tag for fluorescent visualisation or on-bead enrichment of modified proteins. Fluorophosphonates were early reactive probes targeting active site serine residues in the serine hydrolase family [116]. Further development led to more promiscuous and broadly reactive probes, containing iodo- and chloroacetamide or acrylamide groups [117-119], as well as iodo- and bromoketones [120, 121]. The thiol group of cysteines is highly nucleophilic under physiological conditions ($pK_a \leq 8.5$) [122], yet hyperreactive cysteines can occur when the local microenvironment surrounding the thiol group elevates the acidity of these residues. Hyperreactive cysteines make up around 10 % of solvent-exposed cysteines [123]. Amino acid reactivity can be monitored in ABPP by using tiered concentrations of reactive probe, e.g. Lin et al. distinguished hyperreactive from less reactive methionine residues by varying the dose of the label [124]. By functionalising the reactive probe with a fluorescent tag, gel based ABPP techniques enable the assessment of modified targets [125]. Recombinant protein or probe pre-treated proteomes derived from cells can be resolved by 2-dimensional SDS-PAGE, and labelled bands are followingly visualised via Western blotting or fluorescent dyes. Gel-based readouts are convenient for optimisation of experimental parameters such as probe concentration, buffer conditions, pH, or incubation times.

Competitive ABPP for profiling of covalent ligands as competitors is a powerful tool to characterise reactive amino acid residues and to map ligandable hotspots *en masse* in complex systems, such as cells and lysate, in the presence of native state proteins [126]. A typical reactive probe utilised in isotopically differentiated Tandem Orthogonal Proteolysis-ABPP (isoTOP-ABPP) is composed of four features: 1. reactive group, 2. alkyne-handle, 3. TEV-tag, containing 4. heavy or light valine isotope [123, 127, 128]. The reactive group, an electrophilic covalent warhead, is conjugated to an alkyne handle for

further functionalisation. A copper(I)-catalysed azide-alkyne cycloaddition (CuAAC) with the reporter group bearing an azide yields 1,4-disubstituted 1,2,3-triazoles [129, 130]. Earlier activity-based probes combined the aforementioned features into one moiety, causing poor properties due to the bulkiness of the whole molecule. By contrast, separating the reactive warhead from the reporter-tag facilitated cell-permeability whilst reducing the risk of impeding interactions of the warhead.

The competitive isoTOP-ABPP workflow is depicted in Figure 3A. By pre-incubating cells or lysates with electrophilic competitors, reactive residues (nucleophilic amino acids) on proteins can be profiled against the promiscuous reactive probe. In contrast, these residues remain unreacted in a DMSO control sample. When the reactive probe is added, the remainder of the nucleophilic amino acids react with the probe, which can be further functionalised. Commonly in global cysteinome studies, iodoacetamide-alkyne (IAA) is used in combination with the azide-containing TEV-cleavable biotin tag (Figure 3B). By performing CuAAC, the tag is conjugated to the modified amino acids. In the next step, both the DMSO control and fragment pre-treated samples are mixed, enriched on streptavidin beads, and subjected to on-bead tryptic digestion before the TEV-tag cleavage to elute modified peptides. Both protein identity and binding site can then be determined in LC-MS/MS analysis. Competition ratios (R) are derived from the quantification of MS1 chromatographic heavy/light peptide peak ratios, generally a cut-off of $R > 4$ is applied, equivalent to 75 % competition [119].

IsoTOP-ABPP has been shown to be a powerful and versatile approach capable of interrogating a range of ligands, from small fragments to large and complex natural products. The platform can be used to reveal exact binding sites and inform about changes

in protein abundance and off-targets while quantitatively probing the proteome treated with reactive probe or competitors. The TEV-cleavable tag requires using TEV protease to elute modified peptides from the beads, as the interaction between biotin and streptavidin is strong. Further advances resulted in the design of a smaller, isotopically differentiated desthiobiotin (isoDTB)-tag (Figure 3B), superseding the TEV cleavage step as the interaction via desthiobiotin is reversible and peptides can simply be eluted from the beads with organic solvent [131]. Streamlined cysteine activity-based protein profiling (SLC-ABPP) studies employed TMT-labelling and replaced IAA with a dual desthiobiotin iodoacetamide (DBIA) probe (Figure 3B). SLC-ABPP was shown to increase the throughput for screening large electrophilic compound libraries while requiring 20-fold lower sample input and reduced MS analysis time [132]. Optimised sample preparation in combination with online high-field asymmetric waveform ion mobility spectrometry (FAIMS) separation has been shown to allow for in-depth profiling of the human cysteinome in isoTOP ABPP [133].

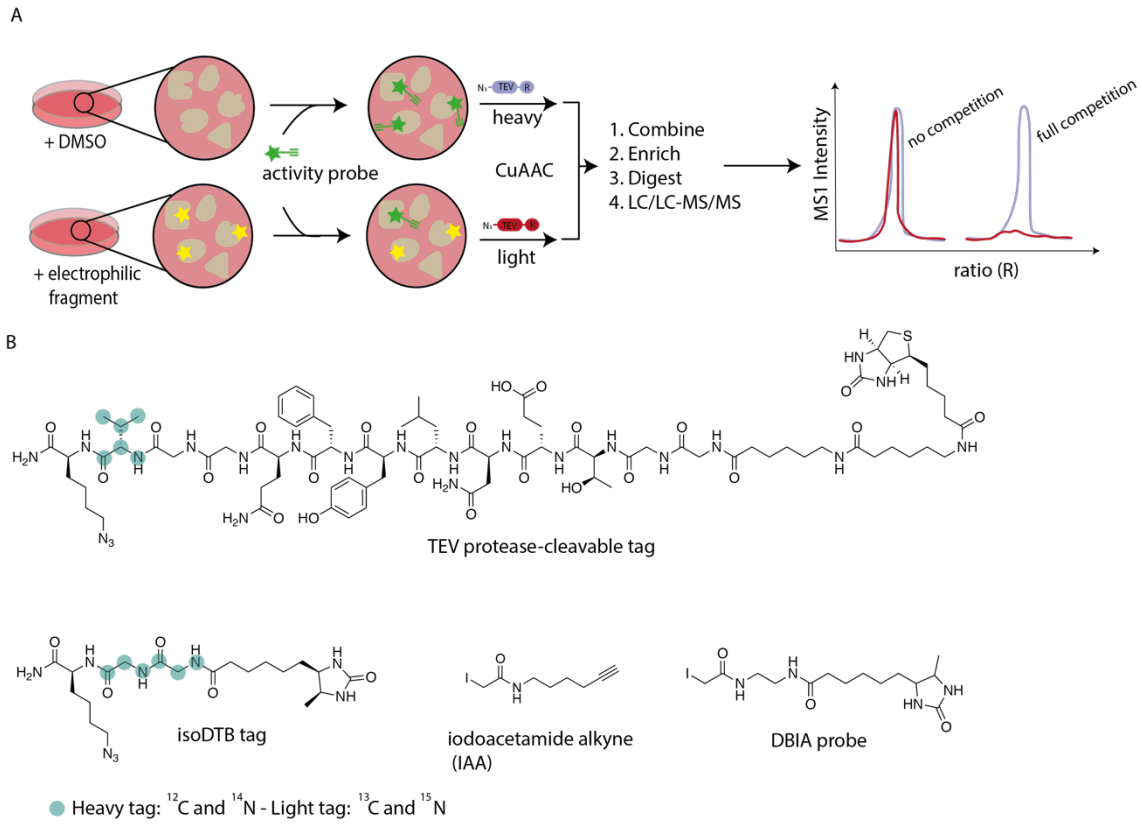


Figure 3: isoTOP-ABPP as schematic workflow and commonly used tags and probes. A) isoTOP-ABPP workflow. B) Different tags used in ABPP approaches. Top: TEV protease-cleavable tag, employing biotin. Bottom: isoDTB tag (left) and DBIA probe (right), both employing desthiobiotin. Middle: iodoacetamide-alkyne probe.

As described above, isoTOP-ABPP is a powerful tool to interrogate the reactivity of hundreds and thousands of cysteine residues in the human proteome. The identification of site-specific, selective covalent ligands which engage certain cysteines and the translation into mechanistic tool compounds is facilitated by employing phenotypic assays upstream as a pre-selection step. For example, isoTOP ABPP has been utilised to investigate vulnerabilities in altered biochemical pathways of genetically defined cancers. Mapping of cysteine ligandability in wild-type cells versus KEAP1-mutant cancer cells revealed a restricted subset of ligandable cysteines in the aberrant cell line. This comparison led to the identification of an advanced chemical probe targeting the lowly expressed protein NR0B1, which had been difficult to target with other therapeutic modalities [134]. In another example, target deconvolution by isoTOP-ABPP followed a cell-based autophagic flux assay, which led to the identification of a covalent fragment (EN6) as an autophagy activator engaging v-ATPase [117]. Vinogradova et al. created a comprehensive ligandability map for activated human T cells by applying TMT-ABPP [126]. Crowley et al. established an Enzyme-Linked Immunosorbent Assay (ELISA)-ABPP approach and developed a potent, active-site-directed inhibitor binding a cysteine in retinaldehyde reductase AKR1B10 [135]. ABPP has helped to deliver a potent clinical drug candidate, compound ABX-1431, to control neuronal lipid metabolism by covalently inhibiting monoacylglycerol lipase [136]. The ABPP workflow can also be multiplexed with fluorescent probes. Janssen et al. recently reported a multiplexed ABPP assay using a newly developed fluorophosphonates-BODIPY probe to visualise the activity and selectivity of endocannabinoid hydrolase inhibitors in mouse brains [137]. Based on a protein arginine deiminase (PAD) inhibitor, a fluorescent rhodamine-conjugated F-amidine (RFA) probe for gel-based ABPP was developed, which was successfully optimised into

a HTS approach for profiling changes in fluorescence polarization, which occur when RFA binds to PAD protein (fluopol-ABPP) [138, 139]. Drechsel et al. investigated a tranylcypromine analogue bearing an alkyne-diazirine minimal photo crosslinker and found promiscuous labelling and enrichment of MAOA protein [140].

1.3.3 Covalent fragment screening

Screening of covalent ligands is an emerging paradigm in drug discovery [141]. As only a small percentage of human protein classes can be addressed with non-covalent molecules [142], covalent ligands may facilitate the development of binders for novel proteins while offering significant advantages over non-covalent ligands (Table 2). In contrast to the latter, covalent binders do not necessarily require well-defined binding pockets to form protein-ligand adducts and can covalently react with amino acid side chains in more shallow crevices or with surface-exposed residues. The formation of a covalent bond results in a prolonged ligand residence time and an elevated pharmacodynamic half-life of the ligand as the protein and ligand engage in a 1:1 stoichiometry that is dictated by the protein re-synthesis rate [143]. The increased potency of covalent ligands may allow for the use of lower drug doses and thus may potentially reduce side effects in patients. The reactivity of covalent warheads can be synthetically adjusted to achieve highly selective compounds addressing specific residues on distinct protein targets, e.g. for KRAS G12C, a selective warhead for a disease-relevant mutant was reported [144]. Covalent ligands may help to tackle drug resistance, address “undruggable” binding sites, and displace high-affinity endogenous binders [145]. However, to avoid toxicity and off-target binding due to promiscuous, non-selective interactions, the reactivity of covalent warheads requires

careful consideration [146, 147]. Such cytotoxic effects may also originate from non-specific aggregation of off-target proteins as indicated for two DUB inhibitors containing Michael acceptor-motifs [148]. A major issue stemming from covalent fragment reactivity is poor stability in liquid stock solutions. Covalent fragments can potentially react with water and degrade when stored for prolonged periods in DMSO solution (> 6 months, 4 °C) [149], thus, careful monitoring of storage conditions and frequent quality control sampling is required.

Covalent ligands	
Advantage:	Disadvantage:
- prolonged residence time	- idiosyncratic toxicity
- selective towards residues	- hyperreactivity
- irreversible mechanism	- promiscuity
- binding of novel targets	- off-target binding
- no need for defined pocket	
- enhanced potency	
- overcome/circumvent resistance	

Table 2: Advantages and disadvantages of covalent ligands listed.

A number of recent studies have demonstrated that fragment-based covalent ligand screening employing covalent fragment libraries can be applied to ligand discovery in cells with great success [150-152]. Fragments are usually defined according to the rule of three: low molecular weight (≤ 300 Da), hydrogen bond donors ≤ 3, hydrogen bond acceptors ≤ 3, and a calculated lipophilicity clogP of ≤ 3 [153]. Due to their comparably small size, fragments can sample available chemical space efficiently by fitting into regions of shallow binding pockets, crevices, and allosteric sites, which may be shut off to larger molecules [154]. Additionally, they are less prone to unfavourable perturbations such as steric clashes due to their low structural complexity. As fragments form a limited number of interactions with their target, they bind with low affinity and require screening at

concentrations in a μM-mM range to identify initial hits. As these high concentrations increase the risk of non-specific and off-target binding to multiple proteins, orthogonal screens are required to eliminate false-positive hits [155]. Generally, fragments provide the potential for structure-based optimisation of preliminary hits into potent binders. After identifying initial fragment hits, their MoA and TE can be evaluated through site-specific mutagenesis or mass spectrometry studies, respectively [156]. Resnick et al. successfully identified potent electrophilic OTUB2 and NUDT7 binders by employing native MS experiments and complementary crystallography studies [157]. Similar efforts yielded a covalent inhibitor of the RBR E3 ligase HOIP originating from a library screen of 104 α,β-unsaturated methyl esters [149]. Expanding fragments by fragment growing, merging, or linking is a useful strategy to convert initial hits into larger and more potent binders exerting selective, high-quality interactions [158].

1.4 Aims of the project

This project aimed to employ and further optimise chemoproteomic and non-chemoproteomic methods described in the introduction for the purpose of profiling small molecules and covalent fragments on a global scale.

Chapter 2 introduces how a bioinformatic analysis of a transcriptomic and proteomic dataset provided the basis for the selection of four cancer cell lines to achieve a maximal coverage of E3 ligases contained in four cell lines: K562, NCIH226, DU145 and U251. Our in-house total proteome data exceeded the predicted coverage of E3 ligases, which allowed us to further explore the ligandability of the identified E3 ligases. For this, we selected and monitored the reactivity of a versatile library of eight reactive probes with electrophilic covalent warheads targeting nucleophilic amino acid residues, such as cysteine. To distinguish between highly reactive residues and residues, which require non-covalent interactions and coordination events, we also selected a corresponding set of lipophilic competitors.

Chapter 3 delves into the establishment and optimisation of the isoTOP ABPP workflow using the isoDTB-tag and focusses on profiling the ligandability of E3 ligases with respect to nucleophilic amino acid residues. After successfully demonstrating that the obtained data is in line with recent literature on reactive probe profiling, we screened the library of eight versatile reactive probes and competitors in the four cancer cell lines. Our derived E3 ligase druggability map showed interesting sites for enriched and competed E3 ligase sites, providing a useful information source for further development of starting points for inhibitor or recruiter development. We investigated the effect of labelling in cells and lysates in addition to distinct MS data acquisition modes.

Chapter 4 describes how the optimised isoTOP ABPP platform was successfully employed to profile a chemical probe for KEAP1. The chemical probe was binding to a site which could not be directly addressed by iodoacetamide-alkyne reactive probe, yet we could indirectly show the high selectivity of this probe. Additionally, a chemical probe for NUDT7 was screened, and we could show direct labelling of NUDT7_C72 residue for the first time in isoTOP ABPP using a vinyl sulfone-alkyne reactive probe. Following a phenotypic screen of a covalent fragment library for NLRP3 inflammasome inhibitors, we aimed to utilise the platform for target deconvolution of electrophilic fragment hits. Additionally, CETSA, FRAP, and intact MS methods were used to validate fragment hits derived from the competitive isoTOP screening described in chapter 3.

Chapter 5 demonstrates the development and optimisation of a first-in-class NanoBRET target engagement assay for methyl transferase PRMT5. We synthesised a very potent energy transfer probe, CBH-002, which we demonstrate as suitable for evaluating both SAM- and substrate-competitive PRMT5 inhibitors. Furthermore, we show the effect of co-factor SAM on compound binding in lysates. A compound-centric pulldown highlights the exquisite selectivity of clinical compound GSK3326595, which is supported by a Western blot CETSA.

Chapter 6 reports a NanoBRET protein-protein interaction assay for the evaluation of interrupters of the DENND1A/RAB35 interaction. Multiple rounds of screening a 1500-membered covalent fragment library yielded preliminary hits, which were subsequently tested against recombinant protein. However, the fragments were shown to be promiscuous and rather unselective in intact MS, and mapping of the binding sites on RAB35 were unsuccessful so far.

Statement of Authorship for joint/multi-authored papers for PGR thesis

To appear at the end of each thesis chapter submitted as an article/paper

The statement shall describe the candidate's and co-authors' independent research contributions in the thesis publications. For each publication there should exist a complete statement that is to be filled out and signed by the candidate and supervisor **(only required where there isn't already a statement of contribution within the paper itself).**

Title of Paper	Covalent fragment-based ligand screening approaches for identification of novel ubiquitin proteasome system modulators
Publication Status	X Published □ Accepted for Publication □Submitted for Publication □Unpublished and unsubmitted work written in a manuscript style
Publication Details	Review: Rothweiler EM, Brennan PE, Huber KVM. Covalent fragment-based ligand screening approaches for identification of novel ubiquitin proteasome system modulators. Biol Chem. 2022 Feb 23;403(4):391-402. doi: 10.1515/hsz-2021-0396. PMID: 35191283.

Student Confirmation

Student Name:	Elisabeth Mira Rothweiler		
Contribution to the Paper	Literature research, contributed to all parts of the review, made all figures		
Signature	Elisabeth Mira Rothweiler	Date	13.09.23

Supervisor Confirmation

By signing the Statement of Authorship, you are certifying that the candidate made a substantial contribution to the publication, and that the description described above is accurate.

Supervisor name and title: Kilian Huber		
Supervisor comments		
Signature Huber	Date	18/09/23

This completed form should be included in the thesis, at the end of the relevant chapter.

2. Chemical modulation of protein homeostasis

Parts of this chapter have been published in a first-author review by Rothweiler et al. about covalent fragment-based ligand screening and ubiquitin proteasome modulators [1].

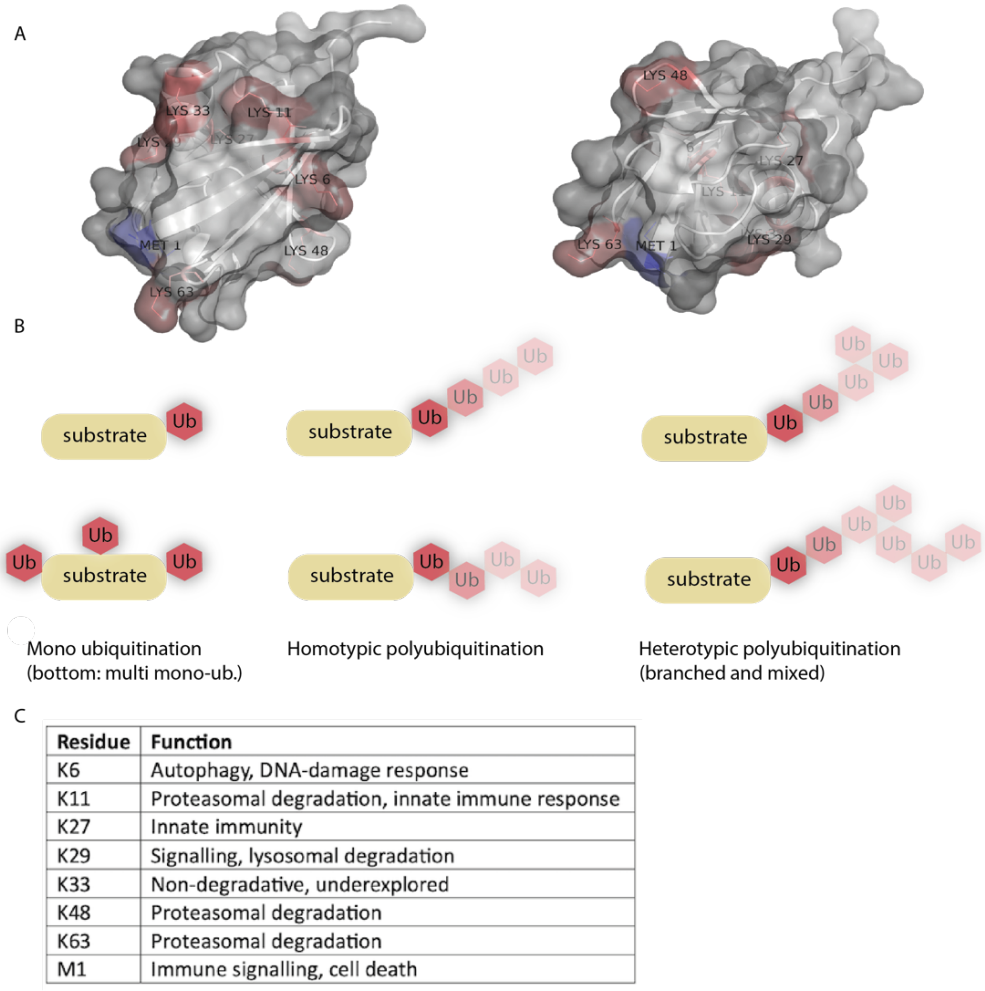
The human proteome is thought to comprise around ten thousand proteins at any given time during the cell cycle, all of which need folding in a specific and unique structure to correctly serve their designated cellular function [159]. As cells are permanently subjected to internal and external cues, constant remodelling, repair, or elimination of defective proteins is required to avoid malfunctions [160]. During the cell cycle, protein homeostasis (proteostasis) regulates the synthesis, folding, conformation, and removal of proteins. Several mechanisms, called the proteostasis network, control that correctly folded and functional proteins are generated at the right time and in the right cellular localisation. A constant supply of vital proteins and a minimal accumulation of misfolded proteins are crucial for maintaining cellular function [161]. In contrast, an imbalanced proteostasis leads to unfolded, metastable proteins which become functionally inactive, paving the way for the accumulation of cytotoxic protein aggregates of damaged proteins or unassembled subunits of multiprotein complexes [162]. Such failure to adapt to cell division or differentiation processes is associated with medical disorders ranging from Alzheimer's to type 2 diabetes as well as cancer, a result of unabated cell proliferation [163, 164].

The two major proteolytic pathways are the autophagosomal-lysosomal pathway and the ubiquitin-proteasome (UPS) pathway [160, 165]. In the former pathway, there are two autophagy types: micro autophagy, where a proportion of the cytosol as well as the contained proteins are fused with nascent lysosomes and become matured lysosomes; and macro autophagy, which occurs in stress situations such as starvation or hypoxia, and

larger entities such as organelles (e.g. mitochondria) or dysfunctional protein aggregates are engulfed and digested [166, 167]. In comparison, the UPS pathway focusses more on short-lived, misfolded and damaged proteins influencing the cell cycle, proliferation, transcription, apoptosis and other biological processes [167]. The UPS-pathway can be chemically modulated via targeted-protein degradation or targeted protein stabilisation.

2.1 Proteostasis: the ubiquitin proteasome pathway

Ubiquitination, the modification of proteins with ubiquitin (Ub) as a PTM alters protein stability, function, and intra- or intermolecular interactions [168, 169]. Ub is a conserved, small globular protein consisting of 76 amino acids that is covalently bound to lysine-residues of target proteins to serve maintenance of cellular proteostasis [170]. The UPS pathway orchestrates signal transduction, and regulates activity, localisation and complex formation of proteins, and controls proteasomal degradation of ubiquitinated proteins. The site of ubiquitination as well as certain Ub chain patterns, collectively called the Ub-code, determine the fate of modified proteins [169, 171]. The discovery of monoubiquitylation, the attachment of a single Ub molecule to histone H2A, led to the identification of the first substrate of the UPS pathway [172]. Ub contains seven lysine residues (K6, K11, K27, K29, K33, K48, and K63) and a N-terminal methionine residue (M1) (Figure 4A), providing eight starting points for Ub chain formation by isopeptide linkage [173]. K6 to K33 ubiquitination is often referred to as non-canonical [174]. Homotypic chains are connected repeatedly through the same residue, in contrast to heterotypic chains (mixed and branched) where residues alternate (Figure 4B) [175]. The polymeric chains are recognised by Ub-binding domains, which trigger downstream processes including recruitment to subcellular location, signalling complex assembly, or protein turnover [176].



C

Residue	Function
K6	Autophagy, DNA-damage response
K11	Proteasomal degradation, innate immune response
K27	Innate immunity
K29	Signalling, lysosomal degradation
K33	Non-degradative, underexplored
K48	Proteasomal degradation
K63	Proteasomal degradation
M1	Immune signalling, cell death

Figure 4:Ubiquitin and it's relevant residues for ubiquitination, and Ub-chain types. A) Position of residues on ubiquitin which can be linked to isopeptide bonds comprising seven K and one M residue (PDB: 1UBQ). The Ub pictures were recorded by Martin Buttenschön in Pymol. B) Ub-chain formation starting with mono- or multimonoubiquitylation. Then either homotypic (linked in the same pattern) or heterotypic chains (linked from alternating residues) can be formed. The linkage type determines the fate of ubiquitinated substrates and therefore is called the "Ub-code". C) Decoded functions of Ub-chain formation.

K48 ubiquitination and Ub chain formation on the substrate lead to transport to the proteasome and degradation into peptides [177]. Several E3 ligases associated with protein degradation, such as SCF [178] or E6-AP [179], form K48 chains and it has been shown that, depending on the substrate, chains of at least two to four Ub molecules are required for recognition by the 26S proteasome [180]. In line with these findings, K48-linked chains trigger degradation via the proteasome in systems relying on purified proteins [181].

Conversely, selective cleavage and removal of K48-linked chains by deubiquitinases (DUBs) [182, 183] can prevent substrate degradation [184]. K11-linked chains, similarly to K48-chains, have been found to drive proteasomal degradation, indicated by their accumulation upon proteasomal inhibition [185, 186]. As another chain type, K63-linked chains are mostly involved in proteasome-independent pathways, such as DNA repair [187], endocytosis, and mitochondrial degradation in inclusion bodies [188, 189]. Yet, K63 has been found to serve as a seed for K63/K48 branched chains for proteasomal degradation [190]. A brief summary of decoded Ub-chain functions is given in
Figure 4C.

The proteasome is of critical importance for the degradation of short-lived substrates involved in cell cycle progression, signal transduction, apoptosis, immune response, metabolism, and protein quality control [191, 192]. The eukaryotic 26S proteasome is a multisubunit ATP-dependent protease of 2.5 MDa [193], consisting of a gated core particle (20S subunit), which is capped by a regulatory particle (19S subunit), jointly forming a base and a peripheral lid. The 19S subunit is responsible for substrate recognition and deubiquitylation and guides the unfolded substrate into a barrel-shaped chamber with proteolytic activity [194]. USP14, a DUB, is associated with the lid and has been shown to activate proteasomal degradation in two steps: initially, it interacts with the ubiquitinated substrate and in the second step, unfolded polypeptide chains are presented to the ATPases in the base, driving substrate degradation and opening the 20S gate [195, 196]. Notably, ubiquitination is no guarantee for proteasomal degradation, recently it has been shown that for Ub chains in disordered regions the distance between the Ub recognition receptor and the site engaging with the substrate's unfolded disordered region are important [197]. Additional Ub-recognition units at the 26S proteasome are the regulatory

subunits RPN10 and RPN13, as well as proteasome-associated proteins RAD23, DSK2, and DDIL1 [160]. After an initial interaction of the substrate with USP14, the DUB RPN10 removes Ub chains *en bloc* in a delayed mode, tightly coordinating the deubiquitylation and degradation of substrates [198, 199]. Otherwise, Ub chains would obstruct the substrate from entering the core particle. The core particle consists out of four seven-membered rings, outer α and inner β rings. While the outer rings form a gated entrance into the barrel, the inner rings bear proteolytic sites on β1, β2, and β3 subunits for degradation of cytosolic, nuclear, and membrane proteins [200]. These β subunits can cleave acidic, basic and hydrophobic amino acid residues from the C-terminus with caspase-, trypsin- and chymotrypsin-like function [201, 202]. Usually, substrates are cleaved into peptides of 3-25 amino acids in length [203].

2.1.1 E3 ligases and their role in cellular homeostasis

Overall, the ubiquitination cascade is characterised by the sequential interplay of E1, E2, and E3 enzymes in three steps, acting as writers of the Ub-code [204, 205]. In the first step (Figure 5), Ub is activated in an ATP-dependent manner by E1 ubiquitin-activating enzymes, forming a thioester linkage between the E1 active site and the Ub C-terminus. In the second step, Ub is transferred from the E1 to one of 41 human ubiquitin-conjugating enzymes (E2) in a trans-thiolation reaction. In the third step, Ub is transferred to a ε-amino group on a lysine residue by interaction with a ubiquitin-protein ligase (E3) [206]. The importance of this cascade and its key role in proteostasis is underscored by the fact that current annotation suggests the human genome encodes > 600 E3 ligases in total [207].

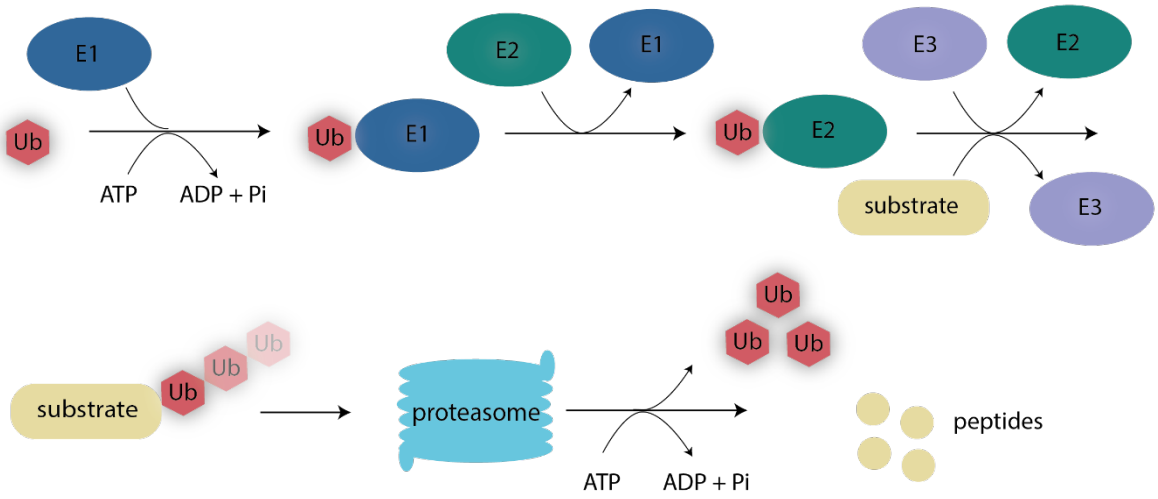


Figure 5: Ubiquitin-proteasome pathway showing interplay of E1, E2 and E3 enzymes which orchestrate substrate ubiquitination and subsequent degradation into peptides via the proteasome.

There are three families of E3 ligases with distinct mechanisms of Ub transfer to their substrates. Really interesting new gene (RING) E3 ligases include RING E3 ligases as well as RING-like U-box family E3 ligases, which account for most of the annotated E3 ligases in the human genome. RING E3 ligases coordinate two Zn^{2+} ions in a closed, cross-braced arrangement to create a surface promoting the binding of E2 ligases, which bear an Ub at their active site cysteine [208]. RING E3 ligases recruit the E2-Ub complex and act as mediators, facilitating a nucleophilic attack of the E2-Ub thioester bond by the substrate nucleophile, thus forming a new isopeptide bond. The E2 ligase is crucial for the E3 ligase substrate specifity, as some E2 ligases perform exclusive Ub-linkages while others are more promiscuous; as a result, distinct E2/E3 pairings enable the generation of different Ub-linkages [209]. The RING E3 ligase diversity and substrate specificity are further highlighted by a broad range substrate receptors and adaptors, such as CRBN and VHL, belonging to the Cullin/RING ubiquitin ligases (CRL) family, the largest subfamily of RING E3 ligases [210]. Another E3 ligase family are Homologous to E6-AP

carboxy terminus (HECT) E3 ligases, which form a covalent E3-Ub intermediate via a cysteine-dependent trans-thiolation reaction before transferring Ub onto a substrate [206]. HECT ligases bear a bilobal HECT domain at their C-terminus, comprising an N-lobe, which contains the E2 binding domain as well as a C-lobe, which carries a catalytic cysteine group. In a transthiolation reaction, Ub is transferred from an E2 ligase onto the catalytic cysteine of the HECT E3 ligases, which is then able to directly ubiquitinates substrate proteins [211]. Described as RING/HECT hybrid ligases [212], RING-between-RING (RBR) E3 ligases use a hybrid mechanism, for which a canonical RING domain is connected to an ancillary domain that catalyses Ub transfer [213]. RBR ligases are formed by a tripartite domain arrangement, consisting of three zinc-binding domains, the RING1 domain binding the E2-Ub complex, the in-between-RING (IBR) and RING2 domains coordinating two Zn^{2+} ions. The RBR ligases are found to act heterogeneously within their family as some adapt multistep Ub-transfer mechanisms [214, 215]. In contrast to RING E3 ligases, RBRs form an open E2-Ub conjugate conformation before the Ub residue is transferred to the RING 2 active site for direct transfer to substrate proteins, which is analogous to HECT E3 ligases [216].

As mentioned previously, acting as antagonists or erasers of these ubiquitination processes, around 100 DUB enzymes exist that can edit and cleave Ub chains [217], therefore rendering ubiquitination a dynamic process that enables cells to react to altered internal and external cues.

2.1.2 The therapeutic means PROTACs and DUBTACs

Over the last twenty years, the growing understanding of the UPS pathway has made it a highly attractive target in drug discovery. The field of targeted protein degradation (TPD) enabled chemical modulation or direct inhibition of untapped targets, such as E3s (for example HOIP and KEAP1 [149, 218]), and DUBs (such as USP7 [219] and OTUB1 [220]), which are involved in aberrant, Ub-dependent protein degradation and signalling pathways. Proteolysis Targeting Chimeras (PROTACs) are heterobifunctional molecules that have emerged in the field, allowing for recruitment of neo-substrates to E3 ligases for proteasomal degradation [221, 222]. Conversely, deubiquitinase-targeting chimeras (DUBTACs) and engineered DUBs (enDUBs) are bifunctional compounds that recruit a DUB to a protein of interest (POI) to prevent degradation by targeted protein stabilisation (TPS) [223, 224]. Currently, there are multiple PROTACs entering and progressing in clinical trials, as for example ARV-110 and ARV-471, respective androgen and oestrogen receptor degraders [225-227].

In general, a PROTACs is composed of three parts: a ligand for a POI, a spacer or linker moiety, as well as a recruiter for an E3 ligase. The formation of a productive ternary complex brings POI and E3 ligase into close proximity, thereby prompting ubiquitination and subsequent proteasomal degradation of biologically native and non-native targets (Figure 6A). Ternary complex formation is necessary, yet alone not sufficient for TPD thus it is being explored with the help of e.g. in silico methods [228], biophysical [229] and crystallisation studies [230] or DNA-encoded libraries [231]. PROTACs can turn non-functional inhibitors into degraders and expand the addressable protein space to challenging targets like scaffolding proteins or transcription factors, which lack enzymatic function and

defined pockets [232]. As of today, only a few E3 ligases and related substrate receptors are tractable for PROTAC design. Currently, there are non-covalent small molecule recruiters for MDM2 [233, 234], VHL [235, 236], cIAP [237], CRBN [24, 238, 239], DCAF15 [240-243], KEAP1 [244], while KLHL20 is targeted by a non-covalent macrocyclic peptide [245]. Chana et al. have shown a peptide binding to GID4-CTLH E3 ligase identified from a DNA-encoded library screen [246]. Acting as molecular glue (MG), HQ461 has been reported to modify CDK12 surface to facilitate interaction and degradation by DDB1-CUL4-RBX1 E3 ligase [247], similarly to compound CR8, which was reported to degrade cyclin K [248]. CRBN and DCAF15 are targeted by MGs [249] which bind to their target E3 ligase and act as adhesives to facilitate molecular recognition of the protein-protein interactions with the POI (Figure 6B). This class of compounds has been shown to address previously unligandable proteins, which were thought to be beyond the scope of small-molecule inhibitors and heterobifunctional degraders [249, 250]. Immunomodulatory drugs (IMiDs), for example thalidomide or lenalidomide, are often utilised as E3 recruiters in PROTACs [251]; and aryl-sulfonamides, such as indisulam, is an prominent example for a MG.

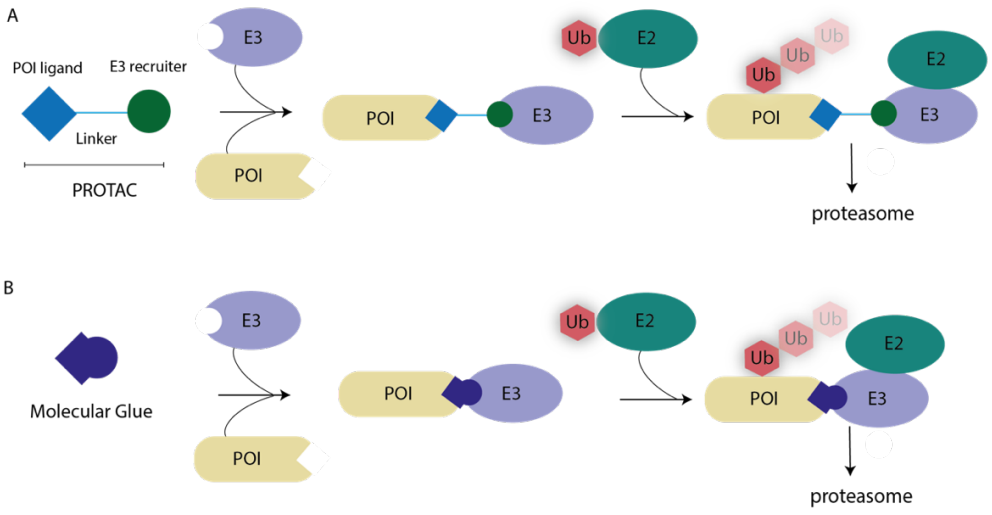


Figure 6: Targeted protein degradation strategies. A) PROTAC principle: a heterobifunctional molecule consisting of a recruiter for an E3 ligase linked to a ligand for a POI. B) Molecular glue principle: monomeric degrader facilitating interaction of E3 ligase and POI.

The substrate spectrum of a given PROTAC has been shown to be influenced by the choice of the E3 ligase, which enables the design of selective molecules. In the context of kinase degradation, Bondeson et al. found that VHL-based PROTACs were less promiscuous than CRBN-based degraders [252]. Donovan et al. also described differing kinase protein degradation patterns with regard to CRBN- and VHL-based PROTACs [253]. Additionally, different degradation patterns regarding BCR-ABL and c-ABL were found for CRBN- and VHL-recruiting PROTACs: VHL-based PROTACs could only degrade c-ABL [254]. Structural insights into selective degradation were given in a crystal structure of degrader MZ1 in complex with VHL and BRD4, which revealed not only PPIs between E3 ligase and substrate but also interactions with the folded linker [255]. Other studies with VHL- and IAP-based PROTACs were shown to degrade CDK6 specifically or in combination with CDK4 [256], underscoring the potential to alter PROTAC-induced degradation patterns by the choice of the recruited E3 ligases. A recent study varying only the linker length of a VHL-PROTAC demonstrated that this was sufficient for isoform-selective degradation of p38 MAPK [257]. Collectively, these findings highlight the potential and importance of characterising and addressing more of the over 600 E3 ligases and DUB enzymes for pharmacological modulation of proteostasis. An emerging area of interest are covalent recruiters to unlock novel E3 ligases as recruiters to realise the full potential of TPD.

2.1.3 Covalent E3 ligase recruiters

Covalent molecules represent an emerging resource to increase chemical coverage of E3 ligases and DUBs in order to expand the TPD/TPS toolbox (Figure 7). Several chemoproteomic studies identified electrophilic covalent warheads, which were addressing novel E3 ligases. For the E3 ligase RNF4, a covalent chloroacetamide recruiter was reported to be binding to zinc-coordinating cysteines in the catalytic RING domain, which enabled the development of a BRD4-degrading PROTAC [258]. Spradlin et al. were able to locate the binding site of the natural product nimbolide in an intrinsically disordered region, and showed the cyclic enone reactive group was binding to C8 on the E3 ligase RNF114. Subsequently, they developed bifunctional degraders recruiting RNF114 for BRD4 and BCR-ABL protein degradation [259]. Following up on these findings, the synthetic covalent fragment EN219 (chloroacetamide) was identified in a competitive ABPP study targeting RNF114 [260]. The triterpenoid bardoxolone, featuring a cyanoenone, has been demonstrated to act as a covalent reversible recruiter for the E3 ligase KEAP1 and was successfully employed to degrade BRD4 as a PROTAC [261]. Zhang et al. identified a DCAF11-directed electrophilic recruiter degrading endogenous proteins including FKBP12 in prostate cancer cells [262]. Covalent recruiters for DCAF16 based on a chloroacetamide [263] warhead have been shown, and recently DCAF1 was targeted via C1113 using azetidine acrylamides, which sucessfully degraded FKBP12 and BRD4 as PROTACs [264]. The CUL2 E3 ligase FEM1B was found to be addressable with the chloroacetamide EN106 at C186 within its substrate binding site [265]. Another chloroacetamide compound, MN551, was shown to address SOCS2 at C111 [266]. For UBR7, the natural product asukamycin has been reported as a binder, featuring poly-unsaturated amide and epoxyketone moieties [267]. Recently, enone-containing scaffold JP-

2-196 was reported acting as a covalent MG for CDK4, BRD4 and androgen receptor degradation [268]. In this study, a zinc-coodrinating cysteine (C32), was identified on RNF126 as a putative target; however, chemoproteomic profiling of JP-2-196 revealed other RING E3 ligases such as RNF40, MID2, RNF219, RNF14, and LRSAM1 as off-targets. The authors discuss that the covalent scaffold targets a common structural motif of RING E3 ligases and therefore requires optimisation for RNF216 selectivity.

Proteasomal degradation achieved via direct recruitment to the proteasome and without the involvement of an E3 ligase has been described by Qi et al., utilising an electrophilic compound termed RA190, which covalently binds to a cysteine of the ubiquitin receptor RPN13 [269]. By using RA190 in bifunctional molecules, BRD-containing proteins and histone methyltransferases were degraded. As a note, also a non-covalent macrocyclic peptide MC1 has been reported to recruit BRD4 via bifunctional molecule to the proteasome [270]. Also circumventing direct recruitment of E3 ligases, the Nomura group has shown degradation by recruitment of E2 ligase UBE2D with compound EN450, which acts as a molecular glue degrading NF-kB [271]. Following up on their hit, they identified electrophile EN67 in gel-based ABPP experiments and sucessfully developed a covalent E2-recruiting PROTAC [272]. Another compound, MM-02-57 (chloroacetamide), was shown to bind C173 on DDB1 covalently, thus directly targeting CUL4A complex adaptor DDB1 [273]. The authors demonstrate DDB1-mediated degradation through BRD4 and androgen-receptor PROTACs. Furthermore, the authors hypothesise that targeting essential components of the UPS, such as E2 ligases or adaptor proteins, might mitigate potential resistance risks in comparison to employing non-essential E3 ligases.

Aiming to modulate deubiquitination, covalent DUB inhibitors have been described for UCHL1 and USP7 [219, 274]. Propargyl warheads linked to Ub have been established as activity-based probes for DUBs [275-277]. Using a chemoproteomic strategy, a covalent recuiter (EN523) for OTUB1 addressing a non-catalytic allosteric cysteine was identified and successfully converted into a DUBTAC to stabilise mutant CFTR protein in human cystic fibrosis bronchial epithelial cells [223]. Based on EN523 covalently recruiting OTUB1 at C23, TF-DUBTACs degrading transcription factors were reported [278].

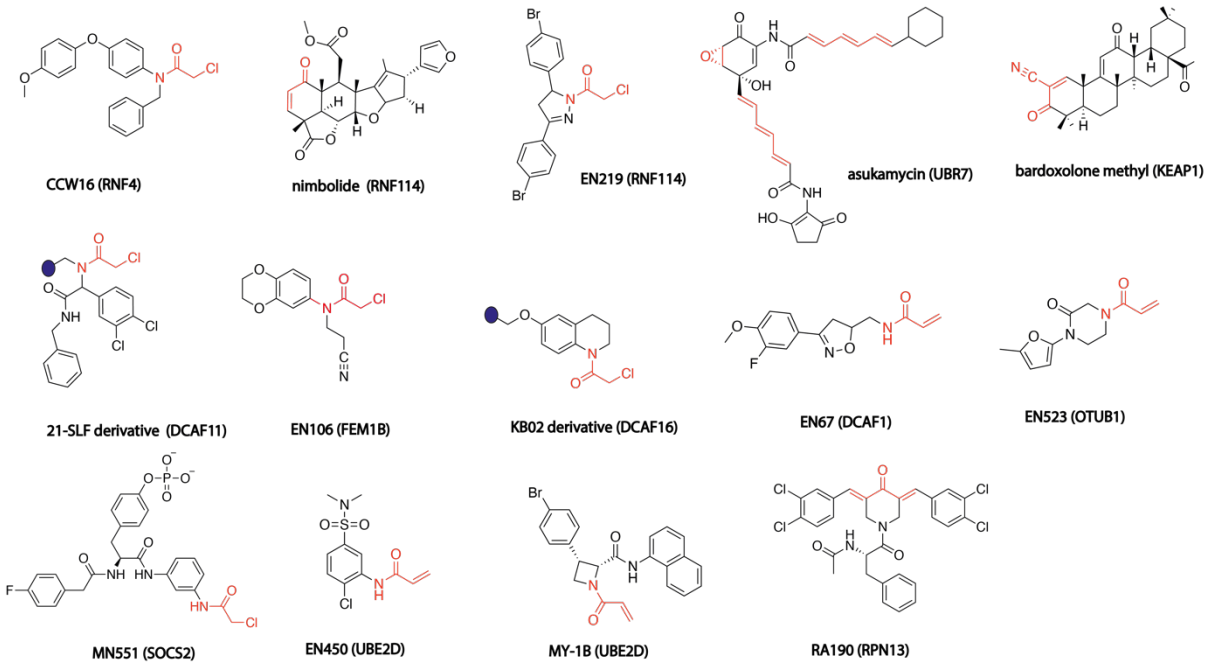


Figure 7: Covalent TPD and TPS recruiters targeting E3 ligases and DUBs. Recruited targets are stated in brackets. The blue dot represents attachment point implemented in PROTAC development.

Table 3 provides an overview of currently established TPD and TPS warheads utilising covalent binders to target cysteines and shows prominently featured chloroacetamide groups. Acrylamides, α,β-unsaturated groups, α-haloketones and boronic acids represent other frequently employed electrophiles [279]. In particular, chloroacetamides are presumed as indiscriminately reactive, hence diligent evaluation of these electrophiles is essential

to de-risk these scaffolds and minimise undesired off-target reactivity. These warheads are debated concerning their applicability in potential drugs with regard to their therapeutic window, promiscuity, reactivity and metabolic conversion products which may result in side effects [147, 280]. These concerns may be influenced by the prevalence of acrylamide and dimethyl amino acrylamides and the lack of chloroacetamides in approved drugs and compounds in advanced development [6]. Several chemoproteomic studies have aimed to further investigate these compounds to mitigate such concerns [281]. For both chloroacetamides and acrylamides limited evidence was obtained for broad unspecificity, especially when the covalent bond formation followed slow kinetics [279]. For example, Resnick et al. found no correlation between promiscuity (referring to nonspecific, irreversible covalent binding) and reactivity [157]. Further selectivity studies have been conducted for a few covalent binders including examples shown in Figure 7 and Table 3. For instance, the chloroacetamide CCW 28-3 was found to target seven unrelated proteins based on MS analysis [258]. Another chloroacetamide, EN219, was moderatively selective for RNF114 with four off-targets, while in both cases none of the off-targets were E3 ligases [260]. However, for MM-02-57 containing a chloroacetamide warhead, DDB1 was recently detected as the primary target ($R > 8$), but also 24 off-targets, and amongst them E3 ligases KEAP1 and ZNRF2 were identified in the isoTOP ABPP data [273].

Acrylamides undergo a two-step binding mechanism, initially interacting non-covalently before forming a covalent bond with the target residue. Unfunctionalised acrylamides were shown to be relatively unreactive towards thiol groups, whereas the introduction of

[6] https://www.cortellis.com

an electron-withdrawing group in the α-position facilitates hetero-Michael addition-type reactions which are reversible [282]. Reversible covalent binders are a potential interesting option to circumvent off-target binding by fine-tuning the fragment residence time and dissociation from the target protein [283]. However, the reversible nature of these interactions makes them more difficult to examine. For example, in a proteome-wide pulldown study for reversible covalent recruiter bardoxolone, other E3 ligases could not be ruled out as contributors to degradation as the direct detection of targets was challenging [261]. For the acrylamide-based DUBTAC NJH-2-05, only five off-targets were identified in competitive isoTOP-ABPP studies, whereby none of these proteins are part of the UPS [223]. For acrylamide EN67, only 11 targets were detected in HEK293 cells, of which only one target was involved in the UPS. These examples underline that isoTOP ABPP can be successfully utilised to investigate and select compounds with suitable reactivity and selectivity towards a POI.

Target	Ligand	Chemical class	Cysteine	POI binder	PROTAC/ DUBTAC
DCAF11 [a,l]	21-SLF	chloroacetamide	C460	SLF	21-SLF
DCAF16 [b]	KB02	chloroacetamide	C177, 178 or 179	SLF, JQ1	KB02-SLF, KB02-JQ1
FEM1B [c]	EN106	chloroacetamide	C186	JQ1	NJH-01-106
KEAP1 [d,l]	CDDO	cyanoenone	C23, 288, 196, 319	JQ1	CDDO-JQ1
OTUB1 [e,q]	EN523	acrylamide	C23	Lumacaftor, DNA oligomer	NJH-2-056, -057 FOXO-DUBTAC6
RNF4 [f]	CCW28-3	chloroacetamide	C132, 135	JQ1	CCW-16
RNF114 [g]	nimbolide	cyclic enone	C8	JQ1	XH2
RNF114 [h]	nimbolide	cyclic enone	C8	dasatinib	BT-1, BT-2
RNF114 [i]	EN219	chloroacetamide	C8	JQ1, dasatinib	ML2-14, ML2-23
RPN13 [j]	RA190	enone	C88	JQ1	RA-JQ-1, -2, -3, -4; LW-RPN13-6, -7
UBR7 [k]	asukamycin	epoxide, poly-unsaturated amide	C374	*nA*	*nA*
DCAF1 [m]	MY-1B	acrylamide	C1113		YT41S, YT41R
UBE2D [n]	EN67	acrylamide	C111	*JQ1, AR ligand*	*NF90, NF500C*
UBE2D [o]	EN450	acrylamide	C111	*nA*	*nA*
SOCS2 [p]	MN551	chloroacetamide	C111	*nA*	*nA*

Table 3: TPD/TPS targets addressed with covalent recruiters, sorted by chemical class, identified reactive cysteines and PROTACs/DUBTACs based on POI binders JQ1, SLF, dasatinib, lumacaftor and androgen receptor (AR) ligand for targeted protein degradation. Literature sources: [a] Zhang et al. [262], [b] Zhang et al. [263], [c] Henning et al. [265], [d] Tong et al. [261], [e] Henning et al. [223], [f] Ward et al. [258], [g] Spradlin et al. [259], [h] Tong et al. [284], [i] Luo et al. [260] , [j] Qi et al. [269], [k] Isobe et al. [267], [l] Belcher et al. [285], [m] Tao et al. [264], [n] Forte et al. [272], [o] King et al. [271], note this molecule acts as an molecular glue and therefore needs no POI ligand, [p] Ramachandran et al. [266], [q] Liu et al. [278].

2.2 Generating a E3 ligase druggability map

To expand the toolbox of covalently ligandable E3 ligases, we aimed to generate a global proteome-wide druggability map covering a maximal number of E3 ligases in the human proteome. For this, we utilised ABPP profiling of eight covalent reactive probes in four cancer cell lines. The cell lines were selected to provide a maximal coverage of E3 ligases for profiling, and the reactive probes were selected to cover distinct nucleophilic amino acids.

2.2.1 Bioinformatic analysis of a proteomic and transcriptomic dataset

To form a basis for our experiments, we assembled a panel of human cancer cell lines covering a maximum number of E3 ligases and focussed on the National Cancer Institute (NCI) [7] repository of over 60 diverse cell lines representing brain, lung, prostate, breast, ovary, colon kidney, leukaemia and melanoma cancers. This repository is widely used for compound screenings to develop anti-cancer drugs. To conduct our analysis, we initially derived a list of 635 E3 ligases from the Ubihub website [207]. In order to predict the coverage of E3 ligases in cell proteomes, we based our analysis on a quantitative proteomic dataset from the Kuster group[8], covering 10350 proteins in total [286]. To find the maximal number of E3 ligases, we utilised the tool kinaseblender[9], originally designed to analyse kinase data, providing a heuristic search algorithm to identify a combination of producers (i.e. cell lines) which are creating the maximal number of products (i.e. E3 ligases). We focussed the analysis on most unique products to maximise the coverage of

[7] https://dtp.cancer.gov/discovery_development/nci-60/default.htm
[8] http://wzw.tum.de/proteomics/nci60
[9] https://github.com/ThomasKuehne/kinaseblender

E3 ligases derived from NCI cell lines. To allow for a balance of handling the number of cell lines (e.g. required culture media, cell line availability) and gained E3 ligase coverage, we set a cut-off of four individual cell lines, resulting in K562 (lymphoma), NCIH226 (lung cancer), DU145 (prostate cancer) and U251 (glioma) cell lines as ideal producers. Based on the dataset, these cell lines were covering a number of 128 E3 ligases. While most of the E3 ligases were shared between these cell lines in the proteomics dataset, there were 16 unique E3 ligases for K562 (Figure 8A).

Additionally, a transcriptomic dataset of NCI cell lines from the Broad Institute[10] was analysed using the kinaseblender tool. As a result, a total number of 612 E3 ligases were identified in four cell lines: OVCAR3 (ovarian cancer), MALME3M (melanoma), SR786 (lymphoma) and NCIH522 (lung cancer) (Figure 8B). Overall, the mRNA data covered a higher percentage of E3 ligases in total, yet we chose to base our experiments on the proteomics dataset as a comprehensive resource covering protein expression, PPI and PTM, which are confined to proteome analysis. Sheer mRNA abundance cannot guarantee for expression of the respective proteins, yet transcriptomic data provides complementary biological information. The overlap of the proteomic and transcriptomic data was > 99%, E3 ligase ubiquitin like with PHD and ring finger domains 1 (UHRF1) was exclusively contained in the proteomic dataset (Figure 8C). This might be due to the different cell lines we found for each dataset as best producers.

[10] https://sites.broadinstitute.org/ccle/datasets

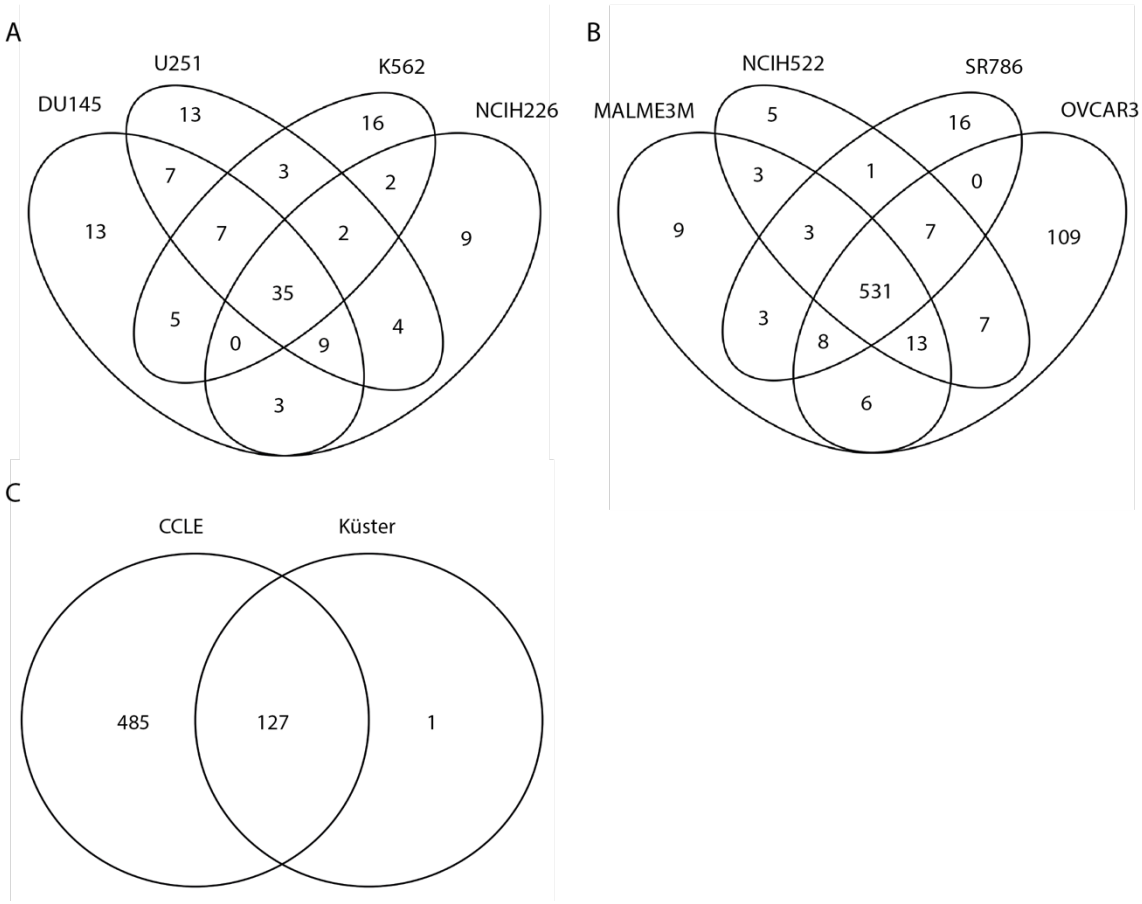


Figure 8: Results of the Kinaseblender analysis for the proteomic and transcriptomic dataset derived from the Küster group and the Broad Institute, respectively. A) Overlap of maximal number of E3 ligases from Küster dataset depicted as a Venn diagram: 127 identified E3 ligases in four cell lines K562, U251, NCIH226 and DU145. B) Overlap of maximal number of E3 ligases from CCLE dataset depicted as a Venn diagram: 612 identified E3 ligases in four cell lines OVCAR3, MALME3M, SR786 and NCIH522. C) Venn diagram depicting over 99% overlap of transcriptomic and proteomic dataset, UHRF1 is the only E3 ligase represented in the proteomics data exclusively.

2.2.2 Total proteome validation in-house

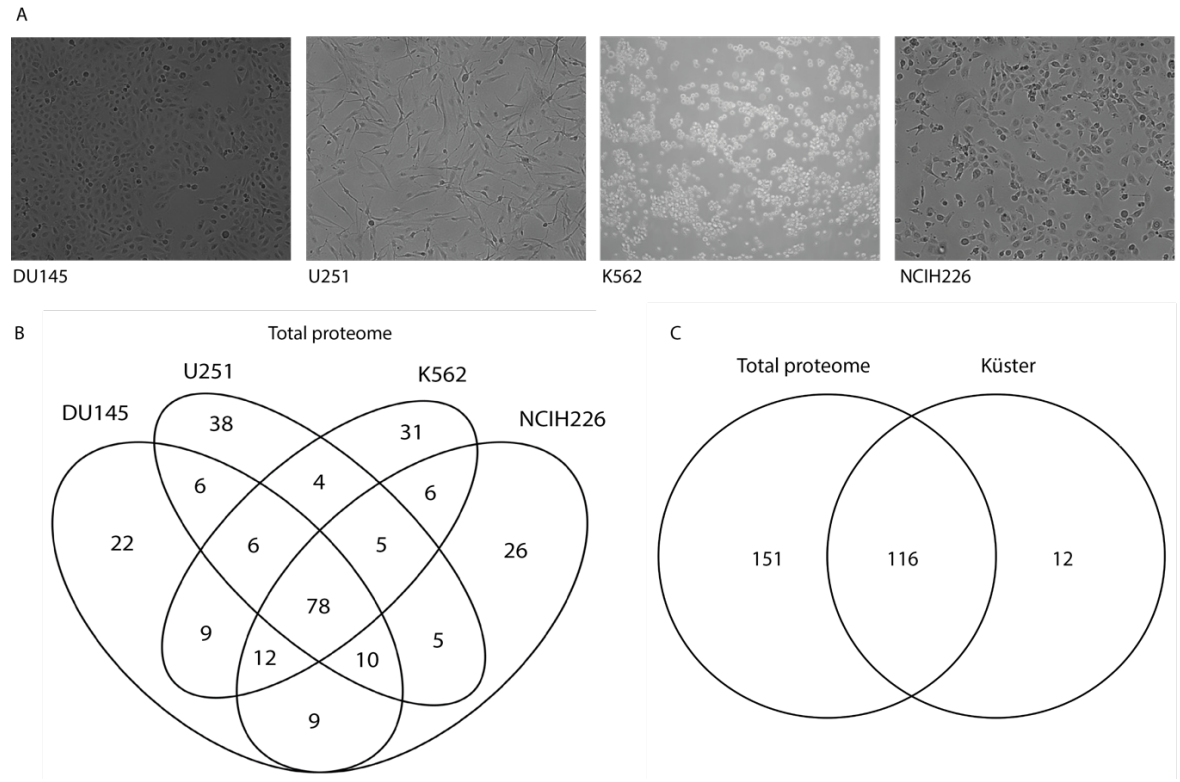


Figure 9: Venn diagrams depicting E3 ligase overlap between DU145, U251, K562 and NCIH226 cell lines. A) Morphology of cells at 10x magnification in the Zeiss light microscope (brightfield). K562 is a suspension cell line, the others are adherent cell lines. B)Venn diagram of identified E3 ligases in respective cell lines. C) Comparison of overlap of Küster dataset covering 128 E3 ligases and total proteome dataset covering 267 E3 ligases.

To confirm these predictions, the cell lines K562, NCIH226, DU145, and U251 were grown in-house (Figure 9A), and samples were subjected to a total proteome digest and high-pH reverse-phase prefractionation before submission to MS, and a total proteome (TP) dataset comprising over 7800 genes was obtained. In line with the previous analysis, most of the E3 ligases were shared between the cell lines (Figure 9B) and we were able to yield 276 E3 ligases in total. There was an agreement of 116 E3 ligases with the Küster group dataset, whereas they reported 12 E3 ligases which were not in our data. In contrast, we reported a number of 151 E3 ligases which were not contained in their dataset (Figure 9C). We highlighted identified E3 ligases in waterfall plots to visualise their distribution

and found, that they were scattered throughout the dataset. The most abundant proteins were housekeeping genes such as GAPDH or HSP proteins (Figure 10). Comparing the obtained proteins to the NCI cell line panel data from the Küster group, we exceeded the number of previously reported proteins and respective genes in those cell lines by > 30 % (Supplementary Table S1). We would like to highlight that the dataset from the Küster group has been obtained in 2013 using gel-based digestion, whereas we optimised the workflow and used an in-solution digest. Also, MS-machine development is rapidly advancing, and our dataset has been measured using the Orbitrap Fusion Lumos Tribrid (Thermo Fisher), whereas the proteomics dataset was recorded on a LTQ Orbitrap XL ETD or Orbitrap Elite mass spectrometer (Thermo Fisher) [286], likely contributing to the exceeded protein and E3 ligase IDs we were able to identify.

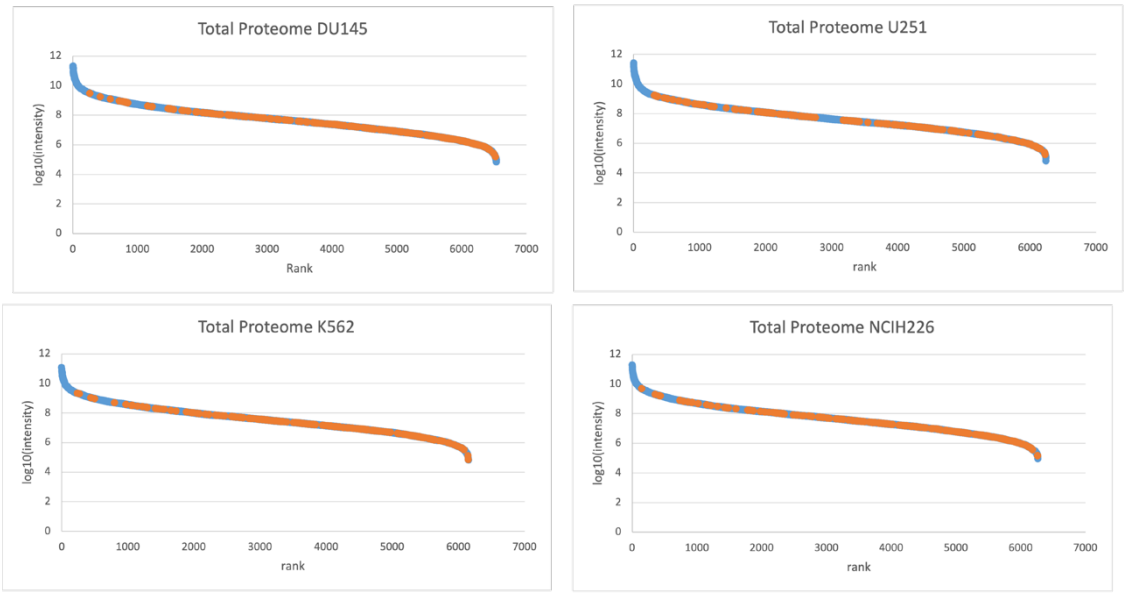


Figure 10: Waterfall plots depicting proteins identified in total proteome data. For cell lines DU145, K562, U251 and NCIH226 the reported E3 ligases are highlighted in orange, other proteins are labelled in blue, and proteins are ranked by obtained log_{10}(intensity) values.

Table 4 shows an overview of the top 10 E3 ligases reported in the total proteome dataset for each cell line, respectively. U251 showed the least overlap in its highest abundant E3 ligases in comparison to the other cell lines. TRIM28, HUWE1, GNB2, and RBBP7 were among the most abundant E3 ligases throughout the selected cell line panel. TRIM28 is a multidomain complex protein containing BRD, PHD, and RBCC domains and is related to RING E3 ligases, of which the 80-membered TRIM family forms a sub-population.[287] The TRIM28 abundance underlines its role in regulation of gene transcription, especially p53 activity, and DNA damage control, additionally it was found to be overexpressed in epithelial cancers, such as lung and prostate [288], as well as in glioma [289]. HUWE1, a large HECT E3 ligase, mediates the ubiquitinylation of over 40 substrates, plays a role in DNA damage response, proliferation, and cell differentiation, and has also been linked to tumorigenesis [290, 291]. Interestingly, we also detected RBBP7, which is a substrate receptor for CRL4B leading to HUWE1 polyubiquitination and proteasomal degradation [292]. The CUL4 substrate receptor GNB2 is thought to exert cardioprotective effects through GRK2 degradation [293]. To investigate the reactivity of E3 ligases against a panel of covalent probes, we proceeded to assemble a compound library for screening experiments.

U251		DU145		K562		NCIH226	
E3 ID	Intensity	E3 ID	Intensity	E3 ID	Intensity	E3 ID	Intensity
XIAP	11.417	TRIM28	11.3203	TRIM28	11.0869	TRIM28	11.2857
TRIM8	11.3715	HUWE1	11.2191	RBCK1	10.9604	HUWE1	11.1676
UBE3C	11.3098	UBR4	11.1774	UBR4	10.8648	FBXO2	11.1585
ARIH2	11.1663	GNB2	11.1618	RBBP7	10.8607	UBR4	11.0983
TRIM25	11.0777	RNF213	10.9785	HUWE1	10.8109	TOR1AIP2	11.0623
RNF14	11.0457	HECTD1	10.9475	GNB2	10.8089	TRIM25	10.9624
WWP2	10.99	PAFAH1B1	10.8673	PDZRN3	10.7921	RBBP7	10.8823
TRIM65	10.9372	NEDD4	10.8549	RBBP4	10.7356	PAFAH1B1	10.8397
RNF113A	10.8875	RBBP7	10.8496	PRPF19	10.7165	NEDD4	10.825
LRRC14	10.8833	TOR1AIP2	10.7526	UBE3A	10.7046	HECTD1	10.8072

Table 4: Tabular view of top 10 identified E3 ligases in total proteome dataset in each cell line. The LUMOS data was processed using MaxQuant without MBR. Duplicate E3 identifiers (E3 ID) in the data are highlighted in yellow. Log_{10}(intensity) is reported in the intensity column.

2.3 Selection of a covalent probe library

To select compounds that address a wide array of distinct amino acids, we reviewed the literature for available information and suitable scaffolds, with focus on alkyne-functionalised probes that can be utilised for ABPP or in-gel fluorescence experiments.

2.3.1 Reactive probes and competitors addressing distinct amino acids

The prospect of being able to expand the scope of protein druggability with covalent molecules is highly attractive. As IAA has been widely used for labelling reactive cysteine residues, we aimed to expand our compound library towards different reactivities. Currently, twelve (Arg, Asp, Cys, Glu, His, Lys, Met, Ser, Thr, Trp, Tyr, Phe) of the 20 canonical amino acids can be addressed [294, 295]. Continuing efforts are aiming to expand the repertoire of covalent warheads and novel reactive groups to allow for fine-tuning of their reactivity towards rather underexplored amino acid residues such as serine, tyrosine, lysine or threonine [296, 297]. Our library consisted of nine reactive-probes (Figure 11A): Probe 1 contains IAA and probe 9 contains a vinyl sulfone (VS) motif; both are Cys reactive warheads [114, 295]. Probe 5 bears an amine-reactive NHS-ester targeting predominantly Lys (also Tyr, Ser, Cys, Arg, and Thr reported as modified residues) [298]. Both probe 6 (sulfur triazole, SuTEX) and probe 8 (sulfonly fluoride, SF) have been shown to target Ser, Thr, Lys and Tyr [299, 300]. The oxaziridine-group in probe 7 reacts with Met residues [124]. The azirine in probe 12 was shown to target Cys , Glu and Asp [301], and the phenylglyoxal-group of probe 11 adresses Arg and Lys residues predominantly [302]. Probe 3, bearing an acrylamide-warhead [295], was meant to evaluate tiered cysteine-reactivity in comparison to probe 1 and probe 9, but was excluded due to low reactivity

in our hands, and was instead used as a control compound, as described below. As a result, the screening library set was reduced to eight reactive probes.

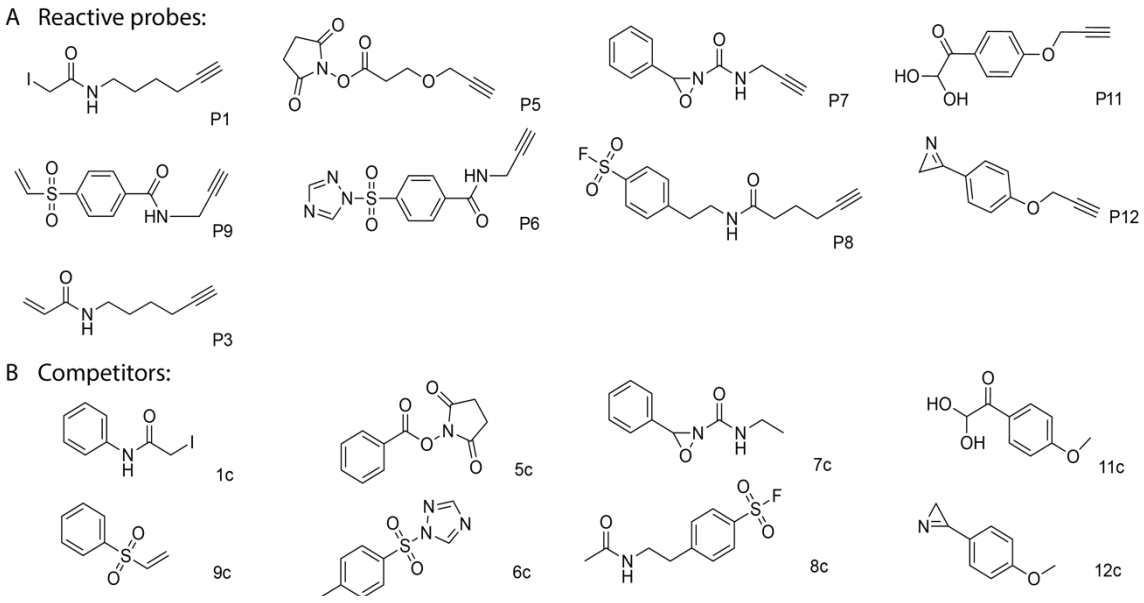


Figure 11: Reactive probe and competitor libraries. A) Reactive-probes (P) with alkyne-tails. B) Competitors (c) bearing phenyl rings as a lipophilic motif.

In order to provide a druggability map not only based on sheer reactivity and surface exposure of nucleophilic amino acid residues, we designed a small library of lipophilic competitors (1c to 12c). While the structures closely align with the warheads, the tail regions, including the alkyne-tails, were omitted (Figure 11B). We envisioned these compounds to require lipophilic and cooperative interactions before binding events, to distinguish those sites from sites labelled purely based on reactivity, in order to provide more meaningful starting points for drug development. To obtain starting points for all warheads, we chose to test only one competitor per reactive probe instead of screening a large library of competitors, as the throughput of the isoTOP ABPP workflow (in triplicates per compound) was limited.

2.3.2 Reactivity survey of the probe library

Initially, the reactivity of the clickable probes was investigated by in-gel fluorescence studies. Often, these probes are used at 100 µM concentration and are incubated in cell for 1 h at RT lysates [303], but we chose to test 3 h incubation time as well (Figure 12A). We performed a comparison of respective incubation times and a concentration gradient for IAA in K562 lysates. In line with expectations, the overall labelling intensity was stronger for the longer incubation time, here the reactive probe had more time to engage with reactive residues. As the lysis buffer did not contain protease inhibitors, some additional residues might have become available after a prolonged incubation time due to protease activity and protein unfolding. Unfolding can also be affected by individual protein stability at RT. The band pattern indicated broad and promiscuous reactivity of the compound. The concentration gradient was illustrating high to low labelling intensities for respective concentrations ranging from 100 to 0.01 µM. The corresponding Coomassie stain confirmed equal loading of the samples (Figure 12B). Based on these results and supported by the literature, we chose to incubate the reactive probes for 1 h at RT in further experiments. We chose 100 µM as a concentration to cover a broad range of residues with the reactive probes.

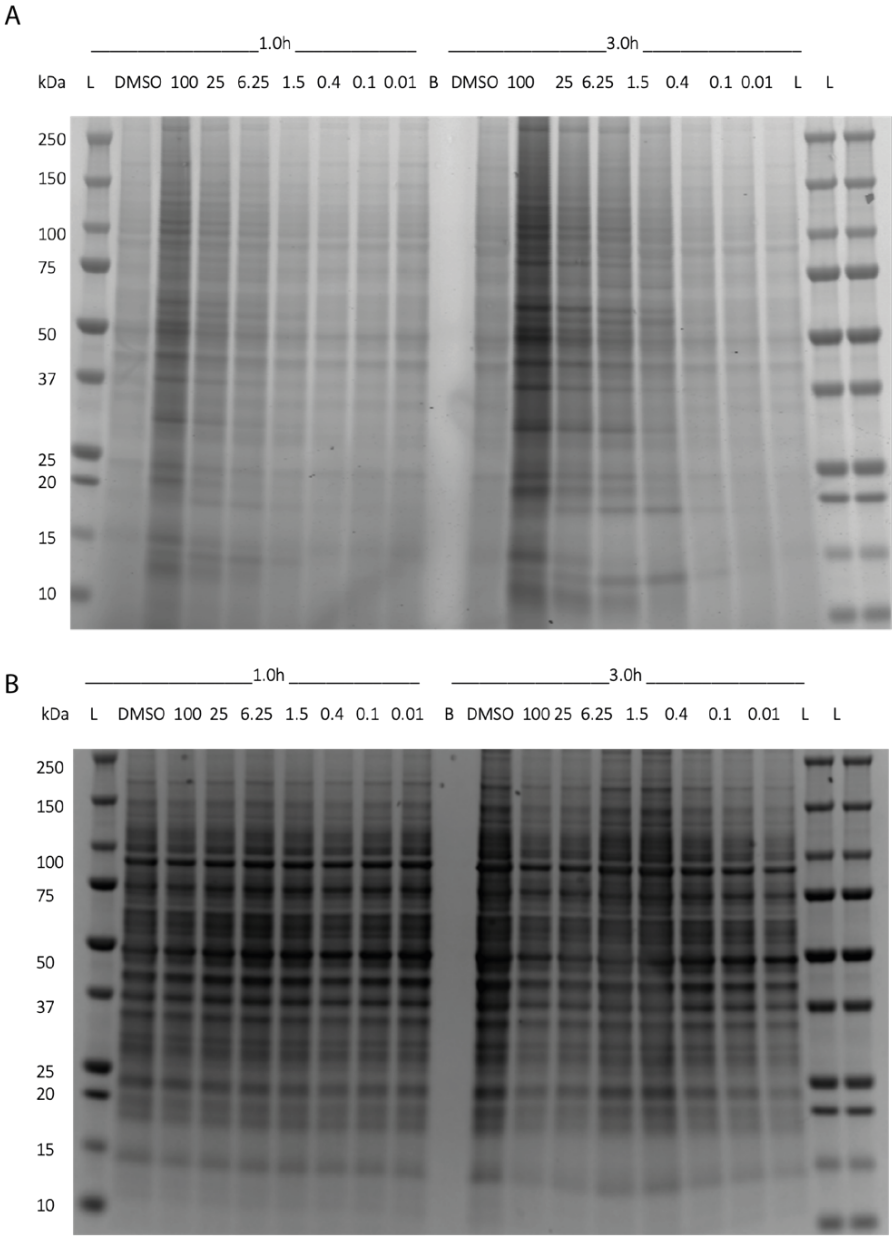


Figure 12: Detection of probe 1 labelling in K562 lysates in in-gel fluorescence. A) Probe 1 was incubated with K562 lysates at 1 mg/mL for respective incubation times before click reaction with a fluorescent Cy5.5-azide (Lumiprobe), followed by protein precipitation, resuspension and visualisation via in-gel fluorescence. B) Corresponding Coomassie staining.

For the lysate preparation, PBS in combination with mechanical lysis (sonication with a probe) is reported in the literature [114, 272, 295]. To avoid any disturbance or mitigating effects of buffer supplements on the reactive probes, we omitted common lysis buffer additives, such as TRIS (contains amines, which could react with the lysine-reactive probe) or DTT (contains thiols, which can react with cysteine-reactive probes). To solubilise more proteins, we investigated the influence on probe labelling using different detergents for preparation of the lysate. As high concentrations of SDS (1 %) had been reported to have a negative effect on the efficiency of the labelling and CuAAC reaction, we chose milder detergents [304]. As a result, we found stronger band labelling when we used PBS buffers supplemented with 0.8 % Nonidet P-40 (NP-40) or 0.35 % n-dodecyl β-d-maltoside (DDM). Both detergents are mild, non-ionic and non-denaturing and can increase solubility of membrane proteins and hydrophobic proteins, which are lost due to precipitation and aggregation in detergent-free proteomic preparations of lysates [305]. However, we were focussed on keeping the proteins in their most unbiased, native state while providing buffer conditions which were not potentially disturbing the activity of the reactive probe, thus we chose pure PBS buffer at pH = 7.5 for our experiments in combination with mechanical lysis (Supplementary Figure S1). A recent study by Li et al. supports the utilisation of native lysates [306].

As the detection via in-gel fluorescence required a click-reaction with a fluorescent reporter-tag, which is not suitable for subsequent enrichment studies, we chose to evaluate the probe reactivity alternatively by visualisation using a conjugated isoDTB-tag. For this, labelled bands were visualised with streptavidin-based IRDye antibody, which recognised the desthiobiotin-residue on modified peptides in Western Blot (Figure 13A). We evaluated the probe library at 100 µM in K562 lysates after 1 h incubation at RT. In line with literature reports, Cys reactive probes 1 and 9, as well as Lys reactive probe 5 were showing strongest bands. In comparison, probes 6, 7, 11 and 12 were less reactive and showed weaker labelling. Probe 8 showed very limited labelling. For probe 3, the labelling intensity marginal. As subsequently no protein enrichment was detected in test MS injections for this probe, this compound was excluded from further screens and treated as an inactive control, closely mimicking the scaffolds of the reactive alkyne-tail probes. A Coomassie stain confirmed equal loading of the sample set (Figure 13B). As we aimed to compare the probe library regarding their displayed reactivity, we decided to examine all probes at 100 µM concentration for MS-based experiments.

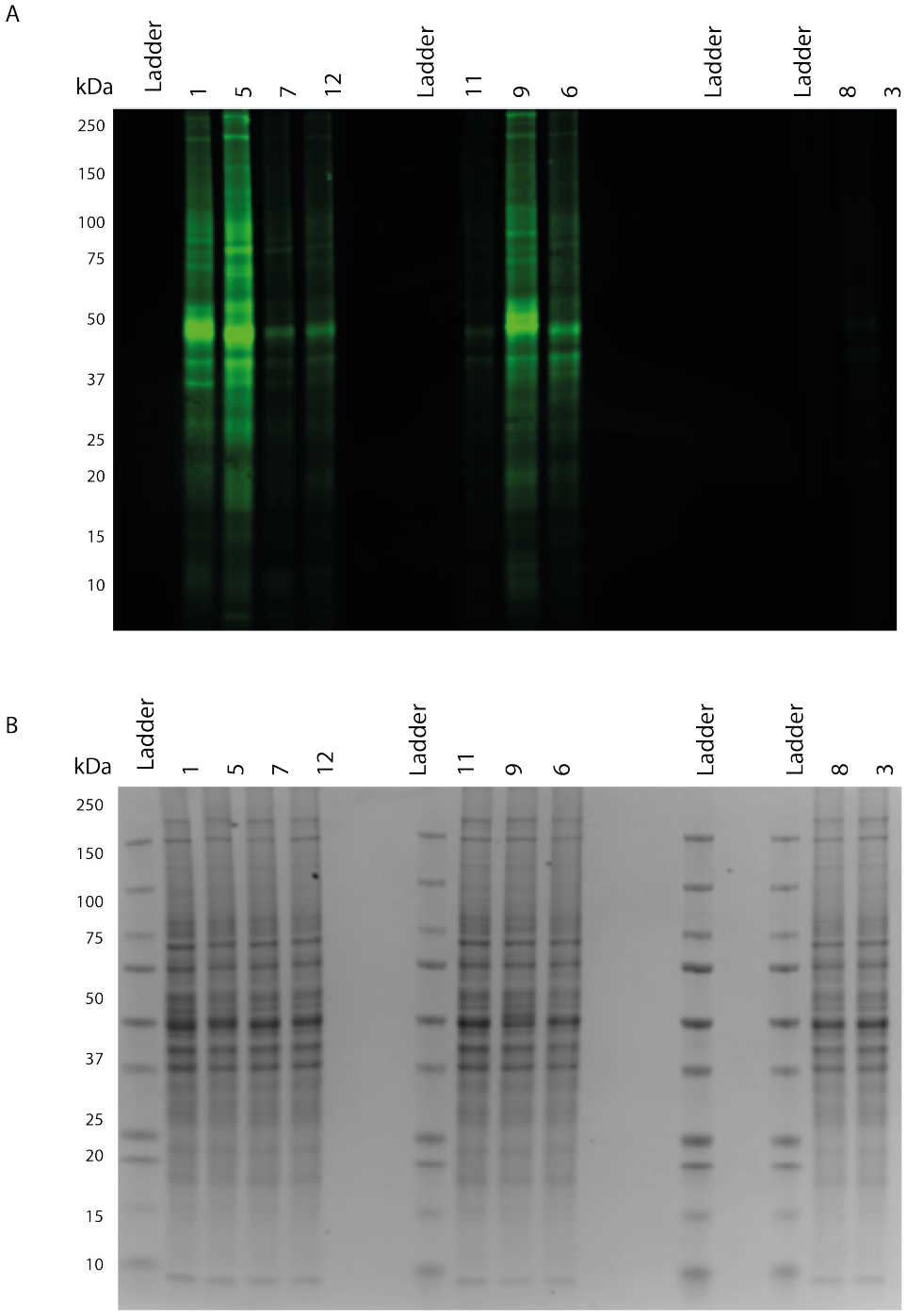


Figure 13: Survey of probe reactivity at 100 µM incubated for 1 h at RT, in K562 lysates at 1 mg/mL. A) Visualisation using IRDye 800 CW streptavidin (Licor, 1:1000) antibody against biotin. B) Coomassie stain confirming equal loading of the probes.

Additionally, to ensure equal reactivity in different cell lysates, a set of probes was also tested in the other three cell lines at 100 µM and 1 h incubation at RT. Probes 1,3 and 9 were investigated in U251, NCIH226 and DU145, as shown in Figure 14A-C. The lysates appear to be equally susceptible to labelling with the reactive probes. IAA labelling intensity in NCIH226 seems a bit weaker in comparison to the other cell lines, which might be influenced by imaging or exposure of the WB. For Probe 3, labelling was marginal throughout the tested cell lines. As no quality control in form of WB or Coomassie/silver stain was possible after the pulldown and on-beads digest, as we were handling peptides at that point in the workflow, the isoTOP ABPP protocol was carefully optimised and subsequently MS results were monitored to judge experimental performance (e.g. histograms, showing distribution of H/L-modified peptides or Venn diagrams of triplicate overlap). The optimisation is described in detail in chapter 3.

To investigate whether reactive probes or lipophilic competitors were affecting cell viability, we performed a cell viability assay (CellTiterGlo) and found only minor effects on the live cell panel, when treated with 100 µM for 1 h with respective compounds (Figure 15A,B) in comparison to DMSO control. The compounds with the greatest effect showed around 5-10 % loss of cell viability. Thus, the cell viability was ensured under our experimental conditions. Longer incubation times might affect the cell viability, as the fragments are promiscuous and may bind to essential housekeeping proteins (e.g. cysteines on histones) affecting their function.

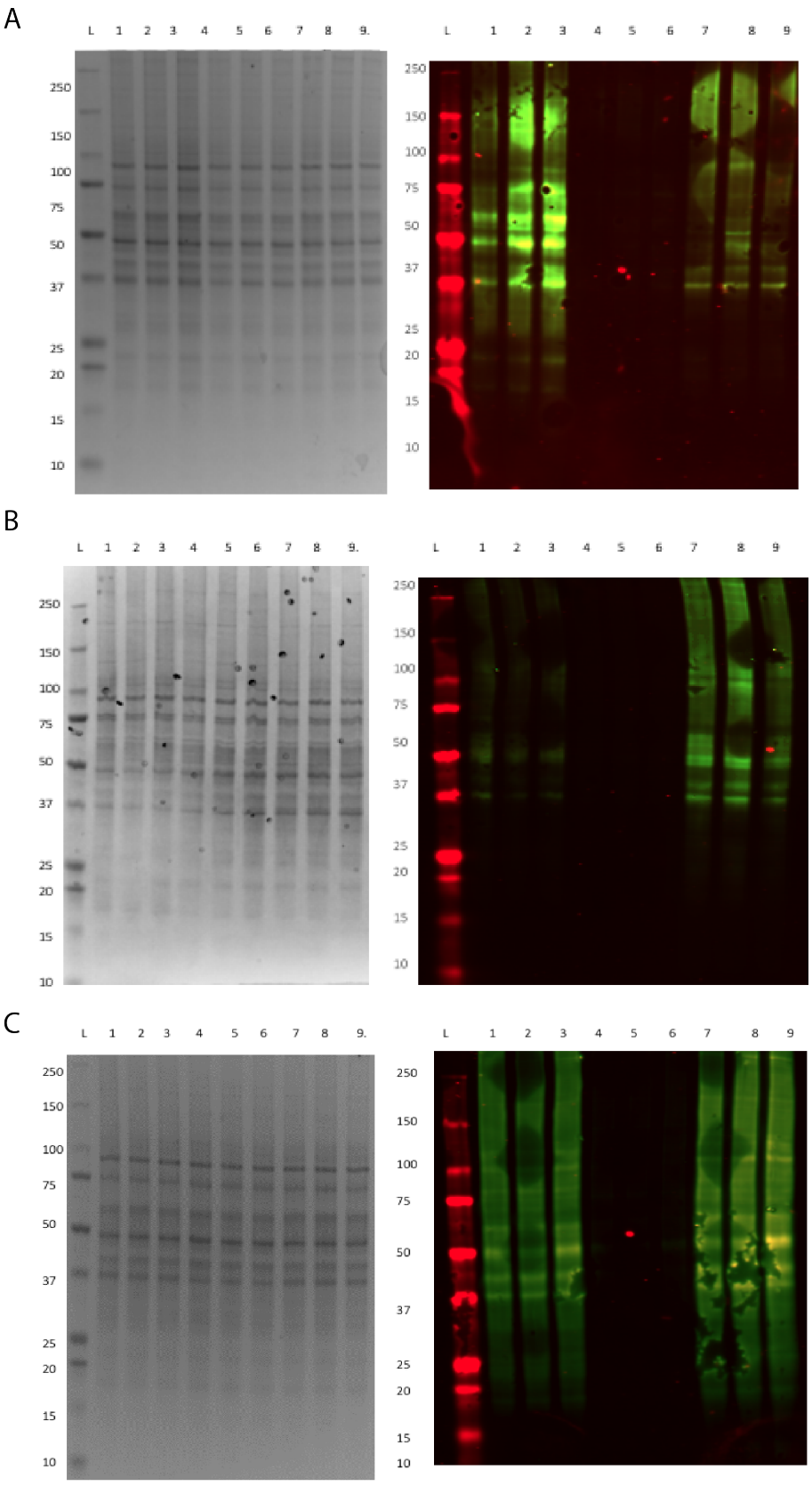


Figure 14: Coomassie stains and western blot detection with IRDye 800 CW streptavidin (Licor, 1:1000) antibody for probes 1, 3 and 9 in triplicate (1-3, 4-6, 7-9) at 100 µM, incubated for 1 h at RT in different cell lysates at 1 mg/mL. A) U251. B) NCIH226. C) DU145.

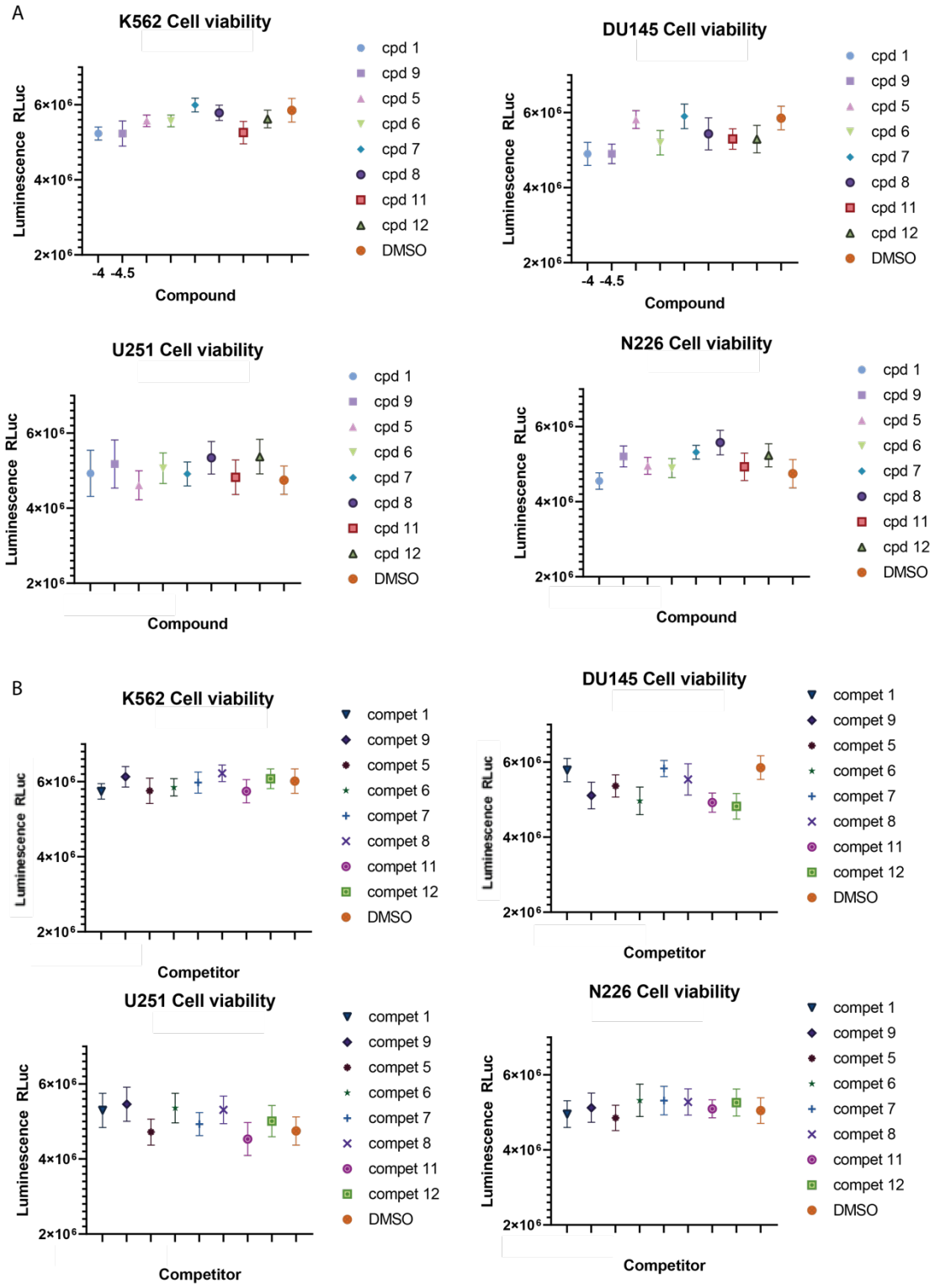


Figure 15: Test of cell viability in CellTiterGlo assay for K562, DU145, U251 and DU145 cell lines. Each data point represents the mean ± SEM of three technical replicates (n=1). A) Treatment with reactive probe library probe 1 (cpd 1) – probe 12 (cpd 12) at 100 µM for 1 h with minor loss of cell viability observed. B) Treatment with competitor 1 (compet 1) – competitor 12 (compet 12) at 100 µM for 1 h with minor loss of cell viability observed.

2.4 Summary

To contribute to this field and unlock more novel E3 ligases, we performed a bioinformatic analysis to select an NCI cell line panel covering a maximal number of E3 ligases for subsequent screening and ligandability experiments. Our idea was similar to the principle of kinobeads [111], where a matrix consisting of multiple kinase binders/inhibitors is utilised to enrich a large number of kinases. However, as there is only a limited number of known covalent E3 recruiters, we aimed to provide a maximal number of E3 ligases in lysates as a basis for an enrichment and reactivity survey against selected promiscuous warheads to create a druggability map for revealing potential novel starting points for E3 ligase recruiter development. Our analysis was based on a previously published dataset by the Küster group [286], for which we found 128 E3 ligases contained in K562, U251, NCIH226 and DU145 cell lines. We could identify a number of 267 E3 ligases in a total proteome dataset derived from these cell lines. The increased number of E3 ligases in our dataset can likely be explained due to advances in MS development, as we used a newer MS machine, as well as optimisations in the method. We used a in-solution digest, whereas the Küster group had used in-gel digest, which might lead to increased sample loss. Furthermore, we reported a set of E3 ligases, which were highly abundant within the cell line panel. For example, TRIM28 was highly abundant in the investigated cell lines, thus making it an interesting target for the following ligandability studies.

To explore the reactivity of the E3 ligases, we selected a nine-membered library based on current literature in the field [123, 124, 295, 298-302], and designed corresponding competitors with a lipophilic motif. We designed respective competitors containing phenyl ring

residues as lipophilic motifs to distinguish labelling sites not based purely on reactivity or surface exposure but to address caveats or pocket-like structures, which require lipophilic interactions for a binding event to occur. In an in-gel fluorescence study, by clicking on an azide-Cy5.5 fluorophore, we initially surveyed IAA reactivity at 100 µM concentration and 1 h and 3 h incubation at RT in K562. With concerns about protein stability and denaturation, we deemed 1 h incubation time as suitable to provide labelling of residues which are ligandable in a native, folded state of the proteins. 100 µM concentration yielded the highest labelling intensity and was selected as a concentration for all probes to provide comparability and a sufficient coverage of modified residues. To provide suitable buffer conditions, which were not potentially ablating reactive probe activity or click-reaction efficiency [304], we omitted any buffer supplements and additives and chose pure PBS buffer. The probe library was tested in K562 and visualised using detection with streptavidin-based IRDye of the proteins modified with the isoDTB-tag. At a concentration of 100 µM we found different labelling intensities for the probe library, likely due to the distinct reactivity and availability of nucleophilic residues within the proteome. Additionally, we probed different cell lysates and yielded equal labelling efficiencies for a set of probes and showed that the compounds and competitors did not influence cell viability at their respective concentration and incubation time.

The constant development in the field of isoTOP ABPP yielded further reactive probes [294], which we will discuss the context of our library screening results in chapter 3 in detail. An example of novel, cysteine-reactive, acrylamide-containing probes are the recently introduced N-acryloylindole-alkynes, which were shown to label around 3000 proteins in lysates, in contrast to the IAA-based DBIA-probe which labelled only around 1000 proteins [307]. For lysines, sulfotetrafluorophenyl probes have been shown to modify over

9000 K residues in the human proteome [308]. Recently, 2-ethynylbenzaldehyde probes have been demonstrated as lysine-selective and cell-active warheads [309]. Abbasov et al. screened a lysine-specific library [310], whereas Brulet et al. focussed on tuning of a sulphur-triazole library for targeting tyrosine residues [311]. Glutamic acids have been demonstrated to be ligandable with a compound based on Woodward's reagent K [312]. As an extension of our selected library, acrolein-containing reactive probes would allow for histidine labelling, which was recently shown for over 8000 residues within the human proteome, as interestingly, 20 % of protein active sites contain histidine side chains [313].

3. Profiling of E3 ligases on proteome-wide scale

After determining a suitable reactive probe concentration and incubation time for the library screen in K562, U251, NCIH226 and DU145, we next focussed on the optimisation of the isoTOP ABPP workflow. In this chapter, we show the successful optimisation and benchmarking of our work in MDAMB231 in comparison to Zanon et al. [295]. Initial isoTOP ABPP experiments were carried out without pre-incubation with competitors, to establish sites available to the promiscuous alkyne-tailed probes. In the next step, competition experiments were conducted on a subset of samples to achieve a maximal number of competed E3 ligase sites with minimal sample effort.

3.1 isoTOP ABPP optimisation

As described in the introduction, the TEV-cleavable biotin-tag [114], as well as the isoDTB-tag [131] and the DBIA-probe [132], containing biotin or desthiobiotin, respectively, may be utilised for the click-reaction with the reactive probe for subsequent enrichment on streptavidin beads. Each tag offers advantages and disadvantages. In case of the DBIA-probe, the covalent warhead is merged with a desthiobiotin-moiety for enrichment therefore, only iodoacetamide can be profiled using this tag. As this work was aiming to profile various warheads, this tag was excluded. When utilising the classic isoTOP ABPP-tag, a TEV-cleavage step is required to free enriched peptides from the beads. This step potentially induces variability, in our hands the TEV digest was inefficient and in addition to that it prolonged the protocol for one day, which reduced the sample throughput. On the contrary, the isoDTB-tag can simply be eluted from the streptavidin beads using high

organic solvent. Therefore, the isoDTB-tag was studied and optimised for this work, as it proved to be efficient and robust in handling.

To ensure optimal procedures in-house, the protocol was optimised and adjusted to available equipment types. Figure 16 provides a systematic overview of the optimisation steps which were undertaken. Initially, cell lysis conditions were evaluated using K562 lysate before the sample volume for labelling and CuAAC reaction was optimised. Here, instead of 2 × 1 mL, the sample was combined to a total volume of 2 mL in one Eppendorf tube before treatment with reactive probes, to avoid loss of residual lysate in the tubes. The click-reaction was performed using a temperature-controlled shaker to ensure uniform experimental conditions. After the acetone precipitation, the pellet was re-suspended in a 15 mL falcon instead of a 2 mL Eppendorf tube, as the tube was too small to hold the liquid during the sonication step and would cause contamination and splashing in the sonication chamber. For the pulldown step, the bead bed volume was combined to 100 µL per sample instead of using 2 × 50 µL in two test tubes to reduce the risk of losing beads while the two samples are combined. The pulldown was performed in a 5 mL Eppendorf tube, bypassing the use of a 15 mL Falcon tube, which potentially risks loss of sample adsorbing to the larger tube surface. The tryptic digest results improved after increasing the trypsin amount to 3 µg (6 µL). After obtaining the dried peptides from the elution step, an optimal re-suspension buffer was determined. Finally, the QExactive method parameters were adjusted to accommodate a longer gradient and a higher organic solvent method, comparable to recent literature [273, 295]. The optimisation steps will be described in more detail below.

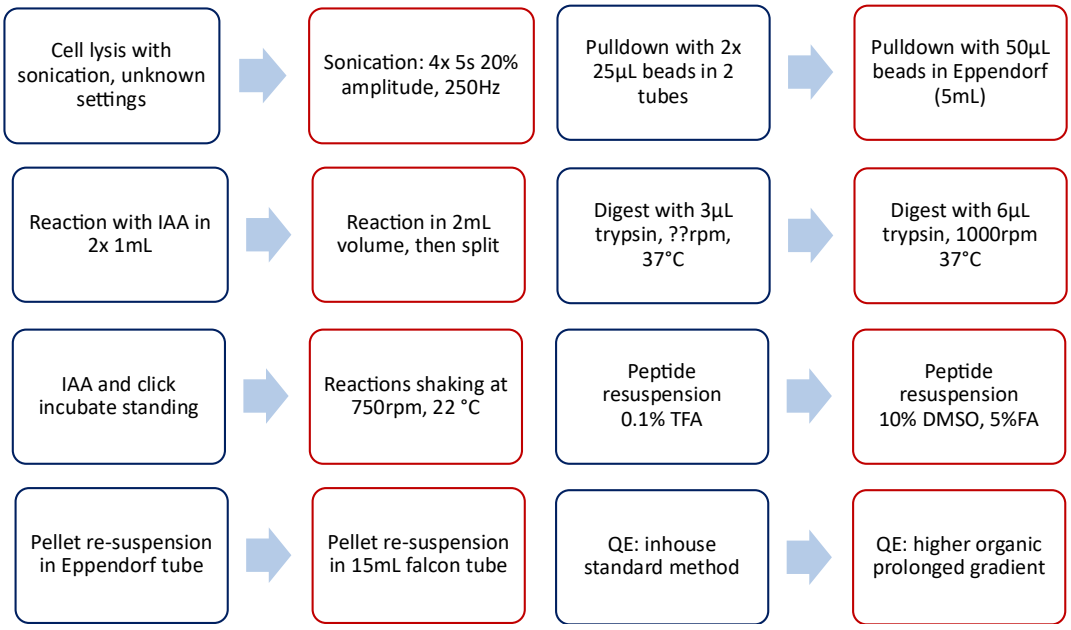
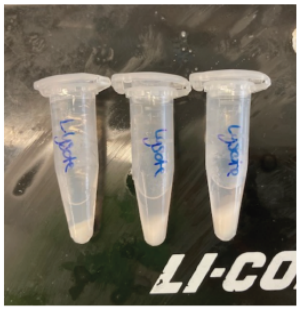


Figure 16: Optimisation steps conducted inhouse (red) for benchmarking data with recent literature. Note, the gradient was adjusted as close as possible to Zanon et al.[295].

3.1.1 Sonication, digest and re-suspension buffer optimisation

For the optimisation of the cell lysis, three conditions were chosen for further investigation. A K562 pellet was thawed on ice by adding 3 × pellet volume PBS (1 % benzonase was added freshly) before being subjected to either 4 × 5 sec on and 10 sec off pulse, or 2 × 10 sec on and 10 sec off pulse at 20 % amplitude, or to 2 × 10 sec on and 10 sec off at 20 % amplitude and additionally 10 sec on at 15 % amplitude. After resting on ice, 1 mL lysate volume of each sonication condition was transferred to a 1.5 mL Eppendorf tube. After 30 min centrifugation, the size of the pellets formed at the bottom of the tubes differed discernibly, which suggested loss of proteins due to heat, adduct formation and precipitation processes (Figure 17A). A DC assay supported this notion, as the protein concentration results were higher for shorter sonication times in comparison to harsher conditions with longer sonication times, yielding around 50 % less protein (Figure 17B).

A)



B)

mg/mL	condition	amplitude
22.96003	Pulse: 4x 5sec on, 10sec off	20%
19.33708	Pulse: 2x 10sec on 10sec off	20%
10.15307	Pulse: 2x 10sec on 10sec off, 10 sec lower amplitude	20%, 15%

Figure 17: Sonication test of different sonication conditions in K562 lysates. A) Precipitates for the different lysis conditions, increasing from left to right in correspondence to longer sonication times shown in the table to the right (top to bottom). B) Lysates yielded different protein concentrations; less yield was obtained for longer sonication conditions.

For the on-bead digest, the trypsin amount was increased from 2 µg to 3 µg as the MS2 charge distribution was showing a great amount of four- or five-times charged peptides, indicating underdigestion (Figure 18A). Basic amino acids, such as Arg, Lys and His can bear positive charges, when peptides are un-cleaved and therefore longer, these peptides

will consequently show a higher number of charged residues. With the higher trypsin amount, the charge of peptides shifted more towards double-charged peptides, indicating an optimised tryptic digestion (Figure 18B).

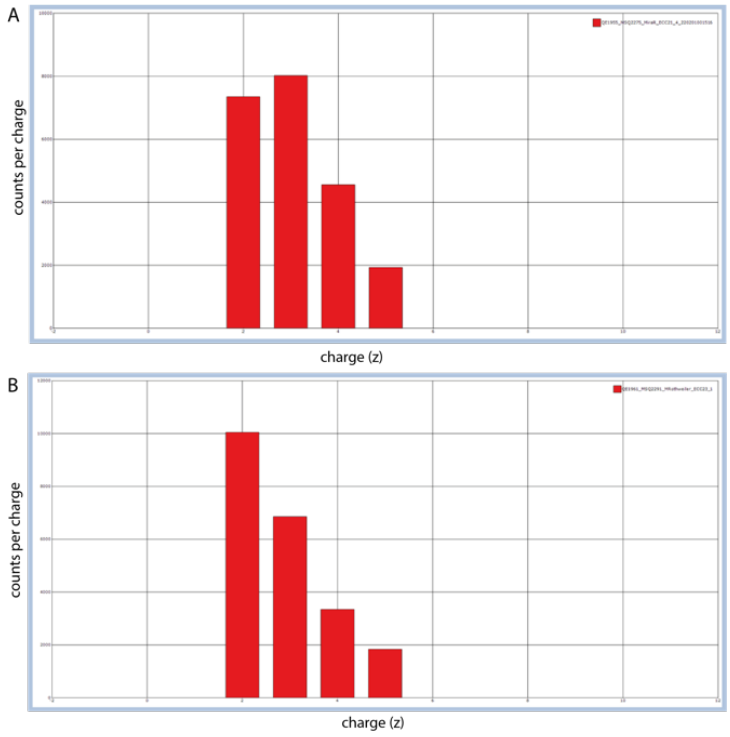


Figure 18: MS² charge distribution depicted in RawMeat software. A) Result using 2 µg trypsin shows more triple charged ions than double charged and high numbers of four- and five-times charged peptides. B) Result using 3 µg trypsin. The digestion using higher amount of trypsin results in a spectrum with most double charged peptides and reduced numbers of four- and five-times charged ions.

To evaluate the effect of a prolonged gradient in line with current literature, we evaluated a 1 h method (5 % to 35 % buffer B (0.1 % FA in acetonitrile and 5 % DMSO) over 60 min) against a prolonged method with higher organic solvent percentage (5 % to 40 % buffer B over 105 min, increase to 60 % B in 10 min and then increase to 90 % B in 10 min) on the QExactive mass spectrometer (Thermo Fischer Scientific). For this, two test samples were prepared in MDAMB231 lysates using 100 µM of IAA probe, and each sample was analysed with each method. Strikingly, the prolonged method had a

remarkable effect on the number of modified peptides and protein IDs obtained from the sample (Figure 19A): the gradient yielded approximately 2500 modified peptides and 1600 protein IDs, whereas the standard method resulted in only in a handful proteins (in total 11). In conclusion, the prolonged gradient with higher organic solvent percentage increased the number of detected modified peptides and proteins drastically. We hypothesise that the introduction of the isoDTB-tag increased the hydrophobicity of the modified peptides, similarly to TMT-labels, for which the introduction of the tag was shown to increase hydrophobicity and retention time [314]. Thus, the prolonged and higher organic solvent gradient likely facilitated the elution and detection of isoDTB-modified peptides.

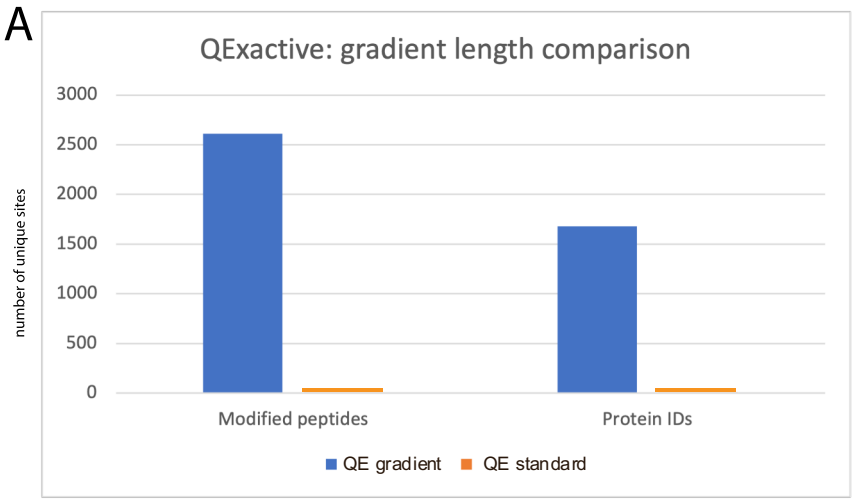


Figure 19: Method comparison on QExactive. A) Modified peptides and protein IDs obtained for a standard method and a prolonged gradient method, n=1.

Next, due to column incompatibility with trifluoroacetic acid (TFA), three different re-suspension buffers were tested. In the literature, 0.1% TFA is often used for buffer re-suspension. Yet, TFA may reduce the analyte signal in electron-spray ionisation (ESI) due to its high conductivity and surface tension, resulting in reduced signal intensity and

it might pair with basic amino acid residues, supressing efficient ionisation in positive ion mode [315]. Formic acid (FA) is a preferred additive over TFA in LC-MS analysis [316]. As an organic solvent in the re-suspension buffer, acetonitrile (ACN) or alternatively DMSO were used to enable better solubilisation of the hydrophobic peptides. Therefore, we used 5 % FA in combination with either 5 % DMSO, 10 % DMSO or 5 % ACN to re-suspend samples and subjected them to MS analysis. The 10 % DMSO condition was proved to yield the highest number of modified peptides (3753) as well as unique protein IDs (2029) in comparison to 5 % DMSO or 10 % ACN with 2582 modified peptides and 1600 proteins, as well as 3215 modified peptides and 1868 proteins, respectively (Figure 20A). Therefore, we chose 10 % DMSO as a suitable sample re-suspension buffer.

The performance of the buffer was suitable to match previously reported numbers of proteins and peptides in MDAMB231 using 100 µM IAA (Figure 20B). We further proceeded to investigate the reproducibility of biological and technical replicates on the QE. An overlap of around 69 % was found in biological replicates, and over 75 % was found in technical replicates (Figure 21A and B). In biological replicates, the variation is generally expected to be higher as the experimental workflow is performed individually on the samples. The result for the technical replicates indicates varying machine performance between the runs due to the biological complexity of the samples. Thus, the overlap among the biological replicates was rather satisfying in direct comparison to the performance of the technical replicates.

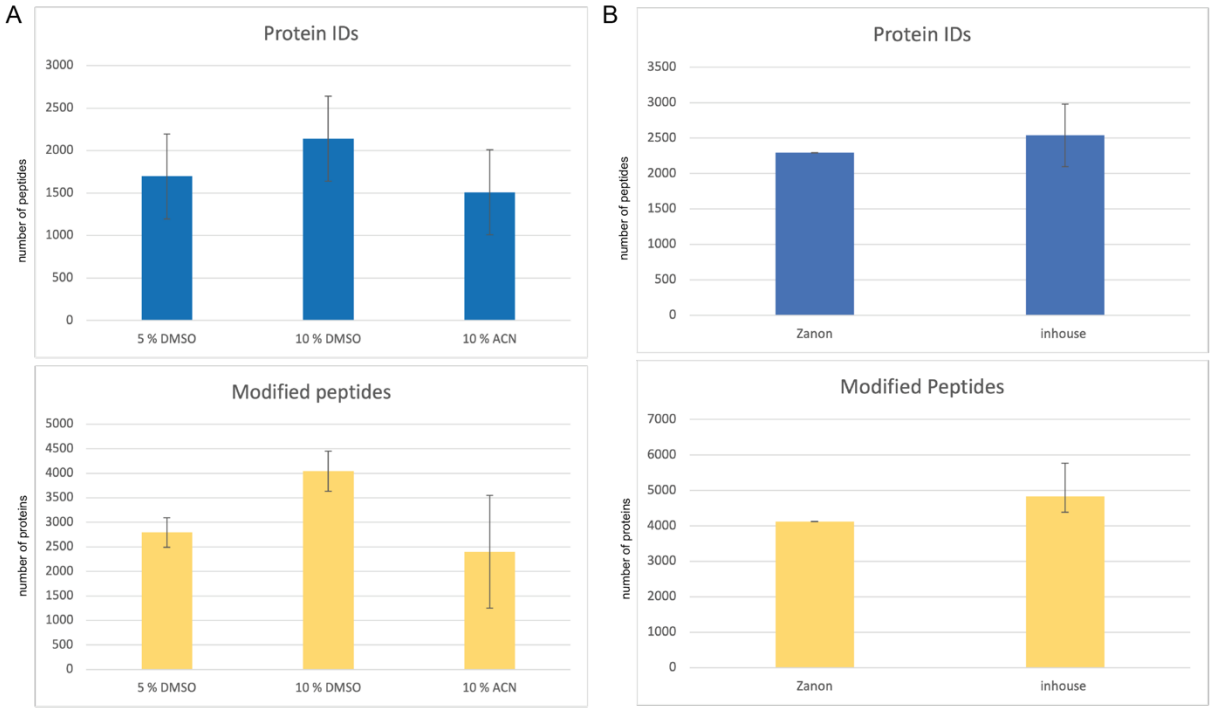


Figure 20: Performance of re-suspension buffers. A) Re-suspension buffers for MS-submission, all buffers contain 5% formic acid plus varying percentage of organic solvent as stated (n=2, error bars are depicted as SD). B) Benchmarking results of 100 µM iodoacetamide-alkyne probe in MDAMB231 lysate incubated for 1h at RT (n=2, error bars are depicted as SD), Zanon et al. dataset derived from Zanon et al., 2021, ChemRXiv (file: zanon-et-al-supplementary-table-3.xlsx, tab: HS IA-alkyne).

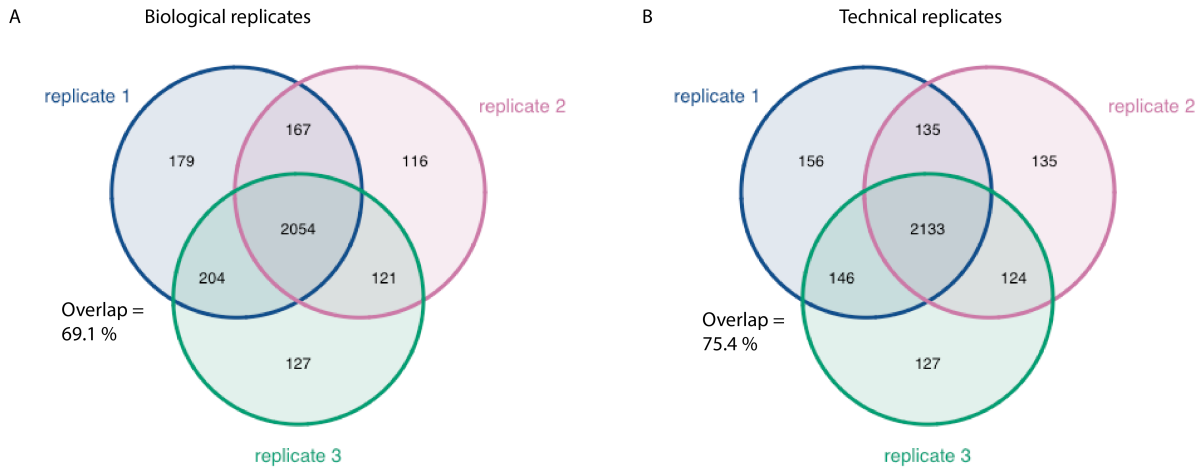


Figure 21: Performance of biological and technical replicates in MDAMB231 treated with 100 µM IAA for 1 h at RT. A) Biological replicates achieve around 69 % overlap, n=1. B) Technical replicates boost the overlap to over 75 %, n=1.

3.1.2 Instrument and gradient performance

To allow for a higher sample throughput and a cost reduction per sample, we compared the QExactive mass spectrometer (Thermo Fisher Scientific) performance at prolonged gradient method (125 min) to the TimsTOF Pro mass spectrometer (Bruker) 21 min gradient, which would save approximately 80 % of MS time and costs for the whole set of our planned experiments. The prolonged gradient delivered around 25 – 30 % more modified peptides and protein IDs in comparison to the TimsTOF (Figure 22A,B). With focus on E3 ligases, we identified a total number of 55 - 60 in the QE whereas the TimsTOF detected 34 E3 ligases (Figure 22C), which were derived from around 50 % more modified peptides identified in the QE (Figure 22D). The method of the TimsTOF instrument is described in detail in the methods section. We hypothesise that the loading in DMSO-containing buffer onto Evotips (desalting C18 trap columns)[11] might lead to sample loss. In combination with the solvent gradient reaching lower organic percentages this likely contributed to the less in-depth data derived from the TimsTOF. Since the prolonged gradient on the QExactive maximised the number of quantified peptides in our hands and was in line with methods reported in recent literature [273, 295], we chose to go forward with our sample set using this lower throughput method instead of a higher throughput with limited depth.

[11] https://www.evosep.com/evotip/

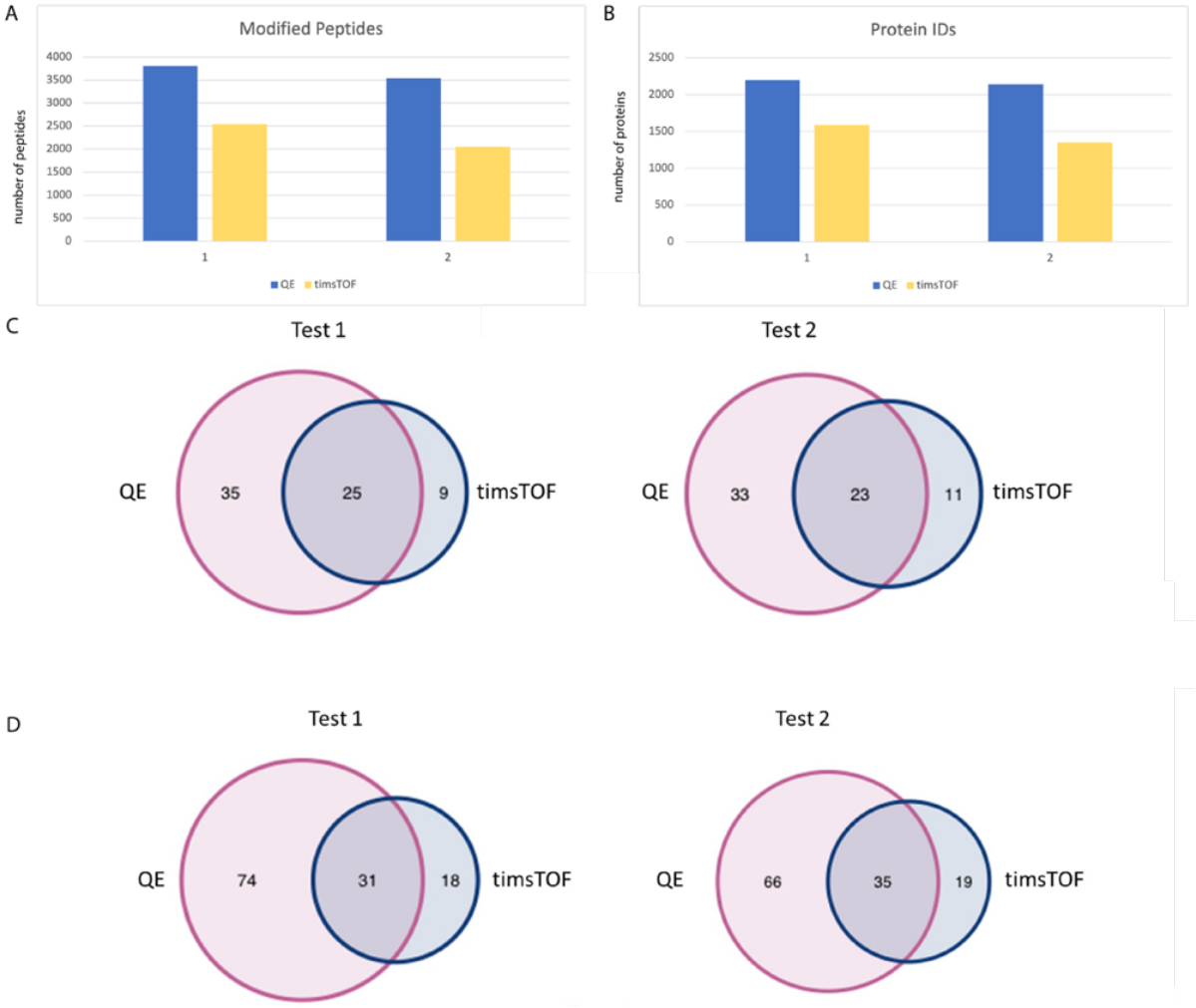


Figure 22: Comparison of QExactive 120 min gradient method to TimsTOF 21 min method using samples of MDAMB231 treated with 100 µM IAA for 1 h at RT. A) Number of modified peptides detected shown for two samples (n=2). B) Number of protein IDs detected shown for two samples (n=2). C) Unique protein IDs reported for E3 ligases only. D) Unique modified peptides reported for E3 ligases only.

3.1.3 Data analysis tools

In order to analyse the large .raw files obtained from the QExactive and to identify and quantify contained peptides, we performed .mzmL file generation using MSConvert[12] to prepare the data for the downstream analysis. The ProteoWizard Toolkit is an open-source program allowing software libraries to bridge field-standard open formats and all common vendor data formats [317]. Subsequently, we used the software FragPipe[13] from the Nesvizhskii group, allowing for identification of custom mass shifts of covalently modified peptides, in combination with an R-script, which enabled data analysis and visualisation. Additionally, an app called ProteomeLabeller[14] has been developed by Jeppe-Tranberg Jensen in our group to specifically analyse and visualise data obtained from this analysis workflow.

3.1.3.1 FragPipe software

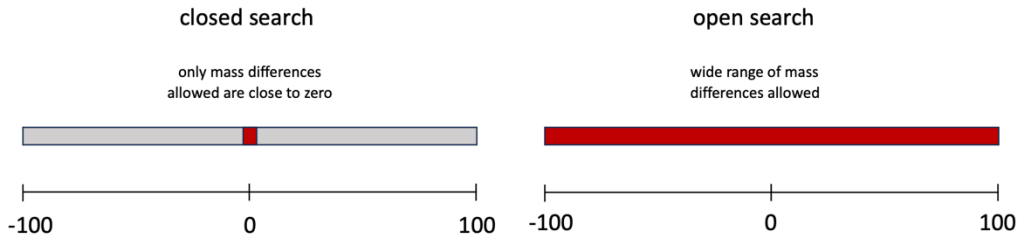


Figure 23: Visualisation of closed search and open search in FragPipe. Figure adapted from https://fragpipe.nesvilab.org/docs/tutorial_offset.html.

The tool PTM Shepherd within the FragPipe software enabled the identification of mass shifts and amino acid localisation for up to 3 amino acids in an open search setting (Figure 23) [318]. The open search can identify mass differences between unmodified versus

[12] https://proteowizard.sourceforge.io/download.html
[13] https://www.nesvilab.org/software.html
[14] https://jeppetranberg.shinyapps.io/ProteomeLabeller/

modified peptides directly from observed precursors in the data without specification in the analytical settings. The open search reported masses of modifications for our probes. The identified masses corresponding to isoDTB-reacted peptides were fed into the closed search. The reported masses of modifications were in line with our predictions, based on the sum formulas of the reacted probe plus isoDTB-modifications derived from ChemDraw (Supplementary Figure S2), which were calculated using in IDCalc[15]. The masses of modification used for the FragPipe searches are reported in Table 5. MSFragger allows for the identification of precursor masses on modified peptides, usually within +/- 20 ppm range in a closed search setting [319].

	Open search		Calculated		
Probe	***L***	***H***	***L***	***H***	***Sum formula***
1	618.3604	624.3672	618.3602	624.3743	C28H46N10O6
9	730.3212	736.3284	730.3221	736.3372	C32H46N10O8S1
5	591.313	597.3214	591.3129	597.3271	C26H41N9O7
6	702.2908	708.2992	702.2908	708.3049	C30H42N10O8S
7	577.308	583.3166	577.3085	583.3226	C24H39N11O6
8	758.3534	764.3604	758.3612	764.3685	C34H50N10O8S
11	652.3448	658.351	652.3202	658.3422	C31H41N9O7
12	667.3086	673.313	667.3311	673.3503	C31H44N10O7

Table 5: Masses of modification for each light (L) and heavy (H) modified peptide identified in open search using FragPipe or calculated based on sum formula using IDCalc.

A typical output table of the FragPipe closed search (combined_ion_lable_quant.tsv) would report peptide sequence, light and heavy modified peptide, mass of modification, protein ID, heavy and light intensities and $\log_{2(}$H/L) ratio. The modified peptide locations would be indicated as the mass of modification in square brackets within the light or heavy modified peptide sequence, e.g. AAAGEFADDPC[618.3602]SSVK or AAAGEFADDPC[624.3743]SSVK.

[15] https://proteome.gs.washington.edu/software/IDCalc/

3.1.3.2 R script and ProteomeLabeller

In order to find the exact position of the modifications, we replaced the whole square brackets obtained from the combined_ion_label_quant.tsv file with an asterisk (*) as a wildcard character in the peptide sequence, e.g. AAAGEFADDPC*SSVK using R. The code then mapped the peptide sequence against protein sequences fetched from the UniProt database and allowed for identification of the position of the * and the protein name. The output was created as: protein, underscore, modified residue, residue number, e.g STRN4_C116. Results from the replicate experiments were combined and the median and standard deviation (SD) was calculated for $\log_2$(H/L) ratios to obtain R.

To visualise the triplicates and to avoid repetitive data analysis steps, Jeppe-Tranberg Jensen developed a Shinyapp, called ProteomeLabeller, based on the R script. The application allows for upload of triplicate data, and researchers can visualise their results, e.g. as a histogram, where competed sites with R > 4 can be depicted. The triplicate performance can be judged in a quality control step visualising the overlap as Venn diagrams. Further information about protein families can be derived as well as a schematic visualisation of each individual protein and respective modified sites, functional sites, or domains are highlighted. Lastly, selected binding sites can be visualised either on PDB or AlphaFold structures in the graphical user interface.

3.2 isoTOP ABPP: uncompetitive determination of ligandable sites

Initial experiments aimed to assess the proteome-wide reactivity of the reactive probe library in the four selected cancer cell lines. The experiments were carried out in biological triplicates under the condition of 100 µM probe concentration and 1 h incubation in lysates. In total, 8 probes were tested in triplicate in four cell lines and were summed up into a set of 96 samples.

3.2.1 Non-competitive results for cell lines K562, DU145, NCIH226 and U251

Overall, the screening effort yielded 30845 sites in total by screening eight probes in four cell lines in a non-competitive experimental setup (Figure 24A). Lys (K) residues were modified at most, followed by Cys (C). This is in line with our previous findings, as we detected probe 5 (NHS-ester) as strong in labelling in the WB visualisation using IRDye, in MS we detected K, Thr (T) and Ser (S) modifications. Both the IAA-probe (P1) and the vinyl sulfone (P9) contributed largely to the C labelling events, but addressed some Met (M) side chains as well. Oxaziridine-probe (P7) targeted both C and M residues. K and Tyr (Y) residues were targeted by the both the sulfonyl-fluoride (P8) and SuTEX-probe (P6), the latter also addressed T. Probe 11 (P11) was found to label K and Arg (R) side chains in our hands. The residues detected by the aziridine-probe (P12) were Asp (D), Glu (E) and C residues. Overall, as we yielded a large proportion of liganded cysteine residues, we compared our findings to the recently published CysDB[16] comprising more than 60000 cysteine sites. CysDB is a collected database of several publications using cysteine-reactive compounds in isoTOP ABPP *[320]*. We found an overlap of > 95 % with

[16] https://backuslab.shinyapps.io/cysdb/

the CysDB data and around 500 sites in our dataset which were previously unreported in the human proteome (Figure 24B, Supplementary Table T2).

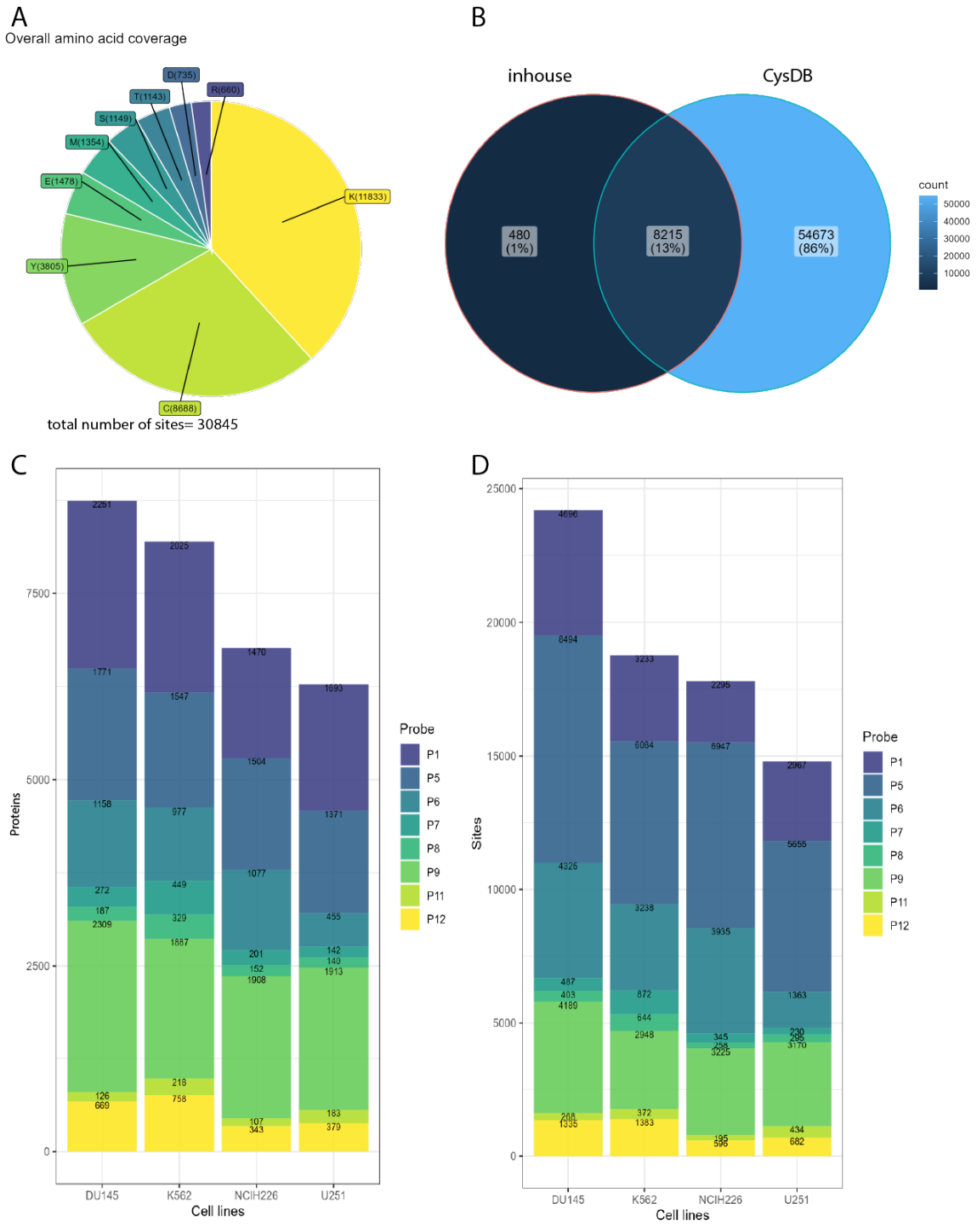


Figure 24: Summary of the non-competitive screening of eight probes in four cell lines. A) Pie chart depicting number of modified amino acid residues. In sum 9 amino acids were detected as modified. B) Overlap of our modified sites with CysDB sites reported by the Backus group. C) Comparison of probe performance in four cancer cell lines DU145, K562, NCIH226 and U251 on gene level. D) Comparison of probe performance in four cancer cell lines DU145, K562, NCIH226 and U251 on modified site level. The bar and pie charts were created by Jeppe-Tranberg Jensen.

Next, we compared the probe performance in the four different cell lines, which showed similar trends in all tested cell lines. On the protein level (Figure 24C), cysteine reactive probe P1 labelled around 1400-2200 proteins, and probe P9 labelled slightly more sites which corresponded to 1900-2300 proteins. Probe P5 was labelling around 1300-1700 and sulfonylfluoride-probe P6 labelled around 1000-1300 proteins in respective cell lines. The rest of the probe library contributed less than 800 sites per probe, corresponding to labelling between 100 and 400 proteins. The general trends of the probes seen in protein labelling events corresponded to respective numbers of modified sites (Figure 24D). Yet, we found a difference of around 1500 proteins, corresponding to 9000 modified sites, between cell lines DU145 and U251. Looking at the probe performance in U251, we found P12 and P7 labelling only around half of the number of sites detected in DU145, which was contributing greatly to this gap. P12 was also labelling less efficiently in NCIH226. Less protein labelling was connected to fewer modified sites in general. We hypothesised that the origin of the cell lines (prostate cancer, lung cancer) contributed to the discrepancies and proteins might not be similarly abundant and expressed, or not equally ligandable. To evaluate the performance of the probes in more detail, we created Venn diagrams comparing their performance in each cell line. Figure 25 shows the probe labelling in the four cell lines. For cysteine reactive probes P1 and P9, as well as for NHS-ester probe P5 and sulfonylfluoride probe P6, most proteins overlap between all cell lines. For the remaining probes K562 contained over 25 % of unique proteins. The analysis of modified sites (Figure 26) revealed that DU145 was containing most unique modified sites for P1, 9, 5 and 6 which indicates more sites were identified on the same genes, whereas in K562 around 10 % less sites were labelled, but the sites corresponded to a greater number of individual proteins.

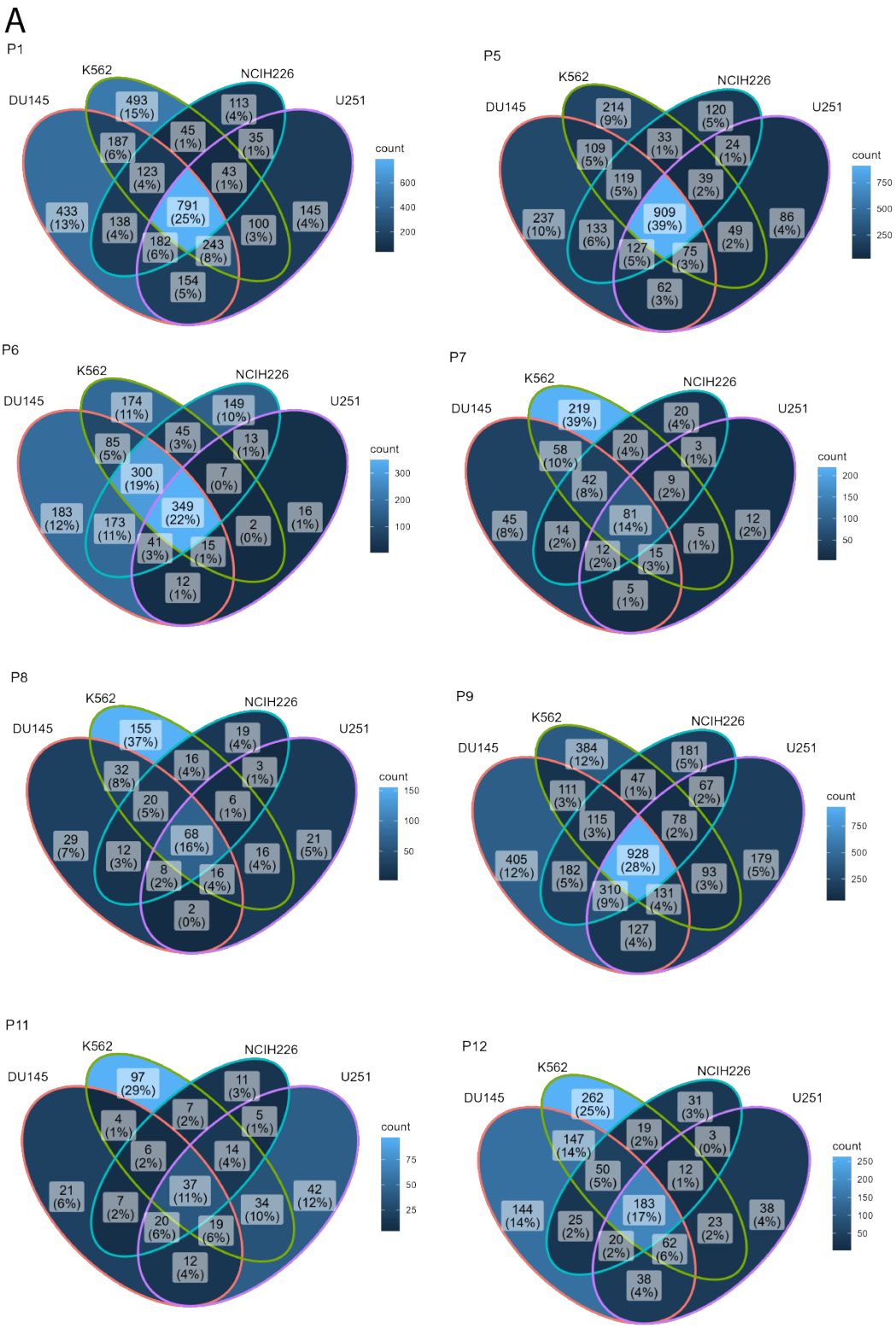


Figure 25: Venn diagrams depicting performance of probes in four cell lines on protein level. A) Venn diagrams of 8 probes (P1-P12) showing overlap in modified protein IDs. The Venn diagrams were created by Jeppe Tranberg-Jensen.

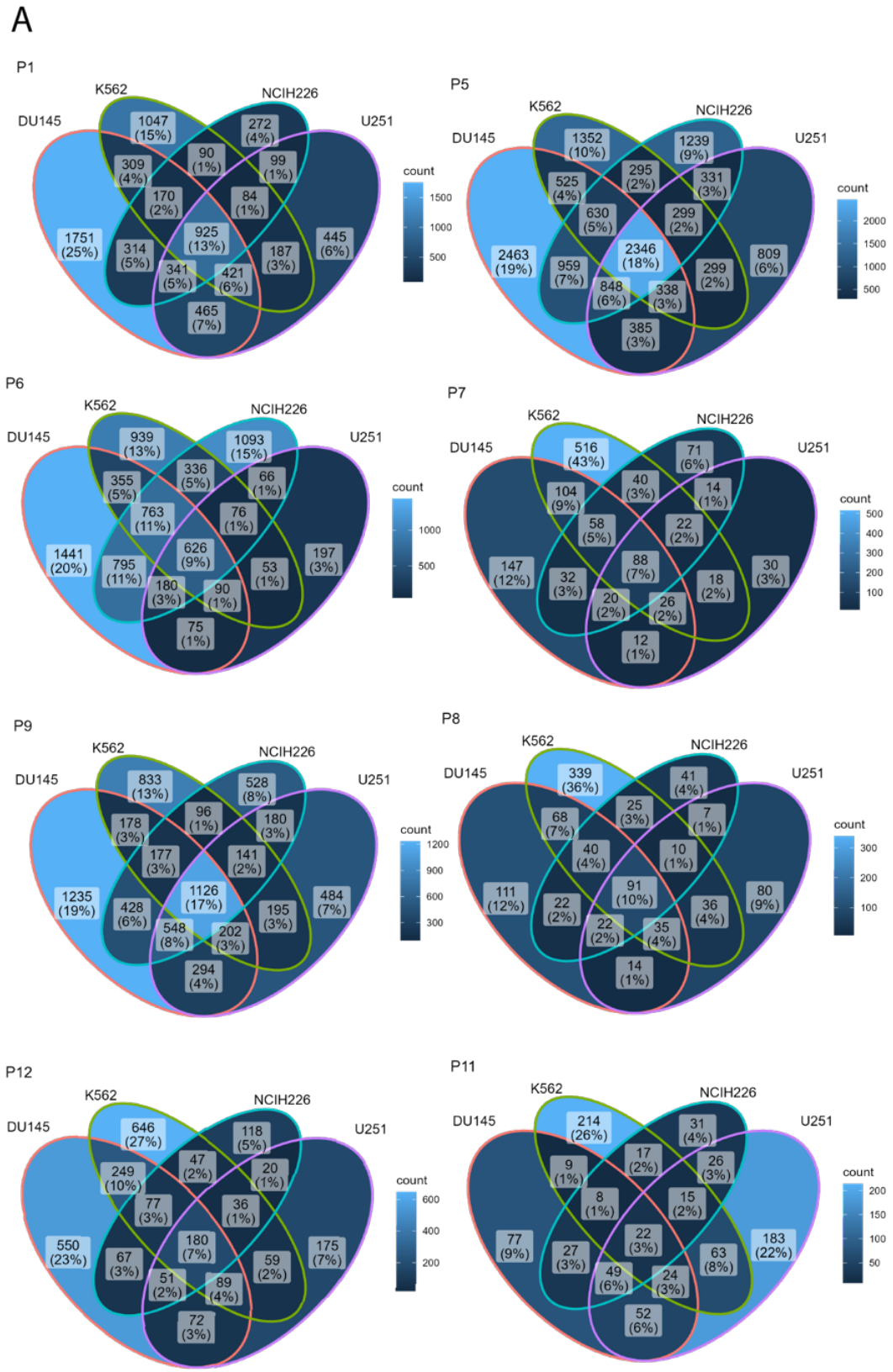


Figure 26: Venn diagrams depicting performance of probes in four cell lines on modified site level. A) Venn diagrams of 8 probes (P1-P12) showing overlap in modified sites. The Venn diagrams were created by Jeppe Tranberg-Jensen.

We evaluated the probe labelling in more detail in comparison to the literature and identified unique proteins which were not reported in previous studies, while our results shared between 10 – 30 % of identified proteins with those studies (Figure 27A-F) [124, 295, 299, 301]. Depending on the probe, we detected around 30 – 80 % unique modified proteins and we assume that the sheer size of our dataset from four human cell lines contributes highly to this gain, in comparison to studies where rather one probe was tested in one cell line. The studies were performed on different MS machines using different cell lines, which contributes to the variation. Additionally, one should bear in mind that the data analysis steps conducted in our work are only directly comparable with the work of Zanon et al. [295]. For P1, we reported a 43 % overlap with the modified proteins from Zanon et al., the authors tested the probe at 100 µM in MDAMB231 cells. We reported a total number of over 3200 modified sites (Figure 27A). Hahm et al. derived around 1100 proteins using sulphur-triazole HHS-475 in isotopically light and heavy amino acid-labelled HEK293T cells (i.e. stable isotope labelling with amino acids in cell culture (SILAC)) at 250 and 25 µM [299], whereas we found around 1400 proteins and confirmed 35 % of the previously reported sites (Figure 27B). The probe HHS-475 differs from P6 (corresponding to HSS-465) in the position of the nitrogen in the five-ring (1,2,4- instead of 1,2,3-triazole). We used the HHS-475 data as a surrogate because no suitable protein level data was available for HSS-465, and both HHS compounds showed great overlap in the study [299]. In Figure 27 C-D, we report our findings for oxaziridine P7 in comparison to Lin et al. (250 µM in HEK293T) [124], here we compared to reported M sites, and in comparison to Zanon et al. (100 µM in MDAMB231) for both C and M sites; we detected around 500 proteins modified at those residues. For P12, we identify around 500 proteins, yet reported only 8 % overlap with Ma et al. [301]; they derived data from SILAC-based

MCF7 experiments using 10 and 100 μM of Az-9 and detected D, E residues; we identified additionally modified C residues (Figure 27E). For P11, the phenylglyoxal-warhead, we found 28 % overlap with the Zanon et al. data (Figure 27F) [295].

We could not directly compare our data for P8 (sulfonyl fluoride), also called DAS-1, as this compound was tested in mouse pancreas proteome [300]. Shannon et al. report 885 DAS-1-modified peptide spectra by isoTOP ABPP, in line with this finding, we report 941. Recently, chiral sulfonyl fluoride probes were profiled in intact Jurkat cells and 2343 probe-modified sites on Y and K residues were reported, derived from screenings with > 180 electrophilic fragments, quantifying a total number 14000 lysines [297]. Ward et al. report a total of 3372 modified peptides for the NHS-ester (P5) in mouse liver proteomes on amino acids K, T, S, Y, R, and C (most to least modified sites) [298]. Our data analysis in FragPipe was limited in the open search to the three most abundant amino acids with the modification of interest. For P5, these were K, T, and S (most to least sites, in line with literature) and we report over 10000 modified sites in four human cell lines. For vinyl-sulfone probe 9, there was no human proteome data available, Zanon et al. reported the probe tested in *Staphylococcus aureus* lysates [295]. Next, we focussed on investigation of the probe modified E3 ligases in the four cell lines to find the number of modified E3 ligases and their distribution within the cell lines.

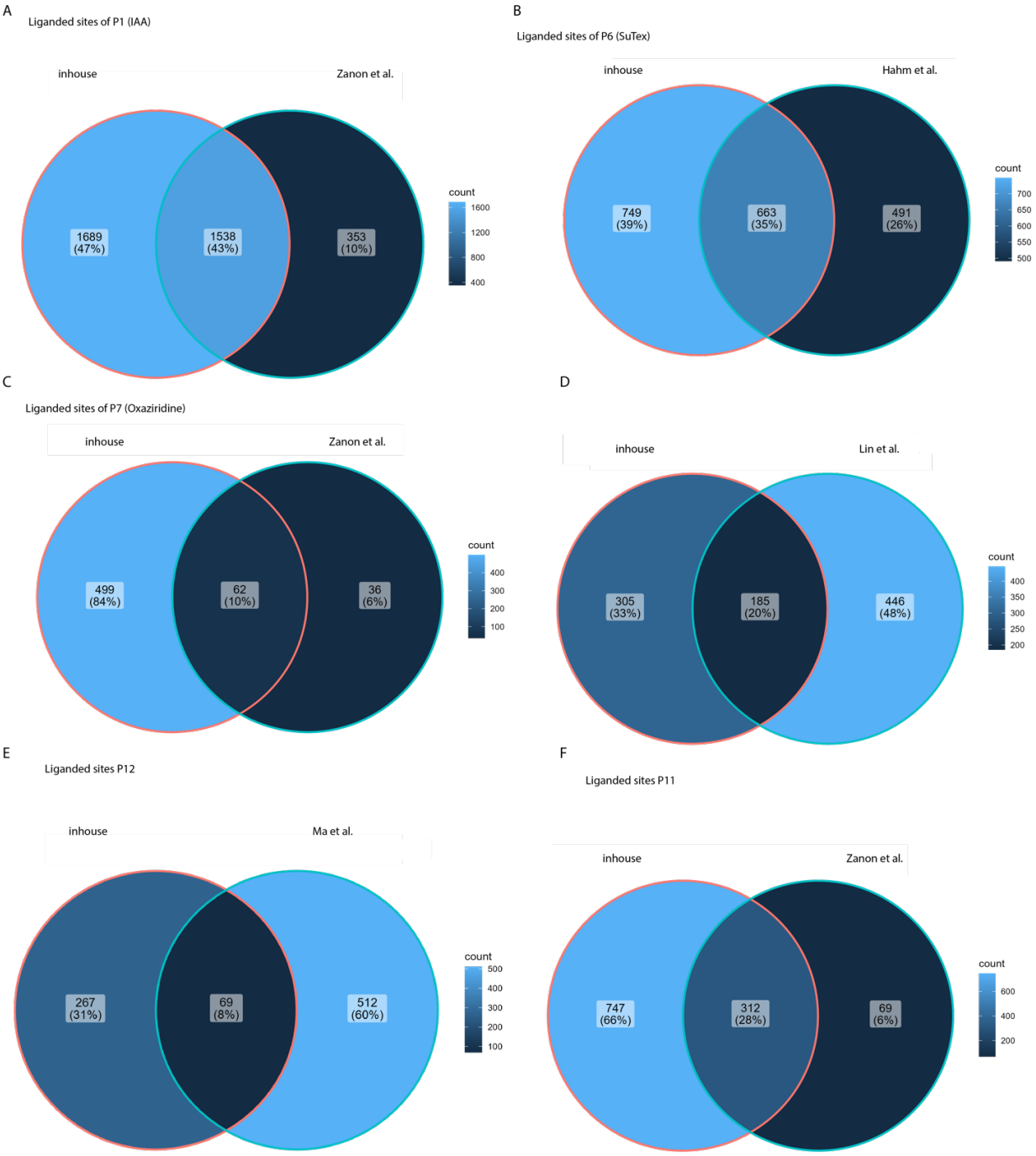


Figure 27: Literature comparison of protein labelling. A) Probe 1/IAA compared to Zanon et al. B) Probe 6/SuTEx compared to Hahm et al. C,D) Probe 7/oxaziridine compared to Zanon et al., Lin et al. E) Probe 12/aziridine compared to Ma et al. F) Probe 11/phenylglyoxal compared to Zanon et al. These Venn diagrams were created by Jeppe Tranberg-Jensen.

3.2.2 Enriched E3 ligases

In the non-competitive dataset, we identified a number of 132 unique E3 ligases and 391 unique modified sites (Supplementary Table T3). The greatest number of modified sites was mapped to E3 ligases RACK1, which exhibited 28 labelled sites, and TRIM28, with 20 labelled sites on distinct amino acids, other E3 ligases had less modified sites per protein. We did not expect any E3 ligases with $R > 4$, as there was no competition performed. However, if the experiment delivers fewer sites in the light-modified experiment, false positives might occur. We performed experiments in triplicates to distinguish outliers, e.g. when they occur in only one replicate. Next, we compared our total proteome data to the E3 ligases which were enriched and found a recovery of 40 % of E3 ligases previously identified in the total proteome. We did not address 152 E3 ligases from the total proteome dataset but could report 18 E3 ligases which were previously not identified, indicating enrichment for these E3 ligases under our experimental conditions (Figure 28A). 11 out of 18 were RING finger E3 ligases, underscoring the susceptibility of this E3 ligase class for modification at cysteine residues. A recent study highlighted zinc-coordinating cysteines in RING finger motifs as attractive sites for E3 ligase recruitment [268]. When we compared the performance of the cell lines, we found that a large proportion of E3 ligases (21 %) were shared between the cell lines, yet K562 contributed a remarkable number of 31 (23 %) unique E3 ligases to the dataset (Figure 28B). Among these E3 ligases was SOCS2, which is predicted to act as a tumour suppressor, and especially in haematopoietic malignancies, such as chronic myeloid leukaemia, SOCS2 was found to be expressed at increased levels [321]. Interestingly, a current publication investigated SOCS2 ligandability in cell line K562 [266].

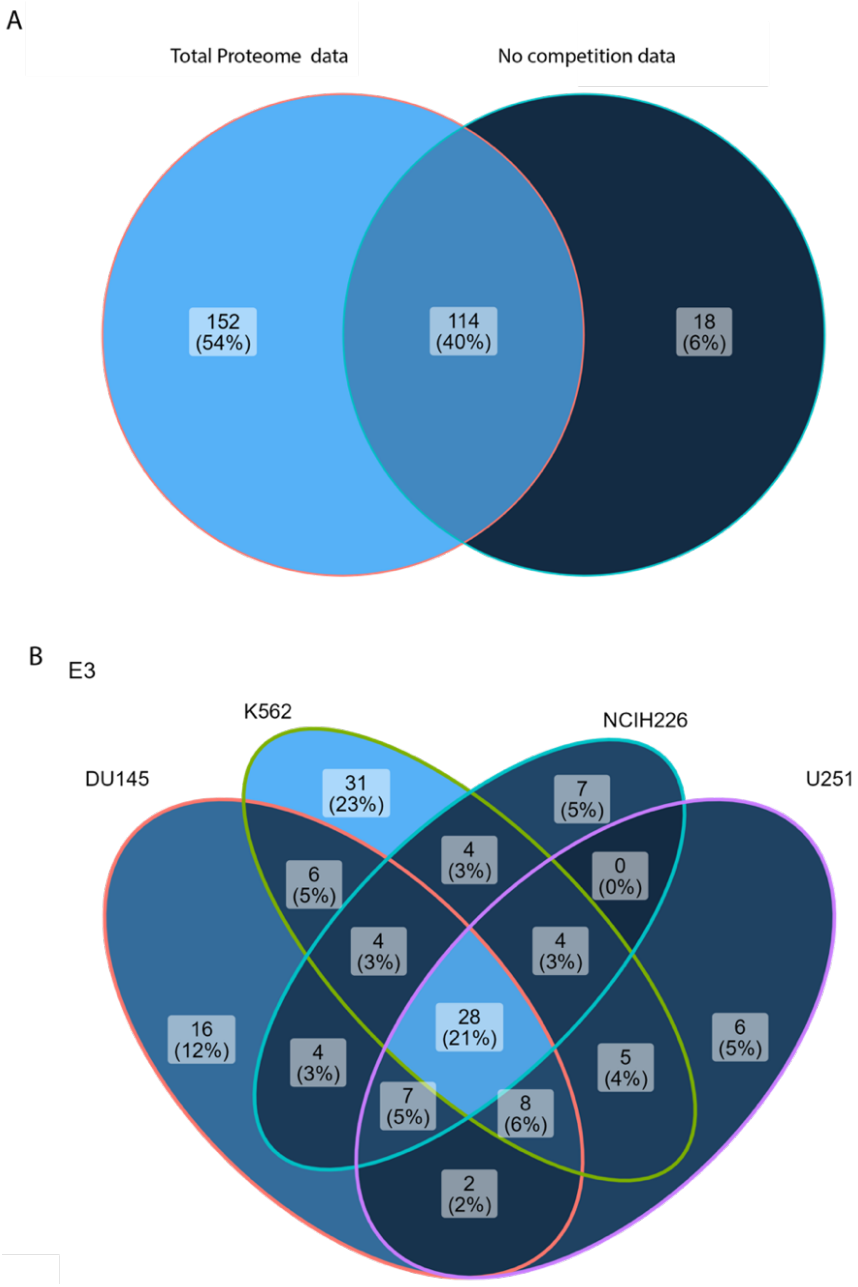


Figure 28: E3 ligases detected in the non-competition dataset. A) Venn diagram depicting overlap of identified E3 ligases in total proteome data and non-competition data; each circle represents the sum of four cell lines DU15, NCHI226, DU145 and U251. The 18 E3 ligases were APPBP2, BRCA1, BTBD10, CBLL1, HERC5, KBTBD11, KCTD16, KCTD20, MEX3A, MKRN1, PJA1, RACK1, RBX1, RNF7, RNF146, RNF166, TLE1, TRIM16. B) Contribution to total number of E3 ligases per individual cell line depicted in Venn diagram. The Venn diagrams were created by Jeppe Tranberg-Jensen.

3.3 isoTOP ABPP: competitive distinction of druggable binding sites

Next, we decided to filter the previously identified sites regarding their requirement of a more lipophilic motif in addition to the covalent warheads for a binding event to occur. All competitors and probes were screened at 100 µM concentration and incubated for 1 h at room temperature in respective lysates. Due to high MS costs, we selected a sub-set of the 96 competitor samples covering > 95 % of the enriched E3 ligases previously identified in the non-competition dataset (

Table 6). This sub-set of 42 samples avoided unnecessary overlap of reported sites in the different cell lines. As K562 was identified as the most productive contributor of E3 ligases from the non-competition data, the full set of 8 competition experiments was measured in K562, alongside additional samples in the other three cell lines to achieve maximal E3 ligase coverage.

Cell line	Probe	E3 yield	E3 total	Coverage (%)
K562	all	90	90	68.2
DU145	P1	20	110	83.3
U251	P9	6	116	87.9
N226	P1	5	121	91.7
DU145	P9	5	126	95.5
U251	P1	2	128	97.0
U251	P5	1	129	97.7

Table 6: Table showing the contribution of probes and cell lines to total coverage of E3 ligases, based on the non-competition dataset. The percentage is calculated based on 132 E3 ligases enriched in the no competition dataset. This analysis was used to select the set of 42 samples for the competition dataset MS run.

3.3.1 Competition results for cell lines

From the selected set of non-competition samples, we could identify a total number of 24657 modified sites in respective cell lines using probes P1, P9, and P5 (Figure 29A). K and C residues were modified around 9000 times, even though lysine-reactive probe P5 was only used in one experiment versus cysteine-reactive probes P1 and P9, which were contained in seven experiments. The probe performance on both protein and site level is shown in Figure 29B and Figure 29C; visualising all probes in K562, three probes in U251, two probes in DU145 and one probe in NCIH226. This result covered around 80 % of the total number of modified sites identified previously in the no competition data, which indicated a good overall coverage of sites. Now, our main focus turned to the analysis of the competition dataset with regard to liganded E3 ligases.

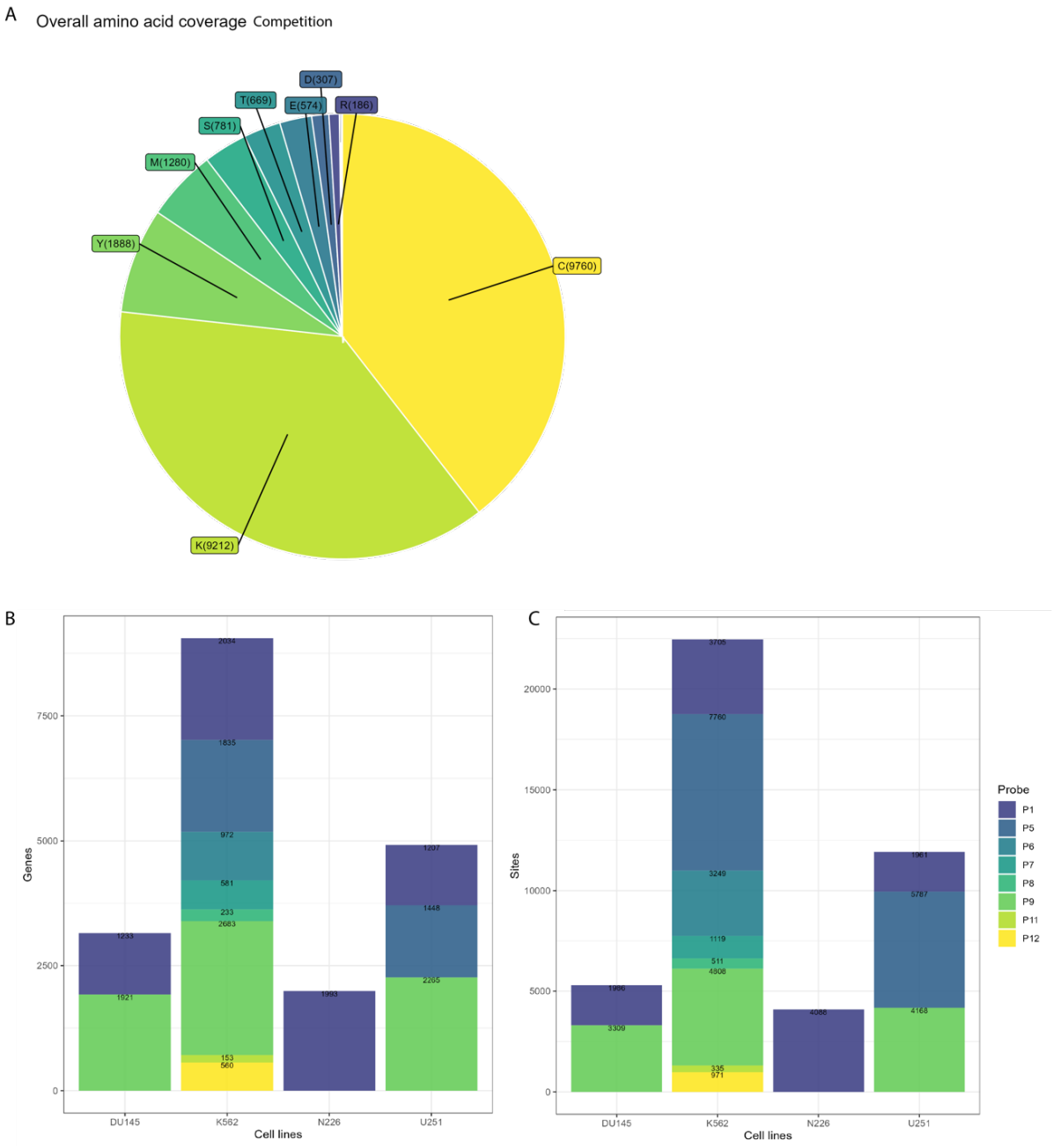


Figure 29: Summary of the competitive screening of probe set in four cell lines. A) Pie chart depicting number of modified amino acid residues. In sum 9 amino acids were detected as modified. B) Comparison of probe performance in four cancer cell lines DU145, K562, NCIH226 and U251 on gene level. C) Comparison of probe performance in four cancer cell lines DU145, K562, NCIH226 and U251 on site level. The bar and pie charts were created by Jeppe-Tranberg Jensen.

3.3.2 Competed E3 ligases

Overall, the competition data resulted in a right shift of the log_2(H/L) ratio, and competed sites, especially R > 4 (corresponding to 75 % competition) was interesting as the focus of subsequent analyses for well-competed sites. An example of the non-competition versus competition distribution is depicted in Figure 30A as histograms for IAA and competitor 1c in K562. We identified a total number of 150 E3 ligases and 770 modified sites in the competition dataset. When we compared this data to the total proteome dataset, we recovered 42 % of previously identified E3 ligases. We did not address 149 E3 ligases from the total proteome dataset but could enrich 27 E3 ligases, which were previously not identified in the total proteome (Figure 30B). Interestingly, 20 of the 27 E3 ligases were RING finger motif containing E3 ligases and they were overlapping to 75 % with the enriched 18 E3 ligases from the non-competition experiment. While 38 modified sites were showing R > 4 (Supplementary Table T4), the highest competed site was UBR5_C2267, which lies in a disordered region between two C-loops responsible for interaction with Ub and E2 ligase. UBR5 is a HECT E3 ligases, which has an active site cysteine residue responsible for Ub transfer and is found overexpressed in breast and ovarian cancers [322]. This residue would be highly interesting for further screenings with analogue compounds to determine a more selective cysteine residue binder. HECT E3 ligase UBR7 site C374 was also highly competed (R > 5), which lies outside of the zinc-finger regions. Notably, E3 ligases RNF214, RNF113A, and RNF25 were among the hits R > 4, which supports the hypothesis that the common RNF motif zinc-coordinating cysteines might be especially susceptible for ABPP screening [268]. Interestingly, RNF214_C655 lies within the zinc-finger region and thus might be a candidate worth pursuing for recruiter development. Studies to evaluate whether addressing this residue

does affect protein function and stability would be required, for this Tm shift or CETSA would be suitable. Notably, all modified residues with R > 4 were cysteines.

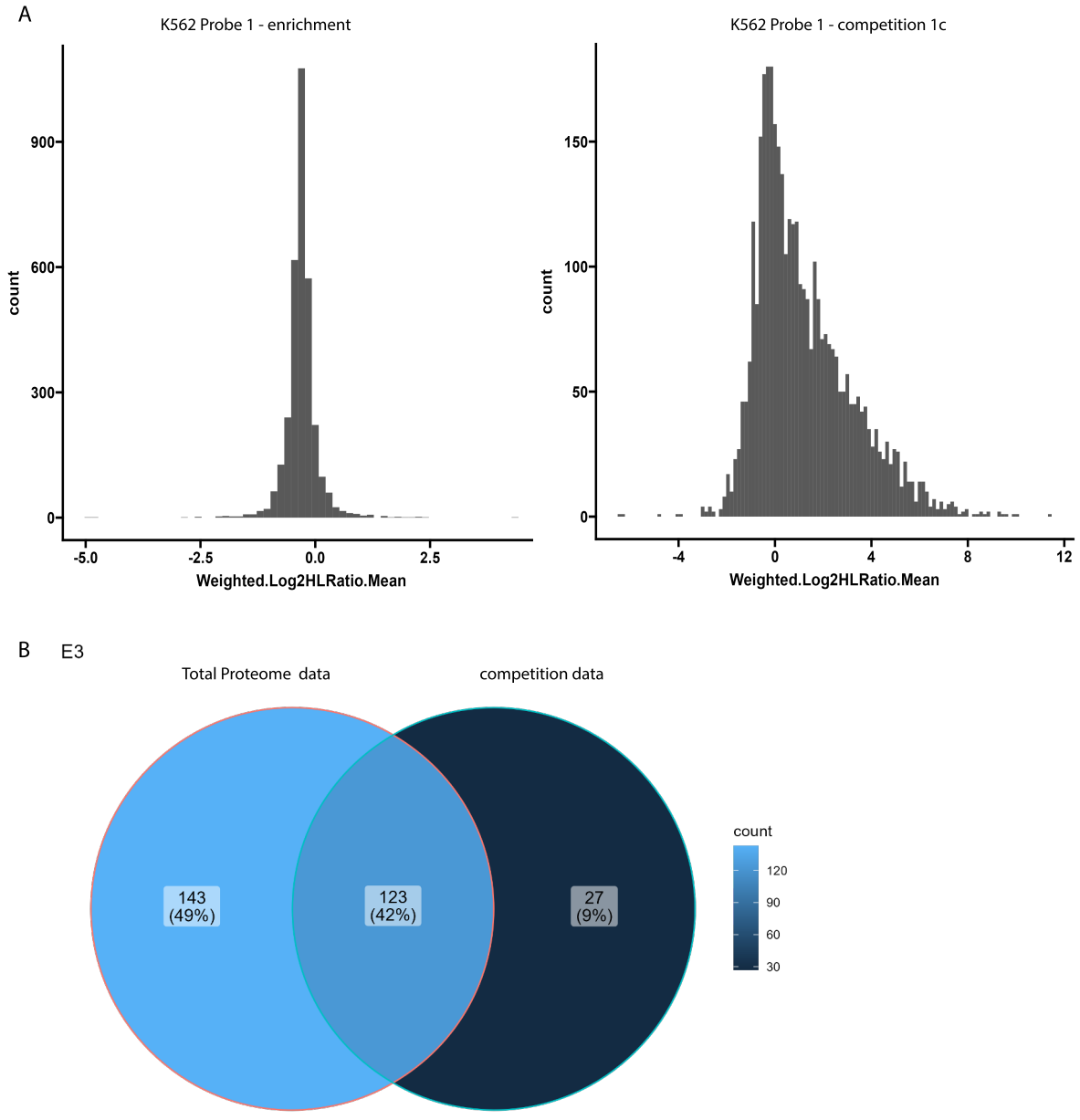


Figure 30: E3 ligases detected in the competition dataset. A) Histogram showing distribution of modified peptides (count) for probe 1 with and without competition using competitor 1c. The competition condition right shifts the weighted log2HLratio mean towards higher R values. B) Venn diagram depicting overlap of identified E3 ligases in total proteome data and competition data; each circle represents the sum of four cell lines DU15, NCHI226, DU145 and U251. The 27 E3 ligases were BRCA1, BTBD10, CBLL1, COP1, DCAF1, FBXO46, KBTBD11, KCTD20, MEX3A/D, MKRN1/3, PDZRN4, PJA1, RACK1, RBX1, RNF7/19A/146/166, SOCS6,TRIM7/16/24/37, TULP4, UBOX5.

Further, we investigated whether the identified sites were solvent-accessible or buried. Solvent-accessible sites might be useful for E3 ligase recruiter development, whereas buried sites, in pocket-like structures might be used to develop tool compounds or chemical probes, and modified active sites would be useful for inhibitor development. For each protein, we obtained the protein structure from the AlphaFold (AF) Protein Structure Database [323] by UniProt identifier. The solvent-accessible surface area (SASA) was calculated using the function `get_sasa_relative´ in PyMOL. In addition, p2rank was used to identify ligand binding sites [324, 325]. Applying the criterion SASA ≥ 20 % to identify solvent exposed residues [326], out of 571 modified sites, there were 485 exposed and 185 buried (Supplementary Table 5). Using p2rank, we identified 67 accessible sites in pockets out of the 571. When we applied R > 4, 20 E3 ligases were matching the criteria, and subsequently one modified site was defined as in a pocket according to p2rank, namely SOCS2_C111 (Table 7). Interestingly, this residue was also recently identified by another group who achieved labelling of this site using a chloroacetamide (MN714) [266]. The authors reported selectivity within a SOCS protein panel, only SOCS6 was showing marginal labelling in intact MS. In a live-cell CETSA, they observed a thermal shift of 2 °C. Efforts are undertaken to further optimise the cell-permeable, covalent recruiter MN714 into a PROTAC-handle. This underlines that our analysis yielded a hit which is confirmed to be experimentally tractable. Nonetheless, machine learning-based predictions are recommended as complementary to experimental data. A recent study by White et al. re-iterated the importance to validate the predicted *in silico* accessibility of sites with experimental data as ligandability and reactivity might differ from the prediction, because PTM, PPI, and co-factor interactions should be considered in an *in vitro/in vivo* environment [327].

Gene	Modified Residue Index	Modified Amino acid	Log2 Ratio	Relative SASA	In Pocket
BRAP	47	C	5.24	0.36	0
CBLL1	73	C	5.61	0.67	0
HECTD1	1368	C	4.31	0.85	0
			4.24	0.85	0
KCTD20	369	C	4.94	0.81	0
MKRN1	186	C	4.59	1.00	0
	305	C	4.49	1.00	0
NOSIP	8	C	4.43	0.88	0
PJA2	48	C	5.72	0.72	0
PML	338	C	4.42	0.85	0
	389	C	4.70	0.78	0
RAD18	64	C	4.41	0.58	0
RING1	279	C	6.54	0.68	0
RNF25	360	C	6.67	0.98	0
RNF40	950	C	6.70	0.57	0
			4.61	0.57	0
RNF113A	15	C	4.62	0.68	0
RNF214	655	C	4.25	0.30	0
			4.13	0.30	0
			5.58	0.30	0
SOCS2	111	C	5.23	0.19	1
TRIM33	150	C	4.56	0.09	0
UBE3A	83	C	4.27	0.22	0
UBR1	1603	C	4.36	0.46	0
			4.59	0.46	0
UBR7	374	C	4.05	0.60	0
WWP2	186	C	4.01	1.00	0

Table 7: Table showing E3 ligases, modified residue numbers and amino acid type as well as log2 ratio (here R > 4 was applied), relative SASA and whether a residue is located within a pocket. This analysis was performed by Martin Buttenschön.

3.3.3. Further optimisation of data acquisition mode

Aiming to further re-fine the workflow, we compared the performance of the reactive probe IAA in cells versus lysates, as well as in different acquisition modes. Both cell and lysate experiments were measured in data-dependent acquisition (DDA) and data-independent acquisition (DIA) modes to validate a newly developed version of FragPipe, which would allow for the identification of custom PTM from DIA data for the first time using the FragPipe software. The package FragPipe 20.0 was developed by Fengchao Yu and Alexey Neshvitzhkii. In DDA mode, the MS machine cherry-picks precursor ions for fragmentation based on abundance and intensity, whereas DIA captures all fragment ions within a pre-determined m/z range [328]. Therefore, DDA data is biased towards highly abundant peptides and will often not fragment lower abundant ones, whereas DIA data is more complete as it fragments those peptides. In general, DIA is considered to provide better reproducibility and sensitivity [329]. A classical workflow for DDA-MS analysis commonly comprises protein extraction, digestion, data acquisition, data processing, and analysis. To increase depth, pre-fractionation steps are undertaken, e.g. as we did for the total proteome, which require a larger sample amount to start with. The same workflow applies to DIA-MS, but since more complex fragment ion spectra are measured post-acquisition, *in silico* data processing steps are required to deconvolute the spectra. This comprises interrogating MS data with spectral libraries, which are generated by DDA analysis of the same sample prior to DIA. These libraries contain information on precursor and fragment m/z values, fragment type, charge, relative intensity, and elution timepoint time for each individual peptide in the sample [330].

For a DDA and DIA data comparison, we measured the identified sites and proteins derived from a cell-based reactive probe treatment sample to a lysate one. We found a gain of up to 30 % modified sites which translated to an increase of around 1000 protein IDs in the DIA data in the cell sample (Figure 31A,B). In both the DDA and DIA data we derived more sites and IDs for the cell-based experiment in comparison to the lysate data. This might indicate that a large percentage of membrane or nuclear proteins is susceptible for IAA reactive probe labelling, which in turn might not be sufficiently solubilised using only PBS and mechanical sonication for the preparation of the lysate. The membrane proteins might be discarded alongside nuclear proteins and cell debris in the centrifugation step after cell lysis and therefore might not be available for reaction with IAA. An analysis using the PANTHER (Protein Analysis Through Evolutionary Relationships) classification system [331] of proteins detected uniquely the cell-based DIA data revealed, that DNA and RNA metabolism-related proteins were more prominently represented in the cellular sample (Supplementary Figure S3). In the future, a nuclear extraction could be performed in addition to the lysis method which we described, to obtain a larger proportion of nuclear proteins [126]. Addition of detergent to the lysis buffer might elevate the solubilisation of membrane-bound proteins.

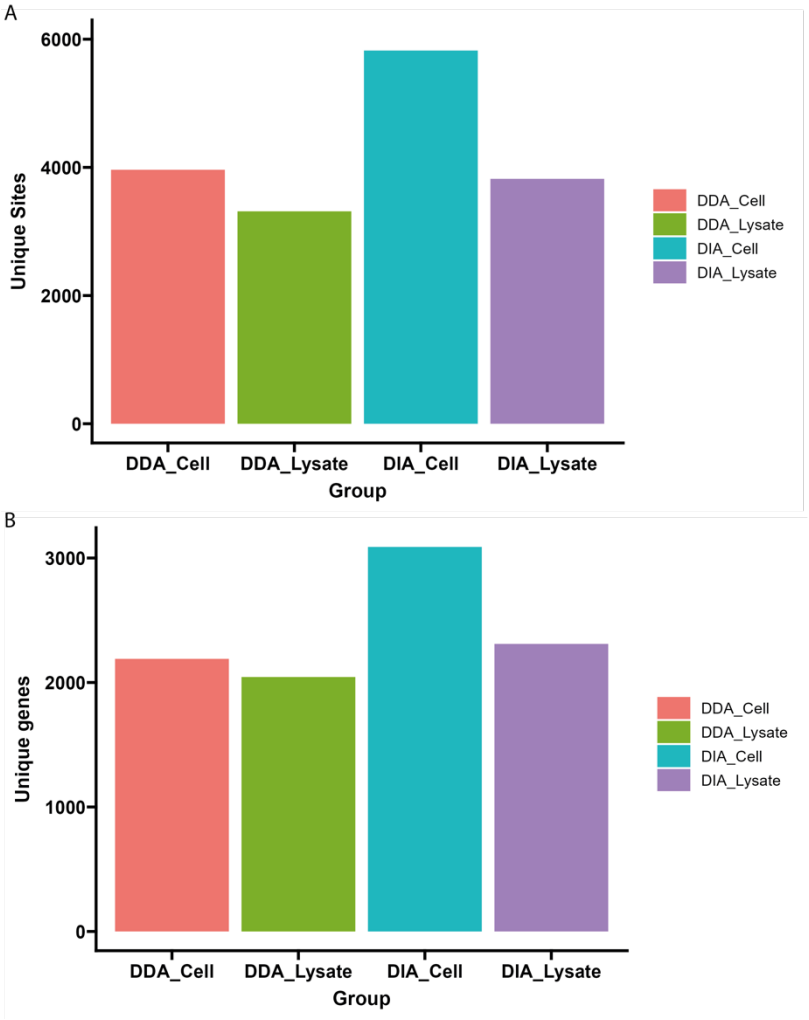


Figure 31: Comparison of data in K562 intact cell and lysate in DDA or DIA mode, treatment with 100 µM IAA for 1 h, each bar represents n=3. A) Unique sites reported for each condition. B) Unique proteins reported for each condition. The charts were produced by Jeppe Tranberg-Jensen.

3.4 Summary and outlook

The large-scale isoTOP ABPP screening campaign of eight reactive-probes and corresponding lipophilic competitors in four distinct cancer cell lines (K562, NCIH226, DU145 and U251) yielded a vast proteomics dataset. In 96 no-competition experiments, the scale of druggable sites on amino acids such as C, M, K, T, Y, R, D, and E was determined to be 30845 sites in total. This dataset provides an overview of addressable sites not only on E3 ligases, DUBs and other UPS-family members but also on the whole proteome in respective cell lines. The data can be mined for valuable starting points for potential competitor binding sites. To add another layer and to distinguish between highly reactive sites and sites, which require a small lipophilic motif for a binding event, we conducted 96 competition experiments. To reduce redundant measurements, the sample set was reduced to cover all previously identified E3 ligases to > 95 %. The effort resulted in our druggability map comprising 24657 sites. We showed 38 promising E3 ligase sites which were competed (R > 4) and which are suitable for further investigation in isoTOP ABPP screening campaigns.

In comparison to recent literature, we show that our data was complementing previous findings, as we confirmed identified sites, but we also reported new probe-modified sites. The cysteine-reactive probes have been widely and extensively studied. In a recent study by White et al. [327], 18 publications have been compared and meta-analysed regarding their cysteine-reactive proteins and modified sites. The authors report total number of 44187 liganded cysteine residues in these studies out of 261260 in the human proteome (based on a UniProt database analysis). They defined a prediction-aware part-sphere exposure (pPSE) indicating whether a residue is buried or highly accessible. Interestingly, a re-

evaluation of a study by Backus et al. [119] regarding temperature influencing the residue accessibility, revealed that heat treatment increased the accessibility of buried cysteines in comparison to native lysate. Further re-evaluation of findings reported by Li et al. supported the notion that native lysates compared to detergent-treated lysates can be utilised to discriminate between essential, reactive cysteines, which are worth pursuing as chemical starting points for inhibitors or binders, and those rather inaccessible and buried residues which can be de-prioritised [306]. Both heat and detergent doubled the number of reported residues in those studies [327]. In sum, these reports underline the importance of the native lysis conditions and the consideration of temperature effects on protein stability as well as changes in residue accessibility due to denaturation or unfolding. Thus, we chose conditions for the screening of our reactive probe library, avoiding long incubation times and harsh lysis steps, to provide insight into ligandability of residues in an unbiased, native protein state. Furthermore, the large overlap we achieved with the CysDB dataset is supporting the relevance of the obtained cysteine sites in our hands. An addition to achieve higher coverage of reactive cysteines would be highly efficient N-acryloylindole-alkynes for isoTOP ABPP studies [307].

The NHS-ester probe was tested in mouse proteomes before, and lysine reactivity could not be compared to our human cell-derived dataset. Lysine reactivity, however, has been evaluated in human MDAMB231, Jurkat, HEK293T, and Ramos cell lines using an amine-reactive pentynoic acid sulfotetrafluorophenyl ester probe (STP-probe) modifying > 9000 residues in total. STP-probe is a promising candidate to screen for distinct K reactivities in isoTOP ABPP using competitors [308]. Efforts to screen lysine reactivity on a broader scale by Abbasov et al. allowed to report > 14000 sites by profiling of 180 compounds distributed across > 30 aminophilic chemotypes, both covalent-reversible and

-irreversible electrophiles, in human cancer cell lines and primary human immune cell proteomes [310]. Methionine labelling has been achieved using oxaziridine-probes and was applied, e.g. to kinase CDK4 [332]. However, these probes have yielded a rather low number of labelled sites, but we achieved a similar number of sites compared to Lin et al. [124] in human cell lines, whereas Zanon et al. modified around 100 residues in bacteria.

Our screening of the SuTEX- and sulfonylfluoride-probe yielded more than 1000 modified residues on K, T, and Y residues. Recent advances in the field of tyrosine-profiling led to chiral sulfonylfluorides, which have been shown to label both tyrosines and lysines [297]. The authors of this study reported that around 100 Lys and 500 Tyr sites reacted with their probes in a non-competitive isoTOP ABPP workflow, of approximately 650000 Lys and 300000 Tyr sites overall in the human proteome. A panel of sulfonylfluorides was applied to profile a set of kinases and were shown to be promising candidates fine-tuneable in their reactivity towards kinases and non-kinase targets on lysine, tyrosine, histidine, and serine residues [333]. Rather understudied side chains are represented by arginine, aspartic- and glutamic acids as they are of lower intrinsic nucleophilicity. In our hands, P11, the phenylglyoxal-alkyne yielded lowest labelling across all four cell lines. The aziridine-alkyne was also rather weak. An additional opportunity to address aspartic- or glutamic acid residues would be compounds based on Woodward's reagent K (WRK) [312].

In the competition data, we derived 38 sites which had an $R > 4$ and provided interesting starting points for the development of binders. Inhibitors can be developed for residues in active sites; additionally, sites which are surface-exposed or in intrinsically disordered regions can be utilised for recruiter design. For example, a recruiter for RNF114 was

developed binding to C8 in the intrinsically disordered region [259]. Our data from a subset of competitors hints to ligandable sites, especially SOCS2_C111 came up as a promising site both ligandable and also positioned in a pocket following an analysis based on SASA of PDB and AF2 structures. Further efforts are aimed at deepening the analysis and incorporate, for example the newly presented pPSE approach from White et al. [327]. It is very intriguing to evaluate residues using AF and machine-learning methods as a support to determine which sidechains are worth pursuing for E3 ligase recruiters and inhibitors. The pPSE analysis was additionally helpful to support the relevance of native lysates versus heated or denatured lysates when we focus on unbiased residue accessibility. However, predictions based on AF should be handled with caution and should ideally be paired with complementary experimental data for reliable results. Further competitive isoTOP ABPP studies could be added to our dataset, comprising profiling studies using higher concentrations of reactive probes. Yan et al. recently showed a greater number of identified sites when using 2 mM instead of 100 µM of the reactive probe [133].

An advantage of the isoTOP ABPP workflow is that experimental parameters (concentration, reactive-probes, incubation times, use of cells or lysates) can be easily varied to obtain datapoints from a different experimental setup, allowing for thorough interrogation of the proteome. For example, we adjusted the workflow to conduct a test of a small DDA and DIA dataset, which revealed that the DIA acquisition mode is yielding higher number of sites and protein IDs. Cell-based experiments gave a higher number of modified sites, indicating the susceptibility of DNA- and RNA-binding proteins to react with IAA. Another advantage of isoTOP ABPP is that researchers can not only screen covalent fragments but also natural products, such as nimbolide or

asukamycin [259, 267]. Encouraged by this, we sought to screen not only fragments but chemical probes and probe candidates to underline their selectivity. This work is presented in the next chapter.

4. Target evaluation of chemical probes and fragments using isoTOP ABPP

Demonstrating target selectivity and target engagement is crucially important for a compound's translation into a safe and efficient drug. Especially electrophilic covalent compounds are prone to promiscuity and high reactivity, whereas chemical probes are highly specific, potent, and selective against their target. In this chapter, we used the isoTOP ABPP platform for screening chemical probes and probe candidates to underline their selectivity. We also utilised a combination of a phenotypic SPECK-formation screen to pre-filter promising covalent fragments as potential NLRP3 inflammasome inhibitors to follow up on with isoTOP ABPP. Lastly, we aimed to validate lipophilic competitors identified in the isoTOP ABPP screening described in chapter 3 using a repertoire of CETSA, FRAP, and intact MS.

4.1 E3 ligase KEAP1 and a selective chemical probe

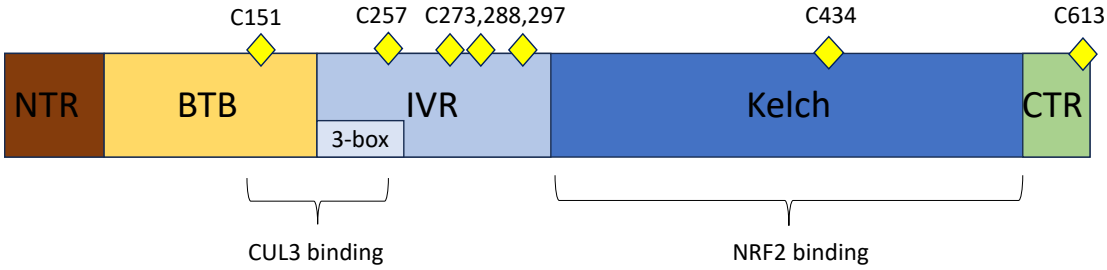


Figure 32: Organisation and binding regions of human KEAP1. Redox sensitive cysteines are C151, 273 and 288. Schematic adapted from Magesh et al. [334].

KEAP1 (KLHL19) is an E3 ligase that is known to promote Ub-dependent degradation of NRF2 by assembling into a heterotetrametric complex with CUL3 [335]. Under normal cellular conditions, KEAP1 polyubiquitinates NRF2, which is subsequently degraded in the proteasome. Cellular stress oxidises KEAP1, which releases NRF2, which in turn activates cellular defence genes (e.g. antioxidant response) [336]. KEAP1 contains a total number of 27 cysteines (Figure 32), of which seven are highly reactive towards reactive oxygen species, or electrophiles, and are involved in redox sensing [334, 337]. Induction of the antioxidant/antitoxification response is especially attractive as a target in neuroinflammation or cardiovascular diseases [338]. Oxidative and electrophilic stress have been shown to result in covalent modifications on cysteine residues on the KEAP1 BTB and BACK domain, ablating interactions with CUL3 [339, 340]. Cysteine residues have been shown to be attacked by covalent compounds, such as bardoxolone methyl (CDDO), which bound to C14, C47, and C101 in vitro [341], and C151 in a crystal structure [342]. Targeting the KEAP1-NRF2-axis, small molecule inhibitors have been developed binding to C residues on KEAP1 and inhibiting interaction with NRF2 [343, 344].

Additionally, peptidomimetic inhibitors, which could serve as lead molecules for further inhibitor development have been reported to block KEAP1-NRF2-PPI [345].

Efforts by Prof. Alex Bullock's group at the University of Oxford in collaboration with Servier Pharmaceuticals to develop a KEAP1 chemical probe yielded compound S213726 (data are currently unpublished). S213726 showed nanomolar potency in cells and formed a corresponding mass adduct in intact MS on KEAP1. Structurally related negative control S214489 did not form a covalent adduct. A co-crystal structure showed covalent binding of the probe to C151, which is exhibited only by KEAP1 and KLHL26 in the KLHL protein family. To determine proteome-wide selectivity of the chemical probe in cells, we chose cell line MDAMB231, as KEAP1 is highly expressed in this breast cancer cell line [346]. The expression was confirmed in WB (Supplementary Figure S4).

4.1.1 isoTOP ABPP of chemical probe S213726

We pre-treated live cells as describedin the previous chapter. In brief, respective compound, negative control, or DMSO vehicle were incubated for 3 h at 1 μM concentration at 37 °C and 5 % CO_2. As the reactive probe, 100 μM of IAA was used. The chemical probe candidate was binding to C151, however in our data, we did not directly detect this residue on KEAP1 when using IAA. Therefore, we could only indirectly show the selectivity of the probe. As a result, for both the negative control and probe, ≤ 1 % of detected proteins were competed with R > 4.5 as a significance cut-off for the chemical probe (Figure 33A,B). For the negative control, HSP90AA4P_M175 was identified above the cut-off, out of around 7000 sites. PCIF1_C626 was the only site that was found as competed for the KEAP1 probe, out of a total of around 6000 sites. PCIF1

is an RNA N6,2′-O-dimethyladenosine methyltransferase thought to have an oncogenic function in gastric cancers [347]. These results underlined the high selectivity of the KEAP1 probe. This notion was supported by Tm shift kinase panel data showing selectivity of the probe and no binding to over 100 protein kinases (Alex Bullock group and Servier, data to be published).

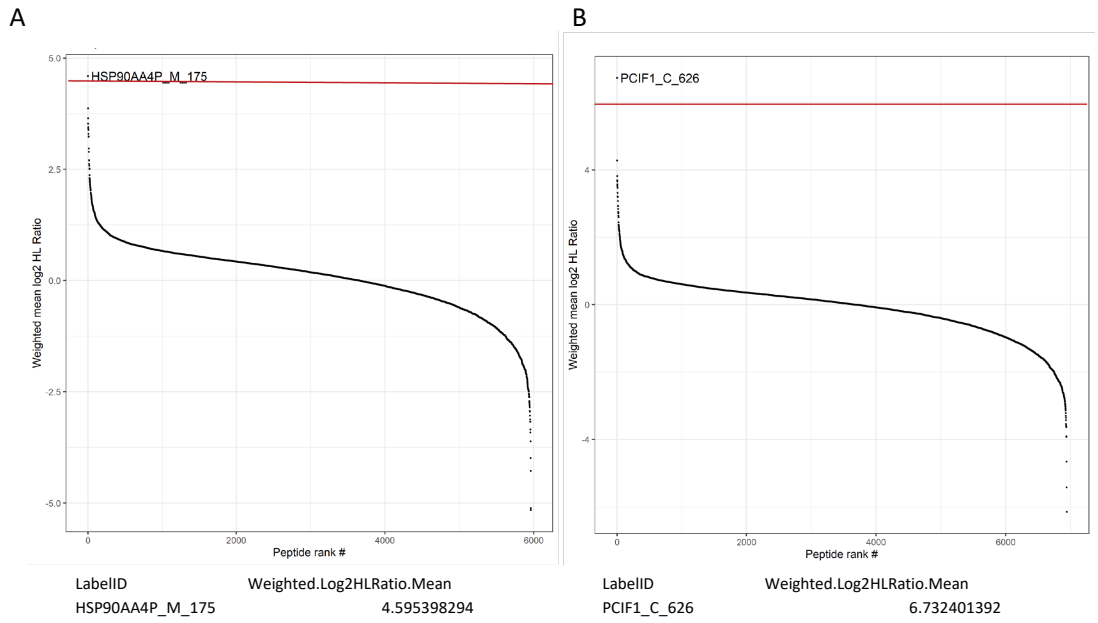


Figure 33: Waterfall plots of isoTOP ABPP screening of negative control S214489 and probe S213726 for KEAP1. The compounds were competed against 100 µM of IAA in MDAMB231 cells (n=3). A) Plot showing results for negative control, significance cut-off R > 4.5 is marked in red. The weighted Log2H/L ratio mean is reported for HSP90AA4P. B) Plot showing results for probe candidate, significance cut-off R > 4.5 is marked in red. The weighted Log2H/L ratio mean is reported for PCIF1.

4.2. Evaluation of a chemical probe for NUDIX-family member NUDT7

NUDT7 is a peroxisomal CoA pyrophosphohydrolase belonging to the NUDIX family, which catalyse substrate hydrolysis via a 23-amino-acid motif, the NUDIX box. The NUDIX family proteins hydrolyse substrates like deoxynucleotide triphosphates, nucleotide sugars and alcohols, and dinucleoside polyphosphates and coenzymes [348]. The NUDT7 gene contains a CoA-binding motif and a C-terminal peroxisomal targeting signal, additionally it is highly expressed in the liver, brown adipose tissue and the heart [349, 350]. NUDT7 is thought to be involved in the regulation of the peroxisomal lipid metabolism, which is supported by metabolomic studies in mice, which revealed that fasted livers overexpressing NUDT7 contained significantly reduced levels of bile acids and accumulated medium- and long-chain acylcarnitines, which correlated with a lower rate of peroxisomal fatty acid oxidation [351]. Furthermore, deletion of NUDT7 altered the composition of the hepatic acyl-CoA pool in mice, leading to increased total liver CoA levels [352]. Neuronal overexpression of a cytosolic version of NUDT7 in mice was linked to a discernible decrease in brain CoA levels in correlation with a reduction in motor coordination, similarly to reduced CoA levels as seen in pantothenate kinase-associated neurodegeneration (PKAN) [351].

The first known NUDT7 inhibitor was reported by Resnick et al.; lead compound NU00443a (also NUDT7-COV-1) binding to NUDT7 was identified in a high throughput screening performed with a library of mild electrophilic warheads (acrylamides and chloroacetamides) [157]. NU00443a showed micromolar activity in a catalytic assay as well as a significant thermal shift in NUDT7 FLAG-tag transfected HEK293 cells in a CETSA experiment. Subsequent isoTOP ABPP experiments using NU00443a against IAA

showed labelling of 37 sites with R > 4 out of 2000 compound modified sites [157]. NUDT7 itself could not be detected, most likely due to low abundance in HEK293 cells. The co-crystal structure of NU00443a and NUDT7 was solved, showing a covalent modification of residue C72 (PDB: 5QHH)[17]. We would like to note that the residue previously reported as C73 was compared to UniProt sequence (H3BRQ8_HUMAN), which clarified that the residue is C72 (Figure 34). Using an array of synthesised compounds, a crystallographic screen against NUDT7 yielded several co-crystal structures [353]. Following up on this work, a chemical probe candidate NU074516a was developed by the SGC and EubOPEN consortium[18] in collaboration with Janssen-Cilag.

MSRLGLPEEP VRNSLLDDAK ARLRKYDIGG KYSHLPYNKY SVLLPLVAKE GKLHLLFTVR

SEKLRRAPGE VCFPGGKRDP TDMDDAATA LREAQEEVG LRPHQVEVV CCLVPCLIDVRVS

Figure 34: Sequence for NUDT7 (H3RBQ8_HUMAN) from UniProt. C72 is highlighted in red.

4.2.1 isoTOP ABPP of chemical probe NU074516a

As we were not successful in identifying modified NUDT7 at endogenous levels via WB in cells likely due to low expression [157], we chose to overexpress NUDT7. For this, we used the CETSA protocol from Resnick et al. and subsequently harvested transfected cells for isoTOP ABPP [157]. In brief, live HEK293 cells were transfected with NUDT7 FLAG-tag, and expression was confirmed by WB using anti-flag antibody (Supplementary Figure S5). Transfection was performed 24 h before being treated with the respective chemical probe candidate (NU074516a), negative controls (NU074586a, NU074679a,

[17] https://zenodo.org/record/1244111
[18] https://www.thesgc.org/tep/nudt7

NU074678a) or DMSO vehicle for 2 h using 1 μM concentrations at 37 °C and 5 % CO_2; as a reference compound NU00443a was included at 10 μM. As IAA was previously reported to not directly address NUDT7, the lysates were alternatively treated with 100 μM of vinylsulfone-probe (P9). In our isoTOP ABPP experiments, we had yielded a higher coverage of cysteine residues in the proteome of the four cancer cell lines with the vinylsulfone-probe. After subsequent click-reaction, enrichment and digest, the MS samples were analysed. We could not only successfully identify NUDT7 but also residue C72, the binding site of the chemical probe (Figure 35A). However, NU074516a marginally competed NUDT7_C72 with R > 0.5 and showed multiple proteins competed more significantly. This indicates that the compound did not show selectivity for NUDT7 in the chosen conditions. We hypothesise that the concentration of 1 μM and incubation time of 2 h was perhaps too low and that a repeat with a higher concentration (e.g. 2 μM) could compete this site more efficiently. In contrast, the reference compound NU00443a yielded the site NUDT7_C72 with R > 3 (Figure 35B). This compound had been tested at 10 μM concentration, however the site was not competed above R > 4, and generally no residue out of > 4000 sites was competed greater than R > 4. The DMSO control showed no enrichment for NUDT7_C72 (Supplementary Figure S6). The negative controls showed no enrichment for NUDT7_C72, one compound showed the site at R > 0.5 (Supplementary Figure S6).

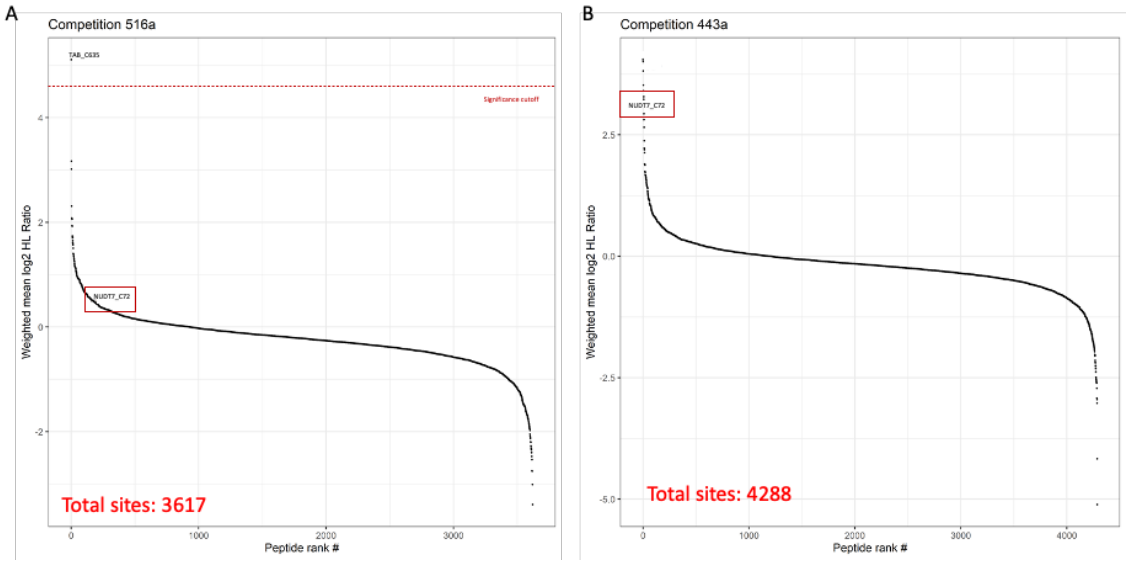


Figure 35: Waterfall plots for competitive isoTOP ABPP with chemical probe (516a) and reference compound (443a) against vinyl sulfone-probe P9 (n=3). A) Competition results for chemical probe show NUDT7_C72 is detected at around R > 0.5 and TAB3_C635 is competed with R > 4.5 B) Competition results with reference compound show NUDT7_C72 detected at around R > 3.

Next, we compared the R values for identified NUDIX family members, shown in Table 8. For compound NU00443a, NUDT7_C72 is the only site competed among the detected NUDIX proteins. For NU074516a, there is only marginal competition for this site. This highlights selectivity within the NUDIX family for NU00443a. There were six additional sites on other proteins that were competed higher than NUDT7_C72 in this dataset (SORT1_C_86, NCK2_C_297, RNF214_C_655, HTATSF1_C_462, HTATSF1_C_471, GRPEL2_C_44; all R > 3). Intriguingly, SORT1 is a member of the VSP10 domain intracellular trafficking family and has been associated with plasma cholesterol levels and cholesterol metabolism in hepatocytes [354]. NCK isoproteins, NCK1 and NCK2, connect tyrosine kinases to the machinery of actin reorganisation and therefore are involved in cell polarisation and migration [355, 356]. Splicing factor HTATSF1 has been identified as a regulator of early mammalian embryogenesis and pluripotency [357]. GRPEL2 is a

nucleotide-exchange factor for mitochondrial HSP70 chaperone and is proposed to have a protective role in mitochondrial proteostasis during oxidative stress [358]. These five proteins were analysed in a STRING network and were not linked to NUDT7. For NU074516a, TAB3_C635 was competed, TAB3 was shown as a signal transducer in both IL-1 and TNF signalling pathways [359]. To determine potential off-targets, the proteins should be further validated, e.g. by using recombinant protein in intact MS or Tm shift assays. NU074516a was not selective for NUDT7 under our experimental conditions.

443a

Site	Weighted.Log2HLRatio.Mean	Weighted.Log2HL.SD
NUDT10_C_3	-0.258473656	0.030949048
NUDT12_C_117	-0.900160629	0.141345039
NUDT15_C_23	-0.136140383	0.464489448
NUDT16L1_C_88	-0.455389973	0.059627344
NUDT4B_C_132	-0.135938302	0.037825048
NUDT5_C_76	-0.039111722	0.036671417
NUDT7_C_72	3.227245612	0.032289469
NUDT9_C_207	-0.27748693	0.119764928
NUDT9_C_347	-0.187338549	0.036698934

516a

Site	Weighted.Log2HLRatio.Mean	Weighted.Log2HL.SD
NUDT10_C_3	-0.315803843	0.106501547
NUDT12_C_117	-0.974341379	0.233852101
NUDT15_C_23	-0.167700167	0.352770423
NUDT16L1_C_88	-0.715897349	0.155479632
NUDT4B_C_132	-0.081350714	0.158420152
NUDT5_C_76	0.104664073	0.151716838
NUDT7_C_72	0.399455515	0.15272249
NUDT9_C_207	-0.172732826	0.716456589
NUDT9_C_347	-0.246387659	0.146946797

Table 8: Tables showing competition ratio R (weighted log2 H/L ratio mean) standard deviation for compound NU00443a (443a) and NU074516a (516a) for the range of identified NUDIX family members and sites.

4.3 NLRP3 inflammasome and neurodegeneration

Generally, inflammation is a protective response to pathogens aiming to fight infections or to repair damaged tissues, yet excessive inflammation is harmful. A multimeric complex, called the NLRP3 inflammasome, is a key component in the inflammatory responses of the innate immune system. NLRP3 (NACHT, LRR and PYD domain-containing protein 3) is a tripartite protein, in which the NACHT domain possesses ATPase activity and the LRR motif functions as an autoinhibitor while being folded back onto the NACHT domain [360]. NLRP3 acts as a sensor that can sense damage- or pathogen-associated molecular patterns, such as lipopolysaccharides on bacterial membranes. Upon NLRP3 oligomerisation, the adaptor ASC (apoptosis-associated speck-like protein containing a CARD) is recruited via PYD-PYD interactions to form an inflammasome complex. Subsequently, caspase-1 is recruited via CARD-CARD interactions and activated (Figure 36), releasing interleukins IL-1β and IL-18 and inducing pyroptotic cell death [361, 362].

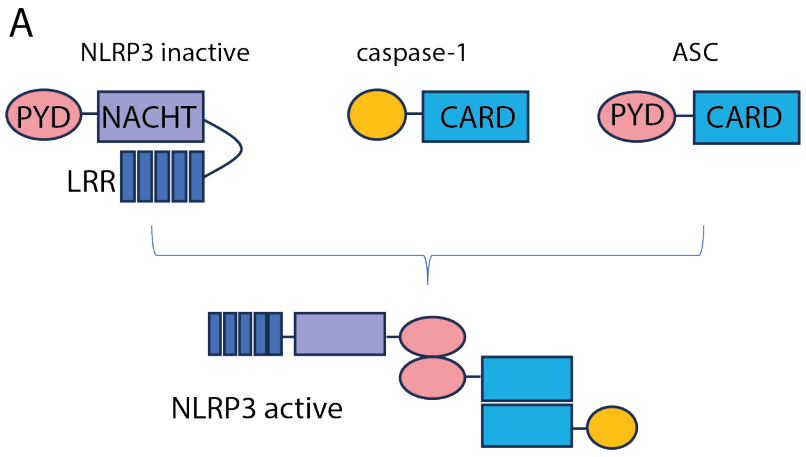


Figure 36: Schematic of tripartite protein NLRP3 with its domains PYD, NACHT and LRR; NLRP3 recruits ASC units via PYD-PYD interactions and subsequently forms an octameric inflammasome, which catalyses caspase-1 activity to release cytokines such as IL1b and IL-18.

The inflammasome is relevant in neuroinflammation, which contributes to disease progression in Alzheimer's disease (AD) [363]. Amyloid β, which accumulates and forms plaques, has been linked to NLRP3 activation and IL-1β release, suggesting a role of NLRP3 in AD [364]. Furthermore, NLRP3 knock-out mice have been shown to be protected from loss of memory and showed enhanced amyloid β clearance, pointing out its relevance in AD [365]. Not only genetic, but also pharmacological modulation showed therapeutic effects, for example fenamates were shown to inhibit IL-1β release and prevented amyloid β-induced memory loss in mice [366]. In 2022, five pharma companies had launched non-covalent NLRP3 inhibitors in clinical trials, among them MCC950 (CRID3) [367], which was exhibiting therapeutic efficacy in pre-clinical models for AD [368]. This sulfonylurea compound inhibited NLRP3 in mice *in vivo* and in human cells and was shown to bind to the ATP-site of NLRP3 directly, which shifted NLRP3 from an active to an inactive state [369, 370]. Yet, MCC950 has been discussed to be limited to WT NLRP3 and failed to inhibit mutated forms in CAPS (cryopyrin-associated periodic syndrome) mice [371]. At the moment, there is one FDA-approved drug called tranilast, which was shown to be a binder of the NACHT domain inhibiting NLRP3-NLRP3 interactions with an IC_{50} of 8 nm [372]. Tranilast is being investigated in the context of AD [373].There are also reports of covalent NLRP3 inhibitors, such as CY-09, which was shown to directly bind to NLRP3 and inhibit ATPase activity of recombinant NLRP3 [374]. The natural product oridonin was reported to covalently bind C297 in the NACHT domain and suppressed inflammasome formation [375]. The same research group identified compound RRx-001 as a covalent binder of NLRP3, presumably targeting C409 via a bromoacetyl group; mutating this cysteine residue was found to abrogate compound binding [376]. Moreover, a

vinyl sulfone, BAY-11-7082 has been shown to block ATPase activity of NLRP3, but also inhibited other targets (e.g. kinases) [377].

4.3.1 Screening of covalent fragment library in speck-formation assay

Encouraged by reports of covalent NLRP3 inhibitors, we screened a 1500-membered covalent fragment library in a speck-formation assay in iBMDM (immortalised bone derived mouse macrophages) to identify novel scaffolds inhibiting NLRP3 inflammasome assembly. The assay utilised a mCherry-tagged ACS subunit to visualise bright specks, which are formed upon inflammasome assembly (Figure 37A) [378]. The assay was performed by the screening team of the ODDI, initially, cells were treated with the compounds before priming with LPS for 2 h and triggering inflammasome assembly using nigericin for 1 h at 37 °C. Before the triggering step, the mCherry-ASC signal is diffuse, once the inflammasome is formed one bright speck per cell is formed. If an inhibitor prevents these steps or inhibits another protein upstream in the NLRP3 inflammasome assembly process, a loss of the speck signal can be detected (Figure 37B). The fragment library contained nine electrophilic reactive warheads such as acrylamide, chloroketone, enone, and sulfonylfluoride groups with a MW ranging from 150 – 300 g/mol.

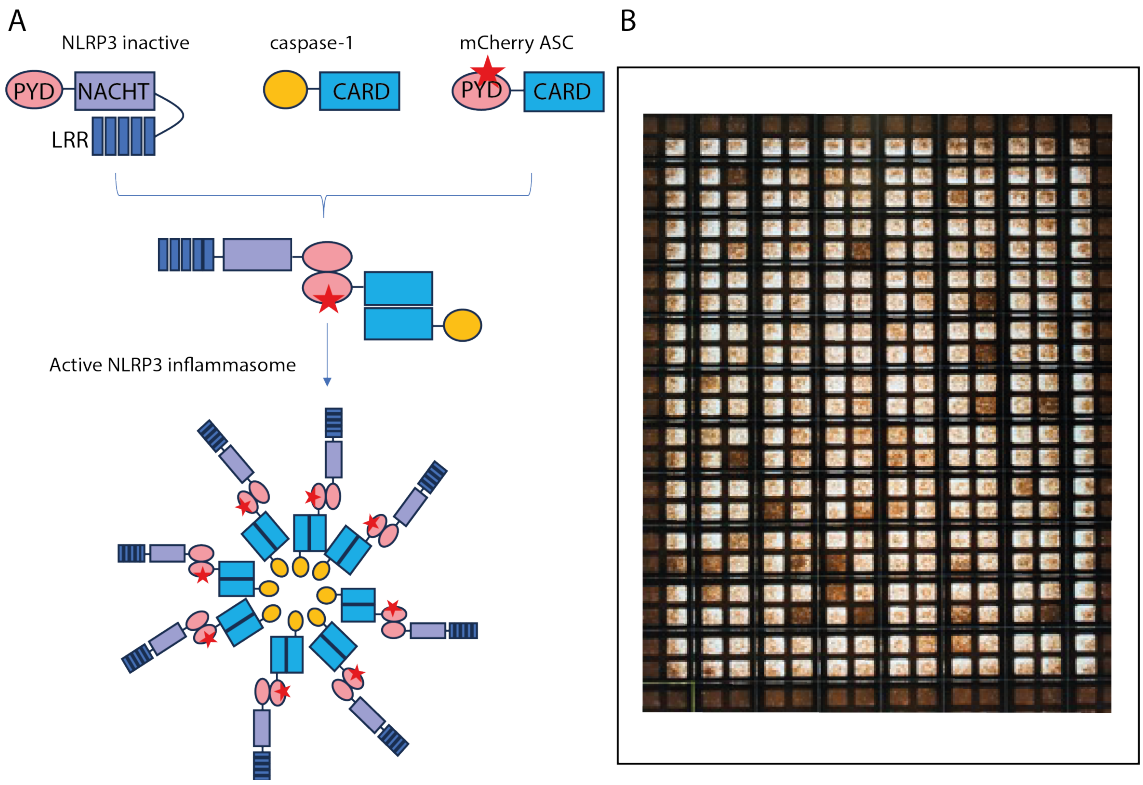
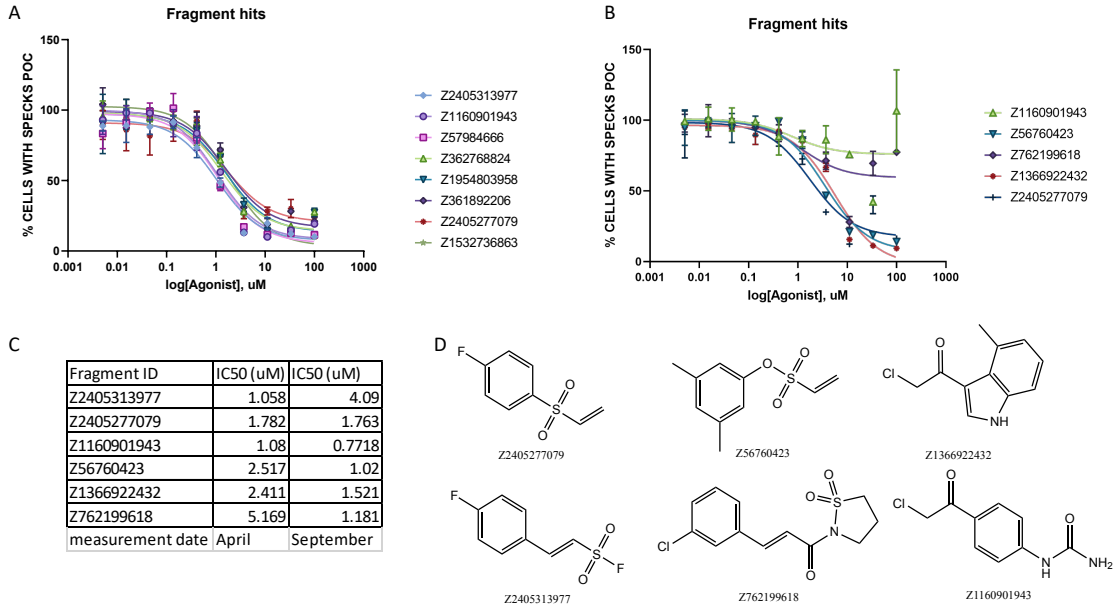


Figure 37: NLRP3 speck-formation assay. A) Schematic of NLRP3 inflammasome with mCherry-tagged ASC. B) Exemplary 384-well plate as an example of speck formation, darker wells contain compounds which had inhibitory effects. The screening and data analysis was performed by the ODDI screening team (Shania Ibarra, Val Millar, Sohaib Nizami, Grace Gregory).

4.3.1.1 Fragment screening campaign

Initially, the fragments were screened a single-shot experiment in duplicates at 100 µM concentration, from which 205 compounds were identified as hits preventing speck formation with a 13.4 % hit rate (Supplementary Table T6). For further validation, the top 52 inhibitory compounds were taken forward for a dose response screening using 100 µM as a top concentration and 1:10 dilution points. The initial dose response experiment revealed eight hit compounds with an IC_{50} < 2 µM. Due to a shortage of tips, the experiment was repeated six months later, and the second dose response yielded five compounds with IC_{50} < 5 µM (Figure 38A,B; Supplementary Figure S7 and S8). The variation in these experiments is likely caused by the electrophilic fragment reactivity and

stability when stored in DMSO. As DMSO is hygroscopic, the fragments may hydrolyse with water present in the solvent. The fragments from both dose responses were combined if they yielded an IC_{50} < 5 µM in both experiments (Figure 38C). The structures are shown in Figure 38D, four of the hits were sulphur-containing vinyl sulfones or sulfonylfluorides, and two were chloroketones.



Fragment ID	IC50 (uM)	IC50 (uM)
Z2405313977	1.058	4.09
Z2405277079	1.782	1.763
Z1160901943	1.08	0.7718
Z56760423	2.517	1.02
Z1366922432	2.411	1.521
Z762199618	5.169	1.181
measurement date	April	September

Figure 38: Speck formation assay results for covalent fragment screening. A) Most potent fragments of dose response experiment 1. B) Most potent fragments of dose response experiment 2. Each data point represents the mean ± SEM of three technical replicates. C) Reported IC_{50} values for hits from both experiments if IC_{50} < 5µM (exception for Z762199618). D) Scaffolds of the hit fragments listed in C.

Based on these hits, we searched for similar structures in the commercial databases and assembled a library of 16 structurally related scaffolds for a follow-up dose response screening campaign. To avoid fragments with highly reactive and rather promiscuous reactivity, we excluded the chloroketones and focussed on the sulphur-containing scaffolds. The compounds were provided as a 100 mM stock solution in DMSO. Within n=3 repeats, we noticed deviation of the derived IC_{50} values in the second experiment,

which was conducted one month after the first screen. We noticed that the percentage of DMSO had sank from 94 % to 85 % and subsequently plated fresh parent DMSO stock (94 % DMSO) and could rescue the IC_{50} values in the third experiment (Table 9). The source plate of the fragments was stored at RT under a nitrogen atmosphere with < 2.5 % humidity. We chose this storage solution to avoid higher humidity, which might occur in -20 °C freezers due to ice crystals. The parent DMSO stock was stored at -20 °C in microcentrifuge tubes sealed with a rubber lid, we hypothesise that the ratio of volume to surface is more unfavourable in the source plate wells, thus more water is accumulated in the DMSO, and subsequently electrophilic compounds might be less stable at RT stored in plate format. Due to our concerns regarding fragment stability, we calculated an averaged IC_{50} value for the fragments based on experiments 1 and 3 and excluded values for the second experimental repeat (Table 9). We selected four fragments (vinylsulfones) with most potent IC_{50} values < 1 µM for evaluation of the target in isoTOP ABPP (Figure 39, Table 9), which additionally showed the corresponding MW in LC-MS after three months in the parent DMSO stock (Supplementary Figure S9).

Fragment ID	1) IC50 (µM)	3) IC50 (µM)	2) IC50 (µM)	average 1) and 3)	LC-MS
Z1020737978	1.795	1.345	28.44	**1.57**	**x**
Z1041704956	2.357	1.077	38.4	**1.717**	**x**
Z1041705076	0.9674	0.4224	NA	**0.6949**	**y**
Z2735479131	42.56	40	3.091	**41.28**	**y**
Z2735957460	55.31	15.68	7.263	**35.495**	**y**
Z277559444	1.164	0.3677	5.895	**0.76585**	**y**
Z3015816484	1.847	1.077	22.07	**1.462**	**y**
Z3015818078	0.7848	0.5972	NA	**0.691**	**y**
Z3023938119	13.17	7.405	10.67	**10.2875**	**x**
Z3401802220	19.74	0.3677	23.27	**10.05385**	**y**
Z3668384727	NA	NA	0.06916	**0.06916**	**x**
Z3774999667	518.4	40.79	956.9	**279.595**	**x**
Z424784962	0.4018	0.257	0.6578	**0.3294**	**y**
Z424784978	1.417	0.9324	25.9	**1.1747**	**y**
Z56765434	1.789	0.4206	0.6578	**1.1048**	**x**
Z57162396	1.373	6.538	13.67	**3.9555**	**x**

Table 9: Table showing results of dose-response screen of 16 fragments. Fragment ID and IC_{50} values for n=3 is given, the average was calculated for experiment 1 and 3, as experiment 2 showed variation in DMSO percentage. LC-MS was conducted to test stability, if the corresponding MW was not detected (x), if the MW was detected (y).

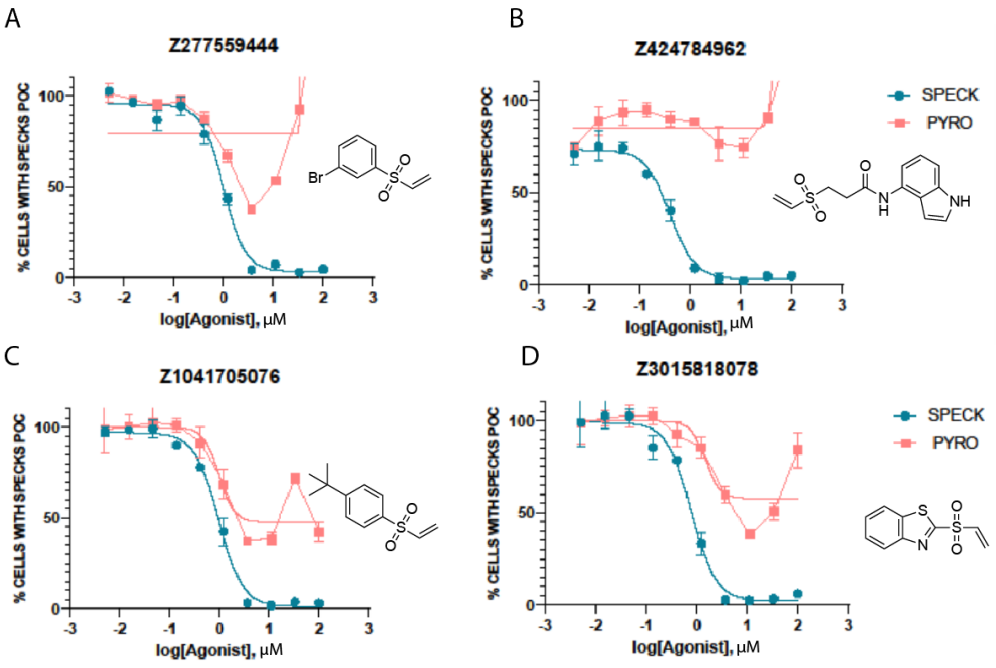


Figure 39: Speck formation (SPECK) and cell death (PYRO) depicted as percentage of control. Speck formation is inhibited with IC_{50} values < 1 µM, however pyroptotic cell death occurs up to 50 % within the top concentration range. Fragments which were taken forward are shown in A-D. Each data point represents the mean ± SEM of three technical replicates (n=1 shown).

4.3.1.2 isoTOP for fragment target identification

The four most promising candidates from the SPECK-formation assay were subsequently taken into the isoTOP ABPP workflow. For this, iBMDM cells were treated with respective fragments at 100 µM. Priming was conducted as described by Nizami et al., however, triggering was shortened to 30 min as this was sufficient to reach maximal inflammasome complex assembly [378]. The isoTOP ABPP workflow was performed with vinyl sulfone P9 as a reactive probe, as our fragment selection consisted of vinylsulfones as well, and we aimed to directly compete the respective binding sites of the fragments. However, in our results none of the compounds were showing a competition ratio R > 4 (Supplementary Figure S10). Due to an technical issue, samples for Z3015818078 could not be measured. Nonetheless, we investigated the competed protein IDs with at least R > 3 and whether they were involved in the NLRP3 inflammasome pathway using STRING database (Figure 40). The proteins were found to be unrelated to NLRP3 (which was added to the analysis manually). The fragments might have required a higher concentration for the incubation with cells. Prior to this an evaluation of compound toxicity should be performed to check whether higher concentrations can be tolerated by living BMBM cells, e.g. by using the CTG cell viability assay.



Figure 40: STRING analysis of proteins which were competed with R > 3 in the datasets of the selected competitors. No correlation between the proteins was found to NLRP3, which was added manually.

4.4 Fragment binding validation using orthogonal methods

Next, we were aiming to validate modified sites that we previously reported in isoTOP ABPP for the four cancer cell lines. To evaluate whether binding to these modified sites would exert a biological effect, we tested reactive probes and competitors in cell-based assays as well as in intact MS experiments using recombinant proteins. TRIM28 was selected as a target as it was among the most abundant E3 ligases throughout the cancer cell lines and thus seemed an ideal target to study in more detail. Additionally, recombinant E3 ligases were tested based on their availability from our collaborators.

4.4.1 Evaluation of covalent fragments in CETSA

For a CETSA experiment, we chose to follow up on TRIM28, as cysteine-reactive IAA (P1) was found to modify sites in the isoDTB data (Table 10). Interestingly, TRIM28 possesses both a BRD and RING-domains [288]. While C_68 lies in a RING-domain, C_232 is coordinating a Zn^{2+} in a zinc finger structure, which is required for interaction with and repression of KRAB zinc-finger proteins; C_628 lies within a PHD-type zinc finger, which acts as an intramolecular SUMO E3 ligase and is responsible for auto-SUMOylating the adjacent BRD [379]; In particular, the zinc-coordinating binding site was interesting, as addressing these sites and interrupting the interaction might lead to a measurable effect, even though the competition indicated by R was only marginal. We sought to detect a thermal effect in the event of the compounds being able to stabilise or destabilise the protein. We focussed on cell line NCIH226 as the sites were uniquely targeted and competed by IAA (P1) and competed by corresponding competitor 1c.

Cell line	Probe	Weighted.Log2HLRatio.Mean	Weighted.Log2HL.SD	Site
NCIH226	P1	-0.26	0.066	TRIM28_C_232
NCIH226	P1	-1.47	0.673	TRIM28_C_628
NCIH226	P1	0.63	0.102	TRIM28_C_68

Table 10: Table showing cell line NCIH226, and cysteine reactive sites on TRIM28 identified with probe 1 and competitor 1c. Weighted Log2HL ratio mean (= R), and standard deviation (SD) are reported.

Initially, the melting temperature for TRIM28 was determined to be 52.4 °C with DMSO treatment in NCIH226 cells. Thus, an experimental temperature gradient with nine points was set to span 40.8 – 65 °C, and one sample was appointed to RT. As a reference, the remarkably stable protein SOD1 was chosen, which remains in a folded state up to 95 °C [380]. The cells were pre-treated with compound 1c at each 100 µM and 200 µM for 30 min in the incubator at 37 °C, before exposure to the temperature gradient (Figure 41A,B). After cell lysis, samples were prepared for SDS-page and Western blotting. The bands were visualised using a ChemiDoc with HRP-secondary antibody, and after imaging, the band intensities were normalised to SOD1 controls. Derived shifts were plotted using GraphPad Prism (Figure 41C), here competitor 1c was showing no thermal shift at 100 µM concentration, but at 200 µM the results indicated a shift of around 4 °C. However, taking the WB bands into account, there is only a marginal difference in the band pattern and in addition, the DMSO band appears to faint earlier in Figure 41B in comparison to Figure 41A.

As a negative control, we tested another cysteine reactive compound, competitor 9c, in NCIH226 cells, as the isoTOP ABPP data suggested the competitor was not competing TRIM28 sites in this cell line, unlike in cell line K562. When the experiment was conducted using competitor 9c at 100 µM and 200 µM concentrations, we found no thermal shift for the lower concentration data but a shift of 4 °C in the 200 µM treatment condition (Figure 42A-C).

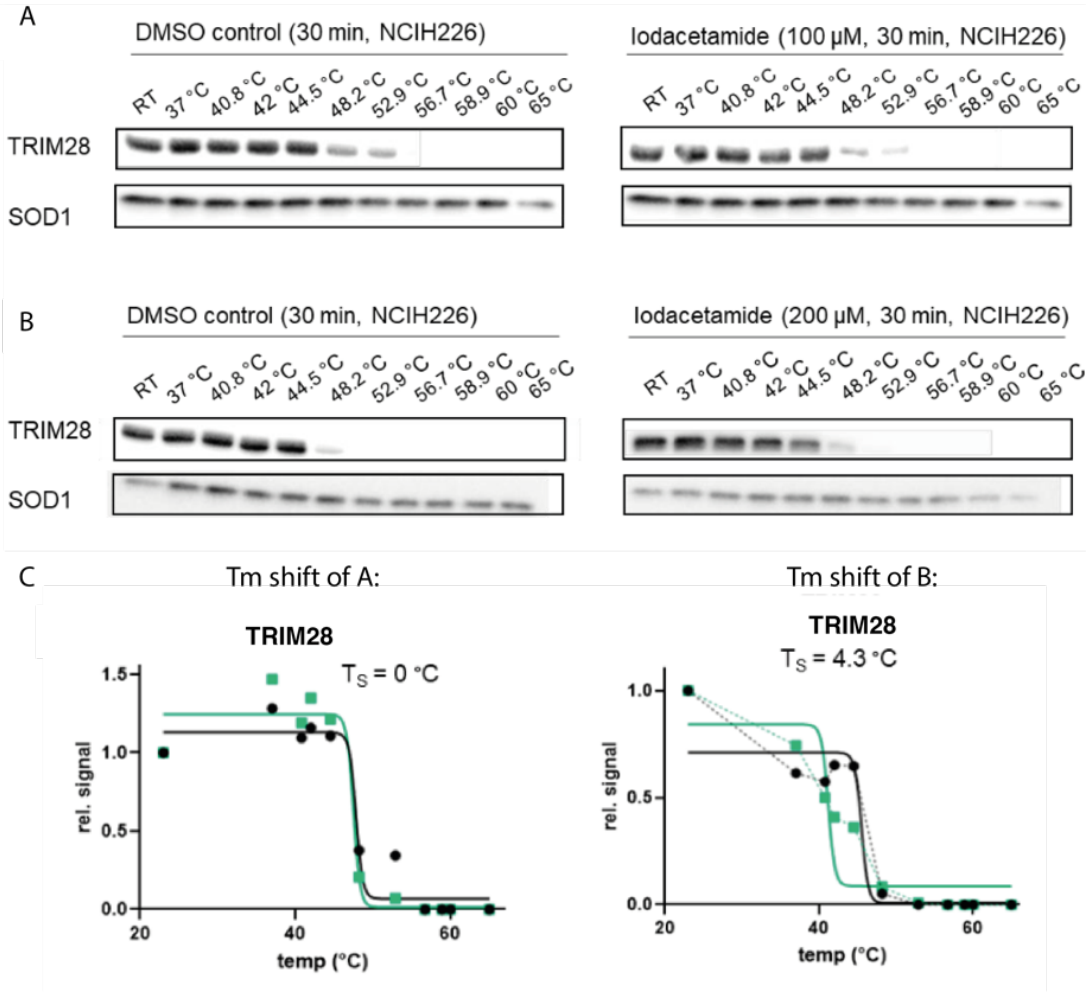


Figure 41: Determination of effect of iodoacetamide-competitor (1c) on NCIH226 thermal profile, CETSA performed by Kathrin Weller. A) Western Blot showing CETSA in NCIH226, treated with 100 µM of 1c and DMSO control (n=1). (B) Western Blot showing CETSA in NCIH226, treated with 200 µM of 1c and DMSO control (n=1). C) Plotted graphs normalised to SOD1 showing thermal shifts detected for each condition. Connecting lines are included for better visualisation.

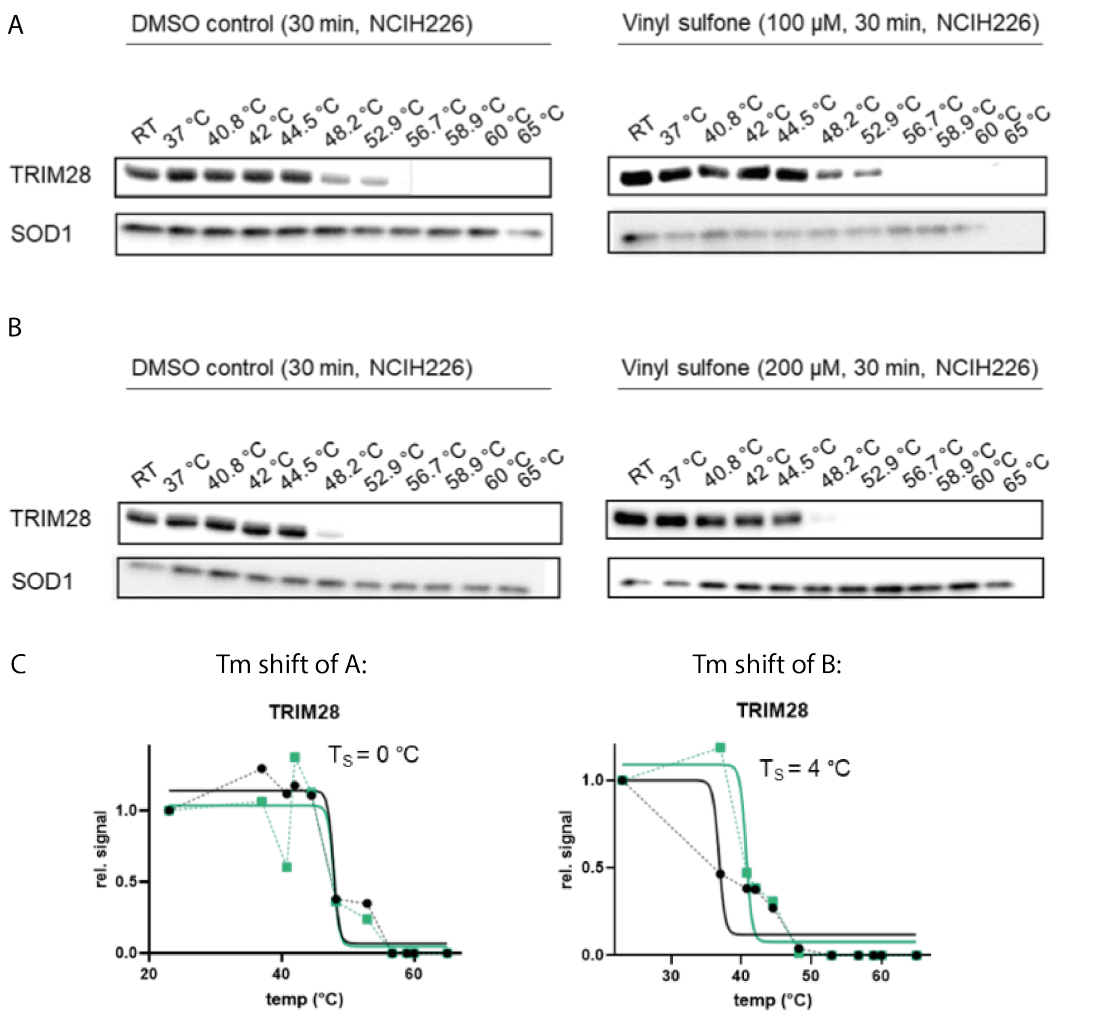


Figure 42: Determination of effect of "vinyl sulfone" (9c) on NCIH226 thermal profile, CETSA performed by Kathrin Weller. A) Western Blot showing CETSA in NCIH226 cells under 100 µM vinyl sulfone (9c) and DMSO control (n=1). (B) Western Blot showing CETSA in NCIH226 cells under 200 µM vinyl sulfone (9c) and DMSO control (n=1). C) Plotted graphs normalised to SOD1 showing thermal shifts detected for each condition. Connecting lines are included for better visualisation.

Overall, the observed thermal shifts require further study and validation. As we detected a similar thermal stabilisation for both competitors 1c and 9c at 200 µM, we are strongly inclined to repeat the assay to determine a clearer trend in the data and to exclude any quantification artefacts. As the SOD1 bands, which we used for normalisation, were partially resulting in impaired or weak bands, as an alternative amyloid precursor protein (APP-αCTF) could be used as a superior loading control in future experiments [381]. Due to the position of the modified Cys residues identified in isoTOP ABPP within the RING-domain or PHD-type zinc finger structure of TRIM28, we considered a thermal destabilisation as a likely outcome of this experiment. For example, for TRIB2, Foulkes et al. have reported a destabilisation due to a compound covalently binding a cysteine and disturbing protein folding [382]. Interestingly, they report C104Y mutants to thermally stabilise the protein (10 °C) in comparison to the WT, underscoring the important structural function of this residue.

Furthermore, we hypothesised that the incubation with 100 µM competitor for 30 min might be an insufficient concentration to achieve an effect in live cells in combination with the short incubation time. For fragments, concentrations from 1 mM up to 5 mM were reported for fragment screens in Tm shift using recombinant protein, consequently cells would require a higher concentration [383]. However, this bears a risk of toxic effects on cells, as cysteine reactive compounds IA and IAA have been shown to deplete cellular glutathione (an antioxidant, responsible for redox homeostasis) and to inhibit GAPDH activity at 1 mM after 90 min incubation in live cells, resulting in cell death [384]. Thus, high concentrations of promiscuous and highly cysteine-reactive fragments might not be feasible in cells. Instead, the identified sites could be subjected to docking studies to

identify structurally related analogue compounds for further validation experiments, such as Tm shift with recombinant protein, before subjecting cells to a CETSA experiment.

4.4.2 FRAP experiment using covalent fragments

An additional orthogonal technique to validate binding effects in cells is FRAP. Commonly, U2OS cells are used as they possess large nuclei. However, in our hands, U2OS viability was reduced after transfection. Instead, NCIH226 tolerated transfection and they also had large nuclei suitable for a FRAP experiment. To validate binding for competitors of P1 and P9, we transiently transfected NCIH226 cells with pEGFP-TRIM28 construct [385] in dishes. After two days, we treated the live cells with either DMSO control or 100 µM competitor for 1 h before imaging under the microscope. An area within selected nuclei was bleached, a second area was used for reference as well as a third area serving as the background reference. The immobile fraction and the T1 half were determined.

However, for both competitors there was no clear effect visible in comparison to DMSO due to a large variability in measurement values (Figure 43A,B). The variability might be influenced by transfection efficiency, background fluorescence, or cell viability. The background fluorescence can be quenched with red azurin, in this case we omitted the addition of azurin to avoid weakening of the GFP-signal, in turn, this might lead to greater variation when selecting the background measurement point. Viability might be affected due to the compound binding promiscuously to many cysteines upstream and downstream in the proteome. In both Figure 43A and B, the compound-treated samples show rather greater variability in comparison to the DMSO samples, which hints at a

compound treatment effect. Overall, the FRAP assay might be more suitable for less promiscuous compounds and can be utilised to screen lead compounds obtained from an isoTOP ABPP screening, with several competitors targeting either of the described TRIM28 binding site more selectively.

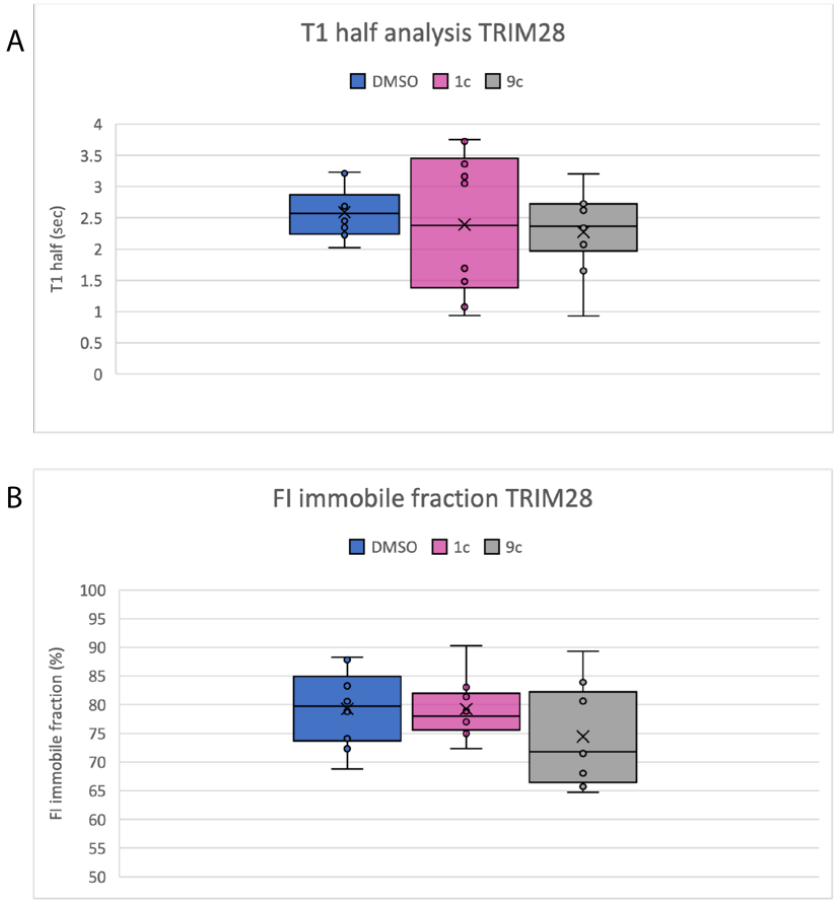


Figure 43: FRAP assay results. A) T1 half analysis showing DMSO and competitors 1c and 9c. B) FI immobile fraction analysis showing DMSO and competitors 1c and 9c (n=2). The variation in both datasets is large, no clear trend is visible for compound treatment.

4.4.3 Intact MS studies with KEAP1

Using recombinant protein, we investigated binding of the compounds to constructs of E3 ligase KEAP1. While KEAP1 was not FL, construct 41 covered residues 48-216 and construct 44 covered 321-620. The proteins were tested against concentrations of 10 and 100μM of competitors and reactive probe, and we were able to observe mass shifts corresponding to covalent mass adduct formation these constructs. The sequence of said KEAP1 constructs contains nine C and M residues for sequence 321-620, and four C and 10 M residues for sequence 48-216. We observed fewer covalent modifications (mass shift +136) than amino acids present in the construct sequence for 1c (Figure 44A,B), which indicated that only some of these residues were accessible under the chosen conditions. For competitor 9c, we identified 3 and 4 mass shifts (+167) on respective constructs (Figure 45A,B). Observed mass shifts are also reported in Supplementary Table S7. However, as the KEAP1 constructs do not cover the full-length protein, some residues might occur in a different conformation in this experimental setup and therefore might not be accessible in a FL version of this protein. In the isoTOP ABPP data we identified the following sites: KEAP1_C_241, KEAP1_M_317, KEAP1_C_434, KEAP1_C_613 and KEAP1_C_622 competed against vinyl sulfone P9, and no sites were detected for IAA and competitor. Therefore, we would have expected no binding events on KEAP1 construct covering residues up to 214. The biological environment between the lysate isoTOP and the intact recombinant protein experiment differed, which likely accounts for the variation in residue reactivity [386].

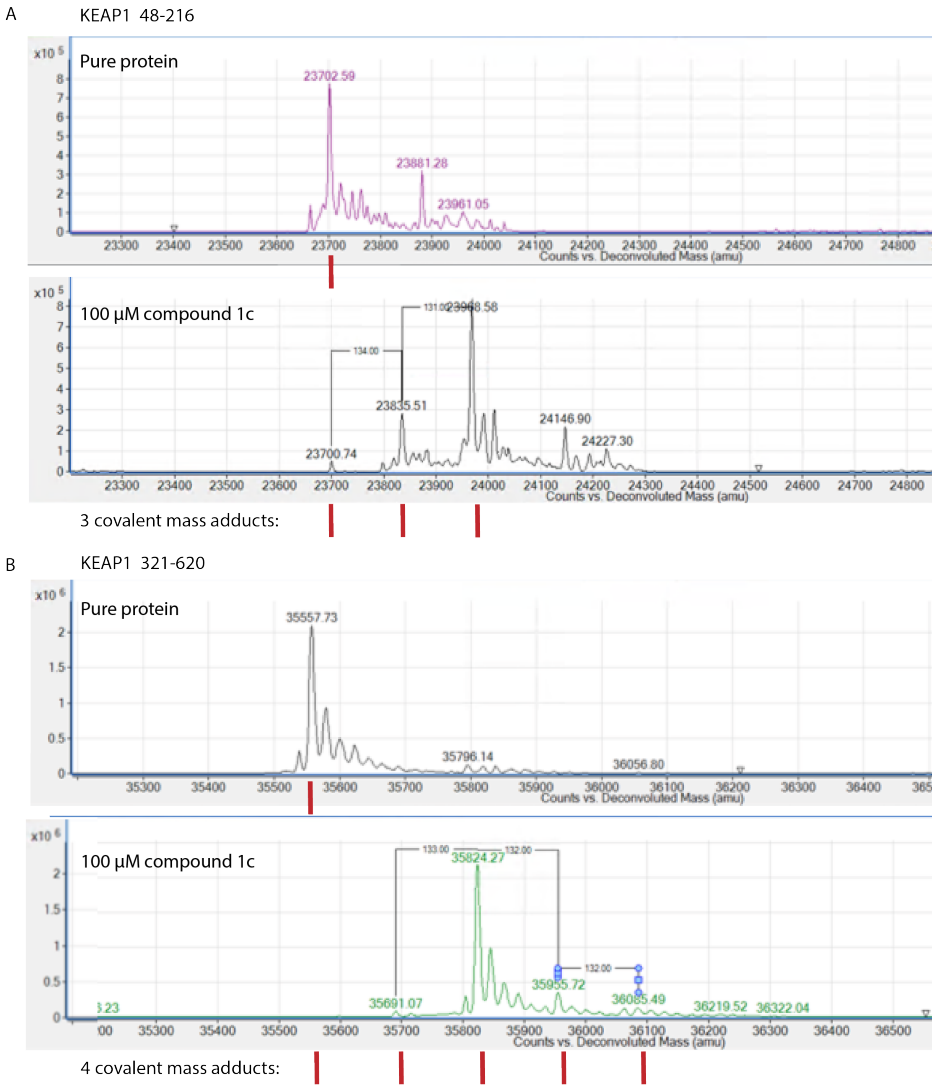


Figure 44: Intact MS performed on KEAP1 recombinant protein constructs shown in A) and B). Mass shifts were observed for the addition of compound 1c, a cysteine-reactive iodoacetamide-phenyl moiety after 1h incubation at RT. Example graph for n=2.

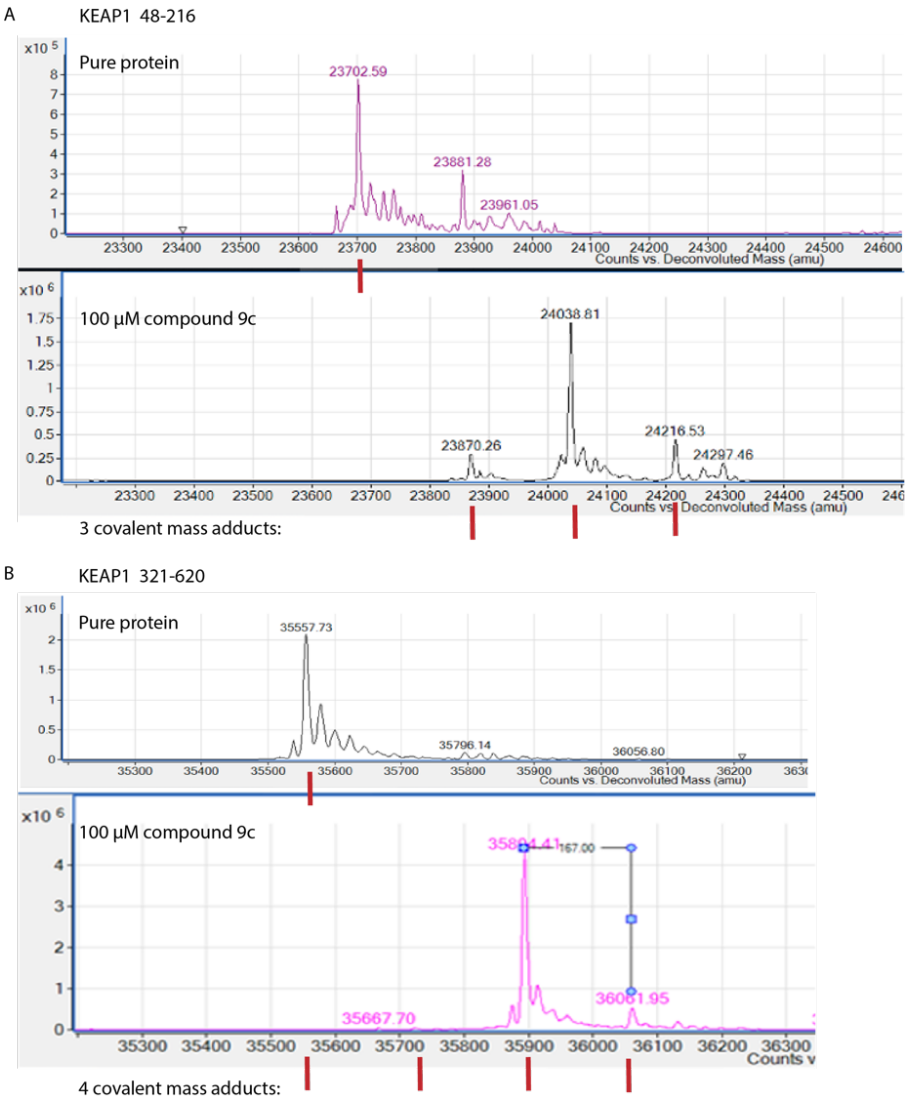


Figure 45: Intact MS performed on KEAP1 recombinant protein constructs shown in A) and B). Mass shifts were observed for the addition of compound 9c, a cysteine-reactive vinyl sulfone moiety after 1h incubation at RT. Example graph for n=2.

The observed modifications for 9c on KEAP1 constructs are encouraging to further investigate the exact binding site. This would usually be done by labelling the proteins and then digesting them with trypsin. Due to time restraints, these experiments could not be performed. As an experimental workflow we would propose to perform the experiment in a 96-deep well format. The respective recombinant proteins can be treated with covalent compounds at desired concentration, temperatures, and incubation times (e.g. 100 µM, RT and 1 h). Then, a sample can be measured using intact MS before the residual sample can be transferred to a FASP filter column. Next, the buffer solution should be used to perform three wash steps on the column to remove any residual compound. The reduction and alkylation can be performed on the column directly, followed by washes and digestion. For the digest, trypsin would be the protease of choice, but depending on the binding site, other proteases such as LysC or Chymotrypsin might be used or combined. The digests need evaporation and desalting at C18 columns before MS samples can be prepared and measured. The PEAKS software allows for detection of custom modifications and mass shifts on peptides.

4.5 Summary and outlook

In summary, we showed that the isoTOP ABPP platform is capable of screening chemical probes to highlight their selectivity. In case of KEAP1, we encountered the difficulty that the direct binding site (C151) of the covalent probe was not addressed by IAA. In this case, we could only indirectly show that other KEAP1 sites were targeted and that there were no related off-targets. PCIF1, which was competed with R > 4 for the chemical probe could be validated further using recombinant protein in intact MS. In addition to other orthogonal experiments and selectivity studies (currently unpublished), isoTOP ABPP proved high selectivity on a proteome-wide scale. The CysDB and Kuljanin et al. report competing C151 directly using acrylamide competitors in HCT116 cells against the DBIA probe [132]. Thus, a test of the smaller DBIA probe in MDAMB231 cell line would be meaningful to determine whether the site can be competed directly.

For the NUDT7 inhibitor NU000443a and chemical probe NU074516a, we used the vinyl sulfone probe to profile compound selectivity on a proteome-wide scale. For the first time, NUDT7 was shown directly modified by this probe in an isoTOP ABPP experiment using overexpressed NUDT7 FLAG-tag. The vinyl sulfone probe (P9) bound to the same residue as the chemical probe and competition could be shown directly for NUDT7_C72. We show a competition with R > 3 for compound NU00443a. However, the concentration of the chemical probe might need to be elevated for the incubation on live cells as the competition ratio is marginal. The probe appears less potent than NU00443a in this study, this might be due to insufficient competition, which could be re-evaluated by using higher concentrations of the probe, e.g. elevating the concentration from 1 µM to 2 µM in cells or by increasing the incubation time. According to recent guidelines for covalent chemical

probes, the probe should show potency in cell-based assays < 1 μM [70]. The six proteins which were competed with R > 3 should be validated in a repeat experiment and additionally by utilising recombinant protein in intact MS or Tm shift assays.

In case of the NLRP3 covalent fragment library screen, we were not able to identify targets of the hits derived from the SPECK formation assay in the isoTOP ABPP workflow. Finding the target is generally challenging, as in this assay the target might be upstream of the NLRP3 pathway, or any protein involved in the NLRP3 inflammasome assembly. As IAA (P1) was not modifying NLRP3 directly, another cysteine reactive probe could be utilised. Another potential option would be the conjugation of alkyne-tails to the hit fragments to create scout compounds, which would directly enrich the modified sites and proteins rather than using the fragment as a competitor against a broadly reactive probe. However, since these fragments are electrophiles, they might react promiscuously and thus require further SAR optimisation. In general, covalent hits can be validated against recombinant proteins using intact MS or WB, however this requires knowledge of the target protein first, e.g. to select suitable antibodies.

To validate binding events detected in the isoTOP ABPP data presented in chapter 3, we sought to perform CETSA and FRAP on TRIM28 with cysteine-reactive compounds (P1, 1c, P9, 9c). However, these experiments were mostly inconclusive, and we hypothesise this might be affected by the promiscuous nature of tested probes and competitors [58]. Fragments were used at concentrations of 1-5 mM in thermal profiling screens [383], and IAA has been shown to exert cytotoxic effects at 1 mM concentration in live cells [384]. Thus, experiments using recombinant protein can be suitable to optimise the compound scaffold in analogue screens, before cellular CETSA or FRAP studies of these re-fined

fragments. The intact MS performed on E3 ligase KEAP1 led to the identification of mass shifts, yet the mapping of the binding sites is needed to confirm the isoTOP ABPP data. All in all, the MS-based datasets provide a vast resource for future experiments indicating addressable sites in the whole proteome. In summary, this underscores the advantage of the isoTOP ABPP workflow: the identification of modified sites is the initial step to allow for screening of competitor libraries, which can be further refined by SAR studies. With a more concise set of similar fragment competitors, multiple publications have yielded selective ligands and most importantly, selective E3 recruiters [265, 268].

5. Characterisation of selectivity of GSK3326595

This chapter is in parts published as a pre-print in BioRxiv [387]. To investigate its selectivity and to potentially detect unwanted off-targets in cell-based experiments, an amine-functionalised version of this compound was designed, CBH-001. Its scaffold was derived from GSK3326595, a substrate competitive PRMT5 inhibitor which is a candidate in clinical trials for acute myeloid leukaemia[19]. Additionally, CBH-001 was used in chemical synthesis to create a potent chemical energy-transfer probe (ETP), surprisingly with the ability to elucidate not only substrate- but also SAM-competitive PRMT5 inhibitors. The effect of co-factor SAM was investigated in the assay.

5.1 Role of PRMT5 as methyltransferase

Methylation of proteins is a common post-translational modification (PTM) of arginine residues. At physiological pH, the methylation of arginine's guanidinium group does not alter its positive charge but its hydrophobicity. By adding a methyl group, a potential hydrogen-bond donor is removed from the arginine residue, and therefore its ability to mediate molecular protein-protein interactions is affected [388, 389]. Especially histone methylation is an essential epigenetic regulation mechanism controlling the transcription of genes [390]. Protein arginine methyl transferases (PRMTs) are a protein family, which transfer a methyl group from their cofactor S-adenosylmethionine (SAM) to protein substrates. A central channel connects cofactor and substrate binding sites where the methyl transfer is catalysed, forming methylarginine and release of S-adenosylhomocysteine (SAH) (Figure 46A). To date, there are nine human PRMTs that

[19] https://classic.clinicaltrials.gov/ct2/show/NCT03614728

are classified by their mode of methyl group transfer into PRMT family types I, II, III, and IV.[391] There are three forms of methylarginine residues: ω-N^G-monomethylarginine (MMA), ω-N^G,N^G-asymmetric dimethylarginine (aDMA) and ω-N^G,N^G-symmetric dimethylarginine (sDMA) (Figure 46B) [392]. Type II PRMTs, comprising PRMT5 and PRMT9, process symmetrical dimethylarginine (sDMA) by adding a CH_3-group to the neighbouring nitrogen atom of guanidine [393].

PRMT5 regulates transcription by methylating H3 histones, transcription factors, nucleosome remodelling- and co-repressor complexes and is thought to play a role in splicing regulation as part of the methylosome [394]. To methylate target proteins, PRMT5 forms complexes via nuclear and cytosolic adaptor proteins such as CLNS1A, WDR77 (MEP50), RIOK1, or COPR5 [395]. PRMT5 overexpression has been reported for a range of aggressive cancer types such as lymphoma [396], melanoma [397], glioblastoma [398], and breast cancer, for which it been designated as a marker for poor prognosis [399]. Furthermore, PRMT5 may promote cell transformation and proliferation [400, 401], and genetic knockdown studies revealed mitigating effects on cancer cell proliferation [402]. Collected evidence for its role as a promotor of growth, proliferation, migration, and invasion in cancer suggests PRMT5 as an emerging target, especially for solid and blood cancer types. Remarkably, methylthioadenosine phosphorylase (MTAP) deletions in cancer types can create increased vulnerability via targeting of the MTA2A/PRMT5/RIOK1 axis by accumulation of methylthioadenosine (MTA), substrate of MTAP. MTA acts as a selective and potent inhibitor of PRMT5, reducing PRMT5 activity and increasing sensitivity to cellular PRMT5 depletion [403, 404]. Excess MTA was found to reduce SAM binding to PRMT5 [405], therefore making it less susceptible to SAM-cooperative inhibitors.

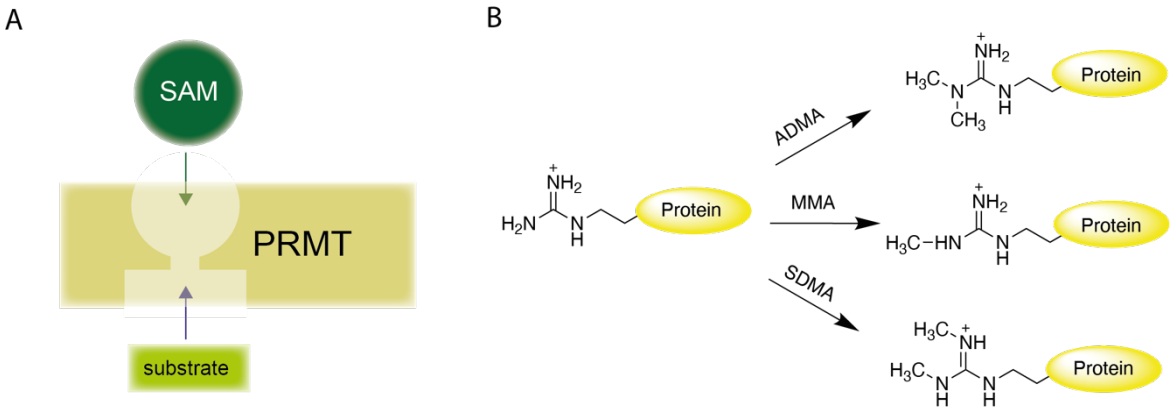


Figure 46: Schematic of PRMT5 and produced methylation patterns. A) PRMT5 binding pockets for SAM and substrates connected by core channel accommodating methyl-transfer. B) Structures of MMA, aDMA and sDMA.

5.1.1 PRMT5 inhibitor classes

Since arginine methylation is essential in maintaining normal cellular homeostasis, nonselective PRMT inhibition would likely lead to undesired effects. Notably, the substrate binding sites are structurally diverse, as PRMTs methylate a range of target proteins, which in turn offers the opportunity for the development of targeted and PRMT-subtype selective inhibitors. Modulation of methylation activity via the cofactor binding pocket is challenging as interactions with SAM are highly conserved. SAM-competitive inhibitors need to strike a balance between polarity, required to access the cofactor binding pocket and hydrophobicity, needed to cross cellular membranes [406]. However, inhibitors for both binding pockets have been identified successfully and can be subdivided into co-factor and substrate pocket addressing inhibitors [407, 408]. SAM-mimicking PRMT5 inhibitors, such as LLY-283, were inspired by MTA, which is inhibiting PRMT5 selectively [403]. LLY-283 is a potent, nanomolar range inhibitor in biochemical assays and showed sub-micromolar potency in cells [409]. Recently, potent inhibitor (MRTX1719) selectively binding to the PRMT5/MTA complex was reported [410].

Belonging to the substrate-competitive inhibitor class is GSK3326595 (pemrametostat), an orally available, highly potent substrate competitive PRMT5 inhibitor, which is currently being investigated in clinical trials.[405] It has been shown to inhibit PRMT5 and to induce p53-mediated cell death, due to a transcriptional switch resulting in a p53 non-inhibitory isoform of MDMX [411]. GSK3203591, a related compound, showed nanomolar potency in vitro and in cellulo [412]. In Figure 47, compounds tested in the newly developed NanoBRET assay are be highlighted, including three non-PRMT5 selective compounds. SGC3027 is a prodrug and selective chemical probe for PRMT7. The active component SGC8158 is released upon reduction by reductase activity [413]. MS023 is a potent PRMT type I inhibitor and selective over PRMT´s of group II and III and has been shown to bind the peptide substrate binding site [414]. TP064 is a selective inhibitor for PRMT4 binding to the substrate binding site [415]. Other novel compounds with e.g. allosteric binding modes have not been tested in the assay and will be discussed in the summary.

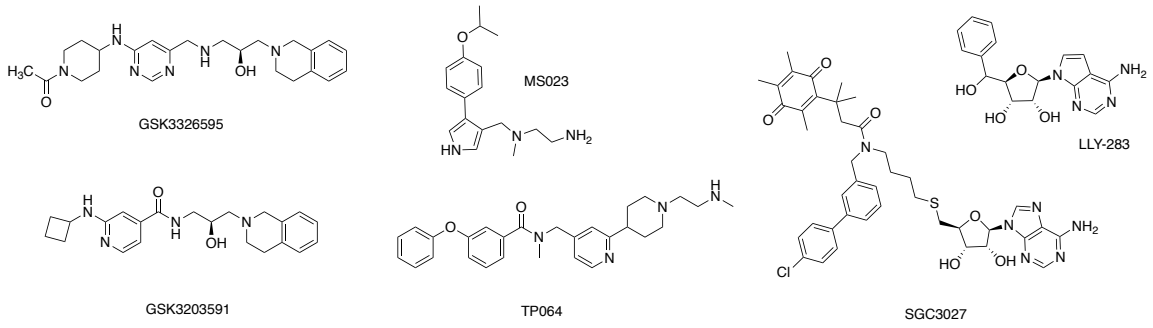


Figure 47: Compounds used in the NanoBRET study presented in this chapter.

5.1.2 First in class study of PRMT5 cellular target engagement via NanoBRET

In a newly developed first-in-class NanoBRET assay, a cell-permeable ETP enabling quantification of target engagement of PRMT5 inhibitors in living cells is presented.[387] Here, the NLuc-fusion of PRMT5 acts as a donor, and the ETP based on GSK3326595, CBH-002, is acting as the acceptor (Figure 48A). Introduction of a short aminobutyl linker enabled convenient conjugation of the BRET acceptor fluorophore to the intermediate CBH-001 via activated NHS-ester amide coupling (Figure 48B). CBH-002 is used to monitor EC_{50} values of known PRMT5 inhibitors as well as non-PRMT5 selective inhibitors to test the specificity of the assay. Both intact cell and lysate experiments were conducted, including exogenous addition of co-factor SAM, to investigate its influence on inhibitor binding.

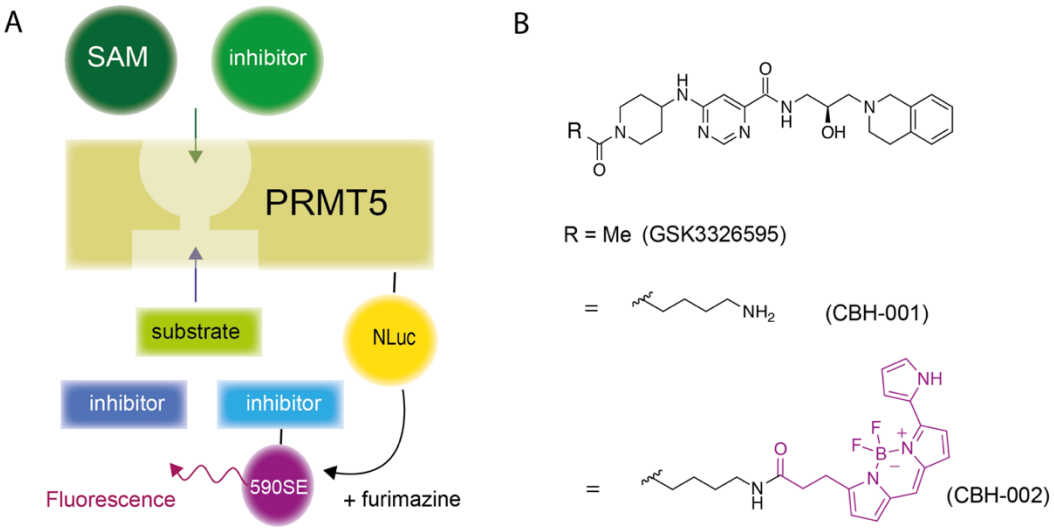


Figure 48: PRMT5 NanoBRET assay and ETP probe development. A) NanoBRET TE assay concept cartoon showing PRMT5 binding pockets for SAM and substrates. Upon addition of furimazine, the PRMT5-NLuc fusion protein excites the ETP's fluorophore resulting in BRET. B) Structures of GSK3326595 and analogues CBH-001 and CBH-002.

5.2 Validation of GSK3326595 selectivity

Bespoke ETP CBH-002 was subsequently established in NanoBRET TE assays. We successfully measured EC_{50} values of multiple PRMT5 inhibitors and compared them to the literature. CBH-001 proved exquisite selectivity in pull-down experiments, as described below.

5.2.1 Establishment of NanoBRET TE-assay with CBH-002

To confirm the co-localisation of endogenous PRMT5 and overexpressed NL-PRMT5 protein, HEK293 cells were examined in intracellular fluorescence experiments (Figure 49). As a result, proteins could be mapped to the same intracellular localisation, howbeit with higher expression for transfected versus un-transfected cells. The co-localisation profile of endogenous PRMT5 and NL-PRMT5 provided validation of the assay.

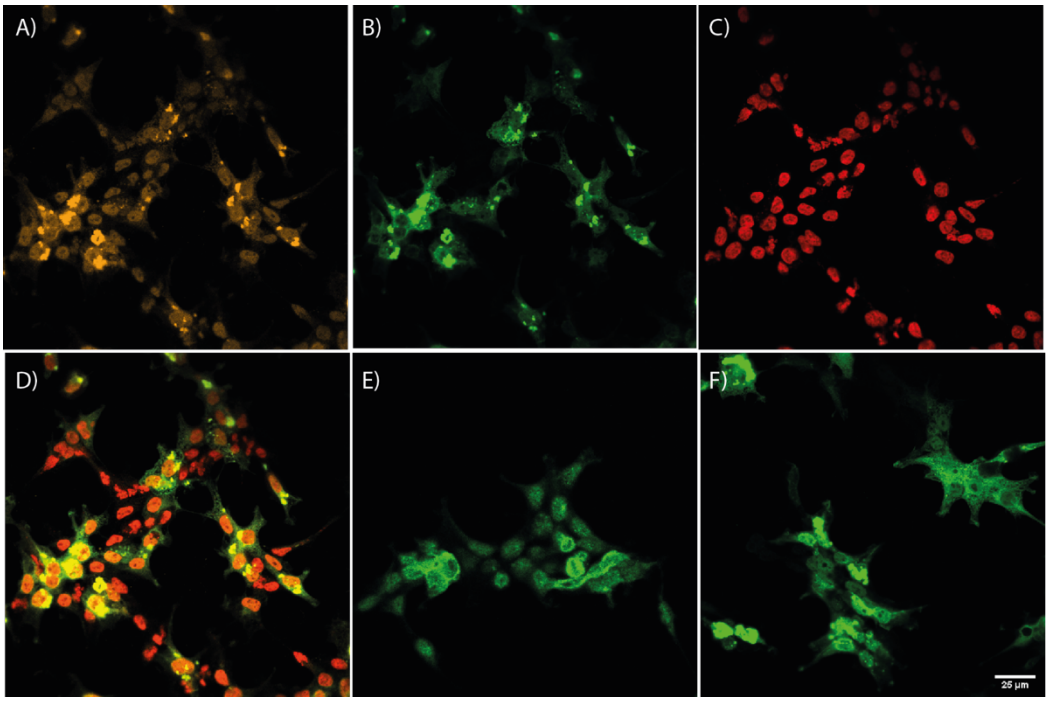


Figure 49: Subcellular localization and co-localization of endogenous PRMT5 and NL-PRMT5. A) NL-PRMT5 stain. B) Endogenous PRMT5 stain. C) Nuclei stain and D) Co-localization. Controls: E) Un-transfected HEK293 and F) Transfected HEK293, highlighting ability to visualize the intracellular localisation of both PRMT and NL-PRMT5.

Initially, a comparison of N- versus C-terminal N-Luc fusions of PRMT5 had examined any potentially preferred orientation for generating BRET signal. The result suggested the N-tagged NLuc-PRMT5 was favoured over the C-terminal fusion (Figure 50A). Next, a titration of CBH-002 against fixed concentrations of DMSO and the parent compound GSK3326595 indicated a suitable assay window between 0.5-0.1 μM ETP (Figure 50B). The apparent K_d was determined by testing eight fixed ETP concentrations against a dilution series of parent compound (Figure 50C). Resulting EC_{50} values were plotted against respective ETP concentrations. Linear regression analysis in combination with the Cheng-Prusoff equation [416] suggested an apparent K_d value of 13.5 ± 6.2 nM (Figure 50D). Based on the obtained results, a concentration of 0.075 μM ETP was selected to evaluate PRMT5 inhibitor binding. This concentration was selected, as it offers a suitable assay window. Ideally, the ETP concentration should provide a good assay window to generate stable EC_{50} values. To achieve accurate quantitation of binding, excess quantities of ETP should be avoided, as they may lead to oversaturation and compromised inhibitor binding. Conversely, suboptimal concentrations may risk competition by the inhibitor.

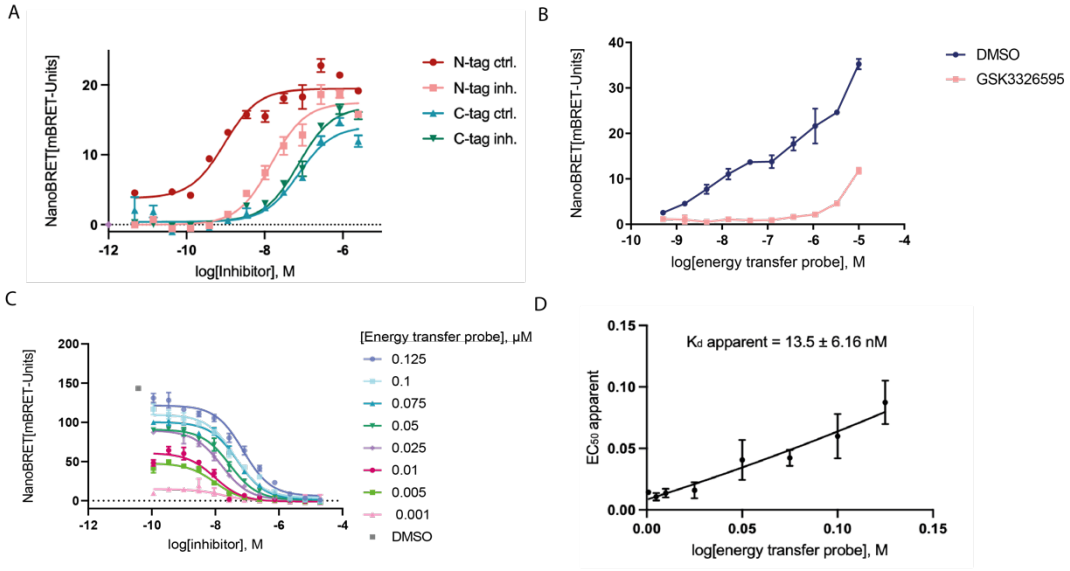


Figure 50: Optimisation of ETP concentration and evaluation of PRMT5 inhibitors in a cell-based NanoBRET assay using CBH-002. Each data point represents the mean ± SEM of three technical replicates. A) Comparison of N- and C-tagged NLuc PRMT5 fusion proteins tested against 10 µM GSK3326595 or DMSO as a control (n=1). B) Hot-cold tracer titration against 10 µM GS3326595 (n=1). C) ETP titration demonstrating cellular TE (n=3). D) The apparent K_d was determined as the Y-intercept of compound EC_{50} values plotted against ETP concentration by linear regression (n=3).

5.2.1.1 Measurement of EC_{50} values in cells

Using established optimal ETP conditions, live cell TE of various well-known cell active PRMT inhibitors was evaluated in the assay. To test the specificity of our assay, we also included inhibitors of other PRMTs, such as SGC3027, which is a selective chemical probe for PRMT7, MS023, a potent substrate-mimetic PRMT type I inhibitor [414] as well as TP064, which is a selective inhibitor for PRMT4 binding to the substrate binding site.[415] Obtained results showed TP064 and MS023 did not exhibit any significant displacement of CBH-002, thus confirming selectivity for their respective targets (Figure 51A). The known PRMT5 inhibitors LLY-283, GSK3203591 and GSK3326595 afforded dose-response curves in line with expectations, and all compounds remained without any apparent effects on cell viability (Figure 51B).

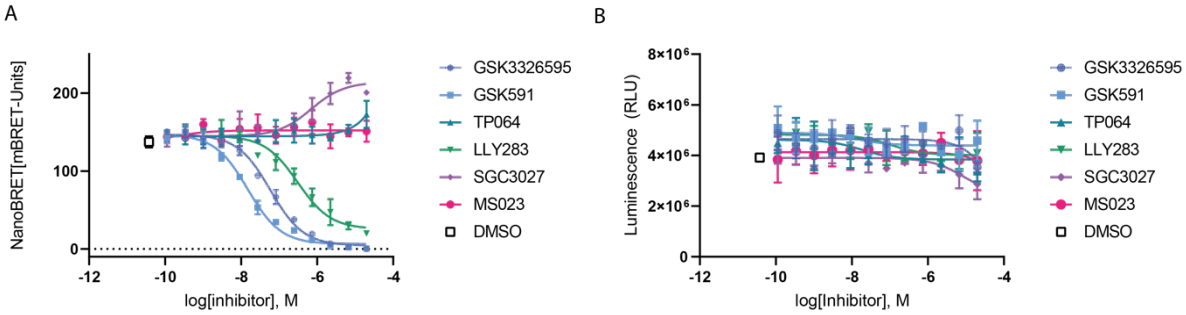


Figure 51: A) Comparison of inhibitor EC_{50} values in HEK293 cells transfected with NL-PRMT5 after treatment for 2 h with compound and ETP. Each data point represents the mean ± SEM of three biological experiments (n=3). B) Cell viability control via CellTiterGlo assay (n=3).

Strikingly, CBH-002 was able to determine EC_{50} values for both substrate- and cofactor-competitive PRMT5 inhibitors, although it was derived from a substrate-competitive inhibitor scaffold. In comparison to acellular biochemical assays monitoring inhibition of methylation using the purified PRMT5:MEP50 complex, the intact cell NanoBRET EC_{50} values were approximately 5- to 10-fold higher for the substrate-competitive compounds GSK3326595 and GSK3203591, while potency for the SAM-competitive LLY-283 was markedly reduced (Table 11).Previously published results of functional cellular assays, evaluating symmetric arginine methylation in various cell lines via functional in-cell Western (ICW) and ELISA, suggested EC_{50} values in the range of 0.3 – 56 nM for GSK3203591 and GSK3326595 [412, 417, 418]. In case of LLY-283, an IC_{50} value of 25 nM has been reported from an assay investigating SmBB' methylation in MCF7 cells [419]. The NanoBRET-obtained EC_{50} values for GSK3203591 aligned well with published data, yet the effective half-maximal concentrations for target engagement for GSK3326595 and LLY283 appeared higher in comparison. As the ETP's displacement by inhibitors indicates compound binding affinity, the NanoBRET results were compared with published biophysical data as well. However, no such data could be retrieved for GSK3326595 and GSK3203591. For the closely related compound GSK3235025

(EPZ015666) SPR K_d values of 171 nM and less than 1 nM have been reported for SAH- and SAM-bound PRMT5:MEP50, respectively [405]. For LLY-283, a K_d value of approximately 6 nM has been determined for PRMT5 [409]. The higher values observed throughout the cell-based assays are likely impacted by the increased complexity of the cellular system, including any uptake or export mechanisms, varying cofactor levels across different cell lines. However, the differences in the impact of SAM- and substrate-competitive compounds were remarkable. Thus, it was further investigated how modulation of SAM levels might affect the different types of inhibitors in bespoken assay setup.

Assay	**EC_{50} (μM)**		
	GSK3326595	**GSK3203591**	**LLY-283**
Biochemical	0.0062 ± 0.0008 [a]	0.004 - 0.011 [b]	0.022 ± 0.003 [b]
SPR	n. a.	n. a.	0.006 ± 0.002 [c]
ELISA	0.0025 [d]	0.0021 [d]	n. a.
ICW	0.0003–0.014 [e]	0.003–0.056 [f]	0.025 ± 0.001 [g]
Proliferation	0.0057–0.106 [h]	0.062 [i]	0.003–2.5 [j]
NanoBRET intact cell	0.062 ± 0.004	0.019 ± 0.004	0.3 ± 0.1

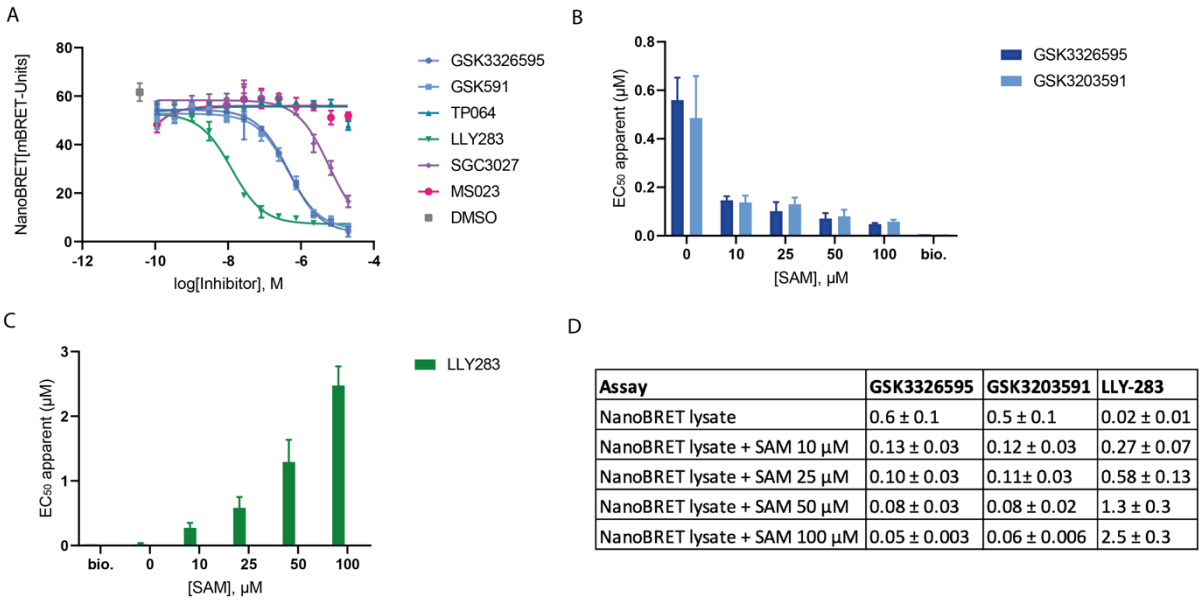
Table 11: Comparison of literature data and NanoBRET TE assay results. [a] HTRF assay monitoring monomethylation of H4R3 on H4 peptide by PRMT5:MEP50; [b] Radioactive assay monitoring methyl transfer from ^{3}H-SAM to peptide substrate; [c] Surface Plasmon Resonance (SPR) with PRMT5:MEP50 complex (K_d) [d] Symmetric dimethylation in cell homogenates from Z-138 cells (EC_{50}) [e] In-Cell Western (ICW): sDMA Western, various cell lines (IC_{50}); [f] Symmetric arginine methylation of SmD3 in Z-138 cells (IC_{50}); [g] Symmetric dimethylation of SmBB' in MCF7 cells (IC_{50}); [h] Long Term Proliferation (LTP) assay, various cell lines (IC_{50}); [i] Proliferation assay in Z-138 cells, (IC_{50}); [j] Cancer cell line proliferation assay (IC_{50}); n. a., not available. Literature for GSK3326595: Gerhart et al.,[411] GSK3203591: Duncan et al. and Scheer et al.,[412, 417, 418] LLY-283: Bonday et al.,[409].

5.2.1.2 SAM influence on PRMT5 inhibitor target engagement

NanoBRET conducted in lysates can serve as a more accurate proxy to compare with biochemical assays. Additionally, the assay performed in cell lysates simulates lower SAM concentration levels as they might occur in other cell types *in vivo*. As a result of the dilution effect, these experiments yielded EC_{50} values closer to the biochemical results reported in case of LLY-283 (Figure 52A). Notably, the decreased SAM concentration in the cell lysates had the opposite effect on the substrate-mimetic inhibitors GSK3326595 and GSK3203591, with their respective EC_{50} values increasing by approximately 100-fold (Figure 52A). Previous mechanistic studies for the structurally related inhibitor GSK3235025 (EPZ015666) suggested that presence of SAM in the active site may enhance PRMT5 binding affinity by stabilising inhibitor binding in the substrate pocket [405].

To further investigate this phenomenon, the concentration of SAM was artificially elevated in the lysates by exogenous addition of SAM at final assay concentrations of 10, 20, 50, and 100 μM, respectively. For LLY-283, previous reports suggested a non-competitive MOA with regard to SAM in a radioactivity-based biochemical assay [409]. However, in this assay EC_{50} values were gradually increasing indicating a direct relationship with SAM levels and thus cofactor-competitive behaviour in lysate (Figure 52D). Conversely, EC_{50} values for GSK3326595 and GSK3203591 decreased upon SAM addition (Figure 52B,D), further supporting the hypothesis that cofactor complementation facilitates substrate-competitive inhibitor binding to PRMT5 via the formation of the ternary PRMT5:SAM:inhibitor complex [405]. Notably, SGC3027 was showing a weak inhibiting behaviour in lysate in contrast to activating behaviour in intact cells. We

hypothesize, that the cellular toxicity effect, leading to activation in cells is lacking in lysates, where additionally reductases might be more readily available to activate the pro-drug SGC3027 to the active compound SGC8158, or the dilution of SAM benefits the potency of the SAM-competitive compound SGC8158. SGC8158 has been shown to be selective for PRMT7 while showing around 100-fold higher IC_{50} values for PRMT5, -9 and -4 in a scintillation proximity assay [420].



Assay	GSK3326595	GSK3203591	LLY-283
NanoBRET lysate	0.6 ± 0.1	0.5 ± 0.1	0.02 ± 0.01
NanoBRET lysate + SAM 10 µM	0.13 ± 0.03	0.12 ± 0.03	0.27 ± 0.07
NanoBRET lysate + SAM 25 µM	0.10 ± 0.03	0.11± 0.03	0.58 ± 0.13
NanoBRET lysate + SAM 50 µM	0.08 ± 0.03	0.08 ± 0.02	1.3 ± 0.3
NanoBRET lysate + SAM 100 µM	0.05 ± 0.003	0.06 ± 0.006	2.5 ± 0.3

Figure 52: Effect of SAM levels on cellular EC_{50} values of PRMT5 inhibitors. A) HEK293 cells were lysed before plating and then treated as stated in Fig. 2. B) and C) Influence of different SAM concentrations on compound EC_{50} values in lysates (bio. = representative biochemical IC_{50} value from literature, see Table 1). For Figures 3A-C (n=3), each data point represents the mean ± SD of three biological experiments. D) Summary table for SAM lysate experiments, EC_{50} values in µM.

To rationalise the concept of ternary complex formation, the crystal structures of PRMT5 in complex with SAM as well as SAM- or substrate-mimetic inhibitors were re-evaluated [387]. In case of the substrate mimetic compound GSK3235025 (EPZ015666), the tetrahydroisoquinoline scaffold plays a significant role upon binding to PRMT5 (Figure 53A). The bicyclic ring structure interacts with F327 via π-π stacking and takes advantage of a cation-π interaction with the positively charged sulfonium group of SAM [405]. In absence of the inhibitor, SAM maintains interactions with PRMT5 mainly via its adenosine core whereas the tail extends towards the substrate binding pocket. Yet, when GSK3235025 is bound, SAM adopts a different conformation to accommodate the inhibitor (Figure 53B). F327 appears to assume distinct positions depending on whether SAM, GSK3235025 or LLY-283 are bound which likely explains our observation that CBH-002 is able quantify TE for both inhibitor types (Figure 53B, C).

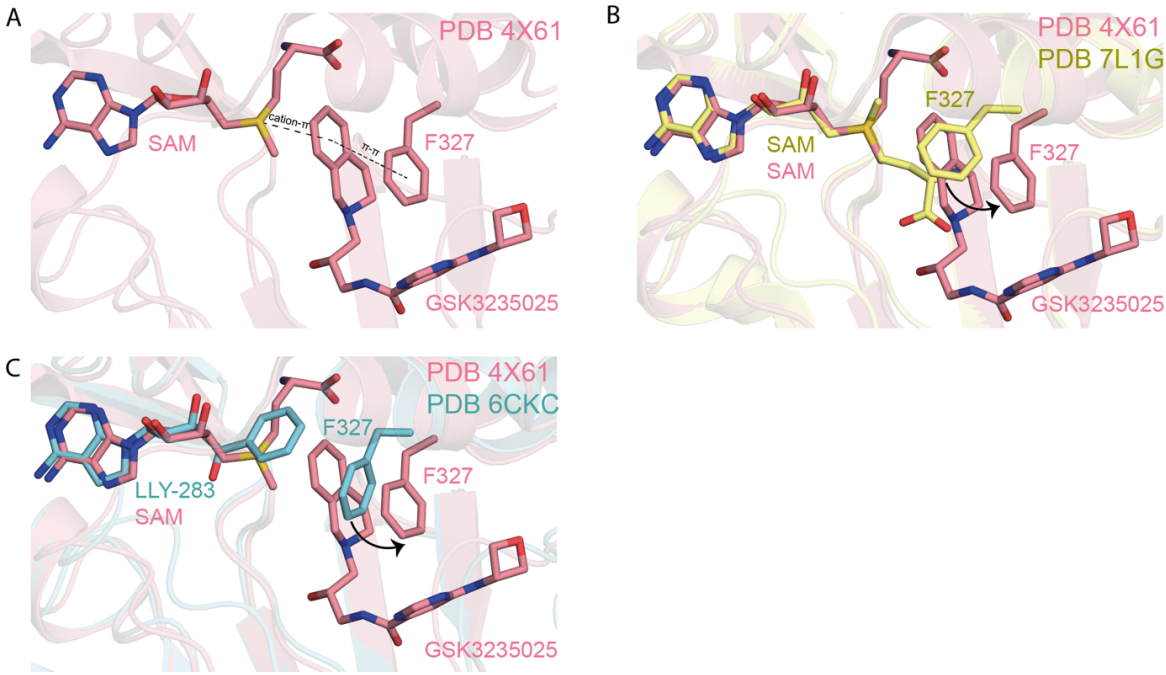


Figure 53: : Co-crystal structures indicate mutually exclusive binding of SAM, LLY-283 and GSK3235025 (EPZ015666). A) SAM and GSK3235025 bind in a stacked manner (PDB: 4X61, pink). B) Induced conformational change of F327 when SAM or GSK3235025 are bound, respectively (PDB: 7L1G, yellow and 4X61, pink). C) Compared to the SAM-mimetic inhibitor LLY-283, binding of GSK3235025 requires re-positioning of F327 to avoid a clash with the inhibitor (PDB: 4X61, pink and 6CKC, blue). This analysis was performed by Esra Balikci.

5.2.2. Chemoproteomic pulldown and orthogonal target validation

After investigating the specific on-target occupancy of mentioned PRMT5 inhibitors, next the proteome-wide selectivity of the clinical candidate GSK3326595 was examined. For a compound-centric approach, the amine-functionalised analogue CBH-001 was immobilised at 20 μM on NHS-activated sepharose beads to generate an affinity matrix enabling chemoproteomic profiling [421]. The remainder of unreacted NHS-groups was blocked using ethanolamine. To distinguish genuine protein targets from non-specific binders, competitive binding experiments were conducted, where KMS11 lysates were pre-incubated with either DMSO or an excess of free GSK3326595 before the analysis of the matrix-enriched proteins.

Western blotting confirmed potent enrichment of PRMT5 and its complex partner WDR77 (MEP50) as both were efficiently competed by parent compound GSK3326595 (Figure 54A). Subsequently, mass spectrometry analysis suggested GSK3326595 to be highly specific for its cognate target among 1610 identified proteins, with significant enrichment and competition observed only for PRMT5 alongside known interactors (Figure 54B). For example CLNS1A (plCln), which has been reported as a substrate adaptor for the PRMT5 complex was enriched [422]. Also identified as significantly enriched in the CBH-001 matrix pull-downs was the zinc finger protein WIZ. WIZ has been found to interact with PRMT5 in a large-scale AP-MS study in HeLa cells [423] and constitutes a core subunit of the protein methyltransferase G9a/GLP complex which catalyses histone methylation for transcription repression [424, 425]. A di-methylated form of WIZ has been identified by MS analysis after enrichment of lysine and arginine methylated peptides in HeLa-S3 cells [426]. Supported by the fact, that WIZ contains a GRG motif, which is

preferred by PRMT5 for arginine methylation [393]. These data suggest WIZ as a candidate substrate of PRMT5. EPB41 is a member of the protein band 4.1 R superfamily of mammalian erythrocyte cytoskeletal proteins and has been described as an interactor of the PRMT5 adaptor CLNS1A in a yeast-two-hybrid assay [426]. Interestingly, as member of the same superfamily sharing the prominent FERM motif, we also observed the Rho guanine exchange factor FARP1 in the CBH-001 pull-down [427]. FARP1 has previously not been reported as a PRMT5 complex binding partner although FARP2 has been identified as a PRMT5 interactor in AP-MS studies using HEK293T cells [428].

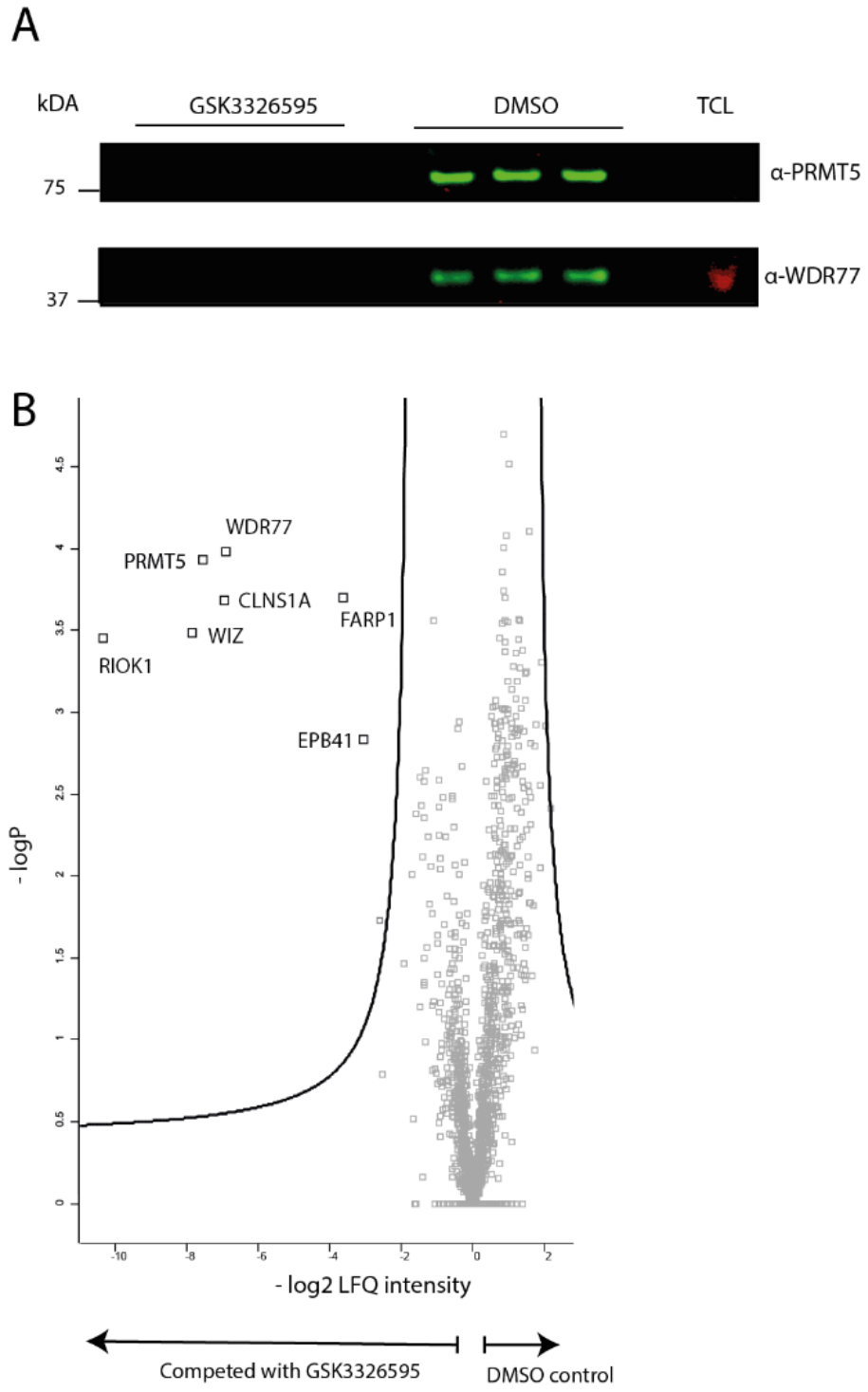


Figure 54: Proteome-wide specificity of GSK3326595 as determined by chemical proteomics. A) Western blot analysis of competitive PRMT5 engagement by affinity probe CBH-001. Competition with either parent inhibitor or DMSO in KMS11 lysate shows inhibitor-dependent enrichment of PRMT5 (72 kDa, green) and WDR77 (36 kDa, green) (TCL, total cell lysate). Red band indicates GAPDH which was used as TCL loading control. B) Volcano plot of CBH-001-enriched proteome from KMS11 cell lysate, with targets significantly competed by 20 μM GSK3326595 versus DMSO control (FDR = 0.05, S0 = 0.2).

To account for any potential bias introduced by installing a linker moiety, an orthogonal thermal profiling experiment with GSK3326595 in live KMS11 cells was performed by Jakub Stefaniak. In a 2D setup [429], cells were treated with four different inhibitor concentrations (i.e., 5, 1, 0.2 and 0.04 μM) or DMSO, and subjected to a denaturing temperature gradient (42-64 °C). This allows for visualisation of any dose-dependent thermal stabilisation of proteins, thereby increasing confidence in direct drug-target interactions. Following mass spectrometry analysis, 5,926 proteins were identified out of which 5,434 were detected with high FDR confidence. Data were processed with an R-script [429], as well as a bespoke, in-house coarse MATLAB filter we established for fast thermal profiling data deconvolution (Figure 55A) [387]. This analysis yielded two high confidence hits, the cognate target PRMT5 and its well-known binding partner WDR77. GSK3326595-dependent stabilisation of PRMT5 and WDR77 was also validated by Western blot (Figure 55B). Taken together, these results suggest that GSK3326595 is a highly specific PRMT5 inhibitor.

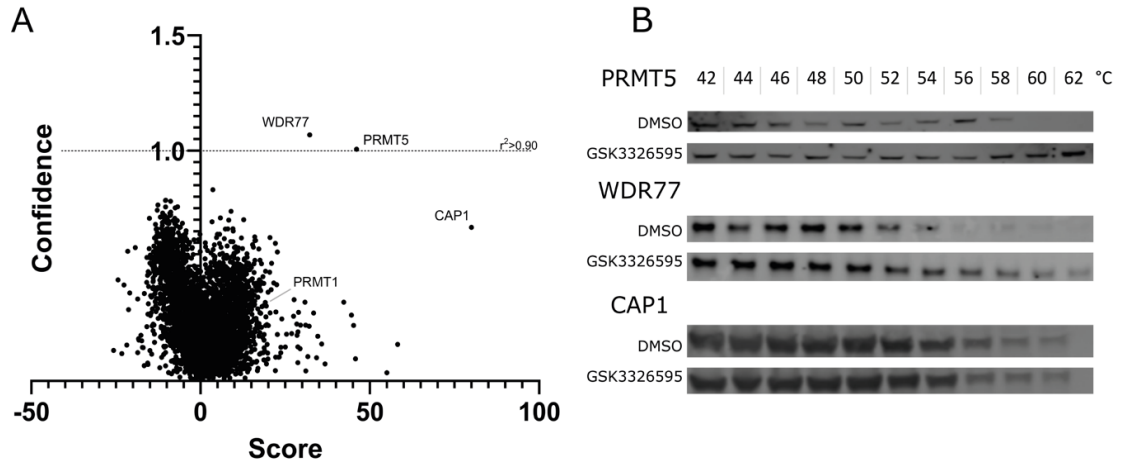


Figure 55: 2D thermal profiling results for GSK3326595 identify the methylosome complex comprising PRMT5 and WDR77 (n=1). A) Volcano plot. For each protein, the score indicates the volume under the surface of stabilization as a 2-dimensional function of temperature and compound concentration as calculated by the algorithm, and confidence is –log(1-r²) of the fitted surface (for more information about the algorithm, see Supp. Fig. 8). B) Validation of PRMT5 and WDR77 via Western blot CETSA using 5 µM GSK3326595 (n=1). This experiment was performed by Jakub Stefaniak.

5.3 Summary and outlook

Previously, cellular target engagement of PRMT5 inhibitors has been demonstrated via imaging-based detection of symmetrically dimethylated nuclear proteins [430, 431] as well as in NanoBIT PRMT5-RIOK1 protein-protein interaction assay using permeabilised cells [432, 433]. While CETSA has been established for PRMT5 [405], a key advantage of the NanoBRET system is its ability to provide a continuous quantitative readout of cellular TE. The intact cell experiments provide EC_{50} values correlating with biochemically derived data and suggest that a decrease in potency stems likely from effects related to cellular uptake, compound distribution and a more complex intracellular environment in general. Additionally, by comparing intact cell, lysate, and SAM complementation experiments, differential cofactor effects on inhibitor binding were demonstrated expanding on previous observations made with purified recombinant proteins [405]. When lysates were tested, EC_{50} values for substrate-competitive inhibitors such as GSK3326595 were found to be increased when SAM is diluted. This implies that less SAM was available to contribute to the formation of a favourable ternary complex. Earlier mechanistic work for GSK3326595 showed that increased pre-incubation times of 1 h in presence of SAM led to a reduction of the respective biochemical EC_{50} values in a PRMT5:MEP50 activity assay [411]. In the NanoBRET assay, artificial addition of SAM facilitated substrate-mimetic inhibitor binding to PRMT5, resulting in more efficient displacement of CBH-002. It is worth mentioning that although GSK3326595 was marginally less potent than GSK3203591 in the intact cell NanoBRET, its EC_{50} values appeared to respond slightly better to exogenous addition of SAM, particularly at high cofactor concentrations.

Conversely, LLY-283, which targets the SAM-pocket of PRMT5, performed better in lysate whereas increased SAM levels resulted in higher EC_{50} values, indicating cofactor-competitive behaviour. These results are largely consistent with previous publications, the fact that our NanoBRET system uses HEK293 cells limits the ability to perform direct comparisons as this cell line has not been evaluated in the literature with these inhibitors. Notably, these findings reinforce the concept of SAM contributing to inhibitor binding which has also been demonstrated for PRMD9 using SPR [434]. Additionally, MTAP deletion leading to higher MTA levels might as well influence inhibitor potency in cells [404], which could be further investigated using respective cell lines in the assay. Moreover, it would be interesting to investigate whether MTA levels affect the tested compounds in our assay, similarly to SAM: either weakening or strengthening compound potency. We used SAM in cell lysates, as it cannot be up taken by mammalian cells due to lack of transporters, but in contrast to SAM, MTA can cross the cellular membrane [435]. Thus, experiments with exogenous MTA addition would allow for intact cell experiments.

Intrigued by the ability of substrate-mimetic ETP CBH-002 to survey both substrate- as well as cofactor-competitive PRMT5 inhibitors, previously published crystal structures were re-examined to rationalise these observations. The analysis strongly supports the idea that F327 plays a key role as a gatekeeper-like sensor which repositions in response to SAM- as well as substrate-mimetic inhibitors [436]. CBH-002 is able to exploit these dynamic interactions allowing for the detection of both substrate- as well as cofactor-mimetic inhibitors. Further experiments can be done to test whether the assay could also be used to evaluate novel dual-competitive orthosteric and allosteric inhibitors [430, 431]. A recent study found that spirodiamines based on a purine scaffold can occupy both the cofactor- as well as parts of the substrate-binding site [437]. However, these compounds are

SAM-competitive but non-competitive with regard to substrates. Interestingly, PRMT5 has several accessible cysteine residues (C278, C449) which has enabled the development of covalent inhibitors [433, 436].

At the moment, there is limited data available regarding the global specificity of PRMT inhibitors. A study investigated the proteome-wide selectivity of the pan-type I PRMT inhibitor MS023 [418]. Here, this effort is extended to the clinical PRMT5 inhibitor GSK3326595 (pemrametostat) using complementary chemoproteomic and 2D thermal profiling experiments. KMS11 cell line was selected as a model system, since PRMT5 is overexpressed in multiple myeloma and has been suggested as a prognostic marker [438]. Genetic knockdown and PRMT5 inhibition using GSK3235025 (EPZ015666) have been shown to inhibit growth and induce apoptosis in MM cell lines. Both chemoproteomic experiments suggest remarkable selectivity of GSK3326595 for PRMT5, although there may be additional targets that are missed by MS detection or are not expressed in KMS11 cells. Nevertheless, a recently reported VHL-based PRMT5 PROTAC derived from GSK3235025 (EPZ015666) was found to be highly specific [439].

Several known PRMT5 interactors such as WDR77 (MEP50), RIOK1, and CLNS1A were identified in the MS data. RIOK1 and CLNS1A have previously been found to bind PRMT5 in a mutually exclusive fashion [440]. The results therefore indicate that GSK3326595 can likely recognise both complexes. In this context, it is interesting to note that COPR5 is thought to utilise the same binding site as RIOK1 and CLNS1A [395, 432], but was not detected in the experiments. However, it is possible that this complex is not stable or inaccessible under the chosen experimental conditions or does not occur in KMS11 cells. With respect to the other proteins identified in the pull-down, FARP1, which was

enriched and competed may be a potentially novel PRMT5 binding partner in human cells. Previous work did not detect any changes in methylated peptides for FARP1 upon GSK3203591 treatment in HeLa cells, suggesting it may not be a substrate for PRMT5 [393]. In contrast, WIZ which contains a sequence motif preferred by PRMT5 for methylation and which was found to interact with PRMT5 in AP-MS studies could be a direct substrate. Pharmacologic inhibition of PRMT5 has been shown to result in a minor down-regulation of methylated EPB41 [393], which is known to bind CLNS1A and was co-purified in the drug pull-down. EPB41 has been linked to anaemia [441], yet any functional consequences of this interaction remain to be elucidated. Notably, the pulldown experiment was able to identify more related proteins than the CETSA, underscoring the importance of utilising different bio-orthogonal methods for target deconvolution, as each technique can add complementary information.

In conclusion, the results reveal new insights into the mechanism of action of PRMT5 inhibitors and provide a toolkit which can be envisioned to support the development of future inhibitors. The proteomic profiling data highlight the selectivity of clinical PRMT5 inhibitors and how these compounds interact with PRMT5 adaptor complexes. The highly versatile NanoBRET system allows to correlate cofactor-dependent cell TE with functional readouts. There is a number of established PRMT5 inhibitors, which could additionally be evaluated, among them PF06939999 [442] or JNJ64619178 [443], which feature scaffold similarities to SAM. DS-437, a dual PRMT5/PRMT7 inhibitor could be investigated to complement cellular data regarding its potency against both targets [444]. Moreover, novel compounds have been reported with distinct binding modes, which could be evaluated in our assay, e.g. MRTX1719 selectively inhibits PRMT5 in MTAP-deleted cells. This compound was derived from a fragment screen and was shown to bind

PRMT5/MTA complex [410]. Another recently developed compound is TNG908, which is currently in clinical trials and has been described as a MTA-cooperative inhibitor selective for MTAP null over MTAP WT cell lines [445]. Intact cell assays with MTA, rather than SAM, which is not cell-permeable, would derive further insights into co-factor contributions to compound binding. Furthermore, since the assay could be easily expanded to other PRMTs, it would be interesting to investigate whether the only other PRMT Type II protein, PRMT9, would be susceptible to react with ETP CBH-002.

Statement of Authorship for joint/multi-authored papers for PGR thesis

To appear at the end of each thesis chapter submitted as an article/paper

The statement shall describe the candidate's and co-authors' independent research contributions in the thesis publications. For each publication there should exist a complete statement that is to be filled out and signed by the candidate and supervisor **(only required where there isn't already a statement of contribution within the paper itself).**

Title of Paper	A chemical biology toolbox to investigate in-cell target engagement and specificity of PRMT5-inhibitors
Publication Status	X Published □ Accepted for Publication □Submitted for Publication □Unpublished and unsubmitted work written in a manuscript style
Publication Details	Pre-Print: Elisabeth M. Rothweiler, Jakub Stefaniak, Jennifer A. Ward, Catherine Rogers, Esra Balikci, Kilian V. M. Huber bioRxiv 2022.01.20.477145; https://doi.org/10.1101/2022.01.20.477145

Student Confirmation

Student Name:	Elisabeth Mira Rothweiler		
Contribution to the Paper	Performed all NanoBRET experiments, performed ETP-synthesis, performed pull-down, analysed and interpreted data and created figures, contributed to all parts of the manuscript Did perform intracellular fluorescence in collaboration with Jesper Hansen Did perform analysis of co-crystal structure in collaboration with Esra Balikci CETSA-WB, CETSA-MS and subsequent Matlab analysis performed by Jakub Stefaniak		
Signature	Elisabeth Mira Rothweiler	Date	13.09.23

Supervisor Confirmation

By signing the Statement of Authorship, you are certifying that the candidate made a substantial contribution to the publication, and that the description described above is accurate.

Supervisor name and title: Kilian Huber		
Supervisor comments		
Signature Huber	Date	18/09/23

This completed form should be included in the thesis, at the end of the relevant chapter.

6. Evaluation of covalent fragments as interrupters of protein-protein interactions

Protein-protein interactions (PPI) play a central role in cellular processes. The activity of proteins is typically regulated through protein complexes, and up to 80 % of our human proteins are estimated to engage in PPI [446]. The interlinked human interactome is predicted to comprise over 130000 interactions [447, 448]. This plethora of interactions includes structural proteins and protein complexes, which regulate transcription, translation, protein synthesis, and protein degradation, as well as cell cycle progression and signal transduction [449]. This number of interactions is around 10-times higher in comparison to the approximately 10000 druggable proteins in the human proteome [450]. By their nature, PPIs can be hetero- or homooligomeric, obligate or nonobligate in their stability, and transient or permanent with regard to persistence [451]. For example, transient interactions are required in signalling pathways, whereas permanent interactions form stable protein complexes. Phizicky and Fields have marked important properties of PPIs [452]:

- altering kinetic properties of enzymes
- acting as a general mechanism to allow for substrate channelling by moving a substrate between domains or units
- forming a novel binding site for small effectors molecules
- inactivating or suppressing proteins
- changing the specificity of a protein for its substrate by interacting with different binding partners
- taking a regulatory role on upstream or downstream events

Understanding and targeting PPIs can lead to new therapeutic strategies distinct from classical drug targets like ion channels, transcription factors or receptors [453]. However, the PPI contact surfaces are large (1500-3000 Å^2) in comparison to protein-small molecule interactions (300-1000 Å^2) and can be rather flat, lacking groves and pockets where small molecules would usually bind [454-456]. In principle, every pathologically significant PPI is a potential drug target for development of small molecule PPI modulators [457].

6.1 Polycystic ovary syndrome: DENND1A and RAB35

The Polycystic Ovary Syndrome (PCOS) affects approximately 5 – 7 % of woman in reproductive age worldwide. PCOS is characterised by elevated androgen levels (hyperandrogenism), oligo- or anovulation and ovarian cysts [458]. PCOS is associated with development of dyslipidaemia, cardiovascular risk factors such as atherosclerosis, insulin resistance, impaired glucose tolerance and type 2 diabetes in women [459, 460]. The pathogenesis of PCOS is not fully understood yet, however a two-stage genome-wide association study (GWAS) in Han Chinese women identified potential genetic markers, and DENN Domain Containing 1A (DENND1A) was suggested as a candidate locus influencing pathogenesis in PCOS [461]. The gene DENND1A was shown to encode two variants, V1 (1009 amino acids) and short isoform V2 (559 amino acids), while V2 has been found as overexpressed in ovarian PCOS theca cells [462]. Intriguingly, a knockdown of V2 in theca cells with this phenotype reduced androgen production whereas overexpression in normal theca cells in turn induced a PCOS phenotype with increased androgen synthesis [463]. DENND1A is a guanine exchange factor (GEF) for RAB35 [464]. RAB35 is a GTPase involved in endocytic recycling and cytokinesis [465]. It has been shown to play a role in polarity initiation and apical lumen positioning during cyst development

[466]. Currently, both DENND1A and RAB35 are lacking inhibitors. The co-crystal structure of DENND1A and RAB35 (PDB: 6EKK) was solved by our group. Figure 56 shows nucleophilic amino acids such as cysteine, methionine, or tyrosine in the PPI-surface, which might potentially be druggable with electrophiles. The RAB35 binding surface of the DENN-domain is formed primarily by residues in its C-terminal lobes (called switch 1 and 2) and the DENN-domain/RAB35 interface has been shown to span approximately 3000 Å^2 of solvent-accessible surfaces [467].

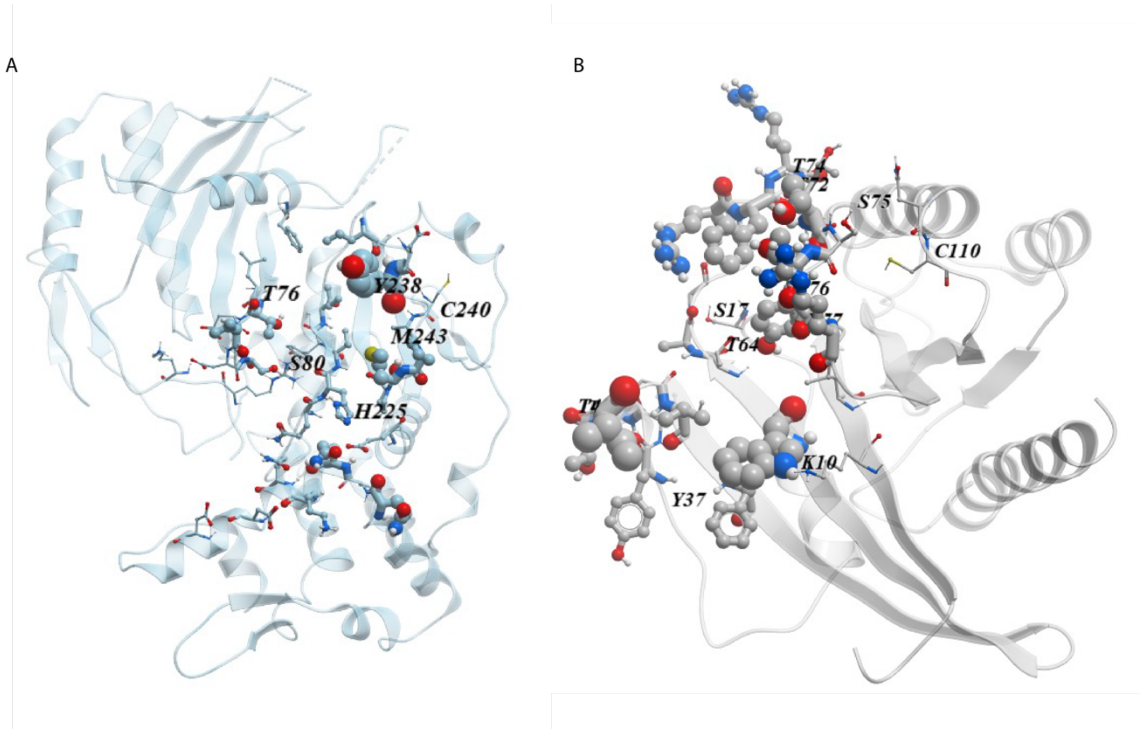


Figure 56: Views of DENND1A and Rab35 based on co-crystal structure (PDB: 6EKK). A) Nucleophilic amino acid residues highlighted in the PPI-surface of DENND1A. B) Nucleophilic amino acid residues highlighted in the PPI-surface of RAB35. These pictures were created by Laura Diaz-Saez.

6.2 Evaluation of fragments as interrupters of PPI

A commercially available electrophilic covalent fragment library containing approximately 1500 compounds in nine reactive groups, such as enones, acrylamides, chloroketones and sulfonylfluorides, was tested in a NanoBRET PPI assay, using HT-RAB35 and DENND1A-NL V1 and V2 in transfected HEK293 cells. The assay had been developed and optimised by student Verena Straub. The NanoBRET platform can be utilised to monitor PPI interactions. In brief, a donor (NLuc) and an acceptor (Halo-tag and ligand) come into close proximity, and a BRET signal can be measured. The experiments aimed to find covalent fragments binding and inhibiting the PPI between RAB35 and DENND1A in living cells. Hits derived from this system might target either protein or proteins up- or downstream in the cellular system. A subsequent CellTiterGlo assay revealed whether compounds exerted cytotoxicity. The fragments were prepared from a solid stock in 40 μL DMSO to liquid DMSO stocks ranging from 88-208 mM. The DMSO stock solutions vary as the solid stocks had different MW and weight of sample in the delivered microtubes and we used a liquid handler only able to dispense equal amount of DMSO into all tubes.

6.2.1 NanoBRET PPI assay DENND1A and RAB35

Initially, a NanoBRET PPI assay using HT-Rab35 and DENND1A-NL V1 was done in single-shot experiments to evaluate the broad range of covalent electrophiles (n=2). For this, ten 384-well plates were prepared using the ECHO liquid handler for compound plating in duplicates. Since the DMSO stocks had varying concentrations to begin with, our final assay concentrations ranged from around 80 – 100 μM. The plates contained DMSO and ligand, and DMSO and no ligand as control wells as an approximation for

highest (0 % inhibition) and lowest signal (100 % inhibition), as no mutated version of DENND1A or RAB35 was available, and there are currently no known inhibitors to use as a control. As a result, preliminary hits over 25 - 40 % and (experiment 1, Figure 57A and Supplementary Figure S11) 35 - 60 % inhibition (experiment 2, Figure 57 C and Supplementary Figure S12) were obtained. In experiment 1, 21 compounds were defined as preliminary hits subsequent test of cytotoxicity revealed 140 cytotoxic compounds, defined as greater than 50% loss of viability (Figure 57B and Supplementary Figure S13). In experiment 2, 63 compounds were defined as preliminary hits and 98 were identified as cytotoxic (Figure 57D and Supplementary Figure S14).

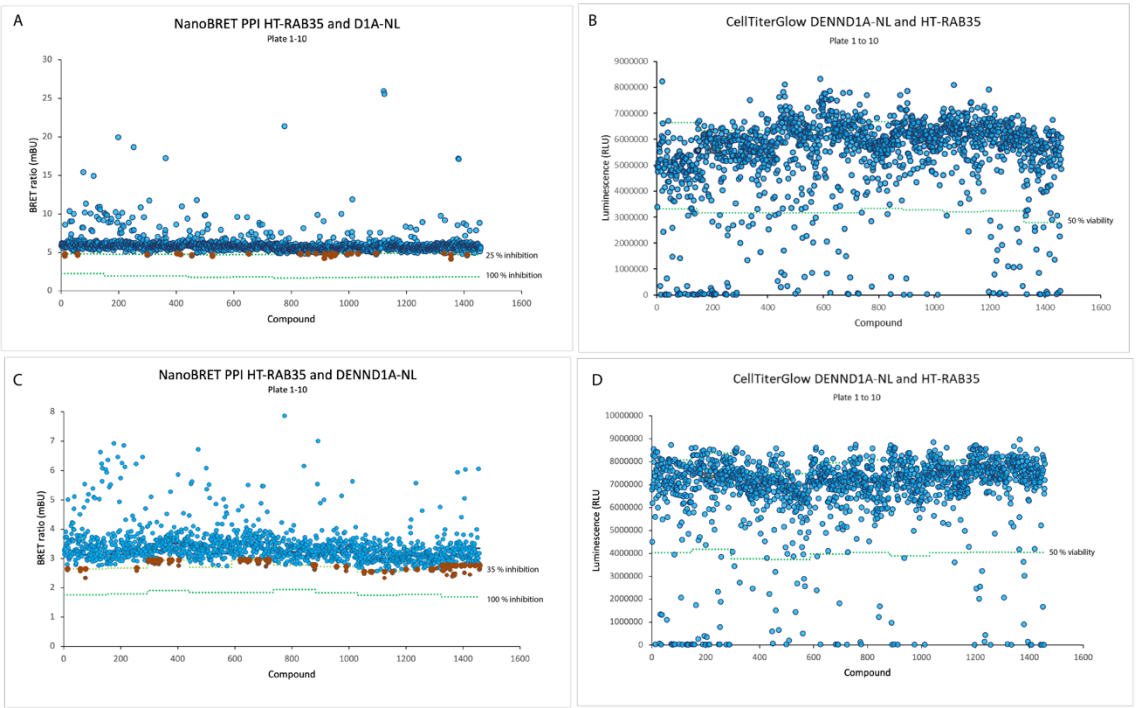


Figure 57:Scatter plots showing 10 plates of NanoBRET PPI and corresponding CellTiterGlo cell viability results for the single shot experiments of the 1500-membered fragment library screen using 80-100 µM of the fragments. A) NanoBRET results for experiment 1 plotted as mBU per compound, preliminary hits (marked in red) were selected > 25 % inhibition. 0 % and 100 % inhibition were calculated based on DMSO without ligand and DMSO without ligand. B) Corresponding CellTiterGlo assay results, plotted as RLU per compound. C) and D) show the respective results for experiment 2. Each plate, including error bars, is depicted in Supplementary Figure S11-S14.

The overlap between the preliminary hits from both experiments was three fragments: Z1747834877 (acrylamide), Z56824392 (chloroketone) and Z228594682 (enone). This was and indication that the promiscuous reactivity of electrophilic warheads might be contributing to assay variability. The Z-factor was determined as 0.2 indicating poor reproducibility. Among all preliminary hits, the largest group were the acrylamides, followed by the enones. This mirrored the composition of the fragment library, where the acrylamides were the largest fraction with 74 %, followed by the enones with 11 %, chloroketones with 6 % and sulfonylfluorides with 3 % and other 6 % fragments. Another reason for the variation in preliminary hits might be the stability of electrophilic covalent fragments. Due to DMSO's hygroscopicity, every source plate opening allows water from the air to dilute the stock and water can react with the electrophilic covalent fragments. The vendor (Enamine) stated, that 20 - 30% of the compounds did not give satisfactory LC/MS after 6 months and 6-fold opening in DMSO stocks stored at -20 °C. Experiment 1 was done at 1st opening, and experiment 2 at 6th opening. Indeed, the latter transfer file of the compound plating showed varying percentage of DMSO ranging from 70 - 90%. The fragments might be degraded and hydrolysed, water could react, e.g. with chloroacetamides and result in an amide and chloroacetic acid. Sulfonyl halides can react to form their corresponding sulfonic acid: $C_6H_5SO_2Cl + H_2O \rightarrow C_6H_5SO_3H + HCl$, whereby fluorides are more stable than chlorides due to the stronger S-F bond [468]. Despite the poor overlap between the experiments, all hits from experiment 1 and all preliminary hits over 35% cut-off from experiment 2 were taken into dose response experiments.

In the dose response experiment, six plates contained fragments in duplicates and over 10 dilution steps (1:2) from a top concentration ranging between 200-300 μM (14 fragments per plate). The plates contained DMSO and ligand, and DMSO and no ligand as control wells. The resulting curves did not show a good dose response, most fragments did not show activity, and IC_{50} could not be reported. In the cell viability assay, at top concentrations there was cell death for most fragments. The fragments showing 10 – 30 % loss of NanoBRET signal were picked alongside activating fragments, resulting in 26 compounds for further dose-response screenings (Figure 58). 9 compounds out of 26 originated from single-shot experiment 1 and 17 compounds originated from single experiment 2 (Supplementary Figure S15). Again, these hits mirrored the fragment library composition with most preliminary hits counting into acrylamides and enones. Particularly interesting were the internal enones flanked by a fluorinated phenyl ring and a substituted pyrazole ring. Overall, the reactive groups of the preliminary hits indicated cysteine reactivity. Warheads such as sulfonylfluoride, which possess serine reactivity, were not showing activity in our hands.

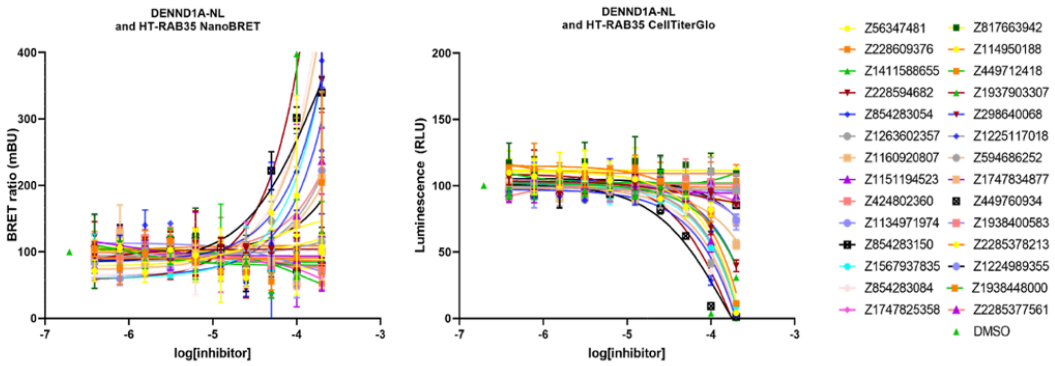


Figure 58: Selection of best 26 fragments from dose-response experiments, graphs showing NanoBRET result and respective CellTiterGlo cell viability results. Exemplary graphs from n=3. Each data point represents the mean ± SEM of technical triplicates.

Of the 26 fragments, six compounds showed partially dose-responsive behaviour against full length DENND1A-NL combined with low loss of cell viability at highest concentrations (Figure 59A-F). The reactive groups amongst these hits contained two acrylamides, one dienamide and one cyanoacrylamide, one chloroacetamide, as well as three enones. Compounds like these are known to possess cysteine reactivity. By acting as Michael acceptors in a Michael addition, the vinyl-group of the acrylamide is attacked by the nucleophilic sulfhydryl group (Michael donor) of cysteine. A new bond is formed, and the fragment is covalently attached to the cysteine. α,β-Unsaturated carbonyl compounds such as enones react in a similar manner.

However, within three repeats of the dose response, the fragments were showing divergent behaviour. The curves of the BRET ratio in two out of three repeats aligned very well, but the third curve was deviating and showed activating behaviour compared to the others, e.g. for compound Z1151194523, where one curve (dark blue) showed a steep signal increase in the BRET ratio as well as cytotoxicity at highest concentrations (Figure 59B). In general, it may be challenging to obtain accurate and precise measurements from complex cell-based assays because of measurement uncertainties [469]. Variations, as seen in our assay, could possibly lie in the transient transfection of the HEK293 cells leading to different expression levels. Transfection efficiency may vary due to confluency, viability or passage number of cells in culture. Establishing stable cell lines would be a possible solution for this. Additionally, the manual handling of the reagents might introduce additional variation in the assay, here automated dispensing of e.g. the NanoLuciferase substrate, furimazine, could reduce variability. However, a test with the Multidrop Combi+ liquid handler (Thermo Fisher) revealed a dead volume of

around 5 mL residual substrate solution, due to the tubing and connections of the machine. As the substrate is expensive and must be used freshly prepared, this option was not feasible. Another reason might be the stability of the electrophilic covalent fragments as discussed earlier. As a solution, the fragments could be stored as solids and be freshly prepared for every new experiment.

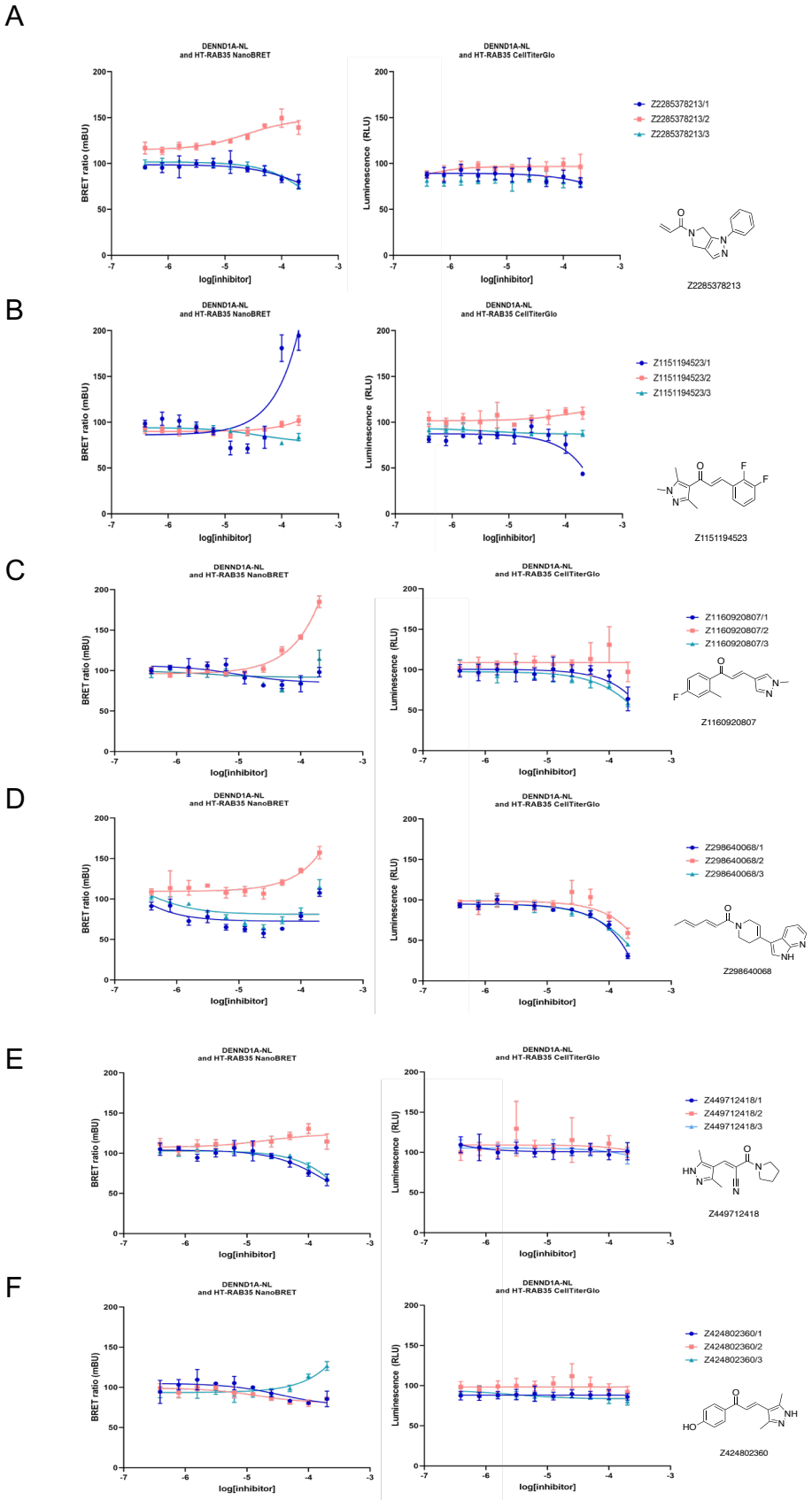


Figure 59: NanoBRET DENND1A-NL and HT-RAB35, and cell viability results for six fragments shown in A-F for n=3. Each data point represents the mean ± SEM of technical triplicates.

In order to further evaluate these hits, we screened the selection against DENND1AV2-NL and also against BRD9 BD-NL and H3.3-HT in a counter screen, to exclude any false positives and fragments which exhibit any target unspecific effects (Figure 60A,B). In the counter screen experiments, the fragments showed activation in combination with cell death instead of inhibitory behaviour. This phenomenon occurred especially for BRD9 BD-NL and H3.3.-HT, were the fragments showed huge increases in the BRET ratio (Figure 60B). This increase could stem from pre-apoptotic stress causing the cells to overexpress proteins, or in this case, the cysteine-reactive fragments might be interfering with the histone H3.3 by covalently binding to its C110 residue. Glutathionylation of this residue has been shown before [470]. The data showed correlation between loss of cell viability and activating BRET signal. In contrast to the full-length DENND1A, for the short isoform V2, we saw only marginally activating behaviour for the six fragments in combination with modest cytotoxicity of the compounds at highest concentration (Figure 60A).

The NanoBRET assay was chosen as a primary screen to indicate whether a fragment exerts an effect on the phenotypic readout, detecting inhibitors binding not only to either DENND1A or RAB35 but also to upstream regulators. In comparison, testing of recombinant protein delivers only binding information about the tested protein. Generally, DENND1A is difficult to express and limited in its availability. Since the NanoBRET assay is based on BRET between donor and acceptor, DMSO without ligand controls were used as an analogue for a negative control. Likewise, DMSO with HT-ligand controls were used as a positive control. Efforts to create a negative control comprised mutating major contributors to the PPI on DENND1A, such as Y238, M243, Q362, and H225, were so far unsuccessful (Supplementary Table T8, Supplementary Figure S16).

To our knowledge, a covalent fragment screen in a NanoBRET PPI assay is a novel approach. However, in-cell target engagement has been demonstrated in NanoBRET TE assays. For example, Forster et al. showed the validation of cellular TE for a dual BMX/BTK-inhibitor, addressing a cysteine residue in the ATP-binding pocket in an NanoBRET assay competing their covalent acrylamide compounds against non-covalent tracer K5 (Promega) [471]. For lysine demethylases (KDMs), a series of acrylamide- and chloroketone-containing molecules was tested with an ETP against a panel of KDM5 family NLuc-fusion proteins and subsequently their potency was determined as in the micromolar range *in cellulo* [472]. Guo et al. reported reversible covalent PROTAC RC-1, which is binding to BTK and showed its submicromolar potency in cell-based NanoBRET assays using both a CRBN- and a BTK-ETP [473].

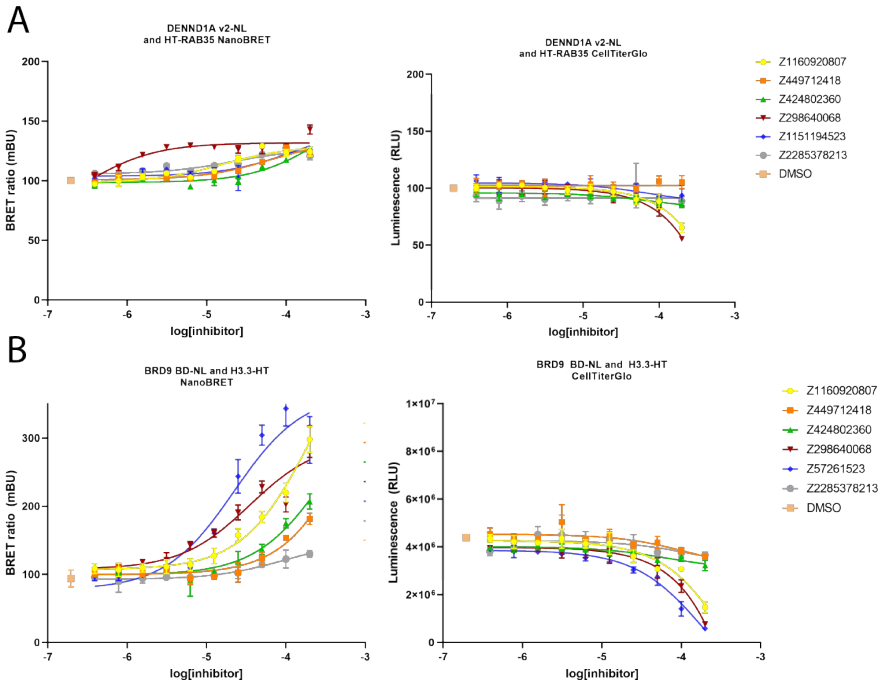


Figure 60: Evaluation of six fragments in NanoBRET using short isoform of DENND1A V2-NL and in counter screen assay using BRD9 BD-NL and H3.3.-HT. Each data point represents the mean ± SEM of technical triplicates. A) NanoBRET and corresponding CellTiterGlo cell viability results for six fragments in the system DENND1A V2-NL and HT-RAB35 (n=1). B) NanoBRET and corresponding CellTiterGlo cell viability results for six fragments in the system BRD9 BD-NL and H3.3.-HT (n=1).

6.2.2 Expression and purification of RAB35-c002

HIS-tagged construct RAB35-c002 was available, and we have expressed and re-purified it when required more material for our experiments. We followed the purification as described by Sun Jung; the protocol is described in the methods section for this chapter. In brief, Rosetta competent cells were transformed using RAB35a-c002 and plated on kanamycin agar plates over night, subsequently a starter culture was inoculated by picking a colony the next day. 6 L medium were inoculated the next day until it reached an optical density of OD = 0.8, before adding IPTG to start protein expression over night. The pellets were harvested and frozen at 20 °C. The next day, pellets were lysed and homogenised using a Dounce homogeniser before centrifugation and performing an affinity purification of the supernatant with nickel beads. Imidazole buffer washes and elutions were performed, as fractions 7-18 were showing a band for HIS-tagged RAB35 (23 kDa) in a gel, these fractions were pooled and concentrated (Figure 61A). TEV-cleavage was performed in a dialysis cassette over night and a negative affinity purification using nickel resin was conducted which showed successful removal of the tag. Fractions 1 – 4 and flowthrough showed cleaved RAB35 in a gel and were pooled and concentrated (Figure 61B). After size exclusion chromatography using an AKTA, fractions 22 – 30 were pooled (Figure 61C) and yielded 1 mL of 9.45 mg/mL RAB35. Identity and purity were confirmed by intact MS (Supplementary Figure S17). The protein was used for intact MS and GEF activity experiments.

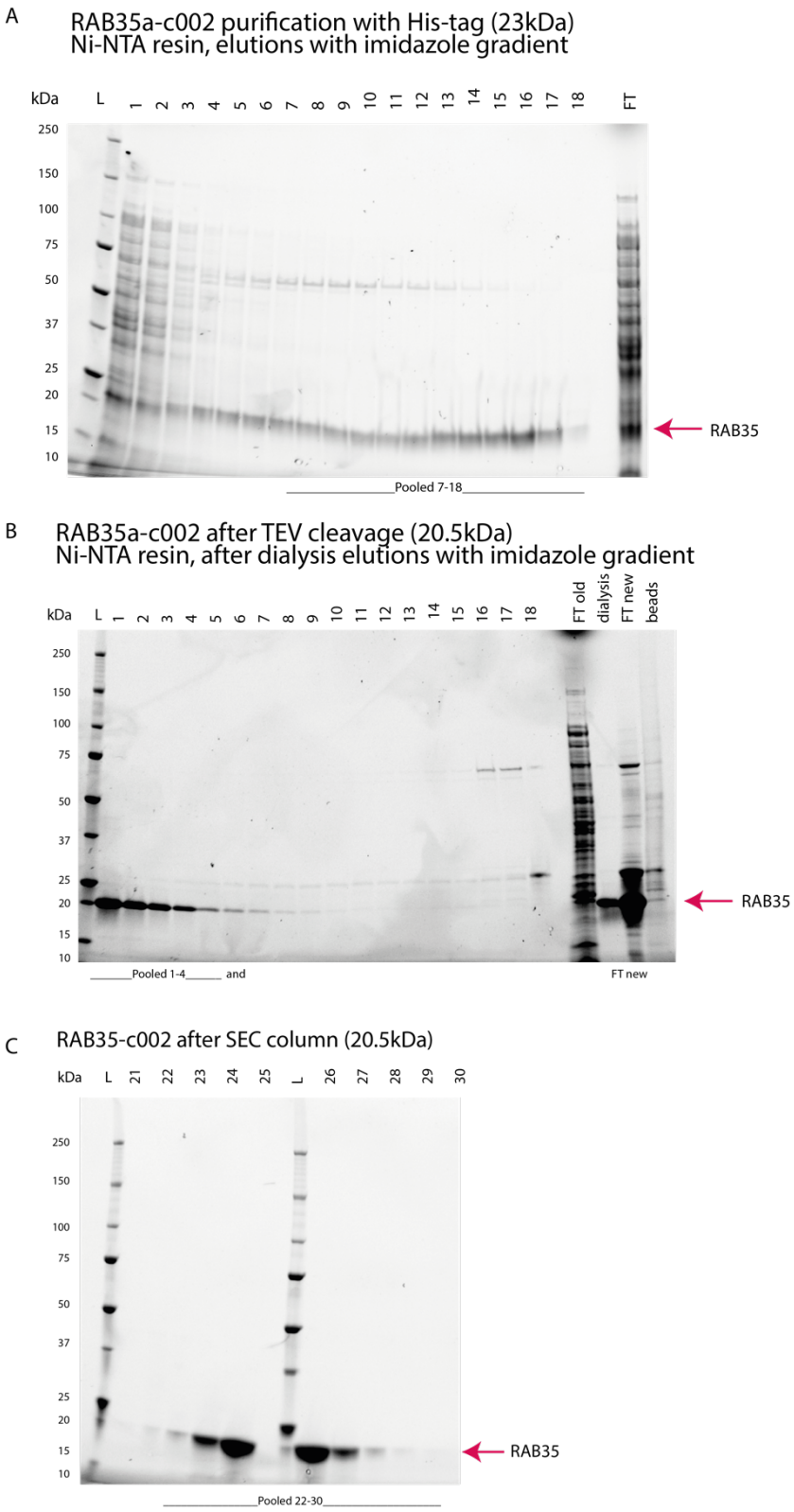


Figure 61: Gels of the purification of RAB35a-c002. A) Elutions and of nickel affinity chromatography using imidazole lysis buffer gradient (LB) showing HIS-tagged RAB35 at 23 kDa. B) Elutions of nickel negative affinity chromatography using imidazole lysis buffer gradient (LB) after TEV-cleavage indicating untagged RAB35 at 20.5 kDa. C) Size exclusion chromatography (SEC) result showing fractions containing untagged RAB35.

6.2.3 Intact MS for binding validation

To evaluate the six fragments obtained from the NanoBRET screen, we tested DENND1A (DENN-domain only) and RAB35 recombinant protein at 2 μM against IA as a control and the fragments using intact MS. IA would react in a SN_2 reaction and form a carboxyamidomethyl-adduct with a nucleophilic thiolate (Figure 62A, + 58 g/mol). DENND1A-c025 construct contained nine cysteines, and RAB35a-c002 construct contained three cysteines in their sequence. Using IA, we observed the formation of adducts for both DENND1A (up to three adducts, Supplementary Figure S18A-C) and RAB35 (up to three adducts, Supplementary Figure S18D-F). The results indicated all three cysteines on RAB35 were susceptible to react with IA, however the peak for one modification was most intense, followed by the second modification, and the third modification peak was very small.

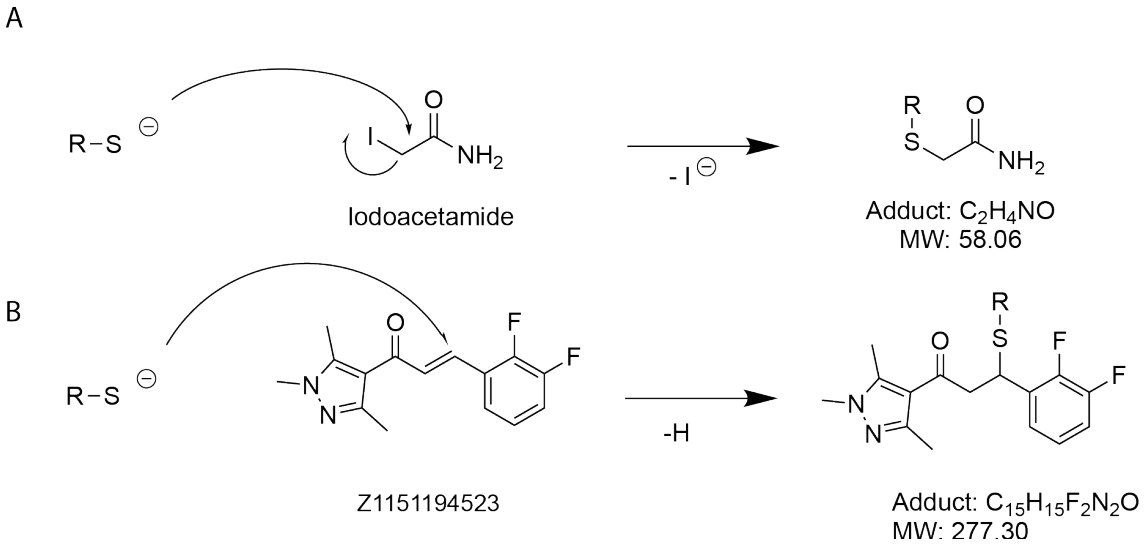


Figure 62: Formation of covalent mass adducts. A) Iodoacetamide reacts in a SN_2 reaction, the nucleophilic thiolate attacks the carbon-atom next to the iodo leaving group and a new bond is formed between sulphur and carbon, resulting in a carboxyamido methyl-adduct. B) The internal enone reacts in a Michael addition reaction, the doublebond is attacked by the thiolate as a nucleophile and forms a Michael adduct on the beta carbon, a new C-C-bond is formed.

Next to the PPI-surface there is a cysteine (C240) on DENND1A and two cysteines (C110 and C114) on RAB35, which could be addressed with the covalent fragments. The fragments were bought as solid stocks and prepared as 100 mM DMSO stocks freshly. Screening the fragments at different concentrations and timepoints, an adduct with the mass of fragment Z1151194523 (+ 277 g/mol) on RAB35 was observed. Z1151194523 would react in a Michael addition reaction with a thiolate and form a covalent adduct on the b carbon (Figure 62B + 277 g/mol). The strongest peak was visible for 600 μM compounds of the fragment (Figure 63A-C). In competition with IA, we also observed one main modification with the fragment. After 6 h treatment of RAB35 with 300 μM IA and fragment Z1151194523 at room temperature, we observed up to two modifications with IA and one modification with fragment (Figure 64A). After 24 h, there were indications of a mix of species of one fragment modification, fragment plus 1 - 2 IA modifications and protein with two IA modifications (Figure 64B). IA alone was showing 1-3 modifications after 24 h (Figure 64C). After a researcher in our laboratory, Srinivasa Adusumalli, conducted additional experiments using the fragment at 25 °C in a shaking incubator, we observed more that one mass shift on RAB35 and also found reactivity on RAB family member RAB39B (Supplementary Figure S19). To evaluate these findings, we aimed to identify the binding site of the fragment Z1151194523 on RAB35.

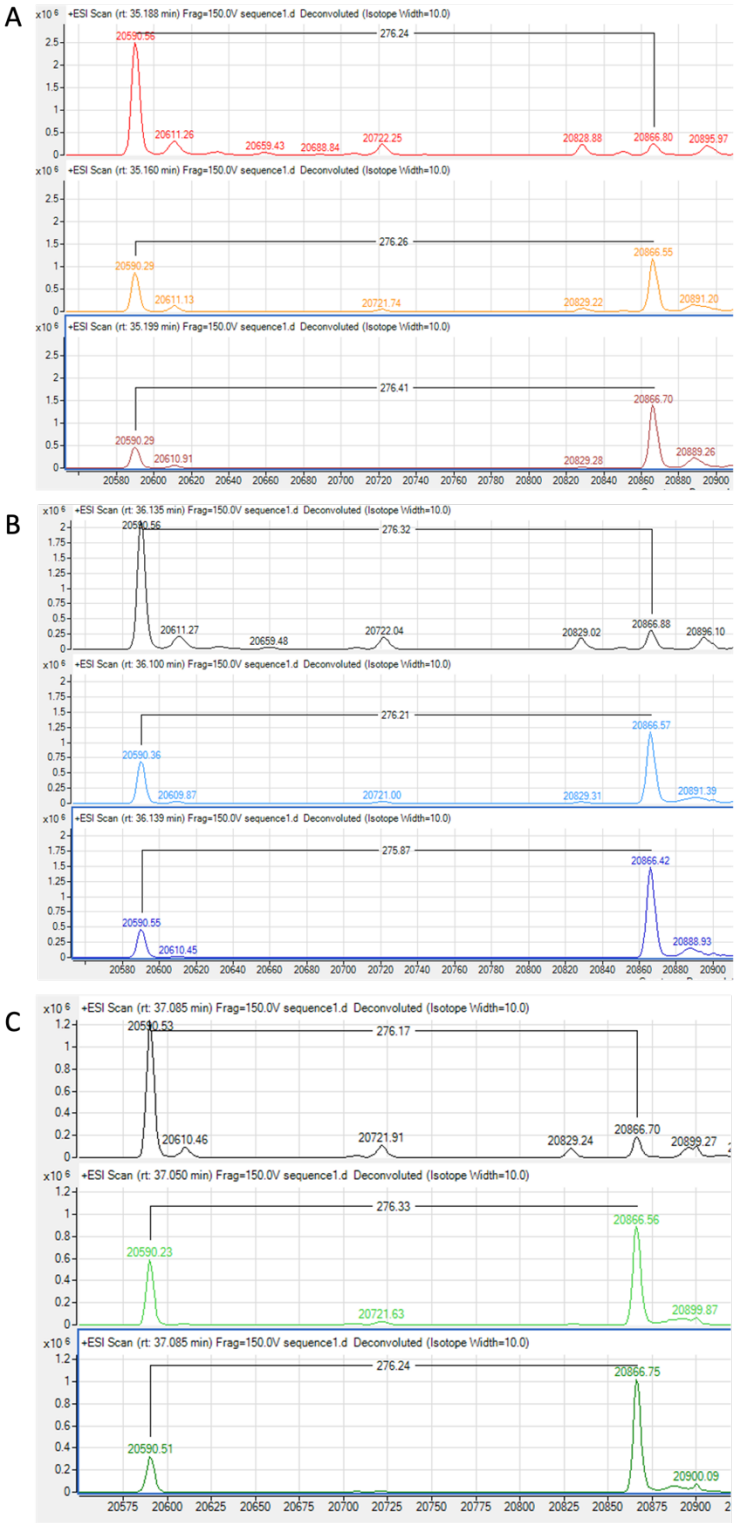


Figure 63: Incubation of RAB35 (2 µM) with fragment Z1151194523 at different concentrations and timepoints, graphs showing mass adduct formation (+276 g/mol). Representative shifts for n=3. A)100 µM IA at 0-3-6h. B) 300 µM IA at 0-3-6h. C) 600 µM IA at 0-3-6h.

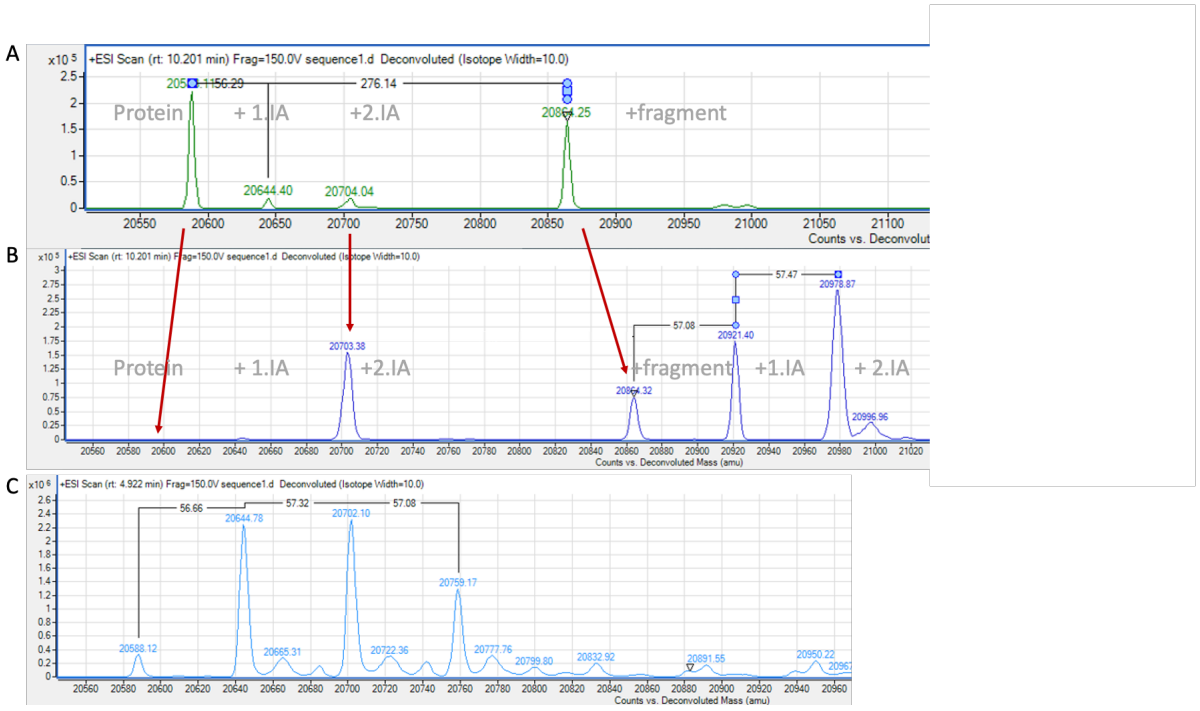


Figure 64: Competition experiment using fragment Z1151194523 and IA at 300 µM, timepoint measured after 6 h and 24 h, n=1. A) Competition after 6 h showing two IA and one fragment modification. B) Competition after 24 h showing consumption of pure protein and mixed species of fragment, fragment plus 1 -2 IA and protein with two IA modifications. C) IA at 300 µM alone measured after 24 h showing three mass shifts.

6.2.4 FASP protein digest for mapping of binding site

In order to determine the binding site(s) of the fragment, recombinant protein was reacted with fragment Z1151194523 and digested with trypsin before submission to MS. A sequence coverage of > 90% was achieved using trypsin and chymotrypsin. However, the results indicated modification of all three cysteines contained in RAB35 (Figure 65). As excess of the fragment would react with the recombinant protein during the digestion step, we loaded reacted samples onto a FASP filter and washed the sample using each 200 µL 8 M urea, 50 % ACN and 6 M urea. Nonetheless, there might have been residual fragment amounts which still reacted with the unfolded protein during the digestion step. An additional challenge was the proximity of C110 and C114 ($NC_{110}DDVC_{114}R$), which we

were not able to cleave with trypsin or chymotrypsin. Commonly, trypsin cleaves peptide bonds at the C-terminus of basic amino acids (K, R), whereas chymotrypsin attacks the C-terminal side of aromatic amino acids like (F, T, Y).

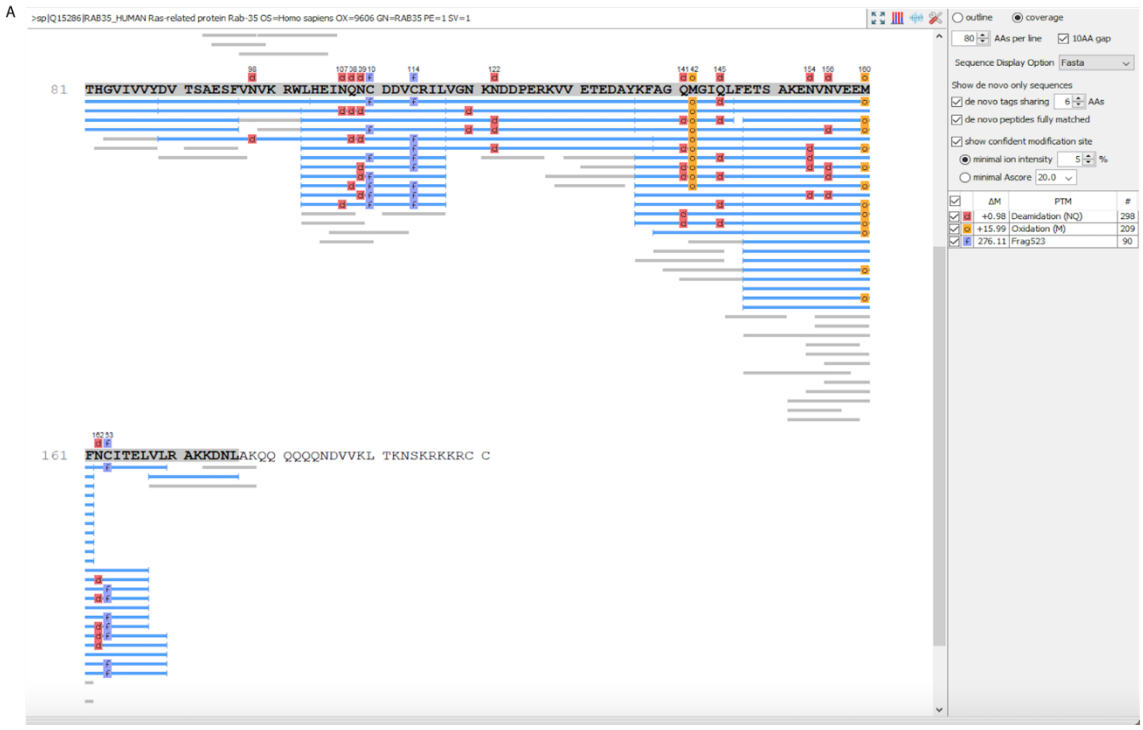


Figure 65: PEAKS software view of trypsin digest of RAB35. Sequence coverage of > 90 % was achieved, three cysteines are shown as modified by the fragment with the mass of modification of + 276.11 g/mol.

As there are two aspartic acid residues between the cysteines, GluC would be a suitable candidate. Endoproteinase GluC is known to cleave bonds at the C-terminus of either aspartic or glutamic acid residues [474]. Using GluC, we were able to separate both cysteines, however, we only quantified a peptide containing C_{114} in triplicates (Figure 66) but missed a peptide containing C_{110}. To circumvent the cleavage and to identify modified residues, the cysteines could be mutated, and the mutated protein could be subjected to labelling experiments. As an alternative to the FASP filter washing approach, the protein could be precipitated and washed with MeOH before being subjected to digestion.

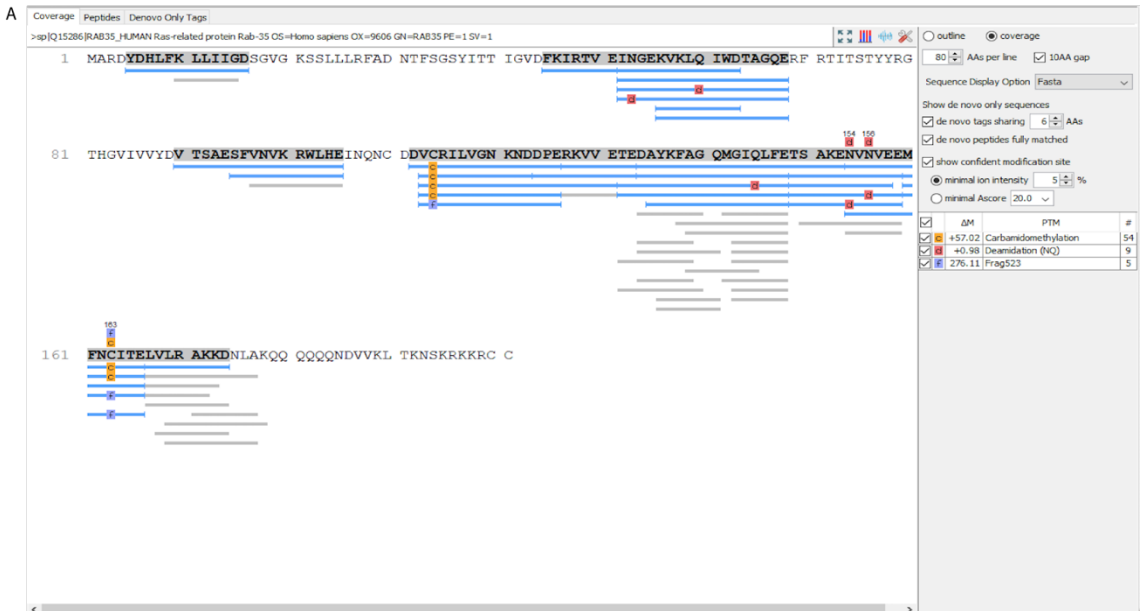


Figure 66: PEAKS software view of GluC digest of RAB35. Sequence coverage of > 50 % was reached, two cysteines are shown as modified by the fragment with the mass of modification of + 276.11 g/mol and one cysteine is missing as the containing peptide was not quantified.

6.2.5 GEF-activity assay

To evaluate whether the fragment Z1151194523 had an inhibitory effect on the PPI between DENND1A and RAB35, a GEF-activity assay was performed by Mia Callens. The assay was developed by Carmen Jimenez Antunes and takes advantage of the interplay of GEF and GTPase. In general, GTPases work as molecular switches that are active in the GTP-bound state and inactive in GDP-bound state. GEFs facilitate the exchange of GDP to GTP to re-activate the GTPase [475]. The assay measures exchange of GDP for GTP by the GTPase when bound to the GEF (Figure 67A). Without a competitive binder, the rate of exchange of GDP for GTP is fast. Alternatively, in presence of an inhibitory compound the exchange will be slower. The exchange can be measured via fluorescence of BODIPY-GTP. When the BODIPY-GTP is free, the GTP acts as a natural quencher of the BODIPY fluorescence. When the exchange of GDP for

the BODIPY-GTP occurs, the bound GTP part of the molecule can no longer quench the BODIPY, and therefore an increase fluorescence is observed. For the system DENND1A and RAB35, the compound tested at 500 μM top concentration in a dose-response study did not show inhibition (Figure 67B). The binding sites C110, C114 and C163 appear not to inhibit the interaction and activity of RAB35. These residues are distanced from switch 1 (around residues 30 - 40) and switch 2 (around residues 70 – 80) sites, which are near the GTP-nucleotide binding pocket [467].

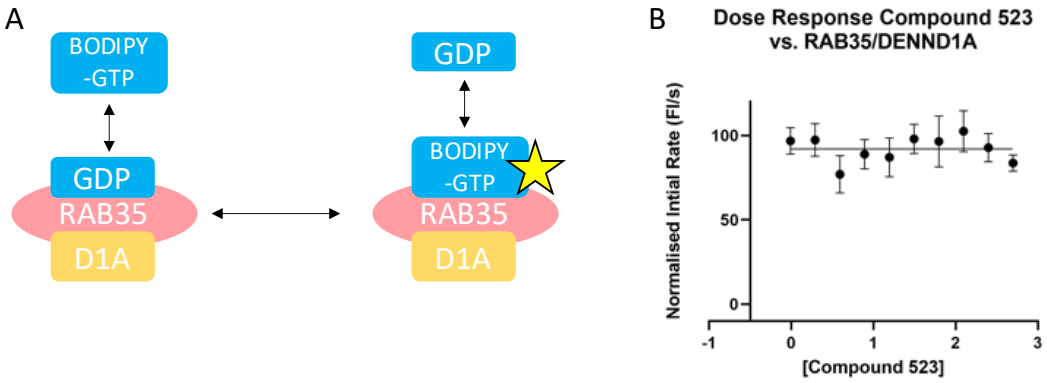


Figure 67: Principle of GEF-activity assay and results for DENND1A and RAB35. A) Schematic of GEF-activity assay, upon exchange of GDP to BODIPY-GTP fluorescence can be measured. Free BODIPY-GTP is quenched. B) The fragment Z1151194523 (compound 523) at 500 µM was showing no inhibition of the GEF activity. This experiment was conducted by Mia Callens (representative graph for n=3, error bars are depicted as mean ± SEM).

6.3 Summary and outlook

Interrupters of PPI interactions can provide a valuable means to expand the scope of druggable proteins. However, the identification of interrupters remains challenging, as the large PPI surfaces are mostly flat and lack pocket-like structures and cavities where traditional small molecule inhibitors would bind [456]. We aimed to identify fragment-sized interrupters of the DENND1A/RAB35 interaction. In GWAS in Han Chinese women, DENND1A had been identified as a candidate locus for PCOS [461]. The DENND1A gene was shown to encode two principal variants, V1 and short isoform V2. The latter was found to be overexpressed in ovarian theca cells of women with PCOS. Intriguingly, knockdown of V2 in those cells reduced excessive androgen production, and overexpression of V2 in healthy theca cells increased androgen synthesis showing a PCOS phenotype [462]. DENND1A was reported as a GEF, facilitating the conversion of RAB35 from its inactive (GDP-bound) to the active (GTP-bound) state, and it is involved in clathrin-coated vesicle trafficking allowing for the transport of active RAB35 to endosomes to control recycling of endosomal cargo [476]. DENND1A and DENND1B were demonstrated to function as GEFs for RAB35, activating it for its role in endosomes, and further studies of the DENND1 family have shown that the DENN-domain alone is sufficient for GEF activity [464, 476]. DENND1C has a kinetically much slower enzymatic activity towards RAB35 and was shown to link it to the actin cytoskeleton [477, 478]. Currently, there are no known inhibitors for DENND1A-C and RAB35.

Our NanoBRET PPI experiments in cells were conducted with full-length DENND1A-NL and short isoform DENND1A V2-NL against HT-RAB35. As momentarily there were no means to chemically inhibit the PPI, DMSO without ligand was used as an

analogue for a negative control to estimate the signal occurring for no interaction between donor and acceptor. Efforts to clone mutated versions of mayor contributors of the PPI on DENND1A, such as Y238, were unsuccessful. We propose the design of more primers and a further optimisation of cloning conditions. As a positive control, DMSO with HT-ligand was used to indicate highest NanoBRET signal. However, the assay overall suffered from variability. In the single shot experiments, the transfection efficiency affected the maximal NanoBRET signal and on average values ranged between 5 – 8 mBU. This signal was rather low in our experience. Generally, transient transfection might lead to high expression of liganded proteins which in turn boosts non-specific interactions and can lead to a low signal-to-noise ratio. Establishing a stable cell line would mitigate inter-assay variability, as demonstrated by Gnatzy et al for an ETP-based NanoBRET assay [479]. A system based on gateway cloning and flpIN cell lines was reported to generate stable cell lines for NanoBRET assays of GPCRs and arrestin proteins and achieved homogenous protein expression and low inter-assay variation [480].

Throughout the dose-response experiments, the fragments showed inter-assay variation and only limited inhibitory effects. A detailed illustration of the curve variation was shown in Figure 59 for six fragments. An additional factor contributing to the variation could have been the fragments themselves. As electrophilic fragments are prone to hydrolysis, preparing fresh DMSO stocks from solids would ensure fragment stability. We hypothesise that each opening of the source plate allowed water to dilute the DMSO stocks and influenced fragment stability which subsequently affected derived NanoBRET signal. The plate survey files of the ECHO liquid handler (BMG Labtech) showed varying DMSO percentage of 70 – 90 %. The fragments were showing cytotoxicity at highest concentrations, especially in the screen with DENND1A V2 and BRD9 BD the loss in

cell viability corresponded to increase in BRET signal. We hypothesise, similarly as discussed in chapter 5, that this increased BRET signal could stem from pre-apoptotic stress and over-expression of tagged proteins. In this assay, the increase might also be explained by activators of the PPI.

The fragment library consisted of cysteine-reactive fragments with a MW < 300 g/mol, such as enones, chloroketones, or sulfonylfluorides, with varying promiscuity and reactivity. These reactive fragments might not only bind DENND1A or RAB35 but also upstream effectors, influencing the readout of assay. For example, AKT-dependent phosphorylation of S536 and S538 is thought to disrupt auto-inhibition of DENND1A, allowing for enhanced interaction with RAB35 and increased GEF activity [481]. Thus, fragments affecting AKT-dependent phosphorylation could likely exert an effect in the assay as well. Additionally, there are multiple cysteines in the sequence of both RAB35 and DENND1A which could potentially react with electrophiles, while on RAB35 C110 and C114 were close to the PPI surface. Nonetheless, the hit compounds achieved around 30 % inhibition and can serve as a foundation for future SAR studies and refinement of the compound structure. These fragments could be enlarged by evaluation in docking studies and a newly selected fragment library could be further tested against recombinant protein. As discussed earlier, the PPI interface of DENND1A/RAB35 has a rather difficult topology. To interrupt this interaction, larger molecules than fragments (MW < 300 g/mol) might be more sufficient. Durrant et al. presented a high-throughput NanoBRET PPI assay aiming to screen for disruptors of RAS signalling [482]. They screened synthetic compounds, targeted inhibitors, and natural products and found a majority of inhibitor hits identified in the assay were natural products with higher molecular mass on average, such as ophiobiolin A (MW > 400 g/mol), which alters KRAS

nanoclustering [483]. Ran et al. reviewed 66 reported PPI inhibitors and reported that the average molecular weight was mostly greater than 500 Da [484], while a large proportion of those inhibitors were peptide-based. These peptides have the advantage of similarity to endogenous ligands and can achieve high affinity combined with low toxicity, yet they were shown suffer from both poor membrane-permeability and oral bioavailability [485]. The conventional method of designing peptide-based inhibitors the introduction of tailored oligopeptides which are modified based on important residues in the PPI interface of interest to disrupt protein binding [486]. Another promising class of PPI interrupters are macrocycles, in addition to their size they have the ability to adopt disc-like conformations which allows them to interact with targets with large, flat binding sites that lack well-defined pockets [487]. Recently, a natural-product derived macrocyclic lead was optimised to yield potent interrupters of productive KEAP1-Nrf2 interaction [488].

As the DENND1A recombinant protein is difficult to purify, we chose to evaluate the fragments in the cell-based assay first. The six fragments derived as preliminary hits from the NanoBRET PPI assay were evaluated against recombinant RAB35 and DENND1A (DENN-domain only) in intact MS. Initially, enone-containing fragment Z1151194523 was showing one corresponding mass-shift on RAB35, samples were incubated in a 96-well plate while standing with 100, 300 and 600 μM of the fragment and measured at several timepoints. Subsequent experiments at 25 °C in Eppendorf tubes in a shaking incubator using 20 μM of the fragment showed two corresponding mass-shifts on RAB35 and also reactivity of the fragment with RAB39B. This result indicated that the fragment was likely non-selective and further screenings with analogue compounds would be required to achieve selectivity. The intact MS results are similar to recent reports of a covalent USP8 inhibitor (30, chloroketone warhead) by Lang et al.; the study reports that

the compound is promiscuous and unselective, supported by the observation of varying numbers of mass adducts and the authors conclude this indicates that the compound binding mainly depends on the reactivity of the warhead rather than non-covalent interactions for binding to the target C residue [489].

A tryptic digest showed > 90 % sequence coverage for RAB35 as well as labelling of all three cysteines with Z1151194523. Efforts to map the binding site were unsuccessful, as C110 and C114 were located too close to each other and an attempt to cleave the peptide at a D residue with GluC, yielded C114 but no peptide containing C110 could be quantified. As the collected results were not clearly indicating one isolated binding site, further digest experiments aiming to map Z1151194523 are remitted. Additionally, the fragment was not showing inhibition in an GEF-activity assay.

In the future, we aim to optimise the NanoBRET assay by introducing a suitable negative control, e.g. in form of a mutant DENND1A interrupting the interaction of donor and acceptor in the future. The introduction of a stable cell line would also help to reduce variation and a screening using larger molecules, such as peptide-based inhibitors or macrocycles may promise greater chances of PPI interruption. As covalent binders have so far only been reported in NanoBRET TE assays [471, 472], the establishment of a NanoBRET PPI assay for investigation of covalent inhibitors would be a valuable addition and contribution to the development of covalent PPI interrupters.

7. Closing Remarks

This work aimed to employ and further develop chemoproteomic and non-chemoproteomic methods with focus on profiling of small molecules and covalent fragments on a proteome-wide scale. High attrition rates in clinical trials encouraged researchers to the development of the five R and four pillar framework, highlighting the importance of re-focussing on investigating the target engagement of compounds *in cellulo* in early stages of drug discovery to provide safe and efficacious drugs [13, 14]. For this, phenotypic-screens have historically been useful means to identify compounds with a pharmacologically relevant effect [15]. Chemoproteomic pulldowns have been utilised to elucidate compound targets and off-targets for failed clinical candidates [21]. Chemical probes have been developed to facilitate the functional annotation of the over 20000 proteins in the human proteome. Novel guidelines focus on covalent chemical probes [70], as they potentially expand the druggable space towards proteins which lack classical binding pockets for small molecule inhibitors. Covalent compounds or fragments have the ability of binding to shallow crevices, additionally, they have a prolonged residence time, and they can be fine-tuned in their selectivity. In combination with ABPP workflows, they have been proven successful to target novel sites and proteins, especially in the space of E3 ligases [285].

Chapter 2 provided a basis for the investigation of E3 ligase ligandability in human cancer cell lines. A bioinformatic analysis of a transcriptomic and proteomic dataset provided a selection of four cell lines K562, NCIH226, DU145, and U251 covering a maximal number of 267 E3 ligases in a total proteome experiment. Similarly to the kinobeads approach [111], we aimed to provide a large number of E3 ligases for screening against a

selected library of eight electrophilic, reactive probes to survey covalent modifications on novel E3 ligases. A set of lipophilic competitors was selected to distinguish sites modified by sheer reactivity from sites which require lipophilic interactions and binding events beforehand in order to create a E3 ligase-focussed druggability map. We investigated probe labelling and reactivity to set conditions for our MS-based experiments as 100 μM and 1 h incubation in lysates.

In chapter 3 the focus was on the establishment and optimisation of the isoTOP ABPP workflow for profiling the ligandability of E3 ligases with respect to modified amino acid sonication conditions, tryptic on-bead digestion, MS instrument type, and solvent gradients and benchmarked our data in MDAMB231 in line with current literature [295]. An initial non-competitive, enrichment-focussed screen of the library of eight reactive probes in the cell lines yielded over 30000 modified sites within the proteome on C, K, M, S, T, Y, R, D, and E amino acid residues. A comparison to the recently published CysDB, we found an overlap of > 99 % and around 500 sites which were not previously reported [320]. among them a total number 132 E3 ligases. Our E3 ligase druggability map derived from competitive screenings showed interesting sites on 150 E3 ligases, whereby 38 sites were competed with R > 4, providing an information source for development of starting points for E3 ligase inhibitor or recruiter development. Especially SOCS2_C111 was an interesting site as statistical analysis including AF models and machine learning algorithms (p2rank) revealed this site as located in a pocket. SOCS2 electrophilic ligands have been reported by other groups recently, underscoring the tractability of this site for E3 ligase recruiter development [266]. Furthermore, we investigated the efficiency of reactive probe labelling in cells and lysates in addition to distinct MS data acquisition modes.

Complementary to previous reports of screenings using covalent fragments or natural products [267, 284], we described in chapter 4 how a set of novel chemical probes was screened employing the isoTOP ABPP platform. A covalent chemical probe for KEAP1, S213726, was reported to bind to C151, which we could not directly compete with iodoacetamide-alkyne and the isoDTB-tag in our experimental setup. However, we reported no related off-targets for the probe on a proteome-wide scale. PCIF1, a methyl transferase was competed with R > 4 and should be further validated as a potential unrelated off-target. The DBIA-probe was shown to ligand this site in HCT116 cells, thus providing an opportunity to further test the DBIA-probe in MDAMB231 cell line [132]. Additionally, NU074516a, a chemical probe for NUDT7 was screened and we could show direct labelling of C72 residue for the first time in isoTOP ABPP using a vinylsulfone-alkyne reactive probe [157]. Covalent fragments which were selected through a phenotypic screen as inhibitors of the NLRP3 inflammasome were investigated using isoTOP ABPP in live BMDM cells, however we hypothesise the fragment concentration or incubation time might have been too low to determine an effect. Furthermore, orthogonal validation methods such as CETSA, FRAP and intact MS methods were used to validate fragment hits derived from the competitive isoTOP screening described in chapter 3. Likely due to the promiscuity and too low concentrations of the competitors, the cell-based experiments yielded inconclusive results. Screenings with a selection of optimised fragment analogues to identify more selective binders are a suitable continuation of this work. The cellular assay concentrations should be selected carefully, to avoid cytotoxic effects of the cysteine-reactive fragments [384].

We report the development and optimisation of a first-in-class NanoBRET target engagement assay for methyl transferase PRMT5 in chapter 5. Based on a very potent energy transfer probe CBH-002 (K_d in 13 nm range) we show the evaluation of both SAM- and substrate-competitive PRMT5 inhibitors in our assay using NL-PRMT5. Interestingly, we were able to show the effect of co-factor SAM on compound binding in lysates: SAM increased the potency of substrate-pocket binding compounds related to GSK3326595 but decreased potency for LLY-283, which is binding in the SAM pocket. Reports of inhibitors targeting PRMT5/MTA complex encourage us to test these compounds in the assay to evaluate observable effects [410]. Additionally, we showed the exquisite selectivity of clinical compound GSK3326595 in both compound-centric pulldown and thermal profiling.

As covalent fragments can bind more shallow surfaces and crevices, we investigated a 1500-membered covalent fragment library as potential interrupters of PPI-interactions in chapter 6. For the first time, we reported a NanoBRET protein-protein interaction assay for the evaluation of covalent fragment-sized interrupters of the DENND1A/RAB35 interaction. Both proteins possess nucleophilic amino acid sidechains in their PPI area. Preliminary hits derived from the cell-based assay could potentially address either DENND1A or RAB35. Thus, the fragments were subsequently tested against recombinant protein in intact MS to validate binding. However, the fragments were shown to be promiscuous and rather unselective in intact MS, and mapping of the binding sites on RAB35 were unsuccessful. Nonetheless, the hits derived from the NanoBRET PPI assay can serve as leads for further optimisation, especially when they are enlarged in size. Higher molecular weight compounds, such as macrocycles, might also be suitable candidates for future screenings to interrupt DENND1A/RAB35 interaction [487].

8. Methods

Please note, for the readers convenience, materials and methods are listed for each chapter separately.

Chapter 2

Data sources

A list of currently annotated NCI cancer cell lines was downloaded from the National cancer institute website https://dtp.cancer.gov/discovery_development/nci-60/default.htm on 22.11.2019. The proteomic dataset was downloaded from the TUM website https://www.ls.tum.de/ls/startseite/ on 22.11.2019 by not inserting any protein name and starting the search with an empty field. The box proteome profile was ticked resulting in 8.079 proteins to download. In the file the protein IP name was removed as it was unnecessary, only the gene names were kept. The transcriptomic dataset was downloaded from the CCLE website on 22.11.2019, file: CCLE_RNAseq _rsem_genes_tpm_20180929.txt.gz. All files were converted to contain only NCI60 cell lines and used in .txt. or .xlsx format.

Bioinformatic analysis of proteomic and transcriptomic dataset

This R code is a tool to analyse transcriptomic and proteomic datasets and filter for contained E3 ligases. The intersection of a list of 635 E3 ligases with a list of gene names (HGNC symbols) can be found and can be displayed as Venn diagrams or tables of gene names. R version 3.1.2 was used for this analysis (https://posit.co/products/open-source/rstudio/).

Required Packages: First, BiocManager needs to be installed. BiocManager allows to install and update packages contained in the Bioconductor project. Bioconductor provides tools for the analysis and comprehension of high-throughput genomic data open source and open development. The Bioconductor 3.10 release contains 1823 software packages, such as biomaRt. This package can annotate a wide range of gene identifiers (e.g. ENSG IDs) from databases like Ensembl or

Uniprot with information such as the gene name or HGNC symbol. The expression `::install` allows to install the most recent version of this package and is the recommended way for installation.[490, 491]

```
if (!requireNamespace("BiocManager", quietly = TRUE))
install.packages("BiocManager")
BiocManager::install("biomaRt")
```

For the subsequent analysis the following packages are needed.

```
library(biomaRt)
library(dplyr)
library(stringr)
library(tidyr)
```

biomaRtballows retrieval of data from databases such as Ensembl. dplyr is a tool for data analysis and manipulation of data frames. stringr can be used to manipulate characters or remove whitespace. tidyr allows for changing the shape (pivoting) of a dataset or extracting values from it. The latter three packages are contained in CRAN, which is part of base R and they are also part of the tidyverse.[492]

Uploading Datasets: For the analysis of E3 ligases a list of these ligases is required as input. In this thesis, a list of 635 E3 ligases was used as input in .txt file format derived from the Ubihub website[20] [207]. The following expression reads a file in table format and creates a dataframe from it.

```
`E3-all` <- read.table("//Users//mira//Desktop//CCLE
RNASeq_rsem//E3.txt", stringsAsFactors=FALSE)
```

Next, a chosen dataset can be uploaded. This dataset from the CCLE website contains 1019 cell lines and their contained genes described by ENSG ID´s with version numbers

[20] Filter for confidence “show all” was applied: Indicates the confidence level that a protein is involved in the ubiquitin proteasome system. "degrad" found in Uniprot function: 1 point. "degrad" found in Reactome pathway(s): 1 point. "degrad" found in a Reactome pathway enriched among biogrid interactors [pathway must be found in at least 3 interactors and enriched at least 3-fold compared with proteome]: 1 point

e.g. ENSG00000000419.8. These ID´s need to be converted into HGNC symbols. Since only the gene name is of interest, the version number will be removed later.

```
`CCLE_RSEM_raw` <- read.delim("//Users//mira//Desktop//CCLE
RNASeq_rsem//100120 CCLE_RNAseq_rsem_genes_tpm_20180929.txt",
stringsAsFactors=FALSE)
```

Query of Ensembl database and creation of gene names: BioMart is used to query a suitable database. For ENSG ID´s the Ensembl database is suitable. To view all available databases first get a list. From this list, choose `ensembl` to connect to this specific database. In Ensembl, every species has it´s own dataset, here the Homo sapiens dataset is of interest and therefore is selected. Attributes display values which can be retrieved, such as `ensembl_gene_id` or `ensembl_gene_id_version`. Next, a BioMart query is created, resulting in a gene map connecting ENSG ID´s to HGNC symbols. The gene map is used to map ENSG ID´s to gene names or HGNC symbols to find the intersection between the E3 list and the transcriptomic dataset.

```
listMarts()
ensembl <- useMart('ensembl')
listDatasets(ensembl)
ensembl <- useDataset("hsapiens_gene_ensembl", mart=ensembl)
listAttributes(ensembl)
geneMap4 <- getBM(attributes = c('ensembl_gene_id', 'hgnc_symbol'),
mart=ensembl)
write.table(`geneMap4`, "geneMap4.txt", sep="\t")
```

Removal of version numbers from ENSG ID: For this analysis, the gene name or HGNC symbol is of interest. The structure or sequence can be neglected and therefore the version number of the ENSG ID e.g. ENSG00000000419.8 can be removed to identify the corresponding gene name. To create a new table from the raw transcriptomic dataset the ENSG ID´s in the column gene_id is manipulated with a regular expression to replace “.” and any subsequent characters from the ENSG ID version number. The result is saved as a table, now the transcriptomic dataset is ready for mapping.

```
`CCLE_RSEM_ALL_ENSG_raw` <- `CCLE_RSEM_raw` %>% mutate(gene_id =
str_replace(gene_id,"\\..*$",""))
write.table(`CCLE_RSEM_ALL_ENSG_raw`, "CCLE_RSEM_ALL_ENSG_raw.txt",
sep="\t")
```

Mapping ENSG ID to gene names: The previously created gene map can be used to map the modified ENSG ID´s to HGNC symbols. Therefore a dplyr function, the `left_join` is used to map the columns gene_id to ensembl_gene_id from the tables. All ensembl_gene_id´s from the gene map are matched to the modified ENSG ID´s. If there is no match in the transcriptomic dataset, then NULL (N/A) will be returned. Not all ENSG ID´s will find a match since some of them might be outdated, such as pseudogenes. The table was saved.

```
`CCLE_RSEM_ALL_mapped_raw` <- left_join(`CCLE_RSEM_ALL_ENSG_raw`,
geneMap4, by = c("gene_id" = "ensembl_gene_id"))
write.table(`CCLE_RSEM_ALL_mapped_raw`, "CCLE_RSEM_ALL_mapped.txt",
sep="\t")
```

Intersection with E3 ligase list: To find the E3 ligases which are contained in the transcriptomic dataset, the intersection needs to be identified. Therefore an `inner_join` is used. This join creates a new table displaying a combination of both tables based on the join-predicate which is the gene name here. Save the result as a table.

```
`CCLE_RSEM_ALL_E3_raw` <- inner_join(`CCLE_RSEM_ALL_mapped_raw`, `E3-
all`, by = c("hgnc_symbol" = "V1"))
write.table(`CCLE_RSEM_ALL_E3_raw`, "CCLE_RSEM_ALL_E3_raw.txt",
sep="\t")
```

Visualisation as Venn Diagrams: From the transcriptomic dataset four cell lines were identified previously as the best producers for the maximum number of E3 ligases. These four cell lines can be presented overlapping and a list of all contained E3 ligases can be created. By joining the four cell lines together in a Venn diagram, shared E3 ligases as well as unique E3 ligases can be depicted. First, the prepared table containing only E3 ligases from the transcriptomic dataset was uploaded and only the column hgnc_symbol was displayed.

```
library(readxl)
CCLE_RSEM_ALL_E3_raw <- read_excel("//Users//mira//Desktop//CCLE
RNASeq_rsem//CCLE_RSEM_ALL_E3_raw.xlsx")
View(CCLE_RSEM_ALL_E3_raw)
```

```
CCLE_RSEM_ALL_E3_raw$`hgnc_symbol`
install.packages("dplyr")
library(dplyr)
```

Next, each cell line (SR786, OVCAR3, NCIH522, MALME3M) was filtered from the whole dataset where the value for the E3 ligase in the table is higher than a determined value. Here, the 10th percentile was chosen as a cutoff to determine whether a E3 ligase is assumed to be expressed or present in the lysate. The result was saved as a list of genes by displaying only the HGNC symbol. Repeat analysis for each cell line.

```
SR786 <- CCLE_RSEM_ALL_E3_raw %>%
filter(SR786_HAEMATOPOIETIC_AND_LYMPHOID_TISSUE >= 0.02)
SR786_genes <- SR786$`hgnc_symbol`

OVCAR3 <- CCLE_RSEM_ALL_E3_raw %>% filter(NIHOVCAR3_OVARY >= 0.02)
OVCAR3_genes <- OVCAR3$`hgnc_symbol`

NCIH522 <- CCLE_RSEM_ALL_E3_raw  %>% filter(NCIH522_LUNG >= 0.02)
NCIH522_genes <- NCIH522$`hgnc_symbol`

MALME3M <- CCLE_RSEM_ALL_E3_raw %>% filter(MALME3M_SKIN >= 0.02)
MALME3M_genes <- MALME3M$`hgnc_symbol`
```

Finally, the results can be depicted in a Venn diagram. First, the package needs to be installed and loaded. A diagram is created by overlapping the identified genes from each cell line and combining them according to their distribution.

```
install.packages("VennDiagram")

library(VennDiagram)

venn.diagram(list("SR786"  =  SR786_genes,  "OVCAR3"  =  OVCAR3_genes,

"NCIH522" = NCIH522_genes, "MALME3M" = MALME3M_genes), "CCL
```

Kinaseblender

The tool Kinaseblender was downloaded from Github (https://github.com/ThomasKuehne/kinaseblender). Proteomic datasets were set to contain raw values if an intensity was > 1, and 0 if there was no intensity reported. In the first rounds of

analysis, the input file was analysed in Kinaseblender to give most unique products (Unique count view). M14, UO31 and UACC62 were listed in the best cell lines but due to difficult culturing methods and non availability these cell lines were eliminated from the cell line panel. As a second result there were two combinations of four best cell line combinations: PC3, KM12, SF268, SKMEL5 and K562, DU145, U251, NCIH226 . The latter combination was favoured due to handling and culturing conditions containing 127 E3 ligases. This set was taken on into experiments. For the transcriptomic dataset, ENSG IDs were translated into gene names using an R script described above. As a cut-off the 10% percentile was chosen for reported values, which equals 0.02. All values in the CCLE dataset > 0.02 remained unchanged, whereas values <0.02 were set to 0. Subsequently, the dataset was put into the kinaseblender (Unique count view). A first run gave as the best 4 cell lines with 614 E3 ligases in view Unique count NIHOVCAR, MALME3M, MDAMB468, NCIH522. Further investigations into those cell lines led to the decision to eliminate MDAMB468 due to difficult culturing methods and media. The sheet Table 1 was modified and MDAMB468 was cut out. As a result, the kinaseblender gave a combination of four best cell lines containing 96.38% (612) E3 ligases NIHOVCAR3, MALME3M, SR786, NCIH522.

Tissue culture

Cells were obtained from ATCC or Sigma and grow in medium supplied by Thermo Fisher as shown in the table below. Cells were harvested at 80-90 % confluency and stored at -80 °C before lysate preparation.

Cell line	Medium
K562 (ATCC, CCL-243)	RPMI + 10 % FBS
DU145 (ATCC, HTB-81)	EMEM + 10 % FBS
U251 (Sigma, 09063001-1VL)	EMEM + 10 % FBS + 5 % NEAA
NCIH226 (ATCC, CRL-5826)	RPMI + 10 % FBS

Total cell lysate

To obtain lysate, the cells were harvested at 80-90 % confluency from 5× T175 flasks (Greiner) and subsequently pelleted and washed with DPBS. The obtained pellets were then lysed by addition of 3× pellet volume of lysis buffer (50 mM Tris pH 7.5, 0.8 % v/v NP-40, 5 % v/v glycerol, 1.5 mM $MgCl_2$, 100 mM NaCl, 25 mM NaF, 1 mM Na_3VO_4, 1 mM PMSF, 1 mM DTT, 10 µg/mL TLCK, 1 µg/mL Leupeptin, 1 µg/mL Aprotinin, 1 µg/mL soybean trypsin) on ice, before being pushed gently 10× through a 21G needle (Braun) using a 1 mL syringe (Braun, InjectF). The lysates were allowed to incubate on ice for 10 min before being ultracentrifuged at 17000 ×G at 4 °C for 30 min. Next, total protein concentration was adjusted to 10 mg/mL and the lysates were stored for further use at -80 °C. In brief, the DC protein assay kit (Bio-Rad, 500011) was used to determine protein concentration. For this a calibration curve of four 1:2 dilutions of 2 mg/mL BSA standard (Thermo Fisher, 23210) was prepared and sample dilutions in 1:20, 1:20 1:30 and 1:40 dilutions in lysis buffer. In a 96-well plate (Greiner, 655061), 5 μL of each sample were plated in triplicate before adding 25 μL of freshly prepared reagent A' (1 mL A and 20 μL reagent 5) and 200 μL reagent B. After 10 min incubation at RT, the absorption was measured using the PheraSTAR FSX.

In solution digestion

For the in-solution digest, 100 μg of protein (10 μL sample) were mixed with 190 μL 0.1M TRIS in 1.5 mL Eppendorf tubes. 5 μL of DTT (final concentration 5 mM) were added and the sample and incubated at 10 rpm for 60 min at RT on the rotating wheel. Then, 20 μL of alkylating reagent IA (final concentration 20 mM) was added and the sample and incubated for 30 min in the dark. To precipitate the proteins, 600 μL MeOH and 150 μL chloroform were added and samples were vortexed before addition of 450 μL water and vortexing again. The samples were centrifuged at 17000 ×G for 5min. A precipitate formed at the interface between aqueous and organic phase.

The upper aqueous phase was removed before adding 450 μL MeOH and vortexing to resuspend the pellet. The sample was centrifuged at 17000 ×G for 1min before carefully removing the supernatant. The protein pellet was resuspended in 50 μL 6M urea buffer to denature and unfold the proteins and briefly sonicated. Then, the urea concentration was reduced to > 1M by adding 250 μL MQ water. Trypsin (Promega, V5111)was added (1:50, 2 μg) and the sample digested ON the shaking incubator at 37 degrees and 450 rpm.

SEP-PAK C18 Purification

300 μL sample were acidified with formic acid 0.1 %. Sola SPE cartridges (Thermo Fisher, 60109-002) were placed on top of a vacuum and columns were equilibrated with 0.5mL solution B (65 % ACN, 35 % water, 0.1 % FA). Then the column was washed with 1 mL solution A (98 % water, 2 % ACN, 0.1 % FA) before loading 300 μL sample by dropping it directly on the column bed. Then the wash with solution A was repeated. The elution was done with 0.6 mL solution B into 2 mL LoBind Eppendorf tubes by pushing through with a pipette tip and creating a pressure with air. The sample was evaporated in a SpeedVac concentrator ON and stored at -20 °C.

Off-line high-pH reverse-phase prefractionation

Off-line high-pH reverse-phase prefractionation was performed on 100 µg of digested material using the loading pump of a Dionex Ultimate 3000 HPLC with an automated fraction collector and a XBridge BEH C18 XP column (3 × 150 mm, 2.5 µm pore size, Waters no. 186006710) over a 100 min gradient using basic pH reverse-phase buffers (A: water, pH 10 with ammonium hydroxide; B: 90% acetonitrile, pH 10 with ammonium hydroxide). The gradient consisted of a 12 min wash with 1% B, then increasing to 35% B over 60 min, with a further increase to 95% B in 8 min, followed by a 10 min wash at 95% B and a 10 min re-equilibration at 1% B, all at a flow rate of 200 µL/min with fractions collected every 2 min throughout the run. Concatenations of 50

samples were done consecutively, for example 1, 11 ,21 ,31 , 41 were combined and fractions were dried in a SpeedVac concentrator ON.

MS analysis LUMOS

Samples were resuspended in 20 µL of 2 % acetonitrile and 0.1 % formic acid for analysis by LC–MS/MS using Ultimate 3000 UHPLC (ThermoFisher Scientific) connected to an Orbitrap Fusion Lumos Tribrid (ThermoFisher Scientific). Briefly, peptides were loaded onto a trap column (PepMapC18; 300 μm x 5 mm, 5 μm particle size, Thermo Fischer) and separated on a 50 cm EasySpray column (ES803, Thermo Fischer) with a gradient of 2-35 % acetonitrile in 5 % dimethyl sulfoxide, 0.1 % formic acid at 250 nl/min flow rate over 60 min. Eluted peptides were then analysed on an Orbitrap Fusion Lumos Tribrid platform (instrument control software v3.3). Data were acquired in data-dependent mode, with the advance peak detection (APD) enabled. Survey scans were acquired in the Orbitrap at 120 k resolution over a m/z range 400-1500, AGC target of $4e^5$ and S-lens RF of 30. Fragment ion spectra (MS/MS) were obtained in the Ion trap (rapid scan mode) with a Quad isolation window of 1.6, 40 % AGC target and a maximum injection time of 35 ms, with HCD activation and 28 % collision energy.

In-gel fluorescence

100 μL of 1 mg/ml lysate incubated at RT for 1 h with 1-25 μM final concentration of IAA-alkyne DMSO stock or DMSO control. A click-mix consisting of 100 μM Cy5.5 azide (B4030, Lumiprobe), 1mM $CuSO_4$, 1mM TCEP, 100 μM TBTA in a ratio of 1:2:2:1 was added to the samples to introduce the fluorophore. The samples were incubated 1 h at RT at 10 rpm on a rotating wheel. Followingly, the reaction was quenched by adding a final concentration of 5 mM EDTA. To precipitate the proteins, 300 µL MeOH and 50 µL Chloroform were added to each vial and after vortexing 250 µL MilliQ-water were added. After centrifugation at 14.8 RPM for 5 min at RT, the upper phase was gently pipetted off without touching the precipitate at the interface.

Next, 300 µL of MeOH was added, and the upper phase was pipetted off gently again. This was repeated once and then the samples were centrifuged at top speed. The supernatant was removed and after re-suspension in 2 % SDS in PBS, the sample was boiled at 95 °C for 5 min with 4x SLB (1:4). For SDS-PAGE, 1 μL Precision Plus Protein All Blue (Biorad) ladder and 10 μL sample was loaded per lane. 4–12% Criterion™ XT Bis-Tris Protein Gel (Biorad) ran at 170 V for 55 min in 1× MES buffer. Bands were visualised using the Odyssee imager (Licor).

Chapter 3

Tissue culture and cell lysis conditions

Cells were obtained from ATCC or Sigma and grow in medium supplied by Thermo Fisher as shown in the table below. Cells were harvested at 80 - 90 % confluency and stored at -80 °C before lysate preparation. The pellet volume was mixed with x3 volume of PBS (1:1000 Benzonase) and incubated on ice for 10 min. For the lysis, a 2 mm sonication probe was set to 20 % amplitude and the sonication duration was 5 sec on and 5 sec off for 40 sec in total, on ice. After lysis, the lysates rested on ice for 30min before centrifugation at 17000 ×G for 30min. Subsequently, the lysate concentrations were measured using the DC assay (Bio-Rad), by mixing 5 μL of sample with 25 μL solvent A' (made freshly from 1mL reagent A and 20 μL reagent S) and adding 200 μL of reagent B, followed by measuring absorption at 650-750 nm with the PheraSTAR plate reader. Lysates were adjusted to 1 mg/mL.

IsoDTB workflow

For the isoDTB ABPP workflow, 2000 μL of 1 mg/ml lysate for both heavy (H)- and light (L)-tag sample or for competition the sample was split in 2 x 1 mL to add either competitor (L) or DMSO (H). The samples incubated at RT for 1 h at 10 rpm on a rotating wheel. Next, 40 μL of 5 mM IAA-alkyne DMSO stock (or other probe stocks, oxaziridine probe 6 in DMF) were added. For competition experiments, 20 μL of 5mM stock were used per each H/L sample. The samples

were incubated 1 h at RT at 10rpm on a rotating wheel. Followingly, a click reaction with L or H isoDTB tag was done, using 120 μL of a master mix consisting of 60 μL TBTA (0.9 mg/mL in DMSO/tBuOH 1:4), 20 μL $CuSO_4$ (12.5 mg/mL in water), 20 μL isoDTB tag (5 mM in DMSO) and 20 μL TCEP (freshly made as 13 mg/mL solution in water). The samples incubated at RT for 1 h at 10rpm on a rotating wheel. Next, H/L samples were combined into 8 mL cold acetone, vortexed, and stored at –20 °C ON. Next, the pellet was centrifuged in a swivel rotor centrifuge (3,500 ×G, 5min), followed by removal of the supernatant. 1000 μL of methanol were added, the sample was resuspended by sonication with a 2 mm probe (20 sec, 20%). The samples were centrifuged again (3,500 ×G, 5 min), and the supernatant was removed before the samples were allowed to dry. 300 μL of an 8 M urea in 0.1 M TEAB were added, followed by sonication (20s, 25%) and addition of 900 μL of an 0.1 M TEAB to dilute the urea.

Per sample, 50 μL streptavidin high capacity agarose beads (Pierce) were washed with each 3× 0.2 % NP40 in PBS, PBS and water. Between the washes, the beads were centrifuged at 0.8 ×G for 3 min. The beads were equally distributed as 50 μL per 5 mL Eppendorf tube. Now, the samples were each added (1200 μL) into the 5mL Eppendorf tube, incubated for 1 h at RT while rotating at 10 rpm on a spinning wheel. The tubes were centrifuged at 1000 ×G for 15 sec before aspiration of the supernatant. The beads were transferred to Biospin columns using 600 μL of a 0.1 % NP40 solution in PBS. To remove the supernatant, the columns were placed in 2 mL Eppendorf tubes and centrifuged (0.1 ×G, 2 sec) and the flowthrough was discarded. The wash was repeated 2× more with 600 μL of a 0.1 % NP40 solution in PBS, then washed 3× with 600 μL PBS, and wash 3× with 600 μL water. Next, the samples were transferred to 1.5 mL LoBind Eppendorf tubes with 600 μL 8M urea/0.1 M TEAB, before centrifugation at 0.8 ×G for 3min and removal of the supernatant. Then, 300 μL 8M urea/0.1 M TEAB were added. For reduction and alkylation, first 15 μL DTT (31 mg/mL in water, freshly made) were added for 45 min at RT while rotating at 10rpm. Then, 15 μL iodoacetamide (74 mg/mL in WATER, freshly made) was

added at RT for 30 min at 10 rpm on a rotating wheel in the dark. Excess of IA was quenched by adding 15 μL DTT (31 mg/mL in water, freshly made) for 30 min at RT, while rotating at 10 rpm. To dilute the urea, 900 μL of 0.1 M TEAB was added before centrifugation at 0.8 ×G for 3 min and removal of the supernatant. 200 μL of 1 M Urea/0.1 M TEAB and 6 μL of 0.5 mg/mL trypsin (3 μg) were added per sample before incubation at 37 °C at 1000 rpm ON.

Next, 400 μL 0.1 % NP40/PBS were added to the tryptic digests to transfer to Biospin columns. Followingly, washes were done with 3× with 600 μL 0.1 % NP40 in PBS, 3× with 800 μL PBS, and 3× with 800 μL water, before transfer of the column to a fresh 1.5 mL LoBind Eppendorf tube. For the elution, 400 μL of 50 % ACN in water with 0.1 % TFA was slowly dripping through, with a final centrifugation of 3000 ×G for 3 min. Obtained peptides were dried in a Speed vac (30 °C, ON) and stored at -20 degrees.

To re-suspend the samples, 20 μL buffer consisting of 5%FA and 10 % DMSO in water was added and samples were incubating for 5 min at 1000 rpm on a shaker. Then, samples were prepared for filtering. Each spin filter (UFC30GVNB) was washed with 300 μL resuspension buffer in a 1.5mL Eppendorf by centrifugation 17000 ×G for 2 min. The sample was then added as 30 μL to the center of the filter and centrifuged 17000 ×G for 2 min into a fresh 1.5 mL Eppendorf tube. Finally, the samples were transferred to MS sample vials.

MS analysis QE

Mass spectrometry data were acquired at the Discovery Proteomics Facility (University of Oxford). Peptides were resuspended in 5 % formic acid and 10 % DMSO and then trapped on an Acclaim™ PepMap™ 100 C18 HPLC Columns (5µm x 0.1mm x 20mm, Thermo Fisher Scientific) using solvent A (0.1 % Formic Acid in water) at a pressure of 60 bar and separated on an Ultimate 3000 UHPLC system (Thermo Fischer Scientific) coupled to a QExactive mass

spectrometer (Thermo Fischer Scientific). The peptides were separated on an Easy Spray PepMap RSLC column (75 µm i.d. x 2 µm x 50 mm, 100 Å, Thermo Fisher) and then electro sprayed directly into an QExactive mass spectrometer (Thermo Fisher Scientific) through an EASY-Spray nano-electrospray ion source (Thermo Fisher Scientific) using a gradient of solvent A (0.1 % formic acid in water) and solvent B solvent B (0.1 % formic acid in acetonitrile and 5 % dimethyl sulfoxide), flow rate: 250 nL/min. Gradient: 5 % solvent B for 7 min followed by a gradient from 5 % to 40 % solvent B over 105 min, an increase to 60 % B in 10 min and another increase to 90% B in 10 min. 90 % B was held for 10 min, then decreased to 5 % in 0.1 min and held at 5 % for 9.9 min. The raw data was acquired on the mass spectrometer in a data-dependent mode (DDA). Full scan MS spectra were acquired in the Orbitrap (scan range 300-1500 m/z, resolution 70000, AGC target $3e^6$, maximum injection time 80 ms). After the MS scans, the 15 most intense peaks were selected for HCD fragmentation at 27 % of normalised collision energy. HCD spectra were also acquired in the Orbitrap (resolution 17500, AGC target 1e5, maximum injection time 100 ms) with first fixed mass at 100 m/z. Charge exclusion was selected for unassigned and 1+ ions.

MS analysis TimsTOF

Peptides were loaded onto Evotips (Evosep) according to the manufacturer's instructions and analysed by LC-MS/MS using an Evosep One liquid chromatography system coupled to a TimsTOF Pro mass spectrometer (Bruker). Peptides were chromatographically separated using the 60 samples per day standard Evosep method using buffer A: 0.1 % formic acid in water and buffer B: 0.1 % formic acid in acetonitrile. Mass spectrometry data were acquired in ddaPASEF mode. The ion mobility window was 0.60 – 1.60 Vs/cm^2, with an accumulation and ramp time of 100 ms. The mass range of MS and MS/MS scans was 100 – 1700 m/z. MS/MS spectra were acquired in 4 PASEF frames with a 3-frame overlap giving a duty cycle of 0.53 s. Ions were selected for PASEF MS/MS if they met an intensity threshold of 2000 and were sampled multiple times until a target intensity of 10000 was reached. A polygon filter was used to exclude singly

charged ions from MS/MS selection. Ions selected for fragmentation were isolated by the quadrupole and fragmented using an ion mobility-dependent collision energy that increased linearly over the ion mobility range. A dynamic exclusion time of 24 seconds was used.

Data processing

Obtained .raw files were converted into .mzML using MSConvert GUI. Files were added and the peak picking option was enabled. Subsequently, FragPipe 19.0 was used to analyse the .mzML files in an open and closed search mode. Masses of modifications were calculated using IDCalc, calculated masses and amended amino acids can be found in the table below.

Probe	**Mass H**	**Mass L**	**AA**
1	624.3743	618.3602	CM
9	736.3296	730.3221	CM
5	597.327	591.3129	KTS
6	708.3049	702.2908	KTY
7	583.3226	577.3085	KCM
8	764.3675	758.3534	KSY
11	673.3153	667.3078	KR

A reviewed human fasta file from UniProt was used for the analysis (https://www.uniprot.org/taxonomy/9606), decoys were added by default in FragPipe. For the open search, parameters were set as follows to observe all identified mass shifts on peptides. Precursor mass tolerance -150-1000 Da, fragment mass tolerance 20 PPM, Calibration and Optimization Mass calibration, parameter optimization enabled, isotope Error 0, enzyme name stricttrypsin, cut after KR, but not before P, cleavage enzymatic, missed cleavages 2, Clip N-term N enabled, peptide length 7-50, peptide mass range 500-5000 Da, split database at 1, no variable

modifications, no fixed modifications, and other options were kept at standard settings. Crystal-C was enabled. PeptideProphet was run with --nonparam --expectscore --decoyprobs --masswidth 1000.0 --clevel -2. PTMProphet was disabled. ProteinProphet was run with --maxppmdiff 2000000 and Generate report was enabled with the following settings --sequential --razor --mapmods --prot 0.01. PTM-Shepherd was enabled with Smoothing factor 2, Precursor tolerance 0.01 Da, Prominence ratio 0.3, Peak picking width 0.002 Da, Localization background 4, and Annotation tolerance 0.01 Da. For Custom mass shifts a list was used including UniMod modifications with less than 400 Da molecular weight. Ion Types for modification with “b” and “y” enabled and mass fragment charge 2. Generate Spectral Library was disabled. For triplicates, the runs were analysed as experiment set to 1 in the workflow tab. For downstream data analysis, the global.modsummary.tsv file was used to see identified mass shifts and modified amino acids.

For the closed search, the parameters were set as follows, in the MS Fragger tab, Precursor mass tolerance was -10-20 PPM, Fragment mass tolerance 20 PPM and Calibration and optimisation were set to Mass calibration, parameter optimisation and Isotope error was kept at 0/1/2. For the Protein Digestion, Cleavage was enzymatic, enabled clip N-term M, Enzyme name 1 and load rules was stricttrypsin, Cuts KR with 2 Missed cleavages and Sense C. Enzyme name 2 was null. Peptide length was 7-50, Peptide mass range 500-5000 Da and Split database kept at 1. The modifications were set as variable modifications according to the mass delta in the table for each probe, Max occurrence set to 2. The site C with the modification 57.02146 was set to Max occurrence 3 and site M with the modification 15.9949 was set to Max occurrence 2. No fixed modifications were set, and advanced options remained unchanged. In the Validation tab, run validation tool was enabled, as well as Predict RT and Predict spectra. Run PSM validation was enabled with Run PeptideProphet Defaults for Closed search, with Single combined pepxml file enabled. Cmd line optsa were set to: --nonparam –expectscore --decoyprobs --masswidth 1000.0 --clevel -2. Run ProteinProphet was enabled with Cmd line opts –maxppmdiff 200000 and for

FDR Filter and Report, generate reports was enabled with Filter --sequential --razor --mapmods --prot 0.02. Generate protein-level summary was enabled. In the Quant(MS1) tab, Run MS1 quant was enabled. IonQuant was enabled with labelling and re-quantification. For each Light and Heavy, the masses of modifications and respective amino acids were listed separated by ";". Advanced options remained unchanged. For triplicates, the runs were analysed as separate experiments (1,2,3) and each ion_label_quant.tsv file was used in subsequent data analysis.

R data analysis

To analyse and visualise the combined_ion_label_quant.tsv output files from FragPipe, an R-script was written. The script maps detected peptides and labelling positions to protein sequences, as well as Uniprot sequence information. Thereby, multiple peptides with the same labelling position can be condensed to a single label id. The data was limited to peptides which were reliably enriched, meaning peptides only detected once in the enrichment samples were discarded. The remaining missing values were imputed, assuming that the values were *missing not at random*, by assigning a random value below the q-th quantile of 0.01. Log2 heavy/light intensity ratios were computed, using the mean across replicates, weighted by the combined intensity of both heavy and light intensities. Lastly, label IDs (e.g. HUWE1_C55) with a SD ≥ 1.41 were discarded. The code is accessible under *https://gitlab.com/chembio/abpp-analysis*. The reviewers may request an access code to view the code.

For the comparison to the CysDB, the data for cysteines was downloaded from backuslab.shinyapps.io/cysdb/ under the help tab and download CysDB data, comprising a list of 62888 entries. This data was overlapped in a Venn Diagram with our data. For the literature comparison, the following datasets were used. To compare probe 12 (aziridine), we used Table S9 from the SI from Ma et al. [301]. For Probe 6 (SuTex) we used tab C) provided in Supplementary Dataset 1 file from Hahm et al. [299]. For Lin et al. and probe 7, we used the High Dose data in file

aal3316datas2.xls. For Zanon et al. [295], we compared our results to and used tabs HS IAA-alkyne, HS OxMet1-alkyne and PhGO-alkyne from the file Supplementary Table 4.

An R-shiny application developed by Jeppe Tranberg-Jensen, allowed for easy interrogation of the labelling sites in AlphaFold predictions or PDB structures, as well as protein schematics of labelling positions.

Tableau analysis

Tableau Public (V10.2.0) was used to analyse the MS data derived from the downstream R analysis. The solvent accessible surface area (SASA) was calculated using the function `get_sasa_relative´ in PyMOL (version 2.5.5). In addition p2rank (version 2.4.1) was used to identify ligand binding sites [324, 325]. Results were displayed as excel tables using a cut-off of R > 4.

Chapter 4

SPECK-formation assay

The experiment was conducted as described previously [378]. In brief, 10,000 iBMDM cells were plated per well in 384-well format with compounds at maximal 0.3 % DMSO. Next, LPS treatment (1 μg/mL) was conducted for 2 h at 37 °C and 5 % CO_2, followed by a treatment with nigericin (10 μM) for another 2 h resulting in maximal speck formation. Plates were imaged utilizing the GE IN Cell Analyzer 6000 (GE, Boston, MA, USA). Data was analysed as described in Nizami et al. [378] and plotted in GraphPad Prism using the fit log(inhibitor) vs. response -- Variable slope (four parameters) to derive IC_{50} values.

isoDTB workflow for BMDM cells

The BMDMs were derived from the ODDI. Cells were treated at 90 % confluency in 30 mL DMEM + 10 % FBS (no phenol red). Per condition 3xT175 flasks were used. The compounds and the LPS (1 μg/mL) incubated for 2 h at 37 °C and 5 % CO_2, followed by a treatment with nigericin (10 μM) for 30 min to allow for harvesting before onset of apoptotic cell death. The isoDTB workflow was conducted as described in the methods for chapter 3.

isoDTB workflow for KEAP1 and NUDT7

For testing of the KEAP1 probe, live MDAMB231 cells (90 % confluency) were treated with 1 μM of probe and respective negative control for 3 h in 30 mL DMEM + 10 % FBS (no phenol red), before harvesting. Per condition 3xT175 flasks were used. After lysis, 100 μM IAA was used for enrichment and the isoDTB workflow was further conducted as described in the methods for chapter 3.

For testing the NUDT7 chemical probe and respective compounds, HEK293T cells were transfected using NUDT7-FLAG tag (11 μg plasmid, 33 μL lipofectamine and 400 μL OptiMEM per T175 flask). The next day, cells were treated with 1-10 μM of respective compound for 2h at 37 °C and 5 % CO2 before harvesting. After lysis, 100 μM vinyl sulfone-alkyne was used for enrichment and the isoDTB workflow was further conducted as described in the methods for chapter 3.

Western Blotting for KEAP1 and NUDT7

Western blotting was performed as described before, for detection of respective bands the following antibodies were used: KEAP1-antibody (Santa Cruz, sc365626, 1:1000) or anti-FLAG

antibody (Merck, F3165-1MG, 1:1000) and secondary antibody HRP-antibody (Thermo Fisher, 7076S, 1:10000) or Alexa Fluor 790 (Thermo Fisher, A 1137. 1:10000), respectively.

Cellular Thermal Shift Assay (CETSA)

K562 and NCIH226 cells were seeded in T175 flasks 24h before starting the assay to reach confluence of 80-90 % the following day. The appropriate drug concentration (e.g. 200 μM) of compound as a DMSO stock (100 mM) or the equivalent volume of DMSO control were added to the media and live cells were treated at 37 °C and 5 % CO_2 in the incubator for 30 min. Cells were detached and transferred into a 50 mL falcon tube for each compound and DMSO treated samples. The cells were counted before centrifugation at 300 ×G for 3 min. The medium was aspirated before the pellet was washed with 10 mL PBS. The centrifugation step was repeated before cells were resuspended in 1.8 mL PBS/T175 and aliquoted as 100 μL x11 into 0.2 mL PCR tubes. The tubes were centrifuged at 300 ×G for 3 min using plate adaptors. Next, 75 μL of PBS supernatant was removed. Then, samples were heated according to a gradient in the PCR cycler:

	1	2	3	4	5	6	7	8	9	10	11
temp. (°C)	23	37	40.8	42	44.5	48.2	52.9	56.7	58.9	60	65

Next, 30 μL PBS were added to resuspend the cells. Cells incubated on ice for 10 min. The lysis was done by 3 freeze-thaw cycles using dry ice. The PCR tubes were centrifuged at 17000 ×G for 20 min at 4°C, then 35 μL of supernatant was transferred into new 1.5 mL Eppendorf tube. A sample of 2 μL was taken, 8 μL PBS were added to perform a DC assay to determine protein concentration. Next, samples were boiled at 95 °C for 5 min with 15 μL 4×SLB before storage at -20°C. For SDS-page, 1 μL Precision Plus Protein All Blue (Biorad) ladder and 10 μL sample was loaded per lane. 4–12% Criterion™ XT Bis-Tris Protein Gel (Biorad) ran at 170 V for 55 min in 1× MES buffer. For Western Blotting, a PVDF membrane was activated in MeOH before blotting for 1.5h at 0.4 A. Blots were blocked in 5 % milk for 45 min at RT. Incubation with primary antibodies (SOD1 (810269-1-AP, Proteintech, 1:1000) , TRIM28 (14208-1-AP, Proteintech, 1:2000) was done ON at 4 °C, followed by 3× wash steps with PBST. HRP-

secondaries (7074S, 7076S, each 1:10000) incubated at RT for 3 h, before 3× wash steps with PBST followed by activation using chemiluminescent-substrate (Pierce, Super signal, West Pico PLUS). Imaging was done using the ChemiDoc (Bio-rad).

Intact Protein MS (RapidFire)

The respective proteins were diluted in buffer (20 mM HEPES, 20 mM NaCl, pH = 7.5) to 2 μM protein concentration in 100 μL assay volume. Using the ECHO, compounds were transferred to a 384 well PP plate (Greiner) as 200 nL to reach a final concentration of 200 μM. Binding was evaluated after 30 min and 2 h incubation at RT using the RapidFire QTOF Mass Spectrometer 6530 (Agilent). Samples were aspirated under vacuum and loaded onto a C4 solid phase extraction (SPE) cartridge equilibrated and washed for 5.5 sec with 1 mM octyl ammonium acetate in LC-MS grade water to remove non-volatile buffer components. After the aqueous wash, analytes of interest were eluted from the C4 SPE onto an Agilent 6530 accurate mass Q-TOF in an organic elution step (85% acetonitrile in LC-MS grade water). Data was visualised using the MassHunter software 9.0 (Agilent) by deconvoluting MS protein spectra.

Cell viability assay

Compounds were plated from a 100 mM stock into a 384-well PP plate (Greiner). Cells were counted to 200.000 cells/mL and per well 100 μL were added to incubate with the compounds at 37 °C and 5 % CO_2 for 1h. Next, the CellTiterGlo (Promega) components were mixed according to the manufacturer's recommendation, diluted 1:3 with DPBS (Life Technologies) and 25 μL were added to the wells. After 10 min incubation at RT, the plates were measured at the PheraSTAR FSX. For the data analysis, the mean and SEM (Standard Error of the Mean) of the raw triplicate luminescence values were calculated. Subsequently, these values were normalized to the mean of the positive control (DMSO, 100 % viability), and plotted against the logarithm of the compound concentration.

FRAP assay

NCIH226 cells were transiently transfected as 200.000 cells/mL in duplicates with the overexpression construct pEGFP-TRIM28 (Addgene 45568) at 3 μg using FuGENE according to the manufacturers protocol in 5 mL RPMI + 10 % FBS medium in dishes Fluorodish (World Precision Instruments FD35-100). The medium was replaced with 2 mL RPMI (without phenol red) after two days and the compound was added at 100 μM, 1 hour before imaging. The imaging system used was a Zeiss LSM 710 scan head coupled to an inverted Zeiss Axio Observer.Z1 microscope. A 40x oil immersion objective was employed, and a heated chamber set at 37 ˚C with 5 % CO_2 atmosphere was used. 10 cells with nuclei just below saturation within a gain range of 800-1000 were selected for bleaching, per sample. A bleach area of 70 pixels in diameter was employed and a time-lapse series (0.25 second intervals) for 60 seconds was taken to record GFP recovery.

For the data analysis, the average intensity at each imaging time point was measured for 3 regions: bleached region (1), total cell nucleus (2) and a any region outside of the cell (3) for background subtraction. Double exponential association curved were fitted using the OriginPro function ExpAssoc. One way ANOVA with Tukey-Kramer correction for multiple comparison was employed to detect significant differences ($P<0.05$) between samples.

Chapter 5

All solvents were purchased of HPLC grade from commercial suppliers (Sigma, Thermo Fisher) and used without further purification. Anhydrous solvents were purchased from Acros Organics and stored under a nitrogen atmosphere with activated molecular sieves. CBH-001 was purchased from Enamine. GSK3203591 was purchased from Sigma, GSK3326595, MS023, LLY-283 and SCG3027 from MedChem Express, and TP064 from Tocris. NanoBRET 590 SE, NanoBRET™

Nano-Glo® Detection System and CellTiter-Glo® Luminescent Cell Viability Assay were purchased from Promega.

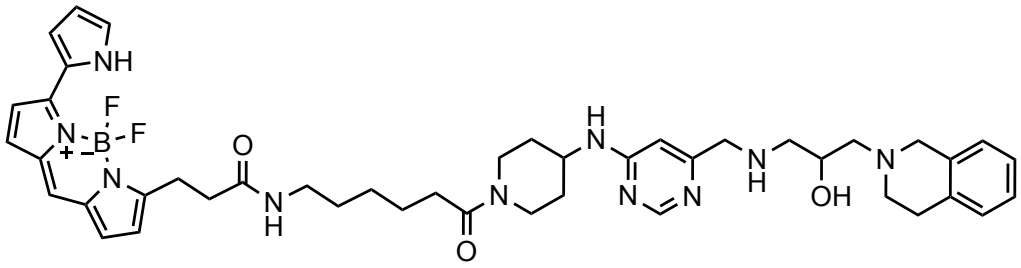
Organic Synthesis

Reaction progress was monitored by TLC (Thin Layer Chromatography) and LC-MS. For the silica gel TLC, aluminium plates coated with 0.25 mm $60F_{254}$ silica gel (Merck) were used and visualized with UV light at l = 254 nm or l = 365 nm.

1H NMR spectra were recorded using a Bruker Avance 400 MHz spectrometer (400 MHz) and the deuterated solvent stated. Chemical shifts (δ) are quoted in parts per million (ppm) and referenced to the residual solvent peak. Multiplicities are denoted as singlet (s), doublet (d), triplet (t), quartet (q) and quintet (p) and derivatives thereof and multiplets (m). (br) denotes a broad resonance peak. Coupling constants are recorded as Hz and rounded to the nearest 0.1 Hz. Spectra were analysed using MestreNova 14.2.1.

LC-MS chromatograms determining mass and purity were obtained using a Waters Auto purification System equipped with Waters 2489 UV/Vis or Water 2998 Photodiode Array detectors, Waters 2424 ELS detector and SQ Detector 2 or Acquity QDa mass detector. A Phenomenex Kinetex 5µm EVO C18 100A, 3 × 100 mm column was used for analytical measurements and a Phenomenex 5 µm EVO C18 100 A, 21.2 x 150 mm column was used for preparative HPLC purifications using a gradient program (eluent I: acetonitrile/water = 5/95 with 20 mM ammonium acetate buffer, pH 6.0; eluent II: acetonitrile/water = 80/20 with 20 mM ammonium acetate buffer, pH 6.0). Compound names were generated using ChemBioDraw Ultra v19.0 systematic naming.

(*S*)-6-((1-(5-(3-(5,5-difluoro-7-(1H-pyrrol-2-yl)-5H-5λ4,6λ4-dipyrrolo[1,2-c:2',1'-f][1,3,2]diazaborinin-3-yl)propanamido)pentanoyl)piperidin-4-yl)amino)-N-(3-(3,4-dihydroisoquinolin-2(1H)-yl)-2-hydroxypropyl)pyrimidine-4-carboxamide (CBH-002)

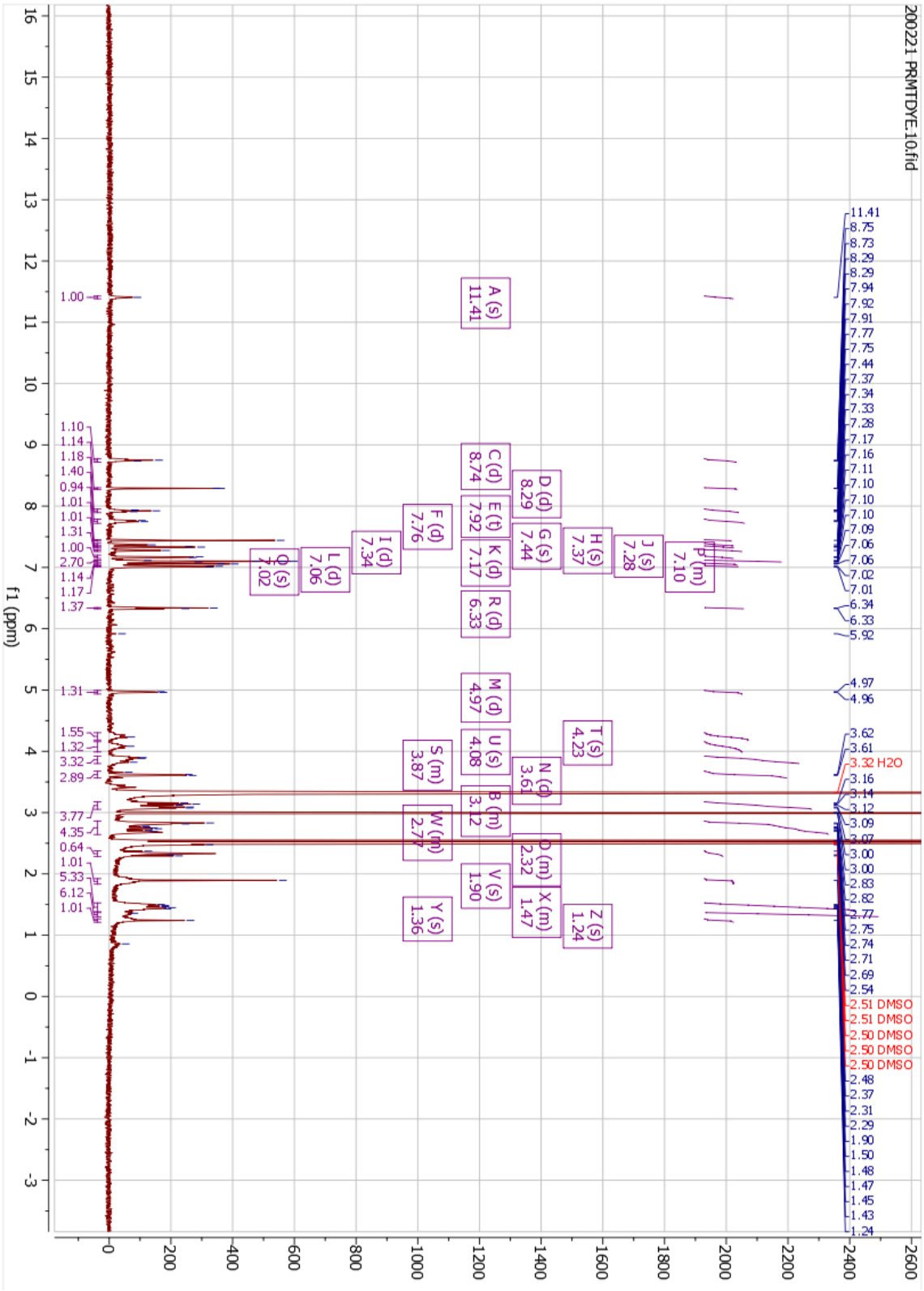


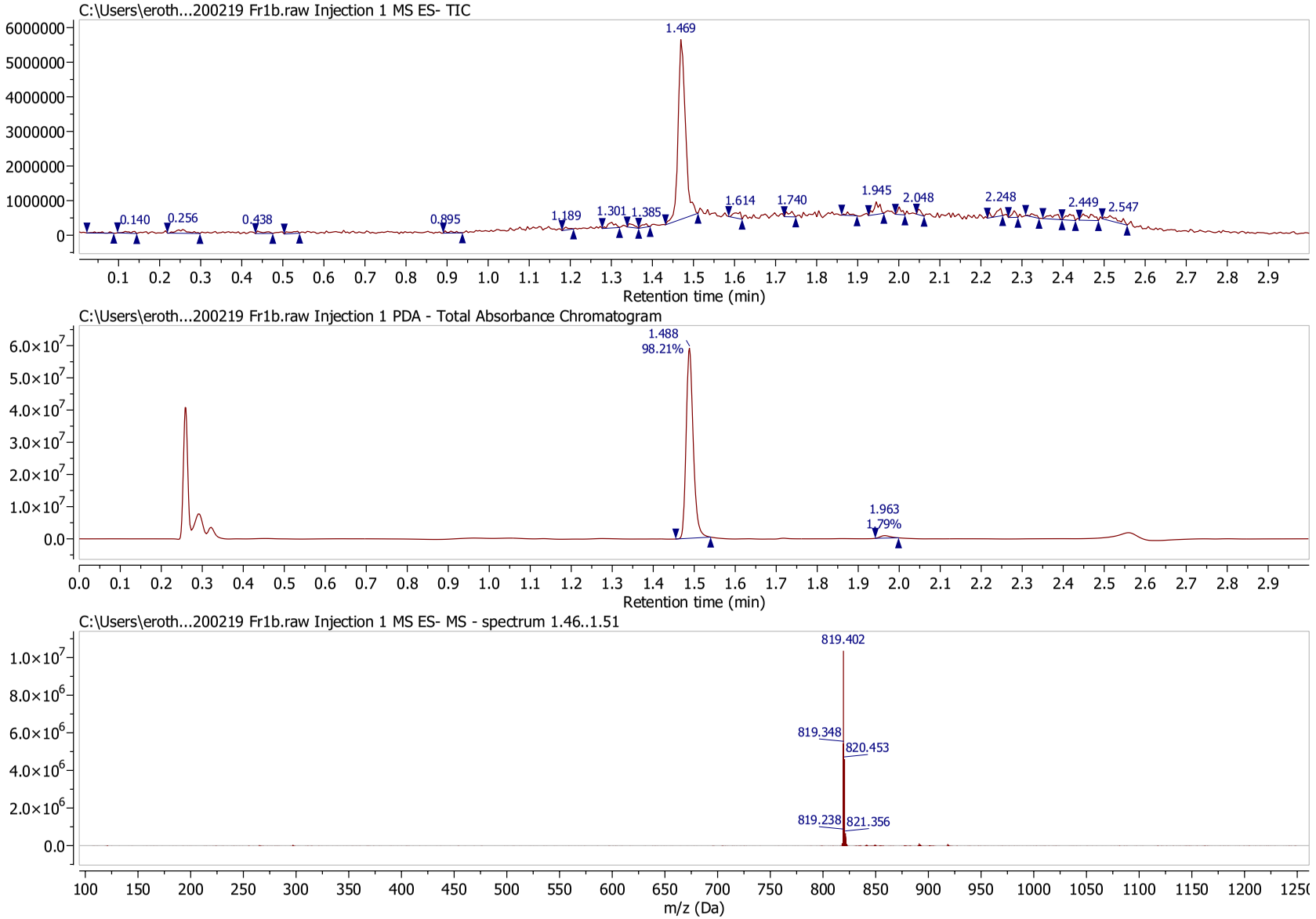
Chemical Formula: $C_{44}H_{55}BF_2N_{10}O_3$

MW: 820.80 g/mol

(*S*)-6-((1-(5-aminopentanoyl)piperidin-4-yl)amino)-*N*-(3-(3,4-dihydroisoquinolin-2(1*H*)-yl)-2-hydroxypropyl)pyrimidine-4-carboxamide (5.4 mg, 0.010 mmol) was dissolved in 1.0 mL of anhydrous DMF. To the stirred mixture DIPEA (5.6 μL, 0.030 mmol) was added and stirring was continued for 10 min. To the clear colourless solution, NanoBRET® 590 SE (5 mg, 0.012 mmol) was added and the reaction was stirred to completion in the dark for 2 h. The sample was dried overnight *in vacuo*. The crude residue was re-solved in DMSO and subjected to reverse-phase preparative HPLC purification (Phenomenex 5 µm EVO C18 100 A, 21.2 × 150 mm column was used with a gradient program: eluent I: acetonitrile/water = 5/95 with 20 mM ammonium acetate buffer, pH 6.0; eluent II: acetonitrile/water = 80/20 with 20 mM ammonium acetate buffer, pH 6.0). Product containing fractions were concentrated *in vacuo*, affording the product (6.0 mg, 0.007 mmol, 69.0 %) as a purple solid. The purity was determined by LC/MS 98.2 %. LC/MS (ESI-1) found 819.4 g/mol (820.45 g/mol calculated for $C_{44}H_{55}BF_2N_{10}O_3$). 1H NMR (400 MHz, DMSO) δ 11.41 (s, 1H), 8.74 (d, J = 6.0 Hz, 1H), 8.29 (d, J = 1.2 Hz, 1H), 7.92 (t, J = 5.5 Hz, 1H), 7.76 (d, J = 7.6 Hz, 1H), 7.44 (s, 1H), 7.37 (s, 1H), 7.34 (d, J = 4.5 Hz, 1H), 7.28 (s, 1H), 7.17 (d, J = 4.6 Hz, 1H), 7.12 – 7.09 (m, 3H), 7.06 (d, J = 1.2 Hz, 1H), 7.02 (s, 1H), 6.33 (d, J = 4.0 Hz, 1H), 4.97 (d, J = 4.7 Hz, 1H), 4.23 (s, 2H), 4.08 (s, 1H), 3.92 – 3.80 (m, 3H), 3.61 (d, J =

5.9 Hz, 3H), 3.18 – 3.05 (m, 4H), 2.86 – 2.64 (m, 4H), 2.38 – 2.28 (m, 1H), 1.90 (s, 1H), 1.53 – 1.38 (m, 5H), 1.36 (s, 6H), 1.24 (s, 1H).




C:\Users\eroth...200219 Fr1b.raw Injection 1 MS ES- TIC
1.469
0.140
0.256
0.438
0.895
1.189
1.301
1.385
1.614
1.740
1.945
2.048
2.248
2.449
2.547
Retention time (min)
C:\Users\eroth...200219 Fr1b.raw Injection 1 PDA - Total Absorbance Chromatogram
1.488
98.21%
1.963
1.79%
Retention time (min)
C:\Users\eroth...200219 Fr1b.raw Injection 1 MS ES- MS - spectrum 1.46..1.51
819.402
819.348
820.453
819.238
821.356
m/z (Da)

NanoBRET TE assay with CBH-002

Cells were split at 80 % confluency. HEK293 cells were prepared as 2×10^5 cells/mL in DMEM (Dulbecco s Modified Eagle Media, Life Technologies) + 10 % FBS (Foetal Bovine Serum, Life Technologies) medium. Transfection 1:20 with NL-PRMT5 (Promega) was done according to the manufacturer's protocol using a transfection solution consisting of 1 μg DNA, 9 μg Transfection Carrier DNA (Promega) and 30 μL FuGENE HD Transfection Reagent (Promega) per 1 mL Opti-MEM (Life Technologies) and cells subsequently incubated at 37 °C in a humidified 5 % CO_2 atmosphere for 24 h. Depending on the size of the experiment, either 6-well plates (Greiner-Bio) or T75 flasks (Greiner-Bio) were used for transfection. The BRET assay was performed in a 384-well plate (UltraCruz, PP) by plating 2×10^5 cells/mL in OptiMEM; for lysates, Passive Lysis 5× buffer (Promega) was added, and SAM (Sigma) was optionally added for competition experiments. The ETP was prepared as a 100× stock in 100 % DMSO (Sigma) and 20× stock in NanoBRET Tracer Dilution buffer (Promega) in a PP 384-well plate, to prevent interactions with the plate material. The test compounds (GSK3203591 (Sigma) GSK3326595, MS023, LLY-283 and SCG3027 (MedChem Express), TP064 (Tocris)) were prepared as 1000x stock in 100 % DMSO and 10× stock in Opti-MEM in a 96-well plate (Starlab). Each test compound dilution was dispensed in triplicates. As controls, no compound and no energy transfer probe/energy transfer probe wells were prepared. After addition of the ETP and the compounds to the wells, the plates were allowed to incubate at 37 °C and 5 % CO_2 for 2 h. Next, the BRET measurement was prepared by adding a mix of NanoBRET Nano-Glo Substrate (1:166) and Extracellular NanoLuc Inhibitor (1:500) in Opti-MEM to the wells. Followed by 10 min incubation at room temperature, the plates were measured at the PheraSTAR FSX at 450 nm (donor) and 610 nm (acceptor). For the data analysis to create raw BRET ratio values, the acceptor value was divided by the donor. For background correction, the no energy transfer probe ratio was subtracted from these values. Next, the corrected BRET ratio values were multiplied by 1000 to obtain milli BRET units (mBU) which are then plotted against the energy transfer probe.

$$\left(\left(\frac{Acceptor\ sample}{Donor\ Sample}\right) - \left(\frac{Acceptor\ no\ tracer}{Donor\ no\ tracer}\right)\right) \times 1000 = mBU$$

Cell Titer Glo Luminescent Cell Viability Assay

Cell Titer Glo Luminescent Cell Viability Assay Kit (Promega) was used and immediately performed after the BRET measurement. The components were mixed according to the manufacturer's recommendation, diluted 1:3 with DPBS (Life Technologies) and 25 μL were added to the wells. After 10 min incubation at room temperature, the plates were measured at the PheraSTAR FSX. For the data analysis, the mean and SEM (Standard Error of the Mean) of the raw triplicate luminescence values were calculated. Subsequently, these values were normalized to the mean of the positive control (DMSO, 100 % viability), which is obtained from wells containing no compound and no energy transfer probe and plotted against the logarithm of the compound concentration.

Intracellular Fluorescence

HEK cells were transfected as described previously for the NanoBRET assay. 3×10^5 cells/mL in DMEM (Life Technologies) + 10 % FBS (Life Technologies) medium were seeded in a glass bottom Fluorodish 35mm (World precision Instruments) and settled ON at 37 °C and 5 % CO_2 atmosphere. After 24 h the medium was aspirated, and the cells were fixed with 4 % formaldehyde (Thermo Scientific) in 1× PBS for 15 min. The solution was aspirated, and the cells were washed three times with 1 mL of 1× PBS for 5 min each. A blocking solution containing 1× PBS, 1 % BSA / 0.1 % saponin was prepared freshly. The cells were blocked with 1 mL blocking solution for 1 h at RT. After aspirating the blocking solution, the following primary antibodies were applied as a 1:50 dilution in blocking solution and incubated standing ON at 4 °C: PRMT5 (ab109451, Abcam) and NL-PRMT5 (N7000, Promega). After repeating the wash step with 1× PBS three times, the secondary antibodies were applied in blocking solution as 1:50 dilutions for

1 h at RT as follows: Donkey Anti-Mouse IgG H&L (Alexa Fluor® 568) (ab175472, Abcam) and Goat Anti Rabbit IgG H&L (Alexa Fluor® 488) (ab150077, Abcam). The solution was aspirated, and the samples kept under 1× PBS. If applicable, for nuclei stain ProLong™ Glass Antifade Mountant with SYTOX™ Deep Red (P36993, Thermo Scientific) was applied to the cells as one drop and the samples were kept at 4 °C until measurement.

Compound-centric pulldown

For profiling PRMT5 inhibitor GSK3326595, label-free quantification (LFQ) mass spectrometry was conducted. Chemical proteomics was conducted as previously described. [418] In brief, KMS11 (ATCC) were cultured at 37 °C, in a humidified 5 % CO_2 atmosphere in RPMI-1640 (Life Technologies) + 10 % FBS. To obtain lysate, the cells were harvested at 80 % confluency from 5× T75 flasks (Greiner) and subsequently pelleted and washed with DPBS. The obtained pellets were then lysed by addition of 3× pellet volume of lysis buffer (50 mM Tris pH 7.5, 0.8 % v/v NP-40, 5 % v/v glycerol, 1.5 mM $MgCl_2$, 100 mM NaCl, 25 mM NaF, 1 mM Na_3VO_4, 1 mM PMSF, 1 mM DTT, 10 µg/mL TLCK, 1 µg/mL Leupeptin, 1 µg/mL Aprotinin, 1 µg/mL soybean trypsin) on ice, before being pushed gently 10 x through a 21 G needle (Braun) using a 1 mL syringe (Braun, Inject-F). The lysates were allowed to incubate on ice for 10 min before being ultracentrifuged at 17000 ×G at 4 °C for 30 min. Next, total protein concentration was adjusted to 10 mg/mL and the lysates were stored for further use at -80 °C. In preparation for a pulldown, the amine derivatized compound CBH-001 was coupled to NHS-activated Sepharose 4 Fast Flow beads (Cytiva). 100 μL beads as a slurry in 50 % isopropanol were used for each experiment, the experiments were done in triplicates (with/without competition). The beads were washed with 500 μL DMSO and centrifuged at 0.1 ×G at RT for 3 min. The supernatant was removed, and the washing step was repeated 3×. Then the bead bed was re-suspended in 50 μL DMSO. To immobilise the couplable compound on the beads, 2 μL of a 10mM stock in DMSO was added to the beads along with 0.75 μL DIPEA (Diisopropylethylamine). Then the tubes were incubated on

the rotor shaker at 10 RPM for 20 h at RT. Subsequently, successful immobilisation and depletion of the free amine from the supernatant was determined by LC-MS analysis. The remaining unreacted NHS (N-Hydroxysuccinimide) groups were blocked with 2.5 μL ethanolamine and incubation again at the rotor shaker 10 RPM for 8 h at RT. The lysates were thawed on ice before pre-treatment with DMSO control or parent compound, GSK3326595, at 10mM and incubating for 30 min at 4 °C. A total cell lysate (TCL) sample was kept aside. The derivatized beads were washed 3× with 500 μL DMSO and then 3× with freshly prepared lysis buffer by centrifugation at 0.1 ×G for 3min at RT and subsequent removal of the supernatant. After that, the derivatized beads were combined with the cell lysate at 1.6 mg of protein per pull-down (10 mg/mL) being either compound or DMSO control pre-treated in triplicates. Beads and lysates were then incubated on the rotor shaker at 10 RPM in the cold room at 4 °C for 2 h. Then the samples were centrifuged at 0.1 ×G for 3 min at 4 °C and 300 μL of the supernatant was removed. Working in the cold room at 4 °C, the slurry was re-suspended in lysis buffer and 500 μL were transferred to a Bio Spin column (Bio-Rad) and the beads were allowed to settle by gravity. Next, the columns were washed with 5 mL lysis buffer via gravity flow and centrifuged at 0.1 ×G for 1 min at 4 °C to the remove the remaining supernatant. The protein was eluted for Western Blot experiments using 100 μL of 2× sample buffer (65.8 mM Tris-HCl pH 6.8, 26.3 % (w/v) glycerol, 2.0 % SDS, 0.01 % bromophenol blue, 50 mM DTT) and boiling the beads at 100 °C for 10 min. The samples were stored in the freezer at -20 °C.

Western Blot validation of Pulldown

The eluted proteins were analysed using a polyacrylamide gel and 1× MES buffer (50 mM MES, 50 mM Tris Base, 0.1 % SDS, 1 mM EDTA, pH 7.3) and transferal to a nitrocellulose blotting membrane. The membrane was blocked with blocking buffer (2.5 % m/v) BLOT-Quick Blocker (Merck) in PBST (Phosphate-buffered saline with Tween: 4.3 mM Na_2HPO_4, 1.47 mM KH_2PO_4, 137 mM NaCl, 2.7 mM KCl, 0.05 % (v/v) Tween 20) on a shaker in the dark for 1 h at RT. Then

the blot was probed with the antibodies EPR5772 (Abcam, ab109451, 1:10000), MEP50 (2823S, Cell Signalling Tech., 1:1000) and G-9 (s-365062, Santa Cruz, 1:200) and imaged at the Odyssey CLx (Li-cor) at wavelength 700 and 800.

Mass spectrometry sample preparation

100 µL of each sample were combined 1:1 freshly prepared 0.1 M TRIS solution. Then 5 µL 200 mM DTT was added, and the mixture incubated for 1 h at RT and was subsequently alkylated with 20 µL 200 mM iodoacetamide and incubated for 30 min in the dark at RT. The samples were diluted to 300 µL with TEAB and incubated at 37 °C overnight. To precipitate the proteins, 600 µL MeOH and 150 µL Chloroform were added to each vial and after vortexing 450 µL MilliQ-water were added. After centrifugation at 14.8 RPM for 5 min at RT, the upper phase was gently pipetted off without touching the precipitate at the interface. Next, 450 µL of MeOH was added, and the upper phase was pipetted off gently again. This was repeated once and then the samples were centrifuged at top speed. The supernatant was removed the vials left to dry 60 min RT. The precipitate was resuspended in 50 µL 6M urea buffer, followed by vortexing and sonication for 5 min. The solution was diluted with 250 µL MilliQ-water. Then trypsin in a 1:50 ratio regarding the total protein content was added, followed by incubation at 37 °C overnight. A SEP-PAK C18 purification was performed using solution A (98 % MilliQ-water, 2 % Acetonitrile, 0.1 % Formic acid) and solution B (35 % MilliQ-water, 65 % Acetonitrile, 0.1 % Formic acid). The samples were acidified with 1 % formic acid. Sola HRP SPE cartridge (Thermo Fisher) was attached to a vacuum manifold. First, the columns were equilibrated with 500 µL solution B. Second, 1000 µL of solution A were put on the column and again a small supernatant was left to prevent the column from running dry. Third, the peptide digest sample was loaded on the column. After that, the column was washed again with 1000 µL solution A. The columns were placed after the washing in fresh 1.5 mL Eppendorf vials. Then 600 µL solution B was used to elute into a fresh vial. Then, the samples were dried in the GeneVac for 24 h. Mass spectrometry data were acquired at the

Discovery Proteomics Facility (University of Oxford). Peptides were resuspended in 5 % formic acid and 5 % DMSO and then trapped on an Acclaim™ PepMap™ 100 C18 HPLC Columns (5μm × 0.1mm × 20mm, Thermo Fisher Scientific) using solvent A (0.1 % Formic Acid in water) at a pressure of 60 bar and separated on an Ultimate 3000 UHPLC system (Thermo Fischer Scientific) coupled to a QExactive mass spectrometer (Thermo Fischer Scientific). The peptides were separated on an Easy Spray PepMap RSLC column (75 μm i.d. × 2 μm × 50 mm, 100 Å, Thermo Fisher) and then electro sprayed directly into an QExactive mass spectrometer (Thermo Fisher Scientific) through an EASY-Spray nano-electrospray ion source (Thermo Fisher Scientific) using a linear gradient (length: 60 min, 5 % to 35 % solvent B (0.1 % formic acid in acetonitrile), flow rate: 250 nL/min). The raw data was acquired on the mass spectrometer in a data-dependent mode (DDA). Full scan MS spectra were acquired in the Orbitrap (scan range 380-1800 m/z, resolution 70000, AGC target $3e^6$, maximum injection time 100 ms). After the MS scans, the 15 most intense peaks were selected for HCD fragmentation at 28 % of normalised collision energy. HCD spectra were also acquired in the Orbitrap (resolution 17500, AGC target $1e^5$, maximum injection time 128 ms) with first fixed mass at 100 m/z.

MS Data analysis

Raw data was processed using MaxQuant version 1.6.1.2 and the reference complete human proteome FASTA file (UniProt). Label-Free Quantification (LFQ) and Match Between Runs were selected; replicates were collated into parameter groups to ensure matching between replicates only. Cysteine carbamidomethylation was selected as a fixed modification and methionine oxidation as a variable modification. Default settings for identification and quantification were used. Specifically, a minimum peptide length of 7, a maximum of 2 missed cleavage sites, and a maximum of 3 labelled amino acids per peptide were employed. Through selection of the 'trypsin/P' general setting, peptide bond cleavage at arginine or lysine (followed by any amino acid) was considered during in silico digest of the reference proteome. The allowed precursor and

fragment ion mass tolerances were 4.5 ppm and 20 ppm, respectively. Peptides and proteins were identified utilizing a 0.01 false discovery rate, with "Unique and razor peptides" mode selected for both identification and quantification of proteins (razor peptides are uniquely assigned to protein groups and not to individual proteins). At least 2 razor + unique peptides were required for valid quantification. Processed data was further analysed using Perseus version 1.6.2.1 and Microsoft Excel. Peptides categorized by MaxQuant as 'potential contaminants', 'only identified by site' or 'reverse' were filtered, and the LFQ intensities transformed by $\log_2$. Experimental replicates were grouped, and two valid LFQ values were required in at least one experimental group. Statistically significant competition was determined through the application of P2 tests, using a permutation-based FDR of 0.05 and an S0 of 2, and visualized in volcano plots. Significantly competed targets were further analysed in STRING (http://string-db.org) and protein interaction networks generated. Basic STRING settings were used for network analysis of enriched proteins. The network edges represent confidence in interaction. Line thickness indicates the strength of data support with a minimum required interaction score of 0.400. All active interaction sources (Text mining, Experiments, Databases, Co-expression, Neighbourhood, Gene Fusion, Co-occurrence) were considered.

Thermal Profiling

2D thermal profiling was performed according to previously described protocols.[429] KMS-11 cells were grown until confluent in T-175 flasks (Greiner). To five flasks of confluent KMS-11 cells GSK3326595 was added up to the concentrations of: 5, 1, 0.2, 0.04 μM or equivalent volume of DMSO for one hour. The cells were then detached using the Tryp-LE trypsin replacement enzyme (Gibco) and pelleted into 12 aliquots per group. Each aliquot was heated to different temperatures for 3 minutes in a PCR machine (Bio-Rad), with the temperature range being 42-64 °C and 2-degree intervals. Cell pellets were then lysed in 0.1 % NP-40 Tris-NaCl lysis buffer supplemented with protease and phosphatase inhibitors (Sigma). Cell lysis was facilitated by three cycles of

rapid freeze-thawing in liquid nitrogen. The lysates were clarified by centrifugation at 17000 × g for 20 minutes, and BCA assay was performed on the soluble fraction. For MS analysis, 100 μg of protein per aliquot was taken.

MS Analysis of TP samples

To reduce and alkylate proteins, lysate was first incubated with DTT up to a final concentration of 5 mM at RT for 1 hour followed by a 1 h incubation with iodoacetamide added to a final concentration of 20 mM. The proteins were then acetone-precipitated overnight –20°C and pelleted at 8,000 ×G for 10 minutes at 4 °C. Dry pellets were resuspended in 100 μL of 50 mM TEAB and 2.5 μg of Trypsin/LysC (Promega) was added for overnight digestion at 37 °C. TMT labelling (Thermo Fisher) was performed according to the manufacturer's protocol, and the samples were pooled according to the following scheme:

Temp (°C)	126	127L	127H	128L	128H	129L	129H	130L	130H	131	RefCol	
42	5	1	0.2	0.04	0	-	-	-	-	-	128H	F1
62	-	-	-	-	-	5	1	0.2	0.04	0	131	
44	5	1	0.2	0.04	0	-	-	-	-	-	128H	F2
64	-	-	-	-	-	5	1	0.2	0.04	0	131	
46	5	1	0.2	0.04	0	-	-	-	-	-	128H	F3
58	-	-	-	-	-	5	1	0.2	0.04	0	131	
48	5	1	0.2	0.04	0	-	-	-	-	-	128H	F4
60	-	-	-	-	-	5	1	0.2	0.04	0	131	
50	5	1	0.2	0.04	0	-	-	-	-	-	128H	F5
54	-	-	-	-	-	5	1	0.2	0.04	0	131	
52	5	1	0.2	0.04	0	-	-	-	-	-	128H	F6
56	-	-	-	-	-	5	1	0.2	0.04	0	131	

Pooled samples were subsequently desalted in C-18 columns (Pierce) and the solvent removed under reduced pressure in a SpeedVac Vacuum concentrator. Dry peptide mass was then resuspended in 120 μL of 98 % MilliQ-water, 2 % Acetonitrile, 0.1 % Formic Acid (v/v) and fractionated using an UltiMate 3000 HPLC system (Thermo) at pH 10 using a 60 min gradient of 0 % to 90 % Acetonitrile in Water. Fractions were then dried using a SpeedVac Vacuum concentrator and resuspended in 100 μL of 98 % MilliQ-WATER, 2 % Acetonitrile, 0.1 % Formic Acid (v/v). MS analysis was performed by nano-HPLC–MS/MS using a Dionex Ultimate 3000 nano HPLC with EASY spray column (75 µm × 500 mm, 2 µm particle size, Thermo Scientific)

with a 60 min gradient of 2% to 35% (v/v) Acetonitrile in Water with 5 % (v/v) DMSO and 0.1 % (v/v) Formic Acid at a flow rate of 250 nL/min (600 bar per 40 °C column temperature). MS1 survey scans were acquired at a resolution of 60,000 at 375-1500 m/z and the 20 most abundant precursors were selected for CID fragmentation in a HCD cell. MS2 data were analysed in Thermo Proteome Discoverer 2.1 according to the manufacturers protocol.

Western Blot CETSA

CETSA was performed according to previously reported procedures [84]. KMS11 cells were grown until confluent in T-175 flasks (Greiner). One flask was treated with 5 μM GSK33265905 in DMSO, whereas the control flask was treated with an equivalent volume of DMSO for one hour. The cells were then harvested and aliquoted for heating to different temperatures for 3 min and lysed in NP-40 lysis buffer. The lysate was clarified by centrifugation at 17000 ×G for 20 min and 30 μg of protein was used for SDS-PAGE and Western Blotting. Antibodies used: anti WDR77 (Cell Signalling, 2823), 1:100. The mass spectrometry proteomics data have been deposited to the ProteomeXchange Consortium via the PRIDE partner repository with the dataset identifier PXD028138.

Chapter 6

NanoBRET Protein-Protein interaction assay

The experiment was conducted using automated liquid handling system ECHO for plating the compounds, working in a class II laminar flow hood under sterile conditions. Each concentration was prepared in triplicates (3 wells/concentration), starting from 100 μM concentration, for dose-response 1:3 dilutions were done. Cells were split when reaching 80 % confluency. To perform the experiment, HEK293 cells were prepared as 4×10^5 cells/mL in DMEM (Life Technologies) + 10% FBS (Life Technologies) medium and allowed to attach for 4h at 37 °C and 5 % CO_2. Cells were subsequently transfected with 1:1000 DENND1A-NL and HT-RAB35 according to the manufacturer's protocol using a transfection solution consisting of respective amount of DNA, 9 μg Transfection Carrier DNA (Promega) and 30 μL FuGENE HD Transfection Reagent (Promega) per 1mL Opti-MEM (Life technologies). After 10 min incubation at RT, the DNA:FuGENE complex was formed, and the cells were transfected 1:20 with the transfection solution and subsequently incubated at 37 °C in a humidified 5 % CO_2 atmosphere for 24 h. The PPI assay was performed in a 384-well PS plate (Greiner) by plating 2×10^5 cells/mL in OptiMEM + 4 % FBS. The HT-ligand was added to the cells (100 nM final concentration). As controls, no compound and no ligand wells were prepared, and the cells incubated at 37 °C and 5 % CO_2 for 24 h. Next, the BRET measurement was prepared by adding a mix of 20 μL NanoBRET Nano-Glo Substrate (1:166) and Extracellular NanoLuc Inhibitor (1:500) in Opti-MEM to the wells. Followed by 15 incubation at RT, the plates were measured at the PheraSTAR FSX at 450 nm (donor) and 610 nm (acceptor), the data was analysed as shown previously.

For multiplexed experiments, the Cell Titer Glo Luminescent Cell Viability Assay Kit (Promega) was used and subsequently performed after the BRET measurement to measure cell viability. The experiment was conducted, and data analysed as described previously.

Expression and Purification of RAB35a-c002

RAB35 had previously been cloned into PNIC28-BSA4 with kanamycin resistance and TEV-cleavable N-terminal hexahistidine tag by Laura Dias-Saez. After transformation into Rosetta DE3 competent cells (Merck), expression was performed in TB auto induction medium (FroMedium). The next day 6 L TB medium (47.6g TB, 1 L water, 20 g/L glycerol and 50 µg/mL kanamycin) were inoculated with 10 mL starting culture each and kept in the shaking incubator at 37 °C until the optical density reached OD = 0.8. Per flask, 300 μL of 1 M IPTG were added to start protein expression. Pellets were harvested the next day by centrifugation at 6000 rpm for 15min and the pellet was frozen at -20 °C. A lysis buffer (500 mM NaCl, 35 mM HEPES, 0.5 mM TCEP (filtered), pH = 7.7) was prepared freshly and the pellet was thawed in 300 mL using a magnetic stirrer. A Complete Protease Inhibitor Cocktail tablet (Sigma, 11836145001), 2 μL benzonase and 1 mL lysozyme stock (0.5 mg/mL) were added. Subsequently, the pellet was homogenised using a Dounce homogenizer with 8 strokes. The lysate was centrifuged at 38.000 ×G for 1h at °C. The supernatant was filtered through a 0.8 filter pad. 20 mL of a 50 % slurry of equilibrated nickel resin (HisPur Ni-NTA Superflow 25215, Thermo Fisher) incubated 2 h in the cold room at 4 °C while rotating, splitted evenly into six 50 mL falcon tubes. The tubes were briefly centrifuges and, the flowthrough was collected. Beads were pooled into a column. Next, the following gradient was applied to perform affinity chromatography to enrich the HIS-tagged protein. To the lysis buffer imidazole was added as following final molarity and washes were performed with mL indicated in brackets: 10 mM (10+10), 20 mM (10+10+10), 30 mM (5+5+5+5), 40 mM (5+5+5), 50 mM (5+5+5), 100 mM (10+10), 500mM (20). All fractions were collected separately and run on a gel. Respective protein containing fractions were pooled and concentrated. To cleave the HIS-tag, 3 mg TEV were added and incubate in Dialysis cassette over night stirring at 350 rpm in 3 L lysis buffer without TCEP. The protein was recovered from the cassette using a 20 mL syringe. A negative affinity chromatography was performed as described above with nickel resin to remove the cleaved tag. All fractions were collected separately and

run on a gel. Respective fractions were pooled and concentrated. Then, size exclusion chromatography was performed using an AKTA Prime plus and a buffer consisting of 500 mM NaCl, 20 mM HEPES and 0.5 mM TCEP and the column (Hiload 16/600 S75PG) was equilibrated. Settings were set as: pressure 0.5 bar, flowrate 1mL/min, fraction size 3 mL, equilibration 10 mL, sample injection volume 5m, total elution 120 mL. A gel of the fractions indicated where cleaved RAB35 was contained, these fractions were pooled and concentrated and yielded 1 mL of 9.45 mg/mL RAB35. Stocks were kept at -80 °C. (Reference scarab: PAGE22-00253).

Intact protein MS

Was conducted using the RapidFire instrument (Agilent) as previously described using the following proteins:

Sequence of DENND1A-c025 (without tag, only DENN-domain):

SMGSRIKQNPETTFEVYVEVAYPRTGGTLSDPEVQRQFPEDYSDQEVLQTLTKFCFPFY
VDSLTVSQVGQNFTFVLTDIDSKQRFGFCRLSSGAKSCFCILSYLPWFEVFYKLLNILAD
YTTKRQENQWNELLETLHKLPIPDPGVSVHLSVHSYFTVPDTRELPSIPENRNLTEYFVA
VDVNNMLHLYASMLYERRILIICSKLSTLTACIHGSAAMLYPMYWQHVYIPVLPPHLLD
YCCAPMPYLIGIHLSLMEKVRNMALDDVVILNVDTNTLETPFDDLQSLPNDVISSLKNR
LKKVSTTTGDGVARAFLKAQAAFFGSYRNALKIEPEEPITFCEEAFVSHYRSGAMRQFL
QNATQLQLFKQFIDGRLDLLNSGEGFSDVFEEEINMGEYAGSDKLYHQWLSTVRKGSG
AILNTVK

Sequence of RAB35a-c002 (without HIS-tag):

SMARDYDHLFKLLIIGDSGVGKSSLLLRFADNTFSGSYITTIGVDFKIRTVEINGEKVKLQ
IWDTAGQERFRTITSTYYRGTHGVIVVYDVTSAESFVNVKRWLHEINQNCDDVCRILV

GNKNDDPERKVVETEDAYKFAGQMGIQLFETSAKENVNVEEMFNCITELVLRAKKDN
LAKQQ

Sequence of RAB35a-c002 (with HIS-tag):

MHHHHHHSSGVDLGTENLYFQSMARDYDHLFKLLIIGDSGVGKSSLLLRFADNTFSGS
YITTIGVDFKIRTVEINGEKVKLQIWDTAGQERFRTITSTYYRGTHGVIVVYDVTSAESF
VNVKRWLHEINQNCDDVCRILVGNKNDDPERKVVETEDAYKFAGQMGIQLFETSAKE
NVNVEEMFNCITELVLRAKKDNLAKQQ

Sequence of RAB39BA-c008 (without tag):

EAIWLYQFRLIVIGDSTVGKSCLIRRFTEGRFAQVSDPTVGVDFFSRLVEIEPGKRIKLQI
WDTAGQERFRSITRAYYRNSVGGLLLFDITNRRSFQNVHEWLEETKVHVQPYQIVFVL
VGHKCDLDTQRQVTRHEAEKLAAAYGMKYIETSARDAINVEKAFTDLTRDIYELVKR
GEITIQEGWEGVKSGFVPNVVHSSEEVVKS

FASP digest

RAB35 was reacted at 2 μM with 200 μM fragment on 300 μL 20 mM HEPES buffer, pH = 7.5. As a control, a 50 μL sample was taken into intact MS to confirm mass adduct formation. 200 μL of the sample (16μg RAB35 protein) were loaded onto a FASP 10kDa column and centrifuged 10 min at 11.5 ×G. The sample was washed with 8 M urea in 100mM TEAB 200 μL, followed by 50 % ACN and 6 M urea in 100mM TEAB 200 μL. Then, 220uL urea were left in the column, before 4.4 μL TCEP (125 mg/mL) and 22.55 μL IA (92mg/mL) were added. Reduction and alkylation were performed for 30min in the dark. The samples were centrifuged 5 min at 11.5 ×G and washed with 200 μL of 50 mM TEAB three times. For the digest, 1μg Trypsin (1μg/μL) was added to 200 μL of 1M urea in 50 mM TEAB, or 500 μg Chymotrypsin (5 μg/μL aliquot) were added to 200 μL of 1M urea in 0.1 M TEAB and 10 mM $CaCl_2$, and the sample was shaking over night at 37 °C and 1000 rpm.

GEF-activity assay

Compounds were tested at 500 μM final concentration using a nucleotide exchange assay. Dose-response curves were obtained using a 10-point 2-fold serial dilution with a high concentration of 500 μM. Compounds were dispensed using an ECHO acoustic dispenser in triplicate into a 384-well PP microplate (Greiner), with a maximum final concentration of 2% DMSO, including control wells. The assay buffer (20 mM Tris PH 7.5, 50 mM NaCl, 1mM $MgCl_2$, 100 μg/mL BSA and 1 mM DTT) was dispensed into sample and negative control wells as 10 μL, and positive control wells added GppNHp (400 μM in assay buffer, 10 μL, Jena BioScience) to give a final concentration of 200 μM. The enzymes were mixed to a concentration of 4 μM DENND1A and 0.1 μM RAB35 in assay buffer and dispensed into all wells as 5 μL, to make a final concentration of 1 μM and 0.025 μM respectively. The plate was centrifuged at 2000 rpm for 5 mins. After 2 h incubation at RT, BODIPY FL GTP (2 μM in assay buffer, 5 μL, ThermoFisher) was dispensed to all wells to give a final concentration of 0.5 μM. The plate was measured using the PheraSTAR FSX (BMG Labtech, FI 485/520, Gain 300) every 0.5 – 2.0 min. The initial rate was calculated and plotted using GraphPad Prism 9, the values being normalised to the positive and negative controls. All values were plotted as normalised initial rate against each compound or concentration in the case of dose responses (FI/s).

9. References

1. Rothweiler, E. M., Brennan, P. E., and Huber, K. V. M. (2022) Covalent fragment-based ligand screening approaches for identification of novel ubiquitin proteasome system modulators, *Biol Chem 403*, 391-402.
2. Brown, D. G., and Wobst, H. J. (2021) A Decade of FDA-Approved Drugs (2010-2019): Trends and Future Directions, *J Med Chem 64*, 2312-2338.
3. Mullard, A. (2023) 2022 FDA approvals, *Nat Rev Drug Discov 22*, 83-88.
4. Yamaguchi, S., Kaneko, M., and Narukawa, M. (2021) Approval success rates of drug candidates based on target, action, modality, application, and their combinations, *Clinical and Translational Science 14*, 1113-1122.
5. Hay, M., Thomas, D. W., Craighead, J. L., Economides, C., and Rosenthal, J. (2014) Clinical development success rates for investigational drugs, *Nature biotechnology 32*, 40-51.
6. Mullard, A. (2016) Parsing clinical success rates, *Nat Rev Drug Discov 15*, 447.
7. Harrison, R. K. (2016) Phase II and phase III failures: 2013-2015, *Nat Rev Drug Discov 15*, 817-818.
8. Sams-Dodd, F. (2005) Target-based drug discovery: is something wrong?, *Drug discovery today 10*, 139-147.
9. Paul, D., Sanap, G., Shenoy, S., Kalyane, D., Kalia, K., and Tekade, R. K. (2021) Artificial intelligence in drug discovery and development, *Drug Discov Today 26*, 80-93.
10. Sadri, A. (2023) Is Target-Based Drug Discovery Efficient? Discovery and "Off-Target" Mechanisms of All Drugs, *J Med Chem*.
11. Hughes, J. P., Rees, S., Kalindjian, S. B., and Philpott, K. L. (2011) Principles of early drug discovery, *Br J Pharmacol 162*, 1239-1249.
12. Sun, D., Gao, W., Hu, H., and Zhou, S. (2022) Why 90% of clinical drug development fails and how to improve it?, *Acta Pharmaceutica Sinica B 12*, 3049-3062.
13. Cook, D., Brown, D., Alexander, R., March, R., Morgan, P., Satterthwaite, G., and Pangalos, M. N. (2014) Lessons learned from the fate of AstraZeneca's drug pipeline: a five-dimensional framework, *Nat Rev Drug Discov 13*, 419-431.
14. Bunnage, M. E., Chekler, E. L., and Jones, L. H. (2013) Target validation using chemical probes, *Nat Chem Biol 9*, 195-199.
15. Moellering, R. E., and Cravatt, B. F. (2012) How chemoproteomics can enable drug discovery and development, *Chem Biol 19*, 11-22.
16. Bunnage, M. E., Gilbert, A. M., Jones, L. H., and Hett, E. C. (2015) Know your target, know your molecule, *Nat Chem Biol 11*, 368-372.
17. Ledford, H. (2012) Drug candidates derailed in case of mistaken identity, *Nature 483*, 519-519.
18. Rose, M., Burgess, J. T., O'Byrne, K., Richard, D. J., and Bolderson, E. (2020) PARP Inhibitors: Clinical Relevance, Mechanisms of Action and Tumor Resistance, *Front Cell Dev Biol 8*, 564601.
19. Patel, A. G., De Lorenzo, S. B., Flatten, K. S., Poirier, G. G., and Kaufmann, S. H. (2012) Failure of iniparib to inhibit poly(ADP-Ribose) polymerase in vitro, *Clin Cancer Res 18*, 1655-1662.
20. Kaur, R., Sidhu, P., and Singh, S. (2016) What failed BIA 10-2474 Phase I clinical trial? Global speculations and recommendations for future Phase I trials, *J Pharmacol Pharmacother 7*, 120-126.
21. Van Esbroeck, A. C., Janssen, A. P., Cognetta III, A. B., Ogasawara, D., Shpak, G., van der Kroeg, M., Kantae, V., Baggelaar, M. P., de Vrij, F. M., and Deng, H. (2017) Activity-based protein profiling reveals off-target proteins of the FAAH inhibitor BIA 10-2474, *Science 356*, 1084-1087.
22. Huang, Z., Ogasawara, D., Seneviratne, U. I., Cognetta, A. B., 3rd, Am Ende, C. W., Nason, D. M., Lapham, K., Litchfield, J., Johnson, D. S., and Cravatt, B. F. (2019) Global Portrait

of Protein Targets of Metabolites of the Neurotoxic Compound BIA 10-2474, *ACS Chem Biol 14*, 192-197.
23. Miller, M. T., and Strömland, K. (1999) Teratogen update: thalidomide: a review, with a focus on ocular findings and new potential uses, *Teratology 60*, 306-321.
24. Ito, T., Ando, H., Suzuki, T., Ogura, T., Hotta, K., Imamura, Y., Yamaguchi, Y., and Handa, H. (2010) Identification of a Primary Target of Thalidomide Teratogenicity, *Sci 327(5971)*, 1345-1350.
25. Lu, G., Middleton, R. E., Sun, H., Naniong, M., Ott, C. J., Mitsiades, C. S., Wong, K.-K., Bradner, J. E., and Kaelin Jr, W. G. (2014) The myeloma drug lenalidomide promotes the cereblon-dependent destruction of Ikaros proteins, *Science 343*, 305-309.
26. Krönke, J., Udeshi, N. D., Narla, A., Grauman, P., Hurst, S. N., McConkey, M., Svinkina, T., Heckl, D., Comer, E., and Li, X. (2014) Lenalidomide causes selective degradation of IKZF1 and IKZF3 in multiple myeloma cells, *Science 343*, 301-305.
27. Swinney, D. C., and Anthony, J. (2011) How were new medicines discovered?, *Nat Rev Drug Discov 10*, 507-519.
28. Eder, J., Sedrani, R., and Wiesmann, C. (2014) The discovery of first-in-class drugs: origins and evolution, *Nat Rev Drug Discov 13*, 577-587.
29. Kaufmann, S. H. (2008) Paul Ehrlich: founder of chemotherapy, *Nature Reviews Drug Discovery 7*, 373-373.
30. Lee, J. A., Uhlik, M. T., Moxham, C. M., Tomandl, D., and Sall, D. J. (2012) Modern phenotypic drug discovery is a viable, neoclassic pharma strategy, *J Med Chem 55*, 4527-4538.
31. Haasen, D., Schopfer, U., Antczak, C., Guy, C., Fuchs, F., and Selzer, P. (2017) How Phenotypic Screening Influenced Drug Discovery: Lessons from Five Years of Practice, *Assay Drug Dev Technol 15*, 239-246.
32. Zheng, W., Thorne, N., and McKew, J. C. (2013) Phenotypic screens as a renewed approach for drug discovery, *Drug Discov Today 18*, 1067-1073.
33. Stefaniak, J., and Huber, K. V. M. (2020) Importance of Quantifying Drug-Target Engagement in Cells, *ACS Medicinal Chemistry Letters 11*, 403-406.
34. Gunaseeli, I., Doss, M., Antzelevitch, C., Hescheler, J., and Sachinidis, A. (2010) Induced pluripotent stem cells as a model for accelerated patient-and disease-specific drug discovery, *Current medicinal chemistry 17*, 759-766.
35. Horman, S. R., Hogan, C., Reyes, K. D., Lo, F., and Antczak, C. (2015) Challenges and opportunities toward enabling phenotypic screening of complex and 3D cell models, *Future Medicinal Chemistry 7*, 513-525.
36. Farfel-Becker, T., Vitner, E. B., and Futerman, A. H. (2011) Animal models for Gaucher disease research, *Dis Model Mech 4*, 746-752.
37. Swinney, D. C., and Lee, J. A. (2020) Recent advances in phenotypic drug discovery, *F1000Res 9*.
38. Vincent, F., Nueda, A., Lee, J., Schenone, M., Prunotto, M., and Mercola, M. (2022) Phenotypic drug discovery: recent successes, lessons learned and new directions, *Nat Rev Drug Discov 21*, 899-914.
39. Van Goor, F., Hadida, S., Grootenhuis, P. D., Burton, B., Cao, D., Neuberger, T., Turnbull, A., Singh, A., Joubran, J., Hazlewood, A., Zhou, J., McCartney, J., Arumugam, V., Decker, C., Yang, J., Young, C., Olson, E. R., Wine, J. J., Frizzell, R. A., Ashlock, M., and Negulescu, P. (2009) Rescue of CF airway epithelial cell function in vitro by a CFTR potentiator, VX-770, *Proc Natl Acad Sci U S A 106*, 18825-18830.
40. Belema, M., and Meanwell, N. A. (2014) Discovery of daclatasvir, a pan-genotypic hepatitis C virus NS5A replication complex inhibitor with potent clinical effect, *J Med Chem 57*, 5057-5071.
41. Ratni, H., Ebeling, M., Baird, J., Bendels, S., Bylund, J., Chen, K. S., Denk, N., Feng, Z., Green, L., Guerard, M., Jablonski, P., Jacobsen, B., Khwaja, O., Kletzl, H., Ko, C. P., Kustermann, S., Marquet, A., Metzger, F., Mueller, B., Naryshkin, N. A., Paushkin, S.

V., Pinard, E., Poirier, A., Reutlinger, M., Weetall, M., Zeller, A., Zhao, X., and Mueller, L. (2018) Discovery of Risdiplam, a Selective Survival of Motor Neuron-2 (SMN2) Gene Splicing Modifier for the Treatment of Spinal Muscular Atrophy (SMA), *J Med Chem 61*, 6501-6517.
42. Choi, D., Stables, J. P., and Kohn, H. (1996) Synthesis and anticonvulsant activities of N-Benzyl-2-acetamidopropionamide derivatives, *J Med Chem 39*, 1907-1916.
43. Wassermann, A. M., Camargo, L. M., and Auld, D. S. (2014) Composition and applications of focus libraries to phenotypic assays, *Front Pharmacol 5*, 164.
44. Bantscheff, M., and Drewes, G. (2012) Chemoproteomic approaches to drug target identification and drug profiling, *Bioorg Med Chem 20*, 1973-1978.
45. Liu, J., Xiao, Q., Xiao, J., Niu, C., Li, Y., Zhang, X., Zhou, Z., Shu, G., and Yin, G. (2022) Wnt/β-catenin signalling: function, biological mechanisms, and therapeutic opportunities, *Signal Transduction and Targeted Therapy 7*, 3.
46. Huang, S. M., Mishina, Y. M., Liu, S., Cheung, A., Stegmeier, F., Michaud, G. A., Charlat, O., Wiellette, E., Zhang, Y., Wiessner, S., Hild, M., Shi, X., Wilson, C. J., Mickanin, C., Myer, V., Fazal, A., Tomlinson, R., Serluca, F., Shao, W., Cheng, H., Shultz, M., Rau, C., Schirle, M., Schlegl, J., Ghidelli, S., Fawell, S., Lu, C., Curtis, D., Kirschner, M. W., Lengauer, C., Finan, P. M., Tallarico, J. A., Bouwmeester, T., Porter, J. A., Bauer, A., and Cong, F. (2009) Tankyrase inhibition stabilizes axin and antagonizes Wnt signalling, *Nature 461*, 614-620.
47. Mazure, N. (2017) VDAC in cancer, *Biochimica et Biophysica Acta (BBA)-Bioenergetics 1858*, 665-673.
48. Yagoda, N., von Rechenberg, M., Zaganjor, E., Bauer, A. J., Yang, W. S., Fridman, D. J., Wolpaw, A. J., Smukste, I., Peltier, J. M., Boniface, J. J., Smith, R., Lessnick, S. L., Sahasrabudhe, S., and Stockwell, B. R. (2007) RAS-RAF-MEK-dependent oxidative cell death involving voltage-dependent anion channels, *Nature 447*, 864-868.
49. Yang, Y., Luo, M., Zhang, K., Zhang, J., Gao, T., Connell, D. O., Yao, F., Mu, C., Cai, B., Shang, Y., and Chen, W. (2020) Nedd4 ubiquitylates VDAC2/3 to suppress erastin-induced ferroptosis in melanoma, *Nature Communications 11*, 433.
50. Vane, J., and Botting, R. (2003) The mechanism of action of aspirin, *Thrombosis research 110*, 255-258.
51. Won, E., and Kim, Y.-K. (2017) An oldie but goodie: lithium in the treatment of bipolar disorder through neuroprotective and neurotrophic mechanisms, *International journal of molecular sciences 18*, 2679.
52. Arrowsmith, C. H., Audia, J. E., Austin, C., Baell, J., Bennett, J., Blagg, J., Bountra, C., Brennan, P. E., Brown, P. J., Bunnage, M. E., Buser-Doepner, C., Campbell, R. M., Carter, A. J., Cohen, P., Copeland, R. A., Cravatt, B., Dahlin, J. L., Dhanak, D., Edwards, A. M., Frederiksen, M., Frye, S. V., Gray, N., Grimshaw, C. E., Hepworth, D., Howe, T., Huber, K. V., Jin, J., Knapp, S., Kotz, J. D., Kruger, R. G., Lowe, D., Mader, M. M., Marsden, B., Mueller-Fahrnow, A., Muller, S., O'Hagan, R. C., Overington, J. P., Owen, D. R., Rosenberg, S. H., Roth, B., Ross, R., Schapira, M., Schreiber, S. L., Shoichet, B., Sundstrom, M., Superti-Furga, G., Taunton, J., Toledo-Sherman, L., Walpole, C., Walters, M. A., Willson, T. M., Workman, P., Young, R. N., and Zuercher, W. J. (2015) The promise and peril of chemical probes, *Nat Chem Biol 11*, 536-541.
53. Workman, P., and Collins, I. (2010) Probing the probes: fitness factors for small molecule tools, *Chem Biol 17*, 561-577.
54. Sweis, R. F. (2015) Target (in) validation: a critical, sometimes unheralded, role of modern medicinal chemistry, pp 618-621, ACS Publications.
55. Tamoki, T., Nomoto, H., Takahashi, I., Kato, Y., Morimoto, M., and Tomita, F. (1986) Staurosporine, a potent inhibitor of phospholipid calcium dependent protein kinase, *Biochem. Biophys. Res. Commun 135*, 397-402.

56. Wang, Y., Cornett, A., King, F. J., Mao, Y., Nigsch, F., Paris, C. G., McAllister, G., and Jenkins, J. L. (2016) Evidence-Based and Quantitative Prioritization of Tool Compounds in Phenotypic Drug Discovery, *Cell Chem Biol 23*, 862-874.
57. Baell, J. B., and Holloway, G. A. (2010) New substructure filters for removal of pan assay interference compounds (PAINS) from screening libraries and for their exclusion in bioassays, *J Med Chem 53*, 2719-2740.
58. Baell, J., and Walters, M. A. (2014) Chemistry: Chemical con artists foil drug discovery, *Nature 513*, 481-483.
59. Pacholec, M., Bleasdale, J. E., Chrunyk, B., Cunningham, D., Flynn, D., Garofalo, R. S., Griffith, D., Griffor, M., Loulakis, P., Pabst, B., Qiu, X., Stockman, B., Thanabal, V., Varghese, A., Ward, J., Withka, J., and Ahn, K. (2010) SRT1720, SRT2183, SRT1460, and resveratrol are not direct activators of SIRT1, *J Biol Chem 285*, 8340-8351.
60. De la Torre, R., De Sola, S., Pons, M., Duchon, A., de Lagran, M. M., Farré, M., Fito, M., Benejam, B., Langohr, K., and Rodriguez, J. (2014) Epigallocatechin-3-gallate, a DYRK1A inhibitor, rescues cognitive deficits in D own syndrome mouse models and in humans, *Molecular nutrition & food research 58*, 278-288.
61. Kanlaya, R., and Thongboonkerd, V. (2019) Molecular Mechanisms of Epigallocatechin-3-Gallate for Prevention of Chronic Kidney Disease and Renal Fibrosis: Preclinical Evidence, *Curr Dev Nutr 3*, nzz101.
62. Baell, J. B., and Nissink, J. W. M. (2018) Seven Year Itch: Pan-Assay Interference Compounds (PAINS) in 2017-Utility and Limitations, *ACS Chem Biol 13*, 36-44.
63. Filippakopoulos, P., Qi, J., Picaud, S., Shen, Y., Smith, W. B., Fedorov, O., Morse, E. M., Keates, T., Hickman, T. T., Felletar, I., Philpott, M., Munro, S., McKeown, M. R., Wang, Y., Christie, A. L., West, N., Cameron, M. J., Schwartz, B., Heightman, T. D., La Thangue, N., French, C. A., Wiest, O., Kung, A. L., Knapp, S., and Bradner, J. E. (2010) Selective inhibition of BET bromodomains, *Nature 468*, 1067-1073.
64. Nicodeme, E., Jeffrey, K. L., Schaefer, U., Beinke, S., Dewell, S., Chung, C. W., Chandwani, R., Marazzi, I., Wilson, P., Coste, H., White, J., Kirilovsky, J., Rice, C. M., Lora, J. M., Prinjha, R. K., Lee, K., and Tarakhovsky, A. (2010) Suppression of inflammation by a synthetic histone mimic, *Nature 468*, 1119-1123.
65. Antolin, A. A., Sanfelice, D., Crisp, A., Villasclaras Fernandez, E., Mica, I. L., Chen, Y., Collins, I., Edwards, A., Muller, S., Al-Lazikani, B., and Workman, P. (2023) The Chemical Probes Portal: an expert review-based public resource to empower chemical probe assessment, selection and use, *Nucleic Acids Res 51*, D1492-D1502.
66. Jones, L. H., Beal, D., Selby, M. D., Everson, O., Burslem, G. M., Dodd, P., Millbank, J., Tran, T.-D., Wakenhut, F., and Graham, E. J. (2011) In-cell click labelling of small molecules to determine subcellular localisation, *Journal of chemical biology 4*, 49-53.
67. Ahn, K., Smith, S. E., Liimatta, M. B., Beidler, D., Sadagopan, N., Dudley, D. T., Young, T., Wren, P., Zhang, Y., and Swaney, S. (2011) Mechanistic and pharmacological characterization of PF-04457845: a highly potent and selective fatty acid amide hydrolase inhibitor that reduces inflammatory and noninflammatory pain, *Journal of Pharmacology and Experimental Therapeutics 338*, 114-124.
68. Mullard, A. (2019) A probe for every protein, *Nat Rev Drug Discov 18*, 733-736.
69. Muller, S., Ackloo, S., Al Chawaf, A., Al-Lazikani, B., Antolin, A., Baell, J. B., Beck, H., Beedie, S., Betz, U. A. K., Bezerra, G. A., Brennan, P. E., Brown, D., Brown, P. J., Bullock, A. N., Carter, A. J., Chaikuad, A., Chaineau, M., Ciulli, A., Collins, I., Dreher, J., Drewry, D., Edfeldt, K., Edwards, A. M., Egner, U., Frye, S. V., Fuchs, S. M., Hall, M. D., Hartung, I. V., Hillisch, A., Hitchcock, S. H., Homan, E., Kannan, N., Kiefer, J. R., Knapp, S., Kostic, M., Kubicek, S., Leach, A. R., Lindemann, S., Marsden, B. D., Matsui, H., Meier, J. L., Merk, D., Michel, M., Morgan, M. R., Mueller-Fahrnow, A., Owen, D. R., Perry, B. G., Rosenberg, S. H., Saikatendu, K. S., Schapira, M., Scholten, C., Sharma, S., Simeonov, A., Sundstrom, M., Superti-Furga, G., Todd, M. H., Tredup, C., Vedadi, M., von Delft, F., Willson, T. M., Winter, G. E., Workman, P., and

Arrowsmith, C. H. (2022) Target 2035 - update on the quest for a probe for every protein, *RSC Med Chem 13*, 13-21.
70. Hartung, I. V., Rudolph, J., Mader, M. M., Mulder, M. P. C., and Workman, P. (2023) Expanding Chemical Probe Space: Quality Criteria for Covalent and Degrader Probes, *J Med Chem 66*, 9297-9312.
71. Hansen, R., Peters, U., Babbar, A., Chen, Y., Feng, J., Janes, M. R., Li, L. S., Ren, P., Liu, Y., and Zarrinkar, P. P. (2018) The reactivity-driven biochemical mechanism of covalent KRAS(G12C) inhibitors, *Nat Struct Mol Biol 25*, 454-462.
72. Dale, N. C., Johnstone, E. K. M., White, C. W., and Pfleger, K. D. G. (2019) NanoBRET: The Bright Future of Proximity-Based Assays, *Front Bioeng Biotechnol 7*, 56.
73. Dacres, H., Michie, M., Wang, J., Pfleger, K. D., and Trowell, S. C. (2012) Effect of enhanced Renilla luciferase and fluorescent protein variants on the Förster distance of Bioluminescence resonance energy transfer (BRET), *Biochemical and biophysical research communications 425*, 625-629.
74. Pfleger, K. D. G., and Eidne, K. A. (2006) Illuminating insights into protein-protein interactions using bioluminescence resonance energy transfer (BRET), *3*, 165-174.
75. Xu, Y., Piston, D. W., and Johnson, C. H. (1999) A bioluminescence resonance energy transfer (BRET) system: application to interacting circadian clock proteins, *Proceedings of the National Academy of Sciences 96*, 151-156.
76. Hall, M. P., Unch, J., Binkowski, B. F., Valley, M. P., Butler, B. L., Wood, M. G., Otto, P., Zimmerman, K., Vidugiris, G., and Machleidt, T. (2012) Engineered luciferase reporter from a deep sea shrimp utilizing a novel imidazopyrazinone substrate, *ACS chemical biology 7*, 1848-1857.
77. Machleidt, T., Woodroofe, C. C., Schwinn, M. K., Mendez, J., Robers, M. B., Zimmerman, K., Otto, P., Daniels, D. L., Kirkland, T. A., and Wood, K. V. (2015) NanoBRET-A Novel BRET Platform for the Analysis of Protein-Protein Interactions, *ACS Chem Biol 10*, 1797-1804.
78. Dixon, A. S., Schwinn, M. K., Hall, M. P., Zimmerman, K., Otto, P., Lubben, T. H., Butler, B. L., Binkowski, B. F., Machleidt, T., and Kirkland, T. A. (2016) NanoLuc complementation reporter optimized for accurate measurement of protein interactions in cells, *ACS chemical biology 11*, 400-408.
79. Storme, J., Cannaert, A., Van Craenenbroeck, K., and Stove, C. P. (2018) Molecular dissection of the human A3 adenosine receptor coupling with β-arrestin2, *Biochemical pharmacology 148*, 298-307.
80. Eidne, K. A., Kroeger, K. M., and Hanyaloglu, A. C. (2002) Applications of novel resonance energy transfer techniques to study dynamic hormone receptor interactions in living cells, *Trends in Endocrinology & Metabolism 13*, 415-421.
81. Vasta, J. D., Corona, C. R., Wilkinson, J., Zimprich, C. A., Hartnett, J. R., Ingold, M. R., Zimmerman, K., Machleidt, T., Kirkland, T. A., Huwiler, K. G., Ohana, R. F., Slater, M., Otto, P., Cong, M., Wells, C. I., Berger, B. T., Hanke, T., Glas, C., Ding, K., Drewry, D. H., Huber, K. V. M., Willson, T. M., Knapp, S., Muller, S., Meisenheimer, P. L., Fan, F., Wood, K. V., and Robers, M. B. (2018) Quantitative, Wide-Spectrum Kinase Profiling in Live Cells for Assessing the Effect of Cellular ATP on Target Engagement, *Cell Chem Biol 25*, 206-214 e211.
82. Wells, C. I., Vasta, J. D., Corona, C. R., Wilkinson, J., Zimprich, C. A., Ingold, M. R., Pickett, J. E., Drewry, D. H., Pugh, K. M., Schwinn, M. K., Hwang, B. B., Zegzouti, H., Huber, K. V. M., Cong, M., Meisenheimer, P. L., Willson, T. M., and Robers, M. B. (2020) Quantifying CDK inhibitor selectivity in live cells, *Nat Commun 11*, 2743.
83. Vasta, J., and Robers, M. (2019) Energy Transfers Reveal Kinetics of Intracellular Binding, *Genetic Engineering & Biotechnology News 39*, 48-50.
84. Molina, D. M., Jafari, R., Ignatushchenko, M., Seki, T., Larsson, E. A., Dan, C., Sreekumar, L., Cao, Y., and Nordlund, P. (2013) Monitoring Drug Target Engagement in Cells and Tissues Using the Cellular Thermal Shift Assay, *Science 341*, 84-87.

85. Fedorov, O., Marsden, B., Pogacic, V., Rellos, P., Muller, S., Bullock, A. N., Schwaller, J., Sundstrom, M., and Knapp, S. (2007) A systematic interaction map of validated kinase inhibitors with Ser/Thr kinases, *Proc Natl Acad Sci U S A 104*, 20523-20528.
86. Gao, K., Oerlemans, R., and Groves, M. R. (2020) Theory and applications of differential scanning fluorimetry in early-stage drug discovery, *Biophys Rev 12*, 85-104.
87. Axelsson, H., Almqvist, H., Seashore-Ludlow, B., and Lundbäck, T. (2016) Screening for target engagement using the cellular thermal shift assay-CETSA, *Assay Guidance Manual [Internet]*.
88. Tolvanen, T. A. (2022) Current Advances in CETSA, *Front Mol Biosci 9*, 866764.
89. Axelrod, D., Koppel, D., Schlessinger, J., Elson, E., and Webb, W. W. (1976) Mobility measurement by analysis of fluorescence photobleaching recovery kinetics, *Biophysical journal 16*, 1055-1069.
90. Reits, E. A., and Neefjes, J. J. (2001) From fixed to FRAP: measuring protein mobility and activity in living cells, *Nature cell biology 3*, E145.
91. Bancaud, A., Huet, S., Rabut, G., and Ellenberg, J. (2010) Fluorescence perturbation techniques to study mobility and molecular dynamics of proteins in live cells: FRAP, photoactivation, photoconversion, and FLIP, *Cold Spring Harbor Protocols 2010*, pdb. top90-pdb. top90.
92. Ahmed, S., Clayton, H. A. A., and Wright, G. (2016) Practical manual for fluorescence microscopy techniques, *PicoQuant GmbH. URL: https://www. picoquant. com/images/uploads/page/files/17319/4 {_} td {_} flim.pdf*.
93. Greig, J., and Bulgakova, N. A. (2021) Fluorescence recovery after photobleaching to study the dynamics of membrane-bound proteins in vivo using the Drosophila embryo, *The Epithelial-to Mesenchymal Transition: Methods and Protocols*, 145-159.
94. Marguet, D., Spiliotis, E. T., Pentcheva, T., Lebowitz, M., Schneck, J., and Edidin, M. (1999) Lateral diffusion of GFP-tagged H2Ld molecules and of GFP-TAP1 reports on the assembly and retention of these molecules in the endoplasmic reticulum, *Immunity 11*, 231-240.
95. Partikian, A., Ölveczky, B., Swaminathan, R., Li, Y., and Verkman, A. (1998) Rapid diffusion of green fluorescent protein in the mitochondrial matrix, *The Journal of cell biology 140*, 821-829.
96. Govindaraj, K., Hendriks, J., Lidke, D. S., Karperien, M., and Post, J. N. (2019) Changes in Fluorescence Recovery After Photobleaching (FRAP) as an indicator of SOX9 transcription factor activity, *Biochim Biophys Acta Gene Regul Mech 1862*, 107-117.
97. Houtsmuller, A. B. (2005) Fluorescence Recovery after Photobleaching: Application to Nuclear Proteins, In *Microscopy Techniques: -/-* (Rietdorf, J., Ed.), pp 177-199, Springer Berlin Heidelberg, Berlin, Heidelberg.
98. Philpott, M., Rogers, C. M., Yapp, C., Wells, C., Lambert, J.-P., Strain-Damerell, C., Burgess-Brown, N. A., Gingras, A.-C., Knapp, S., and Müller, S. (2014) Assessing cellular efficacy of bromodomain inhibitors using fluorescence recovery after photobleaching, *Epigenetics & chromatin 7*, 1-12.
99. Domon, B., and Aebersold, R. (2010) Options and considerations when selecting a quantitative proteomics strategy, *Nature biotechnology 28*, 710-721.
100. Ünlü, M., Morgan, M. E., and Minden, J. S. (1997) Difference gel electrophoresis. A single gel method for detecting changes in protein extracts, *Electrophoresis 18*, 2071-2077.
101. Issaq, H. J., and Veenstra, T. D. (2008) Two-dimensional polyacrylamide gel electrophoresis (2D-PAGE): advances and perspectives, *Biotechniques 44*, 697-700.
102. Bian, Y., The, M., Giansanti, P., Mergner, J., Zheng, R., Wilhelm, M., Boychenko, A., and Kuster, B. (2021) Identification of 7 000-9 000 Proteins from Cell Lines and Tissues by Single-Shot Microflow LC-MS/MS, *Anal Chem 93*, 8687-8692.
103. Hebert, A. S., Prasad, S., Belford, M. W., Bailey, D. J., McAlister, G. C., Abbatiello, S. E., Huguet, R., Wouters, E. R., Dunyach, J. J., Brademan, D. R., Westphall, M. S., and Coon,

J. J. (2018) Comprehensive Single-Shot Proteomics with FAIMS on a Hybrid Orbitrap Mass Spectrometer, *Anal Chem 90*, 9529-9537.
104. Ong, S.-E., Blagoev, B., Kratchmarova, I., Kristensen, D. B., Steen, H., Pandey, A., and Mann, M. (2002) Stable isotope labeling by amino acids in cell culture, SILAC, as a simple and accurate approach to expression proteomics, *Molecular & cellular proteomics 1*, 376-386.
105. Gygi, S. P., Rist, B., Gerber, S. A., Turecek, F., Gelb, M. H., and Aebersold, R. (1999) Quantitative analysis of complex protein mixtures using isotope-coded affinity tags, *Nature biotechnology 17*, 994-999.
106. Thompson, A., Schäfer, J., Kuhn, K., Kienle, S., Schwarz, J., Schmidt, G., Neumann, T., and and Hamon, C. (2003) Tandem Mass Tags: A Novel Quantification Strategy for Comparative Analysis of Complex Protein Mixtures by MS/MS, *Anal. Chem*.
107. Bantscheff, M., Schirle, M., Sweetman, G., Rick, J., and Kuster, B. (2007) Quantitative mass spectrometry in proteomics: a critical review, *Analytical and bioanalytical chemistry 389*, 1017-1031.
108. Bantscheff, M., Scholten, A., and Heck, A. J. (2009) Revealing promiscuous drug-target interactions by chemical proteomics, *Drug Discov Today 14*, 1021-1029.
109. Brehmer, D., Greff, Z., Godl, K., Blencke, S., Kurtenbach, A., Weber, M., Müller, S., Klebl, B., Cotten, M., and Kéri, G. r. (2005) Cellular targets of gefitinib, *Cancer research 65*, 379-382.
110. Godl, K., Gruss, O. J., Eickhoff, J., Wissing, J., Blencke, S., Weber, M., Degen, H., Brehmer, D., Orfi, L., and Horváth, Z. (2005) Proteomic characterization of the angiogenesis inhibitor SU6668 reveals multiple impacts on cellular kinase signaling, *Cancer Research 65*, 6919-6926.
111. Reinecke, M., Heinzlmeir, S., Wilhelm, M., Médard, G., Klaeger, S., and Kuster, B. (2019) Kinobeads: A chemical proteomic approach for kinase inhibitor selectivity profiling and target discovery, *Target Discovery and Validation: Methods and Strategies for Drug Discovery*, 97-130.
112. Bantscheff, M., Eberhard, D., Abraham, Y., Bastuck, S., Boesche, M., Hobson, S., Mathieson, T., Perrin, J., Raida, M., and Rau, C. (2007) Quantitative chemical proteomics reveals mechanisms of action of clinical ABL kinase inhibitors, *Nature biotechnology 25*, 1035-1044.
113. Eberl, H. C., Werner, T., Reinhard, F. B., Lehmann, S., Thomson, D., Chen, P., Zhang, C., Rau, C., Muelbaier, M., Drewes, G., Drewry, D., and Bantscheff, M. (2019) Chemical proteomics reveals target selectivity of clinical Jak inhibitors in human primary cells, *Sci Rep 9*, 14159.
114. Weerapana, E., Speers, A. E., and Cravatt, B. F. (2007) Tandem orthogonal proteolysis-activity-based protein profiling (TOP-ABPP)—a general method for mapping sites of probe modification in proteomes, *Nature Protocols 2*, 1414-1425.
115. Cravatt, B. F., Wright, A. T., and Kozarich, J. W. (2008) Activity-Based Protein Profiling: From Enzyme Chemistry to Proteomic Chemistry, *Annu Rev Biochem 77*, 383-414.
116. Liu, Y., Patricelli, M. P., and Cravatt, B. F. (1999) Activity-based protein profiling: The serine hydrolases, *PNAS 96*, 14694-14699.
117. Chung, C. Y.-S., Shin, H. R., Berdan, C. A., Ford, B., Ward, C. C., Olzmann, J. A., Zoncu, R., and Nomura, D. K. (2019) Covalent targeting of the vacuolar H+-ATPase activates autophagy via mTORC1 inhibition, *Nature Chemical Biology 15*, 776-785.
118. Couvertier, S. M., and Weerapana, E. (2014) Cysteine-reactive chemical probes based on a modular 4-aminopiperidine scaffold, *Med. Chem. Commun. 5*, 358-362.
119. Backus, K. M., Correia, B. E., Lum, K. M., Forli, S., Horning, B. D., Gonzalez-Paez, G. E., Chatterjee, S., Lanning, B. R., Teijaro, J. R., Olson, A. J., Wolan, D. W., and Cravatt, B. F. (2016) Proteome-wide covalent ligand discovery in native biological systems, *Nat 534*, 570-574.

120. Abo, M., Bak, D. W., and Weerapana, E. (2017) Optimization of Caged Electrophiles for Improved Monitoring of Cysteine Reactivity in Living Cells, *Chembiochem 18*, 81-84.
121. Abo, M., and Weerapana, E. (2015) A Caged Electrophilic Probe for Global Analysis of Cysteine Reactivity in Living Cells, *J Am Chem Soc 137*, 7087-7090.
122. Poole, L. B. (2015) The basics of thiols and cysteines in redox biology and chemistry, *Free Radic Biol Med 80*, 148-157.
123. Weerapana, E., Wang, C., Simon, G. M., Richter, F., Khare, S., Dillon, M. B. D., Bachovchin, D. A., Mowen, K., Baker, D., and Cravatt, B. F. (2010) Quantitative reactivity profiling predicts functional cysteines in proteomes, *Nat 468*, 790-795.
124. Lin, S., Yang, X., Jia, S., Weeks, A. M., Hornsby, M., Lee, P. S., Nichiporuk, R. V., Iavarone, A. T., Wells, J. A., Toste, F. D., and Chang, C. J. (2017) Redox-based reagents for chemoselective methionine bioconjugation, *Science 355*, 597-602.
125. Greenbaum, D., Baruch, A., Hayrapetian, L., Darula, Z., Burlingame, A., Medzihradszky, K. F., and Bogyo, M. (2002) Chemical approaches for functionally probing the proteome, *Mol Cell Proteomics 1*, 60-68.
126. Vinogradova, E. V., Zhang, X., Remillard, D., Lazar, D. C., Suciu, R. M., Wang, Y., Bianco, G., Yamashita, Y., Crowley, V. M., Schafroth, M. A., Yokoyama, M., Konrad, D. B., Lum, K. M., Simon, G. M., Kemper, E. K., Lazear, M. R., Yin, S., Blewett, M. M., Dix, M. M., Nguyen, N., Shokhirev, M. N., Chin, E. N., Lairson, L. L., Melillo, B., Schreiber, S. L., Forli, S., Teijaro, J. R., and Cravatt, B. F. (2020) An Activity-Guided Map of Electrophile-Cysteine Interactions in Primary Human T Cells, *Cell 182*, 1009-1026.e1029.
127. Wang, C., Weerapana, E., Blewett, M. M., and Cravatt, B. F. (2014) A chemoproteomic platform to quantitatively map targets of lipid-derived electrophiles, *Nat Methods 11*, 79-88.
128. Chen, X., Wong, Y. K., Wang, J., Zhang, J., Lee, Y. M., Shen, H. M., Lin, Q., and Hua, Z. C. (2017) Target identification with quantitative activity based protein profiling (ABPP), *Proteomics 17*, 3-4.
129. Hein, J. E., and Fokin, V. V. (2010) Copper-catalyzed azide-alkyne cycloaddition (CuAAC) and beyond: new reactivity of copper(I) acetylides, *Chem Soc Rev 39*, 1302-1315.
130. Hoch, D. G., Abegg, D., and Adibekian, A. (2018) Cysteine-reactive probes and their use in chemical proteomics, *Chem Commun (Camb) 54*, 4501-4512.
131. Zanon, P. R. A., Lewald, L., and Hacker, S. M. (2020) Isotopically Labeled Desthiobiotin Azide (isoDTB) Tags Enable Global Profiling of the Bacterial Cysteinome, *Angew Chem Int Ed Engl 59*, 2829-2836.
132. Kuljanin, M., Mitchell, D. C., Schweppe, D. K., Gikandi, A. S., Nusinow, D. P., Bulloch, N. J., Vinogradova, E. V., Wilson, D. L., Kool, E. T., Mancias, J. D., Cravatt, B. F., and Gygi, S. P. (2021) Reimagining high-throughput profiling of reactive cysteines for cell-based screening of large electrophile libraries, *Nat Biotechnol 39*, 630–641
133. Yan, T., Desai, H. S., Boatner, L. M., Yen, S. L., Cao, J., Palafox, M. F., Jami-Alahmadi, Y., and Backus, K. M. (2021) SP3-FAIMS Chemoproteomics for High-Coverage Profiling of the Human Cysteinome*, *Chembiochem 22*, 1841-1851.
134. Bar-Peled, L., Kemper, E. K., Suciu, R. M., Vinogradova, E. V., Backus, K. M., Horning, B. D., Paul, T. A., Ichu, T. A., Svensson, R. U., Olucha, J., Chang, M. W., Kok, B. P., Zhu, Z., Ihle, N. T., Dix, M. M., Jiang, P., Hayward, M. M., Saez, E., Shaw, R. J., and Cravatt, B. F. (2017) Chemical Proteomics Identifies Druggable Vulnerabilities in a Genetically Defined Cancer, *Cell 171*, 696-709 e623.
135. Crowley, V. M., Thielert, M., and Cravatt, B. F. (2021) Functionalized Scout Fragments for Site-Specific Covalent Ligand Discovery and Optimization, *ACS Central Science 7*, 613-623.
136. Cisar, J. S., Weber, O. D., Clapper, J. R., Blankman, J. L., Henry, C. L., Simon, G. M., Alexander, J. P., Jones, T. K., Ezekowitz, R. A. B., O'Neill, G. P., and Grice, C. A. (2018)

Identification of ABX-1431, a Selective Inhibitor of Monoacylglycerol Lipase and Clinical Candidate for Treatment of Neurological Disorders, *J Med Chem 61*, 9062-9084.
137. Janssen, A. P. A., van der Vliet, D., Bakker, A. T., Jiang, M., Grimm, S. H., Campiani, G., Butini, S., and van der Stelt, M. (2018) Development of a Multiplexed Activity-Based Protein Profiling Assay to Evaluate Activity of Endocannabinoid Hydrolase Inhibitors, *ACS Chem Biol 13*, 2406-2413.
138. Knuckley, B., Luo, Y., and Thompson, P. R. (2008) Profiling Protein Arginine Deiminase 4 (PAD4): a novel screen to identify PAD4 inhibitors, *Bioorg Med Chem 16*, 739-745.
139. Knuckley, B., Jones, J. E., Bachovchin, D. A., Slack, J., Causey, C. P., Brown, S. J., Rosen, H., Cravatt, B. F., and Thompson, P. R. (2010) A fluopol-ABPP HTS assay to identify PAD inhibitors, *Chem Commun (Camb) 46*, 7175-7177.
140. Drechsel, J., Kyrousi, C., Cappello, S., and Sieber, S. A. (2020) Tranylcypromine specificity for monoamine oxidase is limited by promiscuous protein labelling and lysosomal trapping, *RSC Chem Biol 1*, 209-213.
141. Aljoundi, A., Bjij, I., El Rashedy, A., and Soliman, M. E. S. (2020) Covalent Versus Non-covalent Enzyme Inhibition: Which Route Should We Take? A Justification of the Good and Bad from Molecular Modelling Perspective, *Protein J 39*, 97-105.
142. Hopkins, A. L., and Groom, C. R. (2002) The druggable genome, *Nat Rev Drug Discov 1*, 727-730.
143. Ray, S., and Murkin, A. S. (2019) New Electrophiles and Strategies for Mechanism-Based and Targeted Covalent Inhibitor Design, *Biochemistry 58*, 5234-5244.
144. Blewett, M. M., Xie, J., Zaro, B. W., Backus, K. M., Altmann, A., Teijaro, J. R., and Cravatt, B. F. (2016) Chemical proteomic map of dimethyl fumarate–sensitive cysteines in primary human T cells, *Sci Signal 9*, rs10-rs10.
145. Tuley, A., and Fast, W. (2018) The Taxonomy of Covalent Inhibitors, *Biochemistry 57*, 3326-3337.
146. Maurais, A. J., and Weerapana, E. (2019) Reactive-cysteine profiling for drug discovery, *Curr Opin Chem Biol 50*, 29-36.
147. Sutanto, F., Konstantinidou, M., and Domling, A. (2020) Covalent inhibitors: a rational approach to drug discovery, *RSC Med Chem 11*, 876-884.
148. Ward, J. A., Pinto-Fernandez, A., Cornelissen, L., Bonham, S., Diaz-Saez, L., Riant, O., Huber, K. V. M., Kessler, B. M., Feron, O., and Tate, E. W. (2020) Re-Evaluating the Mechanism of Action of alpha,beta-Unsaturated Carbonyl DUB Inhibitors b-AP15 and VLX1570: A Paradigmatic Example of Unspecific Protein Cross-linking with Michael Acceptor Motif-Containing Drugs, *J Med Chem 63*, 3756-3762.
149. Johansson, H., Isabella Tsai, Y.-C., Fantom, K., Chung, C.-W., Kümper, S., Martino, L., Thomas, D. A., Eberl, H. C., Muelbaier, M., House, D., and Rittinger, K. (2019) Fragment-Based Covalent Ligand Screening Enables Rapid Discovery of Inhibitors for the RBR E3 Ubiquitin Ligase HOIP, *J Am Chem Soc 141*, 2703-2712.
150. Boike, L., Cioffi, A. G., Majewski, F. C., Co, J., Henning, N. J., Jones, M. D., Liu, G., McKenna, J. M., Tallarico, J. A., Schirle, M., and Nomura, D. K. (2020) Discovery of a Functional Covalent Ligand Targeting an Intrinsically Disordered Cysteine within MYC, *Cell Chem Biol 28(1)*, 4-13.e17.
151. Pinch, B. J., Doctor, Z. M., Nabet, B., Browne, C. M., Seo, H. S., Mohardt, M. L., Kozono, S., Lian, X., Manz, T. D., Chun, Y., Kibe, S., Zaidman, D., Daitchman, D., Yeoh, Z. C., Vangos, N. E., Geffken, E. A., Tan, L., Ficarro, S. B., London, N., Marto, J. A., Buratowski, S., Dhe-Paganon, S., Zhou, X. Z., Lu, K. P., and Gray, N. S. (2020) Identification of a potent and selective covalent Pin1 inhibitor, *Nat Chem Biol 16*, 979-987.
152. Zaidman, D., Gehrtz, P., Filep, M., Fearon, D., Gabizon, R., Douangamath, A., Prilusky, J., Duberstein, S., Cohen, G., Owen, C. D., Resnick, E., Strain-Damerell, C., Lukacik, P., Covid-Moonshot, C., Barr, H., Walsh, M. A., von Delft, F., and London, N. (2021) An

automatic pipeline for the design of irreversible derivatives identifies a potent SARS-CoV-2 M(pro) inhibitor, *Cell Chem Biol S2451-9456*, 00263-00264.
153. Scott, D. E., Coyne, A. G., Hudson, S. A., and Abell, C. (2012) Fragment-based approaches in drug discovery and chemical biology, *Biochemistry 51*, 4990-5003.
154. Doak, B. C., Norton, R. S., and Scanlon, M. J. (2016) The ways and means of fragment-based drug design, *Pharmacol Ther 167*, 28-37.
155. Kirsch, P., Hartman, A. M., Hirsch, A. K. H., and Empting, M. (2019) Concepts and Core Principles of Fragment-Based Drug Design, *Molecules 24(23)*, 4309.
156. Lu, W., Kostic, M., Zhang, T., Che, J., Patricelli, M. P., Jones, L. H., Chouchani, E. T., and Gray, N. S. (2021) Fragment-based covalent ligand discovery, *RSC Chem Biol 2*, 354-367.
157. Resnick, E., Bradley, A., Gan, J., Douangamath, A., Krojer, T., Sethi, R., Geurink, P. P., Aimon, A., Amitai, G., Bellini, D., Bennett, J., Fairhead, M., Fedorov, O., Gabizon, R., Gan, J., Guo, J., Plotnikov, A., Reznik, N., Ruda, G. F., Diaz-Saez, L., Straub, V. M., Szommer, T., Velupillai, S., Zaidman, D., Zhang, Y., Coker, A. R., Dowson, C. G., Barr, H. M., Wang, C., Huber, K. V. M., Brennan, P. E., Ovaa, H., von Delft, F., and London, N. (2019) Rapid Covalent-Probe Discovery by Electrophile-Fragment Screening, *J Am Chem Soc 141*, 8951-8968.
158. Bancet, A., Raingeval, C., Lomberget, T., Le Borgne, M., Guichou, J. F., and Krimm, I. (2020) Fragment Linking Strategies for Structure-Based Drug Design, *J Med Chem 63*, 11420-11435.
159. Kulak, N. A., Geyer, P. E., and Mann, M. (2017) Loss-less Nano-fractionator for High Sensitivity, High Coverage Proteomics, *Mol Cell Proteomics 16*, 694-705.
160. Dikic, I. (2017) Proteasomal and autophagic degradation systems, *Annual review of biochemistry 86*, 193-224.
161. Klaips, C. L., Jayaraj, G. G., and Hartl, F. U. (2018) Pathways of cellular proteostasis in aging and disease, *Journal of Cell Biology 217*, 51-63.
162. Hipp, M. S., Kasturi, P., and Hartl, F. U. (2019) The proteostasis network and its decline in ageing, *Nat Rev Mol Cell Biol 20*, 421-435.
163. Hipp, M. S., Park, S. H., and Hartl, F. U. (2014) Proteostasis impairment in protein-misfolding and -aggregation diseases, *Trends Cell Biol 24*, 506-514.
164. Ross, C. A., and Poirier, M. A. (2004) Protein aggregation and neurodegenerative disease, *Nat Med 10 Suppl*, S10-17.
165. Ciechanover, A. (2017) Intracellular protein degradation: From a vague idea thru the lysosome and the ubiquitin-proteasome system and onto human diseases and drug targeting, *Best Pract Res Clin Haematol 30*, 341-355.
166. Ashford, T. P., and Porter, K. R. (1962) Cytoplasmic components in hepatic cell lysosomes, *J Cell Biol 12*, 198-202.
167. Lamb, C. A., Yoshimori, T., and Tooze, S. A. (2013) The autophagosome: origins unknown, biogenesis complex, *Nat Rev Mol Cell Biol 14*, 759-774.
168. Wertz, I. E., and Wang, X. (2019) From Discovery to Bedside: Targeting the Ubiquitin System, *Cell Chem Biol 26*, 156-177.
169. Komander, D., and Rape, M. (2012) The ubiquitin code, *Annu Rev Biochem 81*, 203-229.
170. Schrader, E. K., Harstad, K. G., and Matouschek, A. (2009) Targeting proteins for degradation, *Nat Chem Biol 5*, 815-822.
171. Dikic, I., and Schulman, B. A. (2023) An expanded lexicon for the ubiquitin code, *Nat Rev Mol Cell Biol 24*, 273-287.
172. Goldknopf, I. L., French, M. F., Musso, R., and Busch, H. (1977) Presence of protein A24 in rat liver nucleosomes, *Proc Natl Acad Sci U S A 74*, 5492-5495.
173. Kwon, Y. T., and Ciechanover, A. (2017) The Ubiquitin Code in the Ubiquitin-Proteasome System and Autophagy, *Trends Biochem Sci 42*, 873-886.
174. Tracz, M., and Bialek, W. (2021) Beyond K48 and K63: non-canonical protein ubiquitination, *Cell Mol Biol Lett 26*, 1.

175. Yau, R., and Rape, M. (2016) The increasing complexity of the ubiquitin code, *Nat Cell Biol 18*, 579-586.
176. Ye, Y., Blaser, G., Horrocks, M. H., Ruedas-Rama, M. J., Ibrahim, S., Zhukov, A. A., Orte, A., Klenerman, D., Jackson, S. E., and Komander, D. (2012) Ubiquitin chain conformation regulates recognition and activity of interacting proteins, *Nature 492*, 266-270.
177. Chau, V., Tobias, J. W., Bachmair, A., Marriott, D., Ecker, D. J., Gonda, D. K., and Varshavsky, A. (1989) A multiubiquitin chain is confined to specific lysine in a targeted short-lived protein, *Science 243*, 1576-1583.
178. Petroski, M. D., and Deshaies, R. J. (2005) Mechanism of lysine 48-linked ubiquitin-chain synthesis by the cullin-RING ubiquitin-ligase complex SCF-Cdc34, *Cell 123*, 1107-1120.
179. Scheffner, M., Huibregtse, J. M., Vierstra, R. D., and Howley, P. M. (1993) The HPV-16 E6 and E6-AP complex functions as a ubiquitin-protein ligase in the ubiquitination of p53, *Cell 75*, 495-505.
180. Thrower, J. S. (2000) Recognition of the polyubiquitin proteolytic signal, *The EMBO Journal 19*, 94-102.
181. Lu, Y., Lee, B. H., King, R. W., Finley, D., and Kirschner, M. W. (2015) Substrate degradation by the proteasome: a single-molecule kinetic analysis, *Science 348*, 1250834.
182. Snyder, N. A., and Silva, G. M. (2021) Deubiquitinating enzymes (DUBs): Regulation, homeostasis, and oxidative stress response, *J Biol Chem 297*, 101077.
183. Abdul Rehman, S. A., Kristariyanto, Y. A., Choi, S. Y., Nkosi, P. J., Weidlich, S., Labib, K., Hofmann, K., and Kulathu, Y. (2016) MINDY-1 Is a Member of an Evolutionarily Conserved and Structurally Distinct New Family of Deubiquitinating Enzymes, *Mol Cell 63*, 146-155.
184. Schwickart, M., Huang, X., Lill, J. R., Liu, J., Ferrando, R., French, D. M., Maecker, H., O'Rourke, K., Bazan, F., Eastham-Anderson, J., Yue, P., Dornan, D., Huang, D. C., and Dixit, V. M. (2010) Deubiquitinase USP9X stabilizes MCL1 and promotes tumour cell survival, *Nature 463*, 103-107.
185. Meyer, H. J., and Rape, M. (2014) Enhanced protein degradation by branched ubiquitin chains, *Cell 157*, 910-921.
186. Castaneda, C. A., Kashyap, T. R., Nakasone, M. A., Krueger, S., and Fushman, D. (2013) Unique structural, dynamical, and functional properties of k11-linked polyubiquitin chains, *Structure 21*, 1168-1181.
187. Liu, P., Gan, W., Su, S., Hauenstein, A. V., Fu, T. M., Brasher, B., Schwerdtfeger, C., Liang, A. C., Xu, M., and Wei, W. (2018) K63-linked polyubiquitin chains bind to DNA to facilitate DNA damage repair, *Sci Signal 11*.
188. Tan, J. M., Wong, E. S., Kirkpatrick, D. S., Pletnikova, O., Ko, H. S., Tay, S.-P., Ho, M. W., Troncoso, J., Gygi, S. P., and Lee, M. K. (2008) Lysine 63-linked ubiquitination promotes the formation and autophagic clearance of protein inclusions associated with neurodegenerative diseases, *Human molecular genetics 17*, 431-439.
189. Richard, T. J. C., Herzog, L. K., Vornberger, J., Rahmanto, A. S., Sangfelt, O., Salomons, F. A., and Dantuma, N. P. (2020) K63-linked ubiquitylation induces global sequestration of mitochondria, *Sci Rep 10*, 22334.
190. Ohtake, F., Tsuchiya, H., Saeki, Y., and Tanaka, K. (2018) K63 ubiquitylation triggers proteasomal degradation by seeding branched ubiquitin chains, *Proc Natl Acad Sci U S A 115*, E1401-E1408.
191. Adams, J. (2003) The proteasome: structure, function, and role in the cell, *Cancer Treat Rev 29 Suppl 1*, 3-9.
192. Adams, J. (2004) The proteasome: a suitable antineoplastic target, *Nat Rev Cancer 4*, 349-360.
193. Coux, O., Tanaka, K., and Goldberg, A. L. (1996) Structure and functions of the 20S and 26S proteasomes, *Annu Rev Biochem 65*, 801-847.

194. Pickart, C. M., and Cohen, R. E. (2004) Proteasomes and their kin: proteases in the machine age, *Nat Rev Mol Cell Biol 5*, 177-187.
195. Kim, H. T., and Goldberg, A. L. (2017) The deubiquitinating enzyme Usp14 allosterically inhibits multiple proteasomal activities and ubiquitin-independent proteolysis, *J Biol Chem 292*, 9830-9839.
196. Peth, A., Besche, H. C., and Goldberg, A. L. (2009) Ubiquitinated proteins activate the proteasome by binding to Usp14/Ubp6, which causes 20S gate opening, *Mol Cell 36*, 794-804.
197. Davis, C., , B. L. S., , E. C., , J. K., , H. C., , S. E., , D. F., and , A. M. (2023) A strict requirement in proteasome substrates for spacing between ubiquitin tag and degradation initiation elements, *bioRxiv*.
198. Verma, R., Aravind, L., Oania, R., McDonald, W. H., Yates, J. R., 3rd, Koonin, E. V., and Deshaies, R. J. (2002) Role of Rpn11 metalloprotease in deubiquitination and degradation by the 26S proteasome, *Science 298*, 611-615.
199. Goldberg, A. L., Kim, H. T., Lee, D., and Collins, G. A. (2021) Mechanisms That Activate 26S Proteasomes and Enhance Protein Degradation, *Biomolecules 11*.
200. Livneh, I., Cohen-Kaplan, V., Cohen-Rosenzweig, C., Avni, N., and Ciechanover, A. (2016) The life cycle of the 26S proteasome: from birth, through regulation and function, and onto its death, *Cell Res 26*, 869-885.
201. Groll, M., Bochtler, M., Brandstetter, H., Clausen, T., and Huber, R. (2005) Molecular machines for protein degradation, *Chembiochem 6*, 222-256.
202. Njomen, E., and Tepe, J. J. (2019) Proteasome Activation as a New Therapeutic Approach To Target Proteotoxic Disorders, *J Med Chem 62*, 6469-6481.
203. Kisselev, A. F., Akopian, T. N., Woo, K. M., and Goldberg, A. L. (1999) The sizes of peptides generated from protein by mammalian 26 and 20 S proteasomes. Implications for understanding the degradative mechanism and antigen presentation, *J Biol Chem 274*, 3363-3371.
204. Wu, H. Q., Baker, D., and Ovaa, H. (2020) Small molecules that target the ubiquitin system, *Biochem Soc Trans 48*, 479-497.
205. Deshaies, R. J., and Joazeiro, C. A. (2009) RING domain E3 ubiquitin ligases, *Annu Rev Biochem 78*, 399-434.
206. Metzger, M. B., Hristova, V. A., and Weissman, A. M. (2012) HECT and RING finger families of E3 ubiquitin ligases at a glance, *J Cell Sci 125*, 531-537.
207. Liu, L., Damerell, D. R., Koukouflis, L., Tong, Y., Marsden, B. D., and Schapira, M. (2019) UbiHub: a data hub for the explorers of ubiquitination pathways, *Bioinformatics 35*, 2882-2884.
208. Metzger, M. B., Pruneda, J. N., Klevit, R. E., and Weissman, A. M. (2014) RING-type E3 ligases: master manipulators of E2 ubiquitin-conjugating enzymes and ubiquitination, *Biochim Biophys Acta 1843*, 47-60.
209. Chang, S. C., Zhang, B. X., and Ding, J. L. (2022) E2-E3 ubiquitin enzyme pairing - partnership in provoking or mitigating cancers, *Biochim Biophys Acta Rev Cancer 1877*, 188679.
210. Petroski, M. D., and Deshaies, R. J. (2005) Function and regulation of cullin-RING ubiquitin ligases, *Nat Rev Mol Cell Biol 6*, 9-20.
211. Weber, J., Polo, S., and Maspero, E. (2019) HECT E3 Ligases: A Tale With Multiple Facets, *Front Physiol 10*, 370.
212. Wenzel, D. M., Lissounov, A., Brzovic, P. S., and Klevit, R. E. (2011) UBCH7 reactivity profile reveals parkin and HHARI to be RING/HECT hybrids, *Nature 474*, 105-108.
213. Pao, K. C., Wood, N. T., Knebel, A., Rafie, K., Stanley, M., Mabbitt, P. D., Sundaramoorthy, R., Hofmann, K., van Aalten, D. M. F., and Virdee, S. (2018) Activity-based E3 ligase profiling uncovers an E3 ligase with esterification activity, *Nat 556*, 381-385.
214. Spratt, D. E., Walden, H., and Shaw, G. S. (2014) RBR E3 ubiquitin ligases: new structures, new insights, new questions, *Biochem J 458*, 421-437.

215. Walden, H., and Rittinger, K. (2018) RBR ligase-mediated ubiquitin transfer: a tale with many twists and turns, *Nat Struct Mol Biol 25*, 440-445.
216. Wang, X. S., Cotton, T. R., Trevelyan, S. J., Richardson, L. W., Lee, W. T., Silke, J., and Lechtenberg, B. C. (2023) The unifying catalytic mechanism of the RING-between-RING E3 ubiquitin ligase family, *Nat Commun 14*, 168.
217. Harrigan, J. A., Jacq, X., Martin, N. M., and Jackson, S. P. (2018) Deubiquitylating enzymes and drug discovery: emerging opportunities, *Nat Rev Drug Discov 17*, 57-78.
218. Tran, K. T., Pallesen, J. S., Solbak, S. M. O., Narayanan, D., Baig, A., Zang, J., Aguayo-Orozco, A., Carmona, R. M. C., Garcia, A. D., and Bach, A. (2019) A Comparative Assessment Study of Known Small-Molecule Keap1-Nrf2 Protein-Protein Interaction Inhibitors: Chemical Synthesis, Binding Properties, and Cellular Activity, *J Med Chem 62*, 8028-8052.
219. Schauer, N. J., Liu, X., Magin, R. S., Doherty, L. M., Chan, W. C., Ficarro, S. B., Hu, W., Roberts, R. M., Iacob, R. E., Stolte, B., Giacomelli, A. O., Perera, S., McKay, K., Boswell, S. A., Weisberg, E. L., Ray, A., Chauhan, D., Dhe-Paganon, S., Anderson, K. C., Griffin, J. D., Li, J., Hahn, W. C., Sorger, P. K., Engen, J. R., Stegmaier, K., Marto, J. A., and Buhrlage, S. J. (2020) Selective USP7 inhibition elicits cancer cell killing through a p53-dependent mechanism, *Sci Rep 10*, 5324.
220. Henning, N. J., Boike, L., Spradlin, J. N., Ward, C. C., Liu, G., Zhang, E., Belcher, B. P., Brittain, S. M., Hesse, M. J., Dovala, D., McGregor, L. M., Valdez Misiolek, R., Plasschaert, L. W., Rowlands, D. J., Wang, F., Frank, A. O., Fuller, D., Estes, A. R., Randal, K. L., Panidapu, A., McKenna, J. M., Tallarico, J. A., Schirle, M., and Nomura, D. K. (2022) Deubiquitinase-targeting chimeras for targeted protein stabilization, *Nat Chem Biol 18*, 412-421.
221. Sakamoto, K. M., Kim, K. B., Kumagai, A., Mercurio, F., Crews, C. M., and Deshaies, R. J. (2001) Protacs: Chimeric molecules that target proteins to the Skp1-Cullin-F box complex for ubiquitination and degradation, *PNAS 98*, 8554-8559.
222. Coleman, K. G., and Crews, C. M. (2018) Proteolysis-Targeting Chimeras: Harnessing the Ubiquitin-Proteasome System to Induce Degradation of Specific Target Proteins, *Annu Rev Cancer Biol 2*, 41-58.
223. Henning, N. J., Boike, L., Spradlin, J. N., Ward, C. C., Belcher, B., Brittain, S. M., Hesse, M., Dovala, D., McGregor, L. M., McKenna, J. M., Tallarico, J. A., Schirle, M., and Nomura, D. K. (2021) Deubiquitinase-Targeting Chimeras for Targeted Protein Stabilization, *bioRxiv*.
224. Kanner, S. A., Shuja, Z., Choudhury, P., Jain, A., and Colecraft, H. M. (2020) Targeted deubiquitination rescues distinct trafficking-deficient ion channelopathies, *Nat Methods 17*, 1245-1253.
225. Bekes, M., Langley, D. R., and Crews, C. M. (2022) PROTAC targeted protein degraders: the past is prologue, *Nat Rev Drug Discov 21*, 181-200.
226. Samarasinghe, K. T. G., and Crews, C. M. (2021) Targeted protein degradation: A promise for undruggable proteins, *Cell Chem Biol 28*, 934-951.
227. Mullard, A. (2021) Targeted protein degraders crowd into the clinic, *Nat Rev Drug Discov 20*, 247-250.
228. Bai, N., Miller, S. A., Andrianov, G. V., Yates, M., Kirubakaran, P., and Karanicolas, J. (2021) Rationalizing PROTAC-Mediated Ternary Complex Formation Using Rosetta, *J Chem Inf Model 61*, 1368-1382.
229. Ward, J. A., Perez-Lopez, C., and Mayor-Ruiz, C. (2023) Biophysical and Computational Approaches to Study Ternary Complexes: A 'Cooperative Relationship' to Rationalize Targeted Protein Degradation, *Chembiochem 24*, e202300163.
230. Wijaya, A. J., Farnaby, W., and Ciulli, A. (2023) Crystallization of VHL-based PROTAC-induced ternary complexes, *Methods Enzymol 681*, 241-263.
231. Chen, Q., Liu, C., Wang, W., Meng, X., Cheng, X., Li, X., Cai, L., Luo, L., He, X., Qu, H., Luo, J., Wei, H., Gao, S., Liu, G., Wan, J., Israel, D. I., Li, J., and Dou, D. (2023)

Optimization of PROTAC Ternary Complex Using DNA Encoded Library Approach, *ACS Chem Biol 18*, 25-33.
232. Pettersson, M., and Crews, C. M. (2019) PROteolysis TArgeting Chimeras (PROTACs) - Past, present and future, *Drug Discov Today Technol 31*, 15-27.
233. Schneekloth, A. R., Pucheault, M., Tae, H. S., and Crews, C. M. (2008) Targeted intracellular protein degradation induced by a small molecule: En route to chemical proteomics, *Bioorganic & Medicinal Chemistry Letters 18*, 5904-5908.
234. Graves, B., Thompson, T., Xia, M., Janson, C., Lukacs, C., Deo, D., Di Lello, P., Fry, D., Garvie, C., Huang, K. S., Gao, L., Tovar, C., Lovey, A., Wanner, J., and Vassilev, L. T. (2012) Activation of the p53 pathway by small-molecule-induced MDM2 and MDMX dimerization, *Proc Natl Acad Sci U S A 109*, 11788-11793.
235. Buckley, D. L., Gustafson, J. L., Van Molle, I., Roth, A. G., Tae, H. S., Gareiss, P. C., Jorgensen, W. L., Ciulli, A., and Crews, C. M. (2012) Small-molecule inhibitors of the interaction between the E3 ligase VHL and HIF1alpha, *Angew Chem Int Ed Engl 51*, 11463-11467.
236. Zengerle, M., Chan, K. H., and Ciulli, A. (2015) Selective Small Molecule Induced Degradation of the BET Bromodomain Protein BRD4, *ACS Chem Biol 10*, 1770-1777.
237. Sekine, K., Takubo, K., Kikuchi, R., Nishimoto, M., Kitagawa, M., Abe, F., Nishikawa, K., Tsuruo, T., and Naito, M. (2008) Small molecules destabilize cIAP1 by activating auto-ubiquitylation, *J Biol Chem 283*, 8961-8968.
238. Winter, G. E., Buckley, D. L., Paulk, J., Roberts, J. M., Souza, A., Dhe-Paganon, S., and Bradner, J. E. (2015) Phthalimide conjugation as a strategy for in vivo target protein degradation, *Sci 348*, 1376-1381.
239. Mori, T., Ito, T., Liu, S., Ando, H., Sakamoto, S., Yamaguchi, Y., Tokunaga, E., Shibata, N., Handa, H., and Hakoshima, T. (2018) Structural basis of thalidomide enantiomer binding to cereblon, *Scientific Reports 8*, 1294.
240. Bussiere, D. E., Xie, L., Srinivas, H., Shu, W., Burke, A., Be, C., Zhao, J., Godbole, A., King, D., Karki, R. G., Hornak, V., Xu, F., Cobb, J., Carte, N., Frank, A. O., Frommlet, A., Graff, P., Knapp, M., Fazal, A., Okram, B., Jiang, S., Michellys, P. Y., Beckwith, R., Voshol, H., Wiesmann, C., Solomon, J. M., and Paulk, J. (2020) Structural basis of indisulam-mediated RBM39 recruitment to DCAF15 E3 ligase complex, *Nat Chem Biol 16*, 15-23.
241. Han, T., Goralski, M., Gaskill, N., Capota, E., Kim, J., Ting, T. C., Xie, Y., Williams, N. S., and Nijhawan, D. (2017) Anticancer sulfonamides target splicing by inducing RBM39 degradation via recruitment to DCAF15, *Science 356*, eaal3755.
242. Faust, T. B., Yoon, H., Nowak, R. P., Donovan, K. A., Li, Z., Cai, Q., Eleuteri, N. A., Zhang, T., Gray, N. S., and Fischer, E. S. (2019) Structural complementarity facilitates E7820-mediated degradation of RBM39 by DCAF15, *Nat Chem Biol 16(1)*, 7-14.
243. Du, X., Volkov, O. A., Czerwinski, R. M., Tan, H., Huerta, C., Morton, E. R., Rizzi, J. P., Wehn, P. M., Xu, R., Nijhawan, D., and Wallace, E. M. (2019) Structural Basis and Kinetic Pathway of RBM39 Recruitment to DCAF15 by a Sulfonamide Molecular Glue E7820, *Structure 27*, 1625-1633.e1623.
244. Wei, J., Meng, F., Park, K. S., Yim, H., Velez, J., Kumar, P., Wang, L., Xie, L., Chen, H., Shen, Y., Teichman, E., Li, D., Wang, G. G., Chen, X., Kaniskan, H. U., and Jin, J. (2021) Harnessing the E3 Ligase KEAP1 for Targeted Protein Degradation, *J Am Chem Soc*.
245. Farrell, B. M., Gerth, F., Yang, C. R., and Yeh, J. T. (2022) A synthetic KLHL20 ligand to validate CUL3(KLHL20) as a potent E3 ligase for targeted protein degradation, *Genes Dev 36*, 1031-1042.
246. Chana, C. K., Maisonneuve, P., Posternak, G., Grinberg, N. G. A., Poirson, J., Ona, S. M., Ceccarelli, D. F., Mader, P., St-Cyr, D. J., and Pau, V. (2022) Discovery and structural characterization of small molecule binders of the human CTLH E3 ligase subunit GID4, *Journal of medicinal chemistry 65*, 12725-12746.

247. Lv, L., Chen, P., Cao, L., Li, Y., Zeng, Z., Cui, Y., Wu, Q., Li, J., Wang, J. H., Dong, M. Q., Qi, X., and Han, T. (2020) Discovery of a molecular glue promoting CDK12-DDB1 interaction to trigger cyclin K degradation, *Elife 9*.
248. Slabicki, M., Kozicka, Z., Petzold, G., Li, Y. D., Manojkumar, M., Bunker, R. D., Donovan, K. A., Sievers, Q. L., Koeppel, J., Suchyta, D., Sperling, A. S., Fink, E. C., Gasser, J. A., Wang, L. R., Corsello, S. M., Sellar, R. S., Jan, M., Gillingham, D., Scholl, C., Frohling, S., Golub, T. R., Fischer, E. S., Thoma, N. H., and Ebert, B. L. (2020) The CDK inhibitor CR8 acts as a molecular glue degrader that depletes cyclin K, *Nature*.
249. Baek, K., and Schulman, B. A. (2020) Molecular glue concept solidifies, *Nat Chem Biol 16*, 2-3.
250. Mayor-Ruiz, C., Bauer, S., Brand, M., Kozicka, Z., Siklos, M., Imrichova, H., Kaltheuner, I. H., Hahn, E., Seiler, K., Koren, A., Petzold, G., Fellner, M., Bock, C., Muller, A. C., Zuber, J., Geyer, M., Thoma, N. H., Kubicek, S., and Winter, G. E. (2020) Rational discovery of molecular glue degraders via scalable chemical profiling, *Nat Chem Biol 16*, 1199–1207.
251. Han, X., and Sun, Y. (2023) PROTACs: A novel strategy for cancer drug discovery and development, *MedComm 4*.
252. Bondeson, D. P., Smith, B. E., Burslem, G. M., Buhimschi, A. D., Hines, J., Jaime-Figueroa, S., Wang, J., Hamman, B. D., Ishchenko, A., and Crews, C. M. (2018) Lessons in PROTAC Design from Selective Degradation with a Promiscuous Warhead, *Cell Chem Biol 25*, 78-87 e75.
253. Donovan, K. A., Ferguson, F. M., Bushman, J. W., Eleuteri, N. A., Bhunia, D., Ryu, S., Tan, L., Shi, K., Yue, H., Liu, X., Dobrovolsky, D., Jiang, B., Wang, J., Hao, M., You, I., Teng, M., Liang, Y., Hatcher, J., Li, Z., Manz, T. D., Groendyke, B., Hu, W., Nam, Y., Sengupta, S., Cho, H., Shin, I., Agius, M. P., Ghobrial, I. M., Ma, M. W., Che, J., Buhrlage, S. J., Sim, T., Gray, N. S., and Fischer, E. S. (2020) Mapping the Degradable Kinome Provides a Resource for Expedited Degrader Development, *Cell 183*, 1714-1731.e1710.
254. Lai, A. C., Toure, M., Hellerschmied, D., Salami, J., Jaime-Figueroa, S., Ko, E., Hines, J., and Crews, C. M. (2016) Modular PROTAC Design for the Degradation of Oncogenic BCR-ABL, *Angew Chem Int Ed Engl 55*, 807-810.
255. Gadd, M. S., Testa, A., Lucas, X., Chan, K. H., Chen, W., Lamont, D. J., Zengerle, M., and Ciulli, A. (2017) Structural basis of PROTAC cooperative recognition for selective protein degradation, *Nat Chem Biol 13*, 514-521.
256. Steinebach, C., Ng, Y. L. D., Sosic, I., Lee, C. S., Chen, S., Lindner, S., Vu, L. P., Bricelj, A., Haschemi, R., Monschke, M., Steinwarz, E., Wagner, K. G., Bendas, G., Luo, J., Gutschow, M., and Kronke, J. (2020) Systematic exploration of different E3 ubiquitin ligases: an approach towards potent and selective CDK6 degraders, *Chem Sci 11*, 3474-3486.
257. Smith, B. E., Wang, S. L., Jaime-Figueroa, S., Harbin, A., Wang, J., Hamman, B. D., and Crews, C. M. (2019) Differential PROTAC substrate specificity dictated by orientation of recruited E3 ligase, *Nat Commun 10*, 131.
258. Ward, C. C., Kleinman, J. I., Brittain, S. M., Lee, P. S., Chung, C. Y. S., Kim, K., Petri, Y., Thomas, J. R., Tallarico, J. A., McKenna, J. M., Schirle, M., and Nomura, D. K. (2019) Covalent Ligand Screening Uncovers a RNF4 E3 Ligase Recruiter for Targeted Protein Degradation Applications, *ACS Chem Biol 14*, 2430-2440.
259. Spradlin, J. N., Hu, X., Ward, C. C., Brittain, S. M., Jones, M. D., Ou, L., To, M., Proudfoot, A., Ornelas, E., Woldegiorgis, M., Olzmann, J. A., Bussiere, D. E., Thomas, J. R., Tallarico, J. A., McKenna, J. M., Schirle, M., Maimone, T. J., and Nomura, D. K. (2019) Harnessing the anti-cancer natural product nimbolide for targeted protein degradation, *Nat Chem Biol 15*, 747-755.
260. Luo, M., Spradlin, J. N., Boike, L., Tong, B., Brittain, S. M., McKenna, J. M., Tallarico, J. A., Schirle, M., Maimone, T. J., and Nomura, D. K. (2021) Chemoproteomics-enabled

discovery of covalent RNF114-based degraders that mimic natural product function, *Cell Chem Biol 28*, 559-566 e515.
261. Tong, B., Luo, M., Xie, Y., Spradlin, J. N., Tallarico, J. A., McKenna, J. M., Schirle, M., Maimone, T. J., and Nomura, D. K. (2020) Bardoxolone conjugation enables targeted protein degradation of BRD4, *Sci Rep 10*, 15543.
262. Zhang, X., Luukkonen, L. M., Eissler, C. L., Crowley, V. M., Yamashita, Y., Schafroth, M. A., Kikuchi, S., Weinstein, D. S., Symons, K. T., Nordin, B. E., Rodriguez, J. L., Wucherpfennig, T. G., Bauer, L. G., Dix, M. M., Stamos, D., Kinsella, T. M., Simon, G. M., Baltgalvis, K. A., and Cravatt, B. F. (2021) DCAF11 Supports Targeted Protein Degradation by Electrophilic Proteolysis-Targeting Chimeras, *J Am Chem Soc 143*, 5141-5149.
263. Zhang, X., Crowley, V. M., Wucherpfennig, T. G., Dix, M. M., and Cravatt, B. F. (2019) Electrophilic PROTACs that degrade nuclear proteins by engaging DCAF16, *Nat Chem Biol 15*, 737-746.
264. Tao, Y., Remillard, D., Vinogradova, E. V., Yokoyama, M., Banchenko, S., Schwefel, D., Melillo, B., Schreiber, S. L., Zhang, X., and Cravatt, B. F. (2022) Targeted Protein Degradation by Electrophilic PROTACs that Stereoselectively and Site-Specifically Engage DCAF1, *Journal of the American Chemical Society*.
265. Henning, N. J., Manford, A. G., Spradlin, J. N., Brittain, S. M., Zhang, E., McKenna, J. M., Tallarico, J. A., Schirle, M., Rape, M., and Nomura, D. K. (2022) Discovery of a Covalent FEM1B Recruiter for Targeted Protein Degradation Applications, *J Am Chem Soc 144*, 701-708.
266. S. Ramachandran, N. Makukhin, K. Haubrich, R. Casement, M. Nagala, D. M. Lynch, A. Testa, E. Bruno, R. Gitto, and Ciulli, A. (2023) Structure-based design of a phosphotyrosine-masked covalent ligand targeting the E3 ligase SOCS2, *ChemRXiv*.
267. Isobe, Y., Okumura, M., McGregor, L. M., Brittain, S. M., Jones, M. D., Liang, X., White, R., Forrester, W., McKenna, J. M., Tallarico, J. A., Schirle, M., Maimone, T. J., and Nomura, D. K. (2020) Manumycin polyketides act as molecular glues between UBR7 and P53, *Nat Chem Biol 16*, 1189–1198.
268. Toriki, E. S., Papatzimas, J. W., Nishikawa, K., Dovala, D., Frank, A. O., Hesse, M. J., Dankova, D., Song, J. G., Bruce-Smythe, M., Struble, H., Garcia, F. J., Brittain, S. M., Kile, A. C., McGregor, L. M., McKenna, J. M., Tallarico, J. A., Schirle, M., and Nomura, D. K. (2023) Rational Chemical Design of Molecular Glue Degraders, *ACS Cent Sci 9*, 915-926.
269. Qi, J., Song, Y., Park, P., Chauhan, D., Wu, L., and Anderson, K., C. (2019) Small molecules for inducing selective protein degradation and uses thereof.
270. Bashore, C., Prakash, S., Johnson, M. C., Conrad, R. J., Kekessie, I. A., Scales, S. J., Ishisoko, N., Kleinheinz, T., Liu, P. S., Popovych, N., Wecksler, A. T., Zhou, L., Tam, C., Zilberleyb, I., Srinivasan, R., Blake, R. A., Song, A., Staben, S. T., Zhang, Y., Arnott, D., Fairbrother, W. J., Foster, S. A., Wertz, I. E., Ciferri, C., and Dueber, E. C. (2023) Targeted degradation via direct 26S proteasome recruitment, *Nat Chem Biol 19*, 55-63.
271. King, E. A., Cho, Y., Hsu, N. S., Dovala, D., McKenna, J. M., Tallarico, J. A., Schirle, M., and Nomura, D. K. (2023) Chemoproteomics-enabled discovery of a covalent molecular glue degrader targeting NF-kappaB, *Cell Chem Biol 30*, 394-402 e399.
272. Forte, N., Dovala, D., Hesse, M. J., McKenna, J. M., Tallarico, J. A., Schirle, M., and Nomura, D. K. (2023) Targeted Protein Degradation through E2 Recruitment, *ACS Chem Biol 18*, 897-904.
273. Meyers, M., Cismoski, S., Panidapu, A., Chie-Leon, B., and Nomura, D. K. (2023) Targeted Protein Degradation through Recruitment of the CUL4A Complex Adaptor Protein DDB1, *bioRxiv*.
274. Panyain, N., Godinat, A., Lanyon-Hogg, T., Lachiondo-Ortega, S., Will, E. J., Soudy, C., Mondal, M., Mason, K., Elkhalifa, S., Smith, L. M., Harrigan, J. A., and Tate, E. W. (2020) Discovery of a Potent and Selective Covalent Inhibitor and Activity-Based Probe

for the Deubiquitylating Enzyme UCHL1, with Antifibrotic Activity, *J Am Chem Soc 142*, 12020-12026.
275. Ekkebus, R., van Kasteren, S. I., Kulathu, Y., Scholten, A., Berlin, I., Geurink, P. P., de Jong, A., Goerdayal, S., Neefjes, J., Heck, A. J., Komander, D., and Ovaa, H. (2013) On terminal alkynes that can react with active-site cysteine nucleophiles in proteases, *J Am Chem Soc 135*, 2867-2870.
276. Mulder, M. P., Witting, K., Berlin, I., Pruneda, J. N., Wu, K. P., Chang, J. G., Merkx, R., Bialas, J., Groettrup, M., Vertegaal, A. C., Schulman, B. A., Komander, D., Neefjes, J., El Oualid, F., and Ovaa, H. (2016) A cascading activity-based probe sequentially targets E1-E2-E3 ubiquitin enzymes, *Nat Chem Biol 12*, 523-530.
277. Mons, E., Kim, R. Q., van Doodewaerd, B. R., van Veelen, P. A., Mulder, M. P. C., and Ovaa, H. (2021) Exploring the Versatility of the Covalent Thiol-Alkyne Reaction with Substituted Propargyl Warheads: A Deciding Role for the Cysteine Protease, *J Am Chem Soc 143*, 6423-6433.
278. Liu, J., Yu, X., Chen, H., Kaniskan, H. U., Xie, L., Chen, X., Jin, J., and Wei, W. (2022) TF-DUBTACs Stabilize Tumor Suppressor Transcription Factors, *J Am Chem Soc 144*, 12934-12941.
279. Jost, C., Nitsche, C., Scholz, T., Roux, L., and Klein, C. D. (2014) Promiscuity and selectivity in covalent enzyme inhibition: a systematic study of electrophilic fragments, *J Med Chem 57*, 7590-7599.
280. Singh, J., Petter, R. C., Baillie, T. A., and Whitty, A. (2011) The resurgence of covalent drugs, *Nat Rev Drug Discov 10*, 307-317.
281. Michaelides, I. N., and Collie, G. W. (2023) E3 Ligases Meet Their Match: Fragment-Based Approaches to Discover New E3 Ligands and to Unravel E3 Biology, *J Med Chem 66*, 3173-3194.
282. Jackson, P. A., Widen, J. C., Harki, D. A., and Brummond, K. M. (2017) Covalent Modifiers: A Chemical Perspective on the Reactivity of alpha,beta-Unsaturated Carbonyls with Thiols via Hetero-Michael Addition Reactions, *J Med Chem 60*, 839-885.
283. Shraga, A., Resnick, E., Gabizon, R., and London, N. (2021) Covalent fragment screening, In *The Design of Covalent-Based Inhibitors*, pp 243-265.
284. Tong, B., Spradlin, J. N., Novaes, L. F. T., Zhang, E., Hu, X., Moeller, M., Brittain, S. M., McGregor, L. M., McKenna, J. M., Tallarico, J. A., Schirle, M., Maimone, T. J., and Nomura, D. K. (2020) A Nimbolide-Based Kinase Degrader Preferentially Degrades Oncogenic BCR-ABL, *ACS Chem Biol 15*, 1788-1794.
285. Belcher, B. P., Ward, C. C., and Nomura, D. K. (2021) Ligandability of E3 Ligases for Targeted Protein Degradation Applications, *Biochemistry*.
286. Gholami, A. M., Hahne, H., Wu, Z., Auer, F. J., Meng, C., Wilhelm, M., and Kuster, B. (2013) Global proteome analysis of the NCI-60 cell line panel, *Cell Rep 4*, 609-620.
287. Yang, Y., Tan, S., Han, Y., Huang, L., Yang, R., Hu, Z., Tao, Y., Oyang, L., Lin, J., Peng, Q., Jiang, X., Xu, X., Xia, L., Peng, M., Wu, N., Tang, Y., Li, X., Liao, Q., and Zhou, Y. (2023) The role of tripartite motif-containing 28 in cancer progression and its therapeutic potentials, *Front Oncol 13*, 1100134.
288. Czerwinska, P., Mazurek, S., and Wiznerowicz, M. (2017) The complexity of TRIM28 contribution to cancer, *J Biomed Sci 24*, 63.
289. Qi, Z. X., Cai, J. J., Chen, L. C., Yue, Q., Gong, Y., Yao, Y., and Mao, Y. (2016) TRIM28 as an independent prognostic marker plays critical roles in glioma progression, *J Neurooncol 126*, 19-26.
290. Qi, L., Xu, X., and Qi, X. (2022) The giant E3 ligase HUWE1 is linked to tumorigenesis, spermatogenesis, intellectual disability, and inflammatory diseases, *Front Cell Infect Microbiol 12*, 905906.
291. Kao, S. H., Wu, H. T., and Wu, K. J. (2018) Ubiquitination by HUWE1 in tumorigenesis and beyond, *J Biomed Sci 25*, 67.

292. Liu, F., Cao, L., Zhang, T., Chang, F., Xu, Y., Li, Q., Deng, J., Li, L., and Shao, G. (2018) CRL4B(RBBP7) targets HUWE1 for ubiquitination and proteasomal degradation, *Biochem Biophys Res Commun 501*, 440-447.
293. Cheng, J., Guo, J., North, B. J., Tao, K., Zhou, P., and Wei, W. (2019) The emerging role for Cullin 4 family of E3 ligases in tumorigenesis, *Biochim Biophys Acta Rev Cancer 1871*, 138-159.
294. Gehringer, M., and Laufer, S. A. (2019) Emerging and Re-Emerging Warheads for Targeted Covalent Inhibitors: Applications in Medicinal Chemistry and Chemical Biology, *J Med Chem 62*, 5673-5724.
295. Zanon, P. R. A., Yu, F., Musacchio, P. Z., Lewald, L., Zollo, M., Krauskopf, K., Mrdović, D., Raunft, P., Maher, T. E., Cigler, M., Chang, C. J., Lang, K., Toste, F. D., Nesvizhskii, A. I., and Hacker, S. M. (2021) Profiling the proteome-wide selectivity of diverse electrophiles, *ChemRXiv*.
296. Grams, R. J., and Hsu, K.-L. (2022) Reactive chemistry for covalent probe and therapeutic development, *Trends in Pharmacological Sciences*.
297. Chen, Y., Craven, G. B., Kamber, R. A., Cuesta, A., Zhersh, S., Moroz, Y. S., Bassik, M. C., and Taunton, J. (2023) Direct mapping of ligandable tyrosines and lysines in cells with chiral sulfonyl fluoride probes, *Nat Chem*.
298. Ward, C. C., Kleinman, J. I., and Nomura, D. K. (2017) NHS-Esters As Versatile Reactivity-Based Probes for Mapping Proteome-Wide Ligandable Hotspots, *ACS Chem Biol 12*, 1478-1483.
299. Hahm, H. S., Toroitich, E. K., Borne, A. L., Brulet, J. W., Libby, A. H., Yuan, K., Ware, T. B., McCloud, R. L., Ciancone, A. M., and Hsu, K.-L. (2019) Global targeting of functional tyrosines using sulfur-triazole exchange chemistry, *Nat Chem Biol*.
300. Shannon, D. A., Gu, C., McLaughlin, C. J., Kaiser, M., van der Hoorn, R. A., and Weerapana, E. (2012) Sulfonyl fluoride analogues as activity-based probes for serine proteases, *ChemBioChem 13*, 2327-2330.
301. Ma, N., Hu, J., Zhang, Z. M., Liu, W., Huang, M., Fan, Y., Yin, X., Wang, J., Ding, K., Ye, W., and Li, Z. (2020) 2H-Azirine-Based Reagents for Chemoselective Bioconjugation at Carboxyl Residues Inside Live Cells, *J Am Chem Soc 142*, 6051-6059.
302. Dovgan, I., Erb, S., Hessmann, S., Ursuegui, S., Michel, C., Muller, C., Chaubet, G., Cianferani, S., and Wagner, A. (2018) Arginine-selective bioconjugation with 4-azidophenyl glyoxal: application to the single and dual functionalisation of native antibodies, *Org Biomol Chem 16*, 1305-1311.
303. Rothweiler, E. M., and Huber, K. V. M. (2023) Global Assessment of Drug Target Engagement and Selectivity of Covalent Cysteine-Reactive Inhibitors Using Alkyne-Functionalized Probes, In *Chemogenomics: Methods and Protocols* (Merk, D., and Chaikuad, A., Eds.), pp 191-200, Springer US, New York, NY.
304. Yang, Y., Yang, X., and Verhelst, S. H. (2013) Comparative analysis of click chemistry mediated activity-based protein profiling in cell lysates, *Molecules 18*, 12599-12608.
305. Zhang, X. (2017) Detergents: Friends not foes for high-performance membrane proteomics toward precision medicine, *Proteomics 17*.
306. Li, H., Remsberg, J., Won, S. J., Zhao, K., Huang, T., Lu, B., Simon, G., Liu, D., and Cravatt, B. (2022) Assigning functionality to cysteines by base editing of cancer dependency genes, *bioRxiv*, 2022.2011. 2017.516964.
307. Koo, T. Y., Lai, H., Nomura, D. K., and Chung, C. Y. (2023) N-Acryloylindole-alkyne (NAIA) enables imaging and profiling new ligandable cysteines and oxidized thiols by chemoproteomics, *Nat Commun 14*, 3564.
308. Hacker, S. M., Backus, K. M., Lazear, M. R., Forli, S., Correia, B. E., and Cravatt, B. F. (2017) Global profiling of lysine reactivity and ligandability in the human proteome, *Nat Chem 9*, 1181-1190.
309. Chen, P., Tang, G., Zhu, C., Sun, J., Wang, X., Xiang, M., Huang, H., Wang, W., Li, L., Zhang, Z. M., Gao, L., and Yao, S. Q. (2023) 2-Ethynylbenzaldehyde-Based, Lysine-

Targeting Irreversible Covalent Inhibitors for Protein Kinases and Nonkinases, *J Am Chem Soc*.
310. Abbasov, M. E., Kavanagh, M. E., Ichu, T. A., Lazear, M. R., Tao, Y., Crowley, V. M., Am Ende, C. W., Hacker, S. M., Ho, J., Dix, M. M., Suciu, R., Hayward, M. M., Kiessling, L. L., and Cravatt, B. F. (2021) A proteome-wide atlas of lysine-reactive chemistry, *Nat Chem 13*, 1081-1092.
311. Brulet, J. W., Ciancone, A. M., Yuan, K., and Hsu, K. L. (2023) Advances in Activity-Based Protein Profiling of Functional Tyrosines in Proteomes, *Israel Journal of Chemistry 63*.
312. Martin-Gago, P., Fansa, E. K., Winzker, M., Murarka, S., Janning, P., Schultz-Fademrecht, C., Baumann, M., Wittinghofer, A., and Waldmann, H. (2017) Covalent Protein Labeling at Glutamic Acids, *Cell Chem Biol 24*, 589-597 e585.
313. Li, J., Zhou, J., Xu, H., Tian, K., Zhu, H., Chen, Y., Huang, Y., Wang, G., Gong, Z., Qin, H., and Ye, M. (2023) ACR-Based Probe for the Quantitative Profiling of Histidine Reactivity in the Human Proteome, *J Am Chem Soc 145*, 5252-5260.
314. Mizero, B., Villacres, C., Spicer, V., Viner, R., Saba, J., Patel, B., Snovida, S., Jensen, P., Huhmer, A., and Krokhin, O. V. (2022) Retention Time Prediction for TMT-Labeled Peptides in Proteomic LC-MS Experiments, *J Proteome Res 21*, 1218-1228.
315. Apffel, A., Fischer, S., Goldberg, G., Goodley, P. C., and Kuhlmann, F. E. (1995) Enhanced sensitivity for peptide mapping with electrospray liquid chromatography-mass spectrometry in the presence of signal suppression due to trifluoroacetic acid-containing mobile phases, *J Chromatogr A 712*, 177-190.
316. Nshanian, M., Lakshmanan, R., Chen, H., Ogorzalek Loo, R. R., and Loo, J. A. (2018) Enhancing Sensitivity of Liquid Chromatography-Mass Spectrometry of Peptides and Proteins Using Supercharging Agents, *Int J Mass Spectrom 427*, 157-164.
317. Chambers, M. C., Maclean, B., Burke, R., Amodei, D., Ruderman, D. L., Neumann, S., Gatto, L., Fischer, B., Pratt, B., Egertson, J., Hoff, K., Kessner, D., Tasman, N., Shulman, N., Frewen, B., Baker, T. A., Brusniak, M. Y., Paulse, C., Creasy, D., Flashner, L., Kani, K., Moulding, C., Seymour, S. L., Nuwaysir, L. M., Lefebvre, B., Kuhlmann, F., Roark, J., Rainer, P., Detlev, S., Hemenway, T., Huhmer, A., Langridge, J., Connolly, B., Chadick, T., Holly, K., Eckels, J., Deutsch, E. W., Moritz, R. L., Katz, J. E., Agus, D. B., MacCoss, M., Tabb, D. L., and Mallick, P. (2012) A cross-platform toolkit for mass spectrometry and proteomics, *Nat Biotechnol 30*, 918-920.
318. Geiszler, D. J., Kong, A. T., Avtonomov, D. M., Yu, F., Leprevost, F. D. V., and Nesvizhskii, A. I. (2021) PTM-Shepherd: Analysis and Summarization of Post-Translational and Chemical Modifications From Open Search Results, *Mol Cell Proteomics 20*, 100018.
319. Kong, A. T., Leprevost, F. V., Avtonomov, D. M., Mellacheruvu, D., and Nesvizhskii, A. I. (2017) MSFragger: ultrafast and comprehensive peptide identification in mass spectrometry-based proteomics, *Nat Methods 14*, 513-520.
320. Boatner, L. M., Palafox, M. F., Schweppe, D. K., and Backus, K. M. (2023) CysDB: a human cysteine database based on experimental quantitative chemoproteomics, *Cell Chem Biol 30*, 683-698 e683.
321. Nguyen, C. H., Glüxam, T., Schlerka, A., Bauer, K., Grandits, A. M., Hackl, H., Dovey, O., Zöchbauer-Müller, S., Cooper, J. L., and Vassiliou, G. S. (2019) SOCS2 is part of a highly prognostic 4-gene signature in AML and promotes disease aggressiveness, *Scientific Reports 9*, 9139.
322. Matta-Camacho, E., Kozlov, G., Menade, M., and Gehring, K. (2012) Structure of the HECT C-lobe of the UBR5 E3 ubiquitin ligase, *Acta Crystallogr Sect F Struct Biol Cryst Commun 68*, 1158-1163.
323. Jumper, J., Evans, R., Pritzel, A., Green, T., Figurnov, M., Ronneberger, O., Tunyasuvunakool, K., Bates, R., Zidek, A., Potapenko, A., Bridgland, A., Meyer, C., Kohl, S. A. A., Ballard, A. J., Cowie, A., Romera-Paredes, B., Nikolov, S., Jain, R., Adler, J., Back, T., Petersen, S., Reiman, D., Clancy, E., Zielinski, M., Steinegger, M., Pacholska, M., Berghammer, T., Bodenstein, S., Silver, D., Vinyals, O., Senior, A. W., Kavukcuoglu,

K., Kohli, P., and Hassabis, D. (2021) Highly accurate protein structure prediction with AlphaFold, *Nature 596*, 583-589.
324. Krivak, R., and Hoksza, D. (2018) P2Rank: machine learning based tool for rapid and accurate prediction of ligand binding sites from protein structure, *J Cheminform 10*, 39.
325. Jakubec, D., Skoda, P., Krivak, R., Novotny, M., and Hoksza, D. (2022) PrankWeb 3: accelerated ligand-binding site predictions for experimental and modelled protein structures, *Nucleic Acids Res 50*, W593-W597.
326. Savojardo, C., Manfredi, M., Martelli, P. L., and Casadio, R. (2020) Solvent Accessibility of Residues Undergoing Pathogenic Variations in Humans: From Protein Structures to Protein Sequences, *Front Mol Biosci 7*, 626363.
327. White, M. E. H., Gil, J., and Tate, E. W. (2023) Proteome-wide structural analysis identifies warhead- and coverage-specific biases in cysteine-focused chemoproteomics, *Cell Chem Biol 30*, 828-838 e824.
328. Krasny, L., and Huang, P. H. (2021) Data-independent acquisition mass spectrometry (DIA-MS) for proteomic applications in oncology, *Mol Omics 17*, 29-42.
329. Gillet, L. C., Navarro, P., Tate, S., Röst, H., Selevsek, N., Reiter, L., Bonner, R., and Aebersold, R. (2012) Targeted Data Extraction of the MS/MS Spectra Generated by Data-independent Acquisition: A New Concept for Consistent and Accurate Proteome Analysis, *Molecular & Cellular Proteomics 11*.
330. Schubert, O. T., Gillet, L. C., Collins, B. C., Navarro, P., Rosenberger, G., Wolski, W. E., Lam, H., Amodei, D., Mallick, P., MacLean, B., and Aebersold, R. (2015) Building high-quality assay libraries for targeted analysis of SWATH MS data, *Nat Protoc 10*, 426-441.
331. Thomas, P. D., Ebert, D., Muruganujan, A., Mushayahama, T., Albou, L. P., and Mi, H. (2022) PANTHER: Making genome-scale phylogenetics accessible to all, *Protein Sci 31*, 8-22.
332. Gonzalez-Valero, A., Reeves, A. G., Page, A. C. S., Moon, P. J., Miller, E., Coulonval, K., Crossley, S. W. M., Xie, X., He, D., Musacchio, P. Z., Christian, A. H., McKenna, J. M., Lewis, R. A., Fang, E., Dovala, D., Lu, Y., McGregor, L. M., Schirle, M., Tallarico, J. A., Roger, P. P., Toste, F. D., and Chang, C. J. (2022) An Activity-Based Oxaziridine Platform for Identifying and Developing Covalent Ligands for Functional Allosteric Methionine Sites: Redox-Dependent Inhibition of Cyclin-Dependent Kinase 4, *J Am Chem Soc 144*, 22890-22901.
333. Gilbert, K. E., Vuorinen, A., Aatkar, A., Pogany, P., Pettinger, J., Grant, E. K., Kirkpatrick, J. M., Rittinger, K., House, D., Burley, G. A., and Bush, J. T. (2023) Profiling Sulfur(VI) Fluorides as Reactive Functionalities for Chemical Biology Tools and Expansion of the Ligandable Proteome, *ACS Chem Biol 18*, 285-295.
334. Magesh, S., Chen, Y., and Hu, L. (2012) Small molecule modulators of Keap1-Nrf2-ARE pathway as potential preventive and therapeutic agents, *Med Res Rev 32*, 687-726.
335. Adamson, R. J., Payne, N. C., Bartual, S. G., Mazitschek, R., and Bullock, A. N. (2023) Structural and biochemical characterization establishes a detailed understanding of KEAP1-CUL3 complex assembly, *Free Radic Biol Med 204*, 215-225.
336. McMahon, M., Itoh, K., Yamamoto, M., and Hayes, J. D. (2003) Keap1-dependent proteasomal degradation of transcription factor Nrf2 contributes to the negative regulation of antioxidant response element-driven gene expression, *J Biol Chem 278*, 21592-21600.
337. Uruno, A., and Motohashi, H. (2011) The Keap1-Nrf2 system as an in vivo sensor for electrophiles, *Nitric Oxide 25*, 153-160.
338. Suzuki, T., Motohashi, H., and Yamamoto, M. (2013) Toward clinical application of the Keap1-Nrf2 pathway, *Trends Pharmacol Sci 34*, 340-346.
339. Wakabayashi, N., Dinkova-Kostova, A. T., Holtzclaw, W. D., Kang, M. I., Kobayashi, A., Yamamoto, M., Kensler, T. W., and Talalay, P. (2004) Protection against electrophile and oxidant stress by induction of the phase 2 response: fate of cysteines of the Keap1 sensor modified by inducers, *Proc Natl Acad Sci U S A 101*, 2040-2045.

340. Zhang, D. D., Lo, S. C., Cross, J. V., Templeton, D. J., and Hannink, M. (2004) Keap1 is a redox-regulated substrate adaptor protein for a Cul3-dependent ubiquitin ligase complex, *Mol Cell Biol 24*, 10941-10953.
341. Meng, X., Waddington, J. C., Tailor, A., Lister, A., Hamlett, J., Berry, N., Park, B. K., and Sporn, M. B. (2020) CDDO-imidazolide Targets Multiple Amino Acid Residues on the Nrf2 Adaptor, Keap1, *J Med Chem 63*, 9965-9976.
342. Cleasby, A., Yon, J., Day, P. J., Richardson, C., Tickle, I. J., Williams, P. A., Callahan, J. F., Carr, R., Concha, N., Kerns, J. K., Qi, H., Sweitzer, T., Ward, P., and Davies, T. G. (2014) Structure of the BTB domain of Keap1 and its interaction with the triterpenoid antagonist CDDO, *PLoS One 9*, e98896.
343. Hu, L., Magesh, S., Chen, L., Wang, L., Lewis, T. A., Chen, Y., Khodier, C., Inoyama, D., Beamer, L. J., Emge, T. J., Shen, J., Kerrigan, J. E., Kong, A. N., Dandapani, S., Palmer, M., Schreiber, S. L., and Munoz, B. (2013) Discovery of a small-molecule inhibitor and cellular probe of Keap1-Nrf2 protein-protein interaction, *Bioorg Med Chem Lett 23*, 3039-3043.
344. Marcotte, D., Zeng, W., Hus, J. C., McKenzie, A., Hession, C., Jin, P., Bergeron, C., Lugovskoy, A., Enyedy, I., Cuervo, H., Wang, D., Atmanene, C., Roecklin, D., Vecchi, M., Vivat, V., Kraemer, J., Winkler, D., Hong, V., Chao, J., Lukashev, M., and Silvian, L. (2013) Small molecules inhibit the interaction of Nrf2 and the Keap1 Kelch domain through a non-covalent mechanism, *Bioorg Med Chem 21*, 4011-4019.
345. Hancock, R., Schaap, M., Pfister, H., and Wells, G. (2013) Peptide inhibitors of the Keap1-Nrf2 protein-protein interaction with improved binding and cellular activity, *Org Biomol Chem 11*, 3553-3557.
346. Eades, G., Yang, M., Yao, Y., Zhang, Y., and Zhou, Q. (2011) miR-200a regulates Nrf2 activation by targeting Keap1 mRNA in breast cancer cells, *J Biol Chem 286*, 40725-40733.
347. Zhuo, W., Sun, M., Wang, K., Zhang, L., Li, K., Yi, D., Li, M., Sun, Q., Ma, X., Liu, W., Teng, L., Yi, C., and Zhou, T. (2022) m(6)Am methyltransferase PCIF1 is essential for aggressiveness of gastric cancer cells by inhibiting TM9SF1 mRNA translation, *Cell Discov 8*, 48.
348. McLennan, A. G. (2006) The Nudix hydrolase superfamily, *Cell Mol Life Sci 63*, 123-143.
349. GASMI, L., and McLENNAN, A. G. (2001) The mouse Nudt7 gene encodes a peroxisomal nudix hydrolase specific for coenzyme A and its derivatives, *Biochemical Journal 357*, 33-38.
350. Reilly, S. J., Tillander, V., Ofman, R., Alexson, S. E., and Hunt, M. C. (2008) The nudix hydrolase 7 is an Acyl-CoA diphosphatase involved in regulating peroxisomal coenzyme A homeostasis, *J Biochem 144*, 655-663.
351. Shumar, S. A., Kerr, E. W., Fagone, P., Infante, A. M., and Leonardi, R. (2019) Overexpression of Nudt7 decreases bile acid levels and peroxisomal fatty acid oxidation in the liver, *J Lipid Res 60*, 1005-1019.
352. Vickers, S. D., Shumar, S. A., Saporito, D. C., Kunovac, A., Hathaway, Q. A., Mintmier, B., King, J. A., King, R. D., Rajendran, V. M., Infante, A. M., Hollander, J. M., and Leonardi, R. (2023) NUDT7 regulates total hepatic CoA levels and the composition of the intestinal bile acid pool in male mice fed a Western diet, *J Biol Chem 299*, 102745.
353. Khan Tareque, R., Hassell-Hart, S., Krojer, T., Bradley, A., Velupillai, S., Talon, R., Fairhead, M., Day, I. J., Bala, K., Felix, R., Kemmitt, P. D., Brennan, P., von Delft, F., Diaz Saez, L., Huber, K., and Spencer, J. (2020) Deliberately Losing Control of C-H Activation Processes in the Design of Small-Molecule-Fragment Arrays Targeting Peroxisomal Metabolism, *ChemMedChem 15*, 2513-2520.
354. Chen, C., Li, J., Matye, D. J., Wang, Y., and Li, T. (2019) Hepatocyte sortilin 1 knockout and treatment with a sortilin 1 inhibitor reduced plasma cholesterol in Western diet-fed mice, *J Lipid Res 60*, 539-549.

355. Buvall, L., Rashmi, P., Lopez-Rivera, E., Andreeva, S., Weins, A., Wallentin, H., Greka, A., and Mundel, P. (2013) Proteasomal degradation of Nck1 but not Nck2 regulates RhoA activation and actin dynamics, *Nat Commun 4*, 2863.
356. Lettau, M., Pieper, J., and Janssen, O. (2009) Nck adapter proteins: functional versatility in T cells, *Cell Commun Signal 7*, 1.
357. Corsini, N. S., Peer, A. M., Moeseneder, P., Roiuk, M., Burkard, T. R., Theussl, H. C., Moll, I., and Knoblich, J. A. (2018) Coordinated Control of mRNA and rRNA Processing Controls Embryonic Stem Cell Pluripotency and Differentiation, *Cell Stem Cell 22*, 543-558 e512.
358. Konovalova, S., Liu, X., Manjunath, P., Baral, S., Neupane, N., Hilander, T., Yang, Y., Balboa, D., Terzioglu, M., Euro, L., Varjosalo, M., and Tyynismaa, H. (2018) Redox regulation of GRPEL2 nucleotide exchange factor for mitochondrial HSP70 chaperone, *Redox Biol 19*, 37-45.
359. Ishitani, T., Takaesu, G., Ninomiya-Tsuji, J., Shibuya, H., Gaynor, R. B., and Matsumoto, K. (2003) Role of the TAB2-related protein TAB3 in IL-1 and TNF signaling, *EMBO J 22*, 6277-6288.
360. Fu, J., and Wu, H. (2023) Structural Mechanisms of NLRP3 Inflammasome Assembly and Activation, *Annu Rev Immunol 41*, 301-316.
361. Swanson, K. V., Deng, M., and Ting, J. P. (2019) The NLRP3 inflammasome: molecular activation and regulation to therapeutics, *Nat Rev Immunol 19*, 477-489.
362. Kelley, N., Jeltema, D., Duan, Y., and He, Y. (2019) The NLRP3 Inflammasome: An Overview of Mechanisms of Activation and Regulation, *Int J Mol Sci 20*.
363. Karch, C. M., and Goate, A. M. (2015) Alzheimer's disease risk genes and mechanisms of disease pathogenesis, *Biol Psychiatry 77*, 43-51.
364. Halle, A., Hornung, V., Petzold, G. C., Stewart, C. R., Monks, B. G., Reinheckel, T., Fitzgerald, K. A., Latz, E., Moore, K. J., and Golenbock, D. T. (2008) The NALP3 inflammasome is involved in the innate immune response to amyloid-beta, *Nat Immunol 9*, 857-865.
365. Heneka, M. T., Kummer, M. P., Stutz, A., Delekate, A., Schwartz, S., Vieira-Saecker, A., Griep, A., Axt, D., Remus, A., Tzeng, T. C., Gelpi, E., Halle, A., Korte, M., Latz, E., and Golenbock, D. T. (2013) NLRP3 is activated in Alzheimer's disease and contributes to pathology in APP/PS1 mice, *Nature 493*, 674-678.
366. Daniels, M. J., Rivers-Auty, J., Schilling, T., Spencer, N. G., Watremez, W., Fasolino, V., Booth, S. J., White, C. S., Baldwin, A. G., Freeman, S., Wong, R., Latta, C., Yu, S., Jackson, J., Fischer, N., Koziel, V., Pillot, T., Bagnall, J., Allan, S. M., Paszek, P., Galea, J., Harte, M. K., Eder, C., Lawrence, C. B., and Brough, D. (2016) Fenamate NSAIDs inhibit the NLRP3 inflammasome and protect against Alzheimer's disease in rodent models, *Nat Commun 7*, 12504.
367. Coll, R. C., Schroder, K., and Pelegrin, P. (2022) NLRP3 and pyroptosis blockers for treating inflammatory diseases, *Trends Pharmacol Sci 43*, 653-668.
368. Dempsey, C., Rubio Araiz, A., Bryson, K. J., Finucane, O., Larkin, C., Mills, E. L., Robertson, A. A. B., Cooper, M. A., O'Neill, L. A. J., and Lynch, M. A. (2017) Inhibiting the NLRP3 inflammasome with MCC950 promotes non-phlogistic clearance of amyloid-beta and cognitive function in APP/PS1 mice, *Brain Behav Immun 61*, 306-316.
369. Tapia-Abellan, A., Angosto-Bazarra, D., Martinez-Banaclocha, H., de Torre-Minguela, C., Ceron-Carrasco, J. P., Perez-Sanchez, H., Arostegui, J. I., and Pelegrin, P. (2019) MCC950 closes the active conformation of NLRP3 to an inactive state, *Nat Chem Biol 15*, 560-564.
370. Coll, R. C., Robertson, A. A., Chae, J. J., Higgins, S. C., Munoz-Planillo, R., Inserra, M. C., Vetter, I., Dungan, L. S., Monks, B. G., Stutz, A., Croker, D. E., Butler, M. S., Haneklaus, M., Sutton, C. E., Nunez, G., Latz, E., Kastner, D. L., Mills, K. H., Masters, S. L., Schroder, K., Cooper, M. A., and O'Neill, L. A. (2015) A small-molecule inhibitor of the NLRP3 inflammasome for the treatment of inflammatory diseases, *Nat Med 21*, 248-255.

371. Vande Walle, L., Stowe, I. B., Sacha, P., Lee, B. L., Demon, D., Fossoul, A., Van Hauwermeiren, F., Saavedra, P. H. V., Simon, P., Subrt, V., Kostka, L., Stivala, C. E., Pham, V. C., Staben, S. T., Yamazoe, S., Konvalinka, J., Kayagaki, N., and Lamkanfi, M. (2019) MCC950/CRID3 potently targets the NACHT domain of wild-type NLRP3 but not disease-associated mutants for inflammasome inhibition, *PLoS Biol 17*, e3000354.
372. Huang, Y., Jiang, H., Chen, Y., Wang, X., Yang, Y., Tao, J., Deng, X., Liang, G., Zhang, H., Jiang, W., and Zhou, R. (2018) Tranilast directly targets NLRP3 to treat inflammasome-driven diseases, *EMBO Mol Med 10*.
373. Thapak, P., Bishnoi, M., and Sharma, S. S. (2022) Tranilast, a Transient Receptor Potential Vanilloid 2 Channel (TRPV2) Inhibitor Attenuates Amyloid beta-Induced Cognitive Impairment: Possible Mechanisms, *Neuromolecular Med 24*, 183-194.
374. Jiang, H., He, H., Chen, Y., Huang, W., Cheng, J., Ye, J., Wang, A., Tao, J., Wang, C., Liu, Q., Jin, T., Jiang, W., Deng, X., and Zhou, R. (2017) Identification of a selective and direct NLRP3 inhibitor to treat inflammatory disorders, *J Exp Med 214*, 3219-3238.
375. He, H., Jiang, H., Chen, Y., Ye, J., Wang, A., Wang, C., Liu, Q., Liang, G., Deng, X., Jiang, W., and Zhou, R. (2018) Oridonin is a covalent NLRP3 inhibitor with strong anti-inflammasome activity, *Nat Commun 9*, 2550.
376. Chen, Y., He, H., Lin, B., Chen, Y., Deng, X., Jiang, W., and Zhou, R. (2021) RRx-001 ameliorates inflammatory diseases by acting as a potent covalent NLRP3 inhibitor, *Cell Mol Immunol 18*, 1425-1436.
377. Irrera, N., Vaccaro, M., Bitto, A., Pallio, G., Pizzino, G., Lentini, M., Arcoraci, V., Minutoli, L., Scuruchi, M., Cutroneo, G., Anastasi, G. P., Ettari, R., Squadrito, F., and Altavilla, D. (2017) BAY 11-7082 inhibits the NF-kappaB and NLRP3 inflammasome pathways and protects against IMQ-induced psoriasis, *Clin Sci (Lond) 131*, 487-498.
378. Nizami, S., Millar, V., Arunasalam, K., Zarganes-Tzitzikas, T., Brough, D., Tresadern, G., Brennan, P. E., Davis, J. B., Ebner, D., and Di Daniel, E. (2021) A phenotypic high-content, high-throughput screen identifies inhibitors of NLRP3 inflammasome activation, *Sci Rep 11*, 15319.
379. Ivanov, A. V., Peng, H., Yurchenko, V., Yap, K. L., Negorev, D. G., Schultz, D. C., Psulkowski, E., Fredericks, W. J., White, D. E., Maul, G. G., Sadofsky, M. J., Zhou, M. M., and Rauscher, F. J., 3rd. (2007) PHD domain-mediated E3 ligase activity directs intramolecular sumoylation of an adjacent bromodomain required for gene silencing, *Mol Cell 28*, 823-837.
380. Rakhit, R., Crow, J. P., Lepock, J. R., Kondejewski, L. H., Cashman, N. R., and Chakrabartty, A. (2004) Monomeric Cu, Zn-superoxide Dismutase Is a Common Misfolding Intermediate in the Oxidation Models of Sporadic and Familial Amyotrophic Lateral Sclerosis*[boxs], *Journal of Biological Chemistry 279*, 15499-15504.
381. Delport, A., and Hewer, R. (2022) A superior loading control for the cellular thermal shift assay, *Sci Rep 12*, 6672.
382. Foulkes, D. M., Byrne, D. P., Yeung, W., Shrestha, S., Bailey, F. P., Ferries, S., Eyers, C. E., Keeshan, K., Wells, C., Drewry, D. H., Zuercher, W. J., Kannan, N., and Eyers, P. A. (2018) Covalent inhibitors of EGFR family protein kinases induce degradation of human Tribbles 2 (TRIB2) pseudokinase in cancer cells, *Sci Signal 11*.
383. Coyle, J., and Walser, R. (2020) Applied Biophysical Methods in Fragment-Based Drug Discovery, *SLAS Discov 25*, 471-490.
384. Schmidt, M. M., and Dringen, R. (2009) Differential effects of iodoacetamide and iodoacetate on glycolysis and glutathione metabolism of cultured astrocytes, *Front Neuroenergetics 1*, 1.
385. Liang, Q., Deng, H., Li, X., Wu, X., Tang, Q., Chang, T. H., Peng, H., Rauscher, F. J., 3rd, Ozato, K., and Zhu, F. (2011) Tripartite motif-containing protein 28 is a small ubiquitin-related modifier E3 ligase and negative regulator of IFN regulatory factor 7, *J Immunol 187*, 4754-4763.

386. Bloom, S., Liu, C., Kolmel, D. K., Qiao, J. X., Zhang, Y., Poss, M. A., Ewing, W. R., and MacMillan, D. W. C. (2018) Decarboxylative alkylation for site-selective bioconjugation of native proteins via oxidation potentials, *Nat Chem 10*, 205-211.
387. Rothweiler, E. M., Stefaniak, J., Ward, J. A., Rogers, C., Balikci, E., and Huber, K. V. M. (2022) A chemical biology toolbox to investigate in-cell target engagement
and specificity of PRMT5-inhibitors *BioRxiv*.
388. Wu, Q., Schapira, M., Arrowsmith, C. H., and Barsyte-Lovejoy, D. (2021) Protein arginine methylation: from enigmatic functions to therapeutic targeting, *Nat Rev Drug Discov*.
389. Zhang, J., Jing, L., Li, M., He, L., and Guo, Z. (2019) Regulation of histone arginine methylation/demethylation by methylase and demethylase (Review), *Mol Med Rep 19*, 3963-3971.
390. Guccione, E., and Richard, S. (2019) The regulation, functions and clinical relevance of arginine methylation, *Nat Rev Mol Cell Biol 20*, 642-657.
391. Hwang, J. W., Cho, Y., Bae, G. U., Kim, S. N., and Kim, Y. K. (2021) Protein arginine methyltransferases: promising targets for cancer therapy, *Exp Mol Med 53*, 788-808.
392. Yang, Y., and Bedford, M. T. (2013) Protein arginine methyltransferases and cancer, *Nat Rev Cancer 13*, 37-50.
393. Musiani, D., Bok, J., Massignani, E., Wu, L., Tabaglio, T., Ippolito, M. R., Cuomo, A., Ozbek, U., Zorgati, H., Ghoshdastider, U., and Robinson, R. C. (2019) Proteomics profiling of arginine methylation defines PRMT5 substrate specificity, *Science signaling 12*.
394. Braun, C. J., Stanciu, M., Boutz, P. L., Patterson, J. C., Calligaris, D., Higuchi, F., Neupane, R., Fenoglio, S., Cahill, D. P., Wakimoto, H., Agar, N. Y. R., Yaffe, M. B., Sharp, P. A., Hemann, M. T., and Lees, J. A. (2017) Coordinated Splicing of Regulatory Detained Introns within Oncogenic Transcripts Creates an Exploitable Vulnerability in Malignant Glioma, *Cancer Cell 32*, 411-426 e411.
395. Krzyzanowski, A., Gasper, R., Adihou, H., t Hart, P., and Waldmann, H. (2021) Biochemical Investigation of the Interaction of pICln, RioK1 and COPR5 with the PRMT5-MEP50 Complex, *Chembiochem*.
396. Zhu, F., Guo, H., Bates, P. D., Zhang, S., Zhang, H., Nomie, K. J., Li, Y., Lu, L., Seibold, K. R., Wang, F., Rumball, I., Cameron, H., Hoang, N. M., Yang, D. T., Xu, W., Zhang, L., Wang, M., Capitini, C. M., and Rui, L. (2019) PRMT5 is upregulated by B-cell receptor signaling and forms a positive-feedback loop with PI3K/AKT in lymphoma cells, *Leukemia 33*, 2898-2911.
397. Tamiya, H., Kim, H., Klymenko, O., Kim, H., Feng, Y., Zhang, T., Han, J. Y., Murao, A., Snipas, S. J., Jilaveanu, L., Brown, K., Kluger, H., Zhang, H., Iwai, K., and Ronai, Z. A. (2018) SHARPIN-mediated regulation of protein arginine methyltransferase 5 controls melanoma growth, *J Clin Invest 128*, 517-530.
398. Yan, F., Alinari, L., Lustberg, M. E., Martin, L. K., Cordero-Nieves, H. M., Banasavadi-Siddegowda, Y., Virk, S., Barnholtz-Sloan, J., Bell, E. H., Wojton, J., Jacob, N. K., Chakravarti, A., Nowicki, M. O., Wu, X., Lapalombella, R., Datta, J., Yu, B., Gordon, K., Haseley, A., Patton, J. T., Smith, P. L., Ryu, J., Zhang, X., Mo, X., Marcucci, G., Nuovo, G., Kwon, C. H., Byrd, J. C., Chiocca, E. A., Li, C., Sif, S., Jacob, S., Lawler, S., Kaur, B., and Baiocchi, R. A. (2014) Genetic validation of the protein arginine methyltransferase PRMT5 as a candidate therapeutic target in glioblastoma, *Cancer Res 74*, 1752-1765.
399. Stopa, N., Krebs, J. E., and Shechter, D. (2015) The PRMT5 arginine methyltransferase: many roles in development, cancer and beyond, *Cell Mol Life Sci 72*, 2041-2059.
400. Powers, M. A., Fay, M. M., Factor, R. E., Welm, A. L., and Ullman, K. S. (2011) Protein arginine methyltransferase 5 accelerates tumor growth by arginine methylation of the tumor suppressor programmed cell death 4, *Cancer Res 71*, 5579-5587.
401. Qi, H., Shi, X., Yu, M., Liu, B., Liu, M., Song, S., Chen, S., Zou, J., Zhu, W. G., and Luo, J. (2018) Sirtuin 7-mediated deacetylation of WD repeat domain 77 (WDR77) suppresses

cancer cell growth by reducing WDR77/PRMT5 transmethylase complex activity, *J Biol Chem 293*, 17769-17779.
402. Wei, T. Y., Juan, C. C., Hisa, J. Y., Su, L. J., Lee, Y. C., Chou, H. Y., Chen, J. M., Wu, Y. C., Chiu, S. C., Hsu, C. P., Liu, K. L., and Yu, C. T. (2012) Protein arginine methyltransferase 5 is a potential oncoprotein that upregulates G1 cyclins/cyclin-dependent kinases and the phosphoinositide 3-kinase/AKT signaling cascade, *Cancer Sci 103*, 1640-1650.
403. Kryukov, G. V., Wilson, F. H., Ruth, J. R., Paulk, J., Tsherniak, A., Marlow, S. E., Vazquez, F., Weir, B. A., Fitzgerald, M. E., Tanaka, M., Bielski, C. M., Scott, J. M., Dennis, C., Cowley, G. S., Boehm, J. S., Root, D. E., Golub, T. R., Clish, C. B., Bradner, J. E., Hahn, W. C., and Garraway, L. A. (2016) MTAP deletion confers enhanced dependency on the PRMT5 arginine methyltransferase in cancer cells, *Science 351*, 1214-1218.
404. Marjon, K., Cameron, M. J., Quang, P., Clasquin, M. F., Mandley, E., Kunii, K., McVay, M., Choe, S., Kernytsky, A., Gross, S., Konteatis, Z., Murtie, J., Blake, M. L., Travins, J., Dorsch, M., Biller, S. A., and Marks, K. M. (2016) MTAP Deletions in Cancer Create Vulnerability to Targeting of the MAT2A/PRMT5/RIOK1 Axis, *Cell Rep 15*, 574-587.
405. Chan-Penebre, E., Kuplast, K. G., Majer, C. R., Boriack-Sjodin, P. A., Wigle, T. J., Johnston, L. D., Rioux, N., Munchhof, M. J., Jin, L., Jacques, S. L., West, K. A., Lingaraj, T., Stickland, K., Ribich, S. A., Raimondi, A., Scott, M. P., Waters, N. J., Pollock, R. M., Smith, J. J., Barbash, O., Pappalardi, M., Ho, T. F., Nurse, K., Oza, K. P., Gallagher, K. T., Kruger, R., Moyer, M. P., Copeland, R. A., Chesworth, R., and Duncan, K. W. (2015) A selective inhibitor of PRMT5 with in vivo and in vitro potency in MCL models, *Nat Chem Biol 11*, 432-437.
406. Schapira, M. (2016) Chemical Inhibition of Protein Methyltransferases, *Cell Chem Biol 23*, 1067-1076.
407. Barczak, W., Jin, L., Carr, S. M., Munro, S., Ward, S., Kanapin, A., Samsonova, A., and La Thangue, N. B. (2020) PRMT5 promotes cancer cell migration and invasion through the E2F pathway, *Cell Death Dis 11*, 572.
408. Xiao, W., Chen, X., Liu, L., Shu, Y., Zhang, M., and Zhong, Y. (2019) Role of protein arginine methyltransferase 5 in human cancers, *Biomed Pharmacother 114*, 108790.
409. Bonday, Z. Q., Cortez, G. S., Grogan, M. J., Antonysamy, S., Weichert, K., Bocchinfuso, W. P., Li, F., Kennedy, S., Li, B., Mader, M. M., Arrowsmith, C. H., Brown, P. J., Eram, M. S., Szewczyk, M. M., Barsyte-Lovejoy, D., Vedadi, M., Guccione, E., and Campbell, R. M. (2018) LLY-283, a Potent and Selective Inhibitor of Arginine Methyltransferase 5, PRMT5, with Antitumor Activity, *ACS Med Chem Lett 9*, 612-617.
410. Smith, C. R., Aranda, R., Bobinski, T. P., Briere, D. M., Burns, A. C., Christensen, J. G., Clarine, J., Engstrom, L. D., Gunn, R. J., Ivetac, A., Jean-Baptiste, R., Ketcham, J. M., Kobayashi, M., Kuehler, J., Kulyk, S., Lawson, J. D., Moya, K., Olson, P., Rahbaek, L., Thomas, N. C., Wang, X., Waters, L. M., and Marx, M. A. (2022) Fragment-Based Discovery of MRTX1719, a Synthetic Lethal Inhibitor of the PRMT5*MTA Complex for the Treatment of MTAP-Deleted Cancers, *J Med Chem 65*, 1749-1766.
411. Gerhart, S. V., Kellner, W. A., Thompson, C., Pappalardi, M. B., Zhang, X. P., Montes de Oca, R., Penebre, E., Duncan, K., Boriack-Sjodin, A., Le, B., Majer, C., McCabe, M. T., Carpenter, C., Johnson, N., Kruger, R. G., and Barbash, O. (2018) Activation of the p53-MDM4 regulatory axis defines the anti-tumour response to PRMT5 inhibition through its role in regulating cellular splicing, *Sci Rep 8*, 9711.
412. Duncan, K. W., Rioux, N., Boriack-Sjodin, P. A., Munchhof, M. J., Reiter, L. A., Majer, C. R., Jin, L., Johnston, L. D., Chan-Penebre, E., Kuplast, K. G., Porter Scott, M., Pollock, R. M., Waters, N. J., Smith, J. J., Moyer, M. P., Copeland, R. A., and Chesworth, R. (2016) Structure and Property Guided Design in the Identification of PRMT5 Tool Compound EPZ015666, *ACS Med Chem Lett 7*, 162-166.
413. Agriculture, U. S. D. o. (2019) https://www.thesgc.org/chemical-probes/SGC3027.

414. Eram, M. S., Shen, Y., Szewczyk, M., Wu, H., Senisterra, G., Li, F., Butler, K. V., Kaniskan, H. U., Speed, B. A., Dela Sena, C., Dong, A., Zeng, H., Schapira, M., Brown, P. J., Arrowsmith, C. H., Barsyte-Lovejoy, D., Liu, J., Vedadi, M., and Jin, J. (2016) A Potent, Selective, and Cell-Active Inhibitor of Human Type I Protein Arginine Methyltransferases, *ACS Chem Biol 11*, 772-781.
415. Nakayama, K., Szewczyk, M. M., dela Sena, C., Wu, H., Dong, A., Zeng, H., Li, F., Ferreira de Freitas, R., Eram, M. S., Schapira, M., Baba, Y., Kunitomo, M., Cary, D. R., Tawada, M., Ohashi, A., Imaeda, Y., Saikatendu, K. S., Grimshaw, C. E., Vedadi, M., Arrowsmith, C. H., Barsyte-Lovejoy, D., Kiba, A., Tomita, D., and Brown, P. J. (2018) TP-064, a potent and selective small molecule inhibitor of PRMT4 for multiple myeloma, *Oncotarget*.
416. Robers, M. B., Vasta, J. D., Corona, C. R., Ohana, R. F., Hurst, R., Jhala, M. A., Comess, K. M., and Wood, K. V. (2019) Quantitative, Real-Time Measurements of Intracellular Target Engagement Using Energy Transfer, *Methods Mol Biol 1888*, 45-71.
417. Duncan, K. W., Chesworth, R., Boriack-Sjodin, P. A., Munchhof, M. J., Jin, L., Penebre, E., and Barbash, O. I. (2016) PRMT5 inhibitors and uses thereof, A61K31/44(2006.01), A61K31/00(2006.010), A61K31/535(2006.01) ed.
418. Scheer, S., Ackloo, S., Medina, T. S., Schapira, M., Li, F., Ward, J. A., Lewis, A. M., Northrop, J. P., Richardson, P. L., Kaniskan, H. U., Shen, Y., Liu, J., Smil, D., McLeod, D., Zepeda-Velazquez, C. A., Luo, M., Jin, J., Barsyte-Lovejoy, D., Huber, K. V. M., De Carvalho, D. D., Vedadi, M., Zaph, C., Brown, P. J., and Arrowsmith, C. H. (2019) A chemical biology toolbox to study protein methyltransferases and epigenetic signaling, *Nat Commun 10*, 19.
419. Kaniskan, H. U., Martini, M. L., and Jin, J. (2018) Inhibitors of Protein Methyltransferases and Demethylases, *Chem Rev 118*, 989-1068.
420. Szewczyk, M. M., Ishikawa, Y., Organ, S., Sakai, N., Li, F., Halabelian, L., Ackloo, S., Couzens, A. L., Eram, M., Dilworth, D., Fukushi, H., Harding, R., Dela Sena, C. C., Sugo, T., Hayashi, K., McLeod, D., Zepeda, C., Aman, A., Sanchez-Osuna, M., Bonneil, E., Takagi, S., Al-Awar, R., Tyers, M., Richard, S., Takizawa, M., Gingras, A. C., Arrowsmith, C. H., Vedadi, M., Brown, P. J., Nara, H., and Barsyte-Lovejoy, D. (2020) Pharmacological inhibition of PRMT7 links arginine monomethylation to the cellular stress response, *Nat Commun 11*, 2396.
421. Schirle, M., Bantscheff, M., and Kuster, B. (2012) Mass spectrometry-based proteomics in preclinical drug discovery, *Chem Biol 19*, 72-84.
422. Pesiridis, G. S., Diamond, E., and Van Duyne, G. D. (2009) Role of pICLn in methylation of Sm proteins by PRMT5, *J Biol Chem 284*, 21347-21359.
423. Hein, M. Y., Hubner, N. C., Poser, I., Cox, J., Nagaraj, N., Toyoda, Y., Gak, I. A., Weisswange, I., Mansfeld, J., Buchholz, F., Hyman, A. A., and Mann, M. (2015) A human interactome in three quantitative dimensions organized by stoichiometries and abundances, *Cell 163*, 712-723.
424. Bian, C., Chen, Q., and Yu, X. (2015) The zinc finger proteins ZNF644 and WIZ regulate the G9a/GLP complex for gene repression, *Elife 4*.
425. Rathert, P., Dhayalan, A., Murakami, M., Zhang, X., Tamas, R., Jurkowska, R., Komatsu, Y., Shinkai, Y., Cheng, X., and Jeltsch, A. (2008) Protein lysine methyltransferase G9a acts on non-histone targets, *Nat Chem Biol 4*, 344-346.
426. Rolland, T., Tasan, M., Charloteaux, B., Pevzner, S. J., Zhong, Q., Sahni, N., Yi, S., Lemmens, I., Fontanillo, C., Mosca, R., Kamburov, A., Ghiassian, S. D., Yang, X., Ghamsari, L., Balcha, D., Begg, B. E., Braun, P., Brehme, M., Broly, M. P., Carvunis, A. R., Convery-Zupan, D., Corominas, R., Coulombe-Huntington, J., Dann, E., Dreze, M., Dricot, A., Fan, C., Franzosa, E., Gebreab, F., Gutierrez, B. J., Hardy, M. F., Jin, M., Kang, S., Kiros, R., Lin, G. N., Luck, K., MacWilliams, A., Menche, J., Murray, R. R., Palagi, A., Poulin, M. M., Rambout, X., Rasla, J., Reichert, P., Romero, V., Ruyssinck, E., Sahalie, J. M., Scholz, A., Shah, A. A., Sharma, A., Shen, Y., Spirohn, K., Tam, S.,

Tejeda, A. O., Trigg, S. A., Twizere, J. C., Vega, K., Walsh, J., Cusick, M. E., Xia, Y., Barabasi, A. L., Iakoucheva, L. M., Aloy, P., De Las Rivas, J., Tavernier, J., Calderwood, M. A., Hill, D. E., Hao, T., Roth, F. P., and Vidal, M. (2014) A proteome-scale map of the human interactome network, *Cell 159*, 1212-1226.

427. Hirano, T., Shinsato, Y., Tanabe, K., Higa, N., Kamil, M., Kawahara, K., Yamamoto, M., Minami, K., Shimokawa, M., Arigami, T., Yanagita, S., Matushita, D., Uenosono, Y., Ishigami, S., Kijima, Y., Maemura, K., Kitazono, I., Tanimoto, A., Furukawa, T., and Natsugoe, S. (2020) FARP1 boosts CDC42 activity from integrin alphavbeta5 signaling and correlates with poor prognosis of advanced gastric cancer, *Oncogenesis 9*, 13.
428. Huttlin, E. L., Bruckner, R. J., Paulo, J. A., Cannon, J. R., Ting, L., Baltier, K., Colby, G., Gebreab, F., Gygi, M. P., Parzen, H., Szpyt, J., Tam, S., Zarraga, G., Pontano-Vaites, L., Swarup, S., White, A. E., Schweppe, D. K., Rad, R., Erickson, B. K., Obar, R. A., Guruharsha, K. G., Li, K., Artavanis-Tsakonas, S., Gygi, S. P., and Harper, J. W. (2017) Architecture of the human interactome defines protein communities and disease networks, *Nature 545*, 505-509.
429. Becher, I., Werner, T., Doce, C., Zaal, E. A., Togel, I., Khan, C. A., Rueger, A., Muelbaier, M., Salzer, E., Berkers, C. R., Fitzpatrick, P. F., Bantscheff, M., and Savitski, M. M. (2016) Thermal profiling reveals phenylalanine hydroxylase as an off-target of panobinostat, *Nat Chem Biol 12*, 908-910.
430. Palte, R. L., Schneider, S. E., Altman, M. D., Hayes, R. P., Kawamura, S., Lacey, B. M., Mansueto, M. S., Reutershan, M., Siliphaivanh, P., Sondey, C., Xu, H., Xu, Z., Ye, Y., and Machacek, M. R. (2020) Allosteric Modulation of Protein Arginine Methyltransferase 5 (PRMT5), *ACS Med Chem Lett 11*, 1688-1693.
431. Quiroz, R. V., Reutershan, M. H., Schneider, S. E., Sloman, D., Lacey, B. M., Swalm, B. M., Yeung, C. S., Gibeau, C., Spellman, D. S., Rankic, D. A., Chen, D., Witter, D., Linn, D., Munsell, E., Feng, G., Xu, H., Hughes, J. M. E., Lim, J., Sauri, J., Geddes, K., Wan, M., Mansueto, M. S., Follmer, N. E., Fier, P. S., Siliphaivanh, P., Daublain, P., Palte, R. L., Hayes, R. P., Lee, S., Kawamura, S., Silverman, S., Sanyal, S., Henderson, T. J., Ye, Y., Gao, Y., Nicholson, B., and Machacek, M. R. (2021) The Discovery of Two Novel Classes of 5,5-Bicyclic Nucleoside-Derived PRMT5 Inhibitors for the Treatment of Cancer, *J Med Chem 64*, 3911-3939.
432. Mulvaney, K. M., Blomquist, C., Acharya, N., Li, R., Ranaghan, M. J., O'Keefe, M., Rodriguez, D. J., Young, M. J., Kesar, D., Pal, D., Stokes, M., Nelson, A. J., Jain, S. S., Yang, A., Mullin-Bernstein, Z., Columbus, J., Bozal, F. K., Skepner, A., Raymond, D., LaRussa, S., McKinney, D. C., Freyzon, Y., Baidi, Y., Porter, D., Aguirre, A. J., Ianari, A., McMillan, B., and Sellers, W. R. (2021) Molecular basis for substrate recruitment to the PRMT5 methylosome, *Mol Cell 81*, 3481-3495 e3487.
433. McKinney, D. C., McMillan, B. J., Ranaghan, M. J., Moroco, J. A., Brousseau, M., Mullin-Bernstein, Z., O'Keefe, M., McCarren, P., Mesleh, M. F., Mulvaney, K. M., Robinson, F., Singh, R., Bajrami, B., Wagner, F. F., Hilgraf, R., Drysdale, M. J., Campbell, A. J., Skepner, A., Timm, D. E., Porter, D., Kaushik, V. K., Sellers, W. R., and Ianari, A. (2021) Discovery of a First-in-Class Inhibitor of the PRMT5-Substrate Adaptor Interaction, *J Med Chem 64*, 11148-11168.
434. Allali-Hassani, A., Szewczyk, M. M., Ivanochko, D., Organ, S. L., Bok, J., Ho, J. S. Y., Gay, F. P. H., Li, F., Blazer, L., Eram, M. S., Halabelian, L., Dilworth, D., Luciani, G. M., Lima-Fernandes, E., Wu, Q., Loppnau, P., Palmer, N., Talib, S. Z. A., Brown, P. J., Schapira, M., Kaldis, P., O'Hagan, R. C., Guccione, E., Barsyte-Lovejoy, D., Arrowsmith, C. H., Sanders, J. M., Kattar, S. D., Bennett, D. J., Nicholson, B., and Vedadi, M. (2019) Discovery of a chemical probe for PRDM9, *Nat Commun 10*, 5759.
435. Sun, Y., and Locasale, J. W. (2022) Rethinking the bioavailability and cellular transport properties of S-adenosylmethionine, *Cell Stress 6*, 1-5.

436. Lin, H., Wang, M., Zhang, Y. W., Tong, S., Leal, R. A., Shetty, R., Vaddi, K., and Luengo, J. I. (2019) Discovery of Potent and Selective Covalent Protein Arginine Methyltransferase 5 (PRMT5) Inhibitors, *ACS Med Chem Lett 10*, 1033-1038.
437. Pande, V., Sun, W., Beke, L., Berthelot, D., Brehmer, D., Brown, D., Corbera, J., Irving, S., Meerpoel, L., Nys, T., Parade, M., Robinson, C., Sommen, C., Viellevoye, M., Wu, T., and Thuring, J. W. (2020) A Chemical Probe for the Methyl Transferase PRMT5 with a Novel Binding Mode, *ACS Med Chem Lett 11*, 2227-2231.
438. Gulla, A., Hideshima, T., Bianchi, G., Fulciniti, M., Kemal Samur, M., Qi, J., Tai, Y. T., Harada, T., Morelli, E., Amodio, N., Carrasco, R., Tagliaferri, P., Munshi, N. C., Tassone, P., and Anderson, K. C. (2018) Protein arginine methyltransferase 5 has prognostic relevance and is a druggable target in multiple myeloma, *Leukemia 32*, 996-1002.
439. Shen, Y., Gao, G., Yu, X., Kim, H., Wang, L., Xie, L., Schwarz, M., Chen, X., Guccione, E., Liu, J., Bedford, M. T., and Jin, J. (2020) Discovery of First-in-Class Protein Arginine Methyltransferase 5 (PRMT5) Degraders, *J Med Chem 63*, 9977-9989.
440. Guderian, G., Peter, C., Wiesner, J., Sickmann, A., Schulze-Osthoff, K., Fischer, U., and Grimmler, M. (2011) RioK1, a new interactor of protein arginine methyltransferase 5 (PRMT5), competes with pICln for binding and modulates PRMT5 complex composition and substrate specificity, *J Biol Chem 286*, 1976-1986.
441. Baines, A. J., Lu, H. C., and Bennett, P. M. (2014) The Protein 4.1 family: hub proteins in animals for organizing membrane proteins, *Biochim Biophys Acta 1838*, 605-619.
442. Rodon Ahnert, J., Perez, C. A., Wong, K. M., Maitland, M. L., Tsai, F., Berlin, J., Liao, K. H., Wang, I.-M., Markovtsova, L., and Jacobs, I. A. (2021) PF-06939999, a potent and selective PRMT5 inhibitor, in patients with advanced or metastatic solid tumors: A phase 1 dose escalation study, Wolters Kluwer Health.
443. Brehmer, D., Beke, L., Wu, T., Millar, H. J., Moy, C., Sun, W., Mannens, G., Pande, V., Boeckx, A., van Heerde, E., Nys, T., Gustin, E. M., Verbist, B., Zhou, L., Fan, Y., Bhargava, V., Safabakhsh, P., Vinken, P., Verhulst, T., Gilbert, A., Rai, S., Graubert, T. A., Pastore, F., Fiore, D., Gu, J., Johnson, A., Philippar, U., Morschhauser, B., Walker, D., De Lange, D., Keersmaekers, V., Viellevoye, M., Diels, G., Schepens, W., Thuring, J. W., Meerpoel, L., Packman, K., Lorenzi, M. V., and Laquerre, S. (2021) Discovery and Pharmacological Characterization of JNJ-64619178, a Novel Small-Molecule Inhibitor of PRMT5 with Potent Antitumor Activity, *Mol Cancer Ther 20*, 2317-2328.
444. Smil, D., Eram, M. S., Li, F., Kennedy, S., Szewczyk, M. M., Brown, P. J., Barsyte-Lovejoy, D., Arrowsmith, C. H., Vedadi, M., and Schapira, M. (2015) Discovery of a Dual PRMT5-PRMT7 Inhibitor, *ACS Med Chem Lett 6*, 408-412.
445. Briggs, K., Cottrell, K., Tsai, A., Zhang, M., Tonini, M., Yoda, S., Lombardo, S., Teng, T., Davis, C., and Whittington, D. (2022) TNG908 is a brain-penetrant, MTA-cooperative PRMT5 inhibitor for the treatment of MTAP-deleted cancer, *European Journal of Cancer 174*, S84.
446. Berggard, T., Linse, S., and James, P. (2007) Methods for the detection and analysis of protein-protein interactions, *Proteomics 7*, 2833-2842.
447. Bonetta, L. (2010) Interactome under construction, *Nature 468*, 851-852.
448. Venkatesan, K., Rual, J. F., Vazquez, A., Stelzl, U., Lemmens, I., Hirozane-Kishikawa, T., Hao, T., Zenkner, M., Xin, X., Goh, K. I., Yildirim, M. A., Simonis, N., Heinzmann, K., Gebreab, F., Sahalie, J. M., Cevik, S., Simon, C., de Smet, A. S., Dann, E., Smolyar, A., Vinayagam, A., Yu, H., Szeto, D., Borick, H., Dricot, A., Klitgord, N., Murray, R. R., Lin, C., Lalowski, M., Timm, J., Rau, K., Boone, C., Braun, P., Cusick, M. E., Roth, F. P., Hill, D. E., Tavernier, J., Wanker, E. E., Barabasi, A. L., and Vidal, M. (2009) An empirical framework for binary interactome mapping, *Nat Methods 6*, 83-90.
449. Kuzmanov, U., and Emili, A. (2013) Protein-protein interaction networks: probing disease mechanisms using model systems, *Genome Medicine 5*, 37.
450. Kana, O., and Brylinski, M. (2019) Elucidating the druggability of the human proteome with eFindSite, *J Comput Aided Mol Des 33*, 509-519.

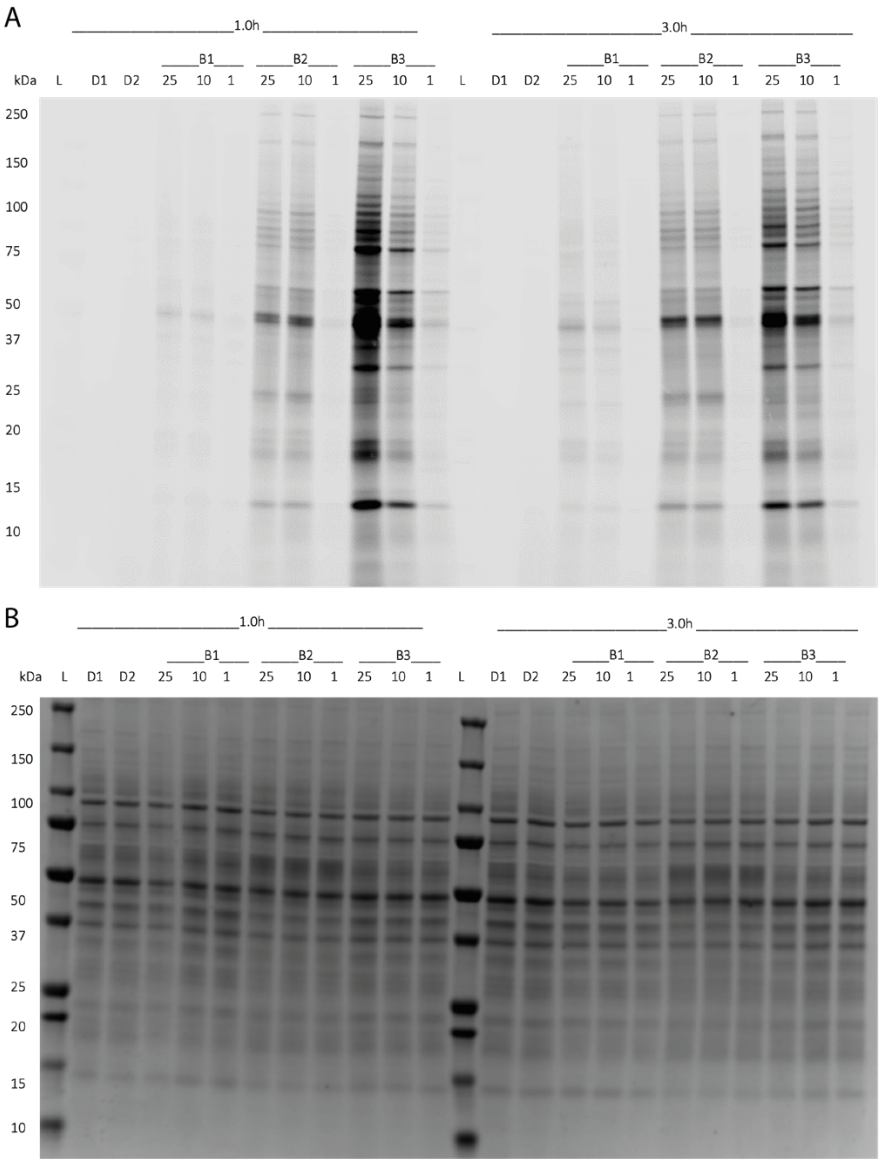
451. Rao, V. S., Srinivas, K., Sujini, G. N., and Kumar, G. N. (2014) Protein-protein interaction detection: methods and analysis, *Int J Proteomics 2014*, 147648.
452. Phizicky, E. M., and Fields, S. (1995) Protein-protein interactions: methods for detection and analysis, *Microbiol Rev 59*, 94-123.
453. Milroy, L. G., Grossmann, T. N., Hennig, S., Brunsveld, L., and Ottmann, C. (2014) Modulators of protein-protein interactions, *Chem Rev 114*, 4695-4748.
454. Jones, S., and Thornton, J. M. (1996) Principles of protein-protein interactions, *Proceedings of the National Academy of Sciences 93*, 13-20.
455. Cheng, A. C., Coleman, R. G., Smyth, K. T., Cao, Q., Soulard, P., Caffrey, D. R., Salzberg, A. C., and Huang, E. S. (2007) Structure-based maximal affinity model predicts small-molecule druggability, *Nat Biotechnol 25*, 71-75.
456. Wells, J. A., and McClendon, C. L. (2007) Reaching for high-hanging fruit in drug discovery at protein-protein interfaces, *Nature 450*, 1001-1009.
457. Jaeger, S., and Aloy, P. (2012) From protein interaction networks to novel therapeutic strategies, *IUBMB Life 64*, 529-537.
458. Goodarzi, M. O., and Azziz, R. (2006) Diagnosis, epidemiology, and genetics of the polycystic ovary syndrome, *Best Pract Res Clin Endocrinol Metab 20*, 193-205.
459. Wild, S., Pierpoint, T., Jacobs, H., and McKeigue, P. (2000) Long-term consequences of polycystic ovary syndrome: results of a 31 year follow-up study, *Hum Fertil (Camb) 3*, 101-105.
460. Dunaif, A. (1997) Insulin Resistance and the Polycystic Ovary Syndrome: Mechanism and Implications for Pathogenesis, *Endocrine Reviews*, 18(16): 774–800.
461. Chen, Z. J., Zhao, H., He, L., Shi, Y., Qin, Y., Shi, Y., Li, Z., You, L., Zhao, J., Liu, J., Liang, X., Zhao, X., Zhao, J., Sun, Y., Zhang, B., Jiang, H., Zhao, D., Bian, Y., Gao, X., Geng, L., Li, Y., Zhu, D., Sun, X., Xu, J. E., Hao, C., Ren, C. E., Zhang, Y., Chen, S., Zhang, W., Yang, A., Yan, J., Li, Y., Ma, J., and Zhao, Y. (2011) Genome-wide association study identifies susceptibility loci for polycystic ovary syndrome on chromosome 2p16.3, 2p21 and 9q33.3, *Nat Genet 43*, 55-59.
462. Tee, M. K., Speek, M., Legeza, B., Modi, B., Teves, M. E., McAllister, J. M., Strauss, J. F., 3rd, and Miller, W. L. (2016) Alternative splicing of DENND1A, a PCOS candidate gene, generates variant 2, *Mol Cell Endocrinol 434*, 25-35.
463. McAllister, J. M., Modi, B., Miller, B. A., Biegler, J., Bruggeman, R., Legro, R. S., and Strauss, J. F., 3rd. (2014) Overexpression of a DENND1A isoform produces a polycystic ovary syndrome theca phenotype, *Proc Natl Acad Sci U S A 111*, E1519-1527.
464. Marat, A. L., and McPherson, P. S. (2010) The connecdenn family, Rab35 guanine nucleotide exchange factors interfacing with the clathrin machinery, *J Biol Chem 285*, 10627-10637.
465. Klinkert, K., and Echard, A. (2016) Rab35 GTPase: A Central Regulator of Phosphoinositides and F-actin in Endocytic Recycling and Beyond, *Traffic 17*, 1063-1077.
466. Klinkert, K., Rocancourt, M., Houdusse, A., and Echard, A. (2016) Rab35 GTPase couples cell division with initiation of epithelial apico-basal polarity and lumen opening, *Nat Commun 7*, 11166.
467. Wu, X., Bradley, M. J., Cai, Y., Kummel, D., De La Cruz, E. M., Barr, F. A., and Reinisch, K. M. (2011) Insights regarding guanine nucleotide exchange from the structure of a DENN-domain protein complexed with its Rab GTPase substrate, *Proc Natl Acad Sci U S A 108*, 18672-18677.
468. Bunton, M. E. A. a. C. A. (1970) The Spontaneous Hydrolysis of Sulfonyl Fluorides, *J. Org. Chem*.
469. Lin-Gibson, S., Sarkar, S., Elliott, J., and Plant, A. (2016) Understanding and managing sources of variability in cell measurements, *Cell and Gene Therapy Insights 2*, 663-673.
470. Garcia-Gimenez, J. L., Olaso, G., Hake, S. B., Bonisch, C., Wiedemann, S. M., Markovic, J., Dasi, F., Gimeno, A., Perez-Quilis, C., Palacios, O., Capdevila, M., Vina, J., and

Pallardo, F. V. (2013) Histone h3 glutathionylation in proliferating mammalian cells destabilizes nucleosomal structure, *Antioxid Redox Signal 19*, 1305-1320.
471. Forster, M., Liang, X. J., Schroder, M., Gerstenecker, S., Chaikuad, A., Knapp, S., Laufer, S., and Gehringer, M. (2020) Discovery of a Novel Class of Covalent Dual Inhibitors Targeting the Protein Kinases BMX and BTK, *Int J Mol Sci 21*.
472. Vazquez-Rodriguez, S., Wright, M., Rogers, C. M., Cribbs, A. P., Velupillai, S., Philpott, M., Lee, H., Dunford, J. E., Huber, K. V. M., Robers, M. B., Vasta, J. D., Thezenas, M. L., Bonham, S., Kessler, B., Bennett, J., Fedorov, O., Raynaud, F., Donovan, A., Blagg, J., Bavetsias, V., Oppermann, U., Bountra, C., Kawamura, A., and Brennan, P. E. (2019) Design, Synthesis and Characterization of Covalent KDM5 Inhibitors, *Angew Chem Int Ed Engl 58*, 515-519.
473. Guo, W.-H., Qi, X., Liu, Y., Chung, C.-I., Bai, F., Lin, X., Wang, L., Chen, J., Nomie, K. J., Li, F., Wang, M. C., Shu, X., Onuchic, J. N., Woyach, J. A., Wang, M. L., and Wang, J. (2019) Enhancing Intracellular Concentration and Target Engagement of PROTACs with Reversible Covalent Chemistry.
474. Schilling, O., and Overall, C. M. (2008) Proteome-derived, database-searchable peptide libraries for identifying protease cleavage sites, *Nat Biotechnol 26*, 685-694.
475. Gray, J. L., von Delft, F., and Brennan, P. E. (2020) Targeting the Small GTPase Superfamily through Their Regulatory Proteins, *Angew Chem Int Ed Engl 59*, 6342-6366.
476. Allaire, P. D., Marat, A. L., Dall'Armi, C., Di Paolo, G., McPherson, P. S., and Ritter, B. (2010) The Connecdenn DENN domain: a GEF for Rab35 mediating cargo-specific exit from early endosomes, *Mol Cell 37*, 370-382.
477. Chaineau, M., Ioannou, M. S., and McPherson, P. S. (2013) Rab35: GEFs, GAPs and effectors, *Traffic 14*, 1109-1117.
478. Marat, A. L., Ioannou, M. S., and McPherson, P. S. (2012) Connecdenn 3/DENND1C binds actin linking Rab35 activation to the actin cytoskeleton, *Mol Biol Cell 23*, 163-175.
479. Gnatzy, M. T., Geiger, T. M., Kuehn, A., Gutfreund, N., Walz, M., Kolos, J. M., and Hausch, F. (2021) Development of NanoBRET-Binding Assays for FKBP-Ligand Profiling in Living Cells, *Chembiochem 22*, 2257-2261.
480. Savage, E. E., Wootten, D., Christopoulos, A., Sexton, P. M., and Furness, S. G. (2013) A simple method to generate stable cell lines for the analysis of transient protein-protein interactions, *Biotechniques 54*, 217-221.
481. Kulasekaran, G., Nossova, N., Marat, A. L., Lund, I., Cremer, C., Ioannou, M. S., and McPherson, P. S. (2015) Phosphorylation-dependent Regulation of Connecdenn/DENND1 Guanine Nucleotide Exchange Factors, *J Biol Chem 290*, 17999-18008.
482. Durrant, D. E., Smith, E. A., Goncharova, E. I., Sharma, N., Alexander, P. A., Stephen, A. G., Henrich, C. J., and Morrison, D. K. (2021) Development of a High-throughput NanoBRET Screening Platform to Identify Modulators of the RAS/RAF Interaction, *Mol Cancer Ther 20*, 1743-1754.
483. Najumudeen, A. K., Jaiswal, A., Lectez, B., Oetken-Lindholm, C., Guzman, C., Siljamaki, E., Posada, I. M., Lacey, E., Aittokallio, T., and Abankwa, D. (2016) Cancer stem cell drugs target K-ras signaling in a stemness context, *Oncogene 35*, 5248-5262.
484. Ran, X., and Gestwicki, J. E. (2018) Inhibitors of protein-protein interactions (PPIs): an analysis of scaffold choices and buried surface area, *Curr Opin Chem Biol 44*, 75-86.
485. Wang, X., Ni, D., Liu, Y., and Lu, S. (2021) Rational Design of Peptide-Based Inhibitors Disrupting Protein-Protein Interactions, *Front Chem 9*, 682675.
486. Schatti, J., Sezer, U., Pedalino, S., Cotter, J. P., Arndt, M., Mayor, M., and Kohler, V. (2017) Tailoring the volatility and stability of oligopeptides, *J Mass Spectrom 52*, 550-556.
487. Villar, E. A., Beglov, D., Chennamadhavuni, S., Porco, J. A., Jr., Kozakov, D., Vajda, S., and Whitty, A. (2014) How proteins bind macrocycles, *Nat Chem Biol 10*, 723-731.
488. Begnini, F., Geschwindner, S., Johansson, P., Wissler, L., Lewis, R. J., Danelius, E., Luttens, A., Matricon, P., Carlsson, J., Lenders, S., Konig, B., Friedel, A., Sjo, P., Schiesser, S.,

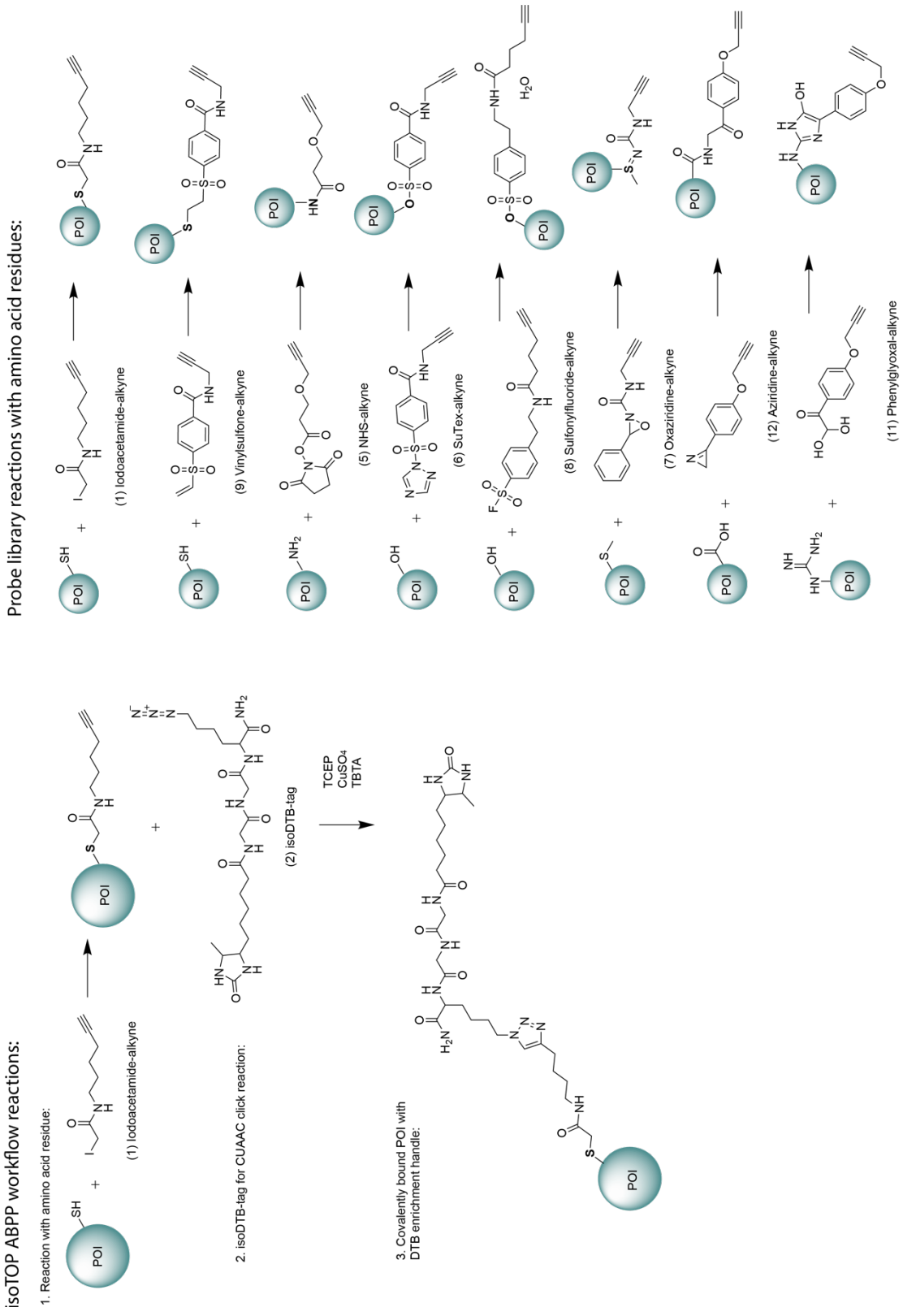
and Kihlberg, J. (2022) Importance of Binding Site Hydration and Flexibility Revealed When Optimizing a Macrocyclic Inhibitor of the Keap1-Nrf2 Protein-Protein Interaction, *J Med Chem 65*, 3473-3517.
489. Lang, S., Bellany, F., Lin, D., Barrett, D. S., Cartmill, K. R., Fletcher, D. A., Kerr, C., Plater, A., Forte, B., and Baragana, B. (2023) The Quest to Identify USP8 Inhibitors for Parkinsons Disease, a PAINful Experience, *bioRxiv*, 2023.2009. 2005.556294.
490. Durinck, S., Moreau, Y., Kasprzyk, A., Davis, S., De Moor, B., Brazma, A., and Huber, W. (2005) BioMart and Bioconductor: a powerful link between biological databases and microarray data analysis, *Bioinformatics 21*, 3439-3440.
491. Durinck, S., Spellman, P., Birney, E., and Huber, W. (2009) Mapping identifiers for the integration of genomic datasets with the R/Bioconductor package biomaRt, *Nature Protocols Nature Protocols*, 1184-1191.
492. Wickham, H., Averick, M., Bryan, J., Chang, W., McGowan, L., François, R., Grolemund, G., Hayes, A., Henry, L., Hester, J., Kuhn, M., Pedersen, T., Miller, E., Bache, S., Müller, K., Ooms, J., Robinson, D., Seidel, D., Spinu, V., Takahashi, K., Vaughan, D., Wilke, C., Woo, K., and Yutani, H. (2019) Welcome to the Tidyverse, *Journal of Open Source Software 4*.

10. Appendix

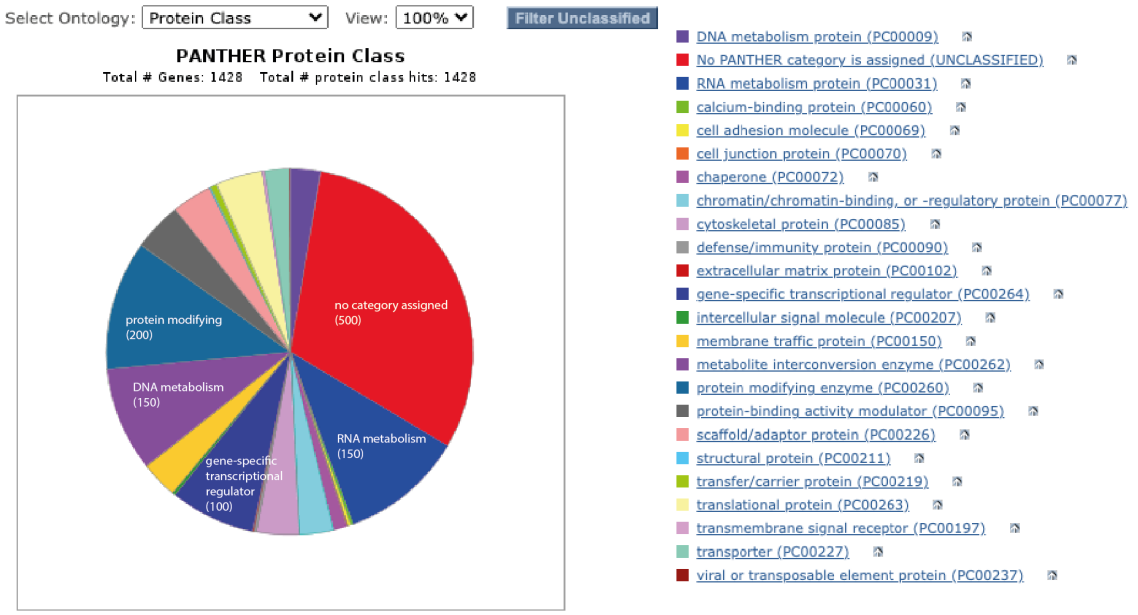
Supplementary Figures



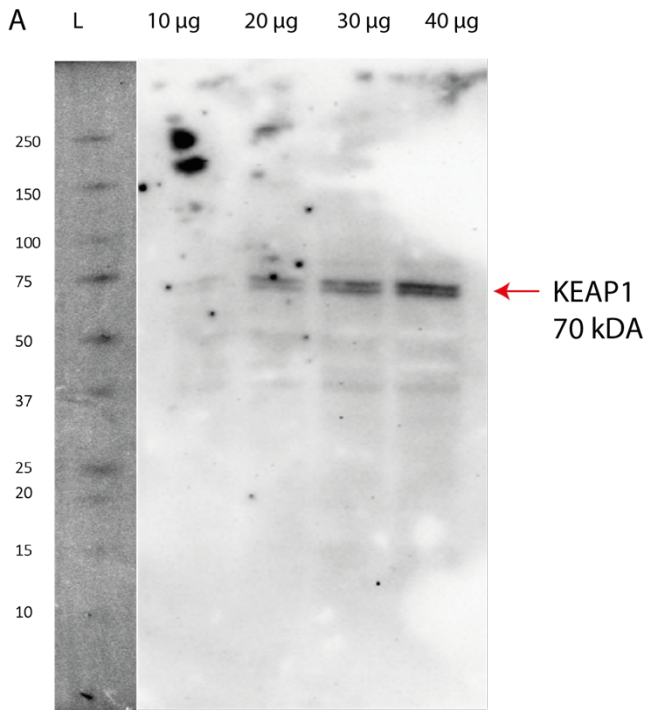
Supplementary Figure S1: Studies using IAA in indicated concentrations 25-1 µM or using DMSO control (D1 and D2) in K562 lysates. Incubation times 1 h and 3 h are compared as well as different lysis buffers. B1 is PBS, B2 is PBS plus 0.8% NP-40, B3 is PBS plus 0.35% DDM. A) In-gel fluorescence visualisation using IRDye 800 CW streptavidin (Licor, 1:1000). B) Coomassie stain showing equal sample loading.



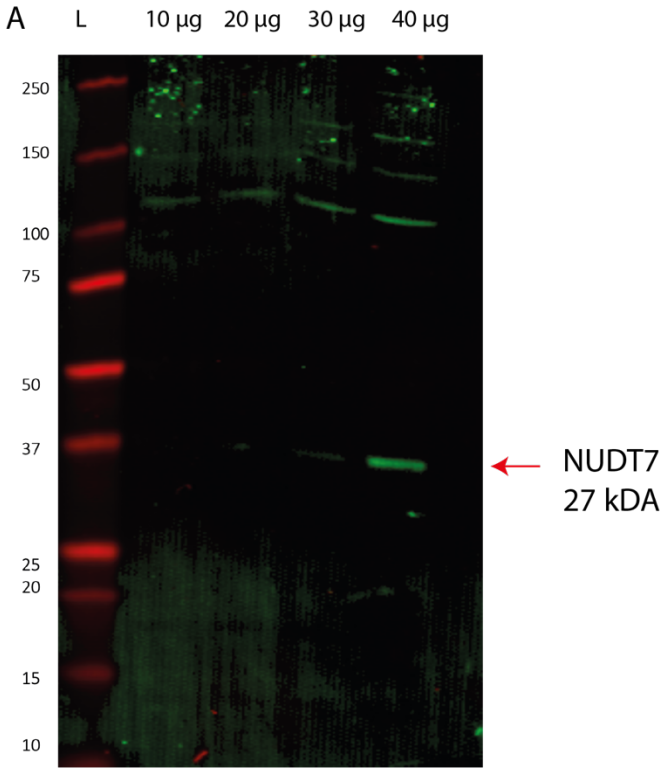
Supplementary Figure S2: isoTOP ABPP workflow chemical reactions shown as an example of IAA reacting with a cysteine amino acid residue, a subsequent CuAAC-reaction with the isoDTB-tag introduces the enrichment handle (left). Reaction of the probe library with respective amino acid residues (right), before click-reaction.



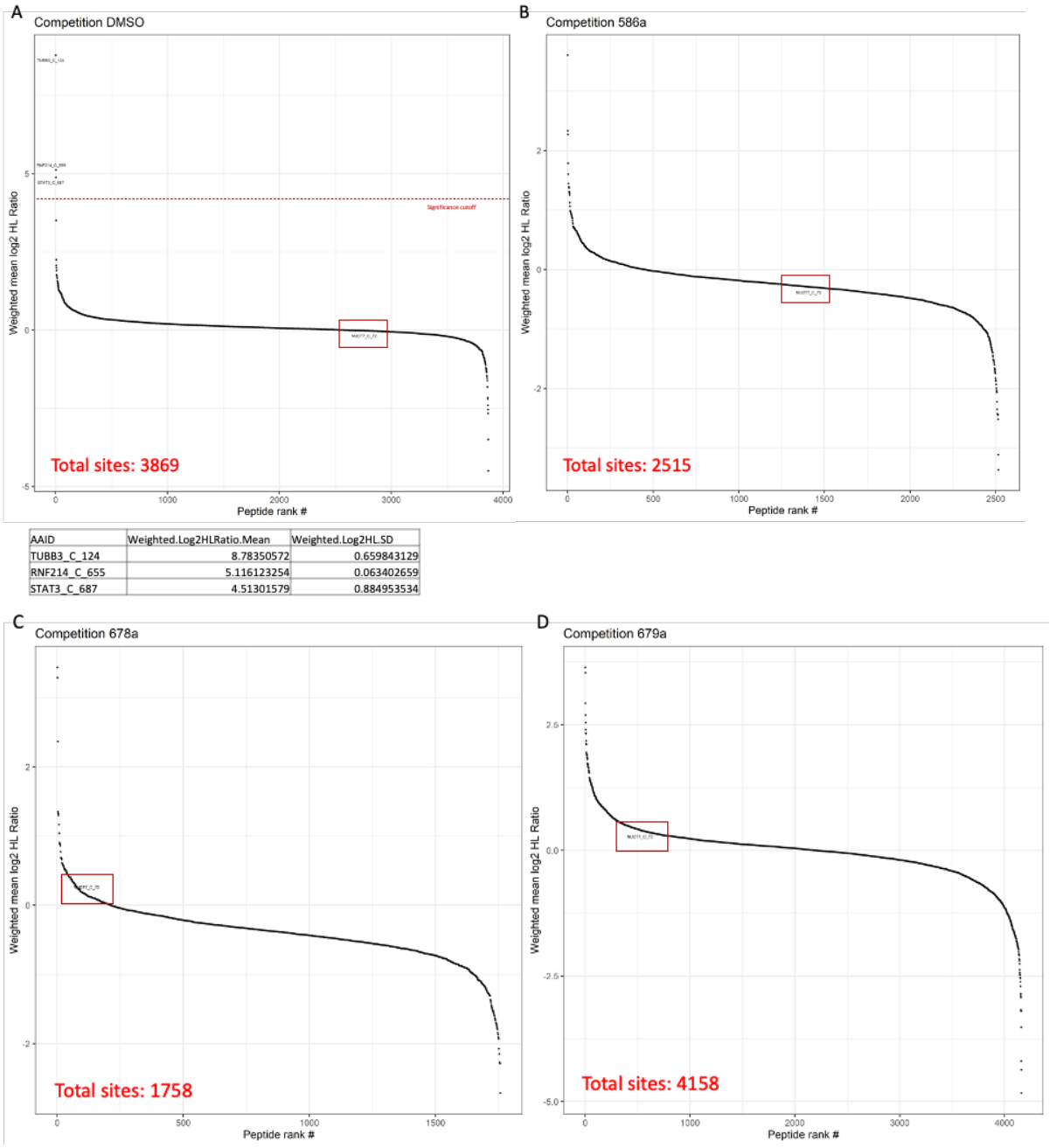
Supplementary Figure S3: Functional classification of unique proteins derived from the cell-based DIA data analysis using PANTHER (Protein ANalysis THrough Evolutionary Relationships) classification system, indicating presence of DNA and RNA metabolism involved proteins (around 30 % of protein class hits). Chart derived from pantherdb.org.



Supplementary Figure S4: Western blot of KEAP1 using 10-40 µg of MDAMB231 lysates. Bands were detected using KEAP1-antibody (Santa Cruz, sc365626, 1:1000) and secondary antibody HRP-antibody (Thermo Fisher, 7076S, 1:10000) and imaged at the ChemiDoc.



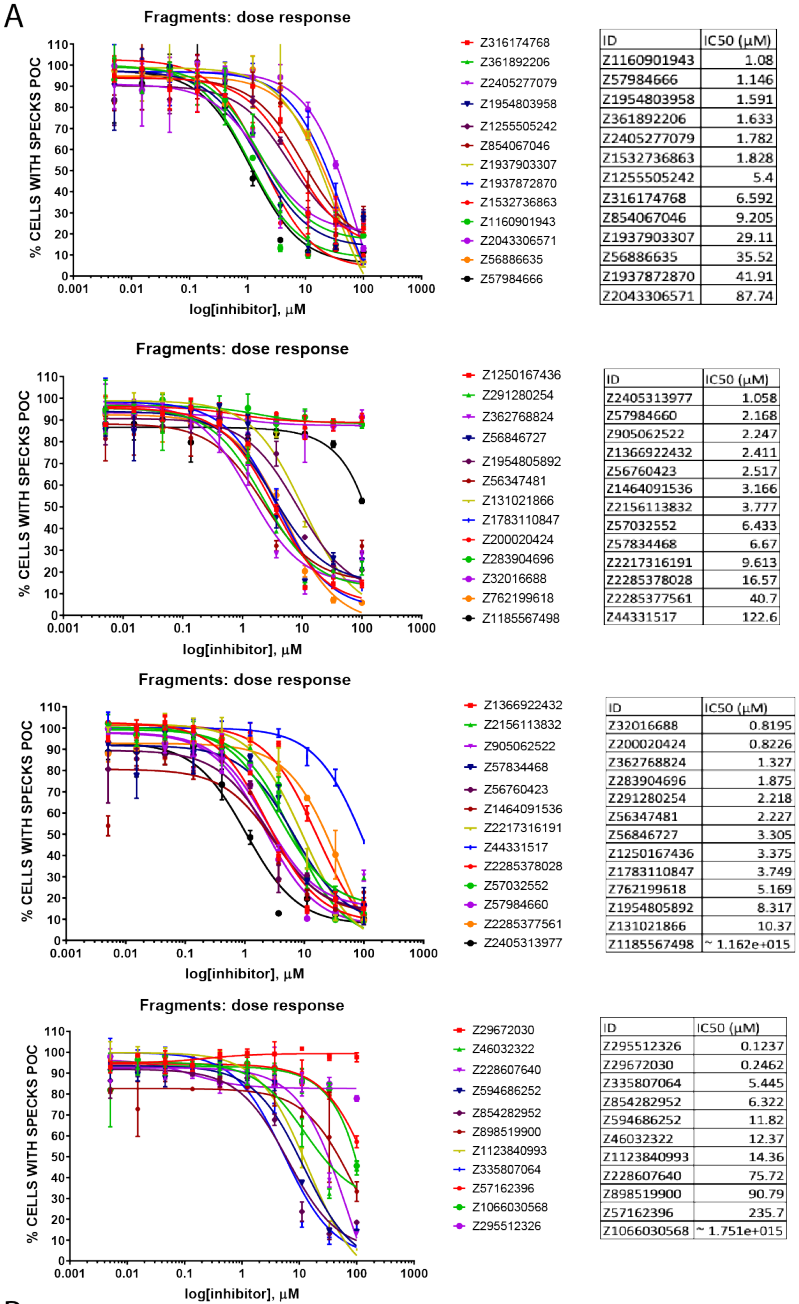
Supplementary Figure S5: Western blot of KEAP1 using 10-40 µg of NUDT7_FLAG tag transfected HEK293T lysates. Visualisation of FLAG-tag using anti-FLAG antibody (Merck, F3165-1MG, 1:1000) and secondary antibody Alexa Fluor 790 (Thermo Fisher, A 1137. 1:10000).



AAID	Weighted.Log2HLRatio.Mean	Weighted.Log2HL.SD
TUBB3_C_124	8.78350572	0.659843129
RNF214_C_655	5.116123254	0.063402659
STAT3_C_687	4.51301579	0.884953534

Supplementary Figure 6: Waterfall plots for NUDT7 competition, all samples show NUDT7_C72. NUDT7-flag tag transfected cells were treated with 10 µM of respective compounds before lysis and treatment with 100 µM VS-alkyne followed by isoTOP ABPP experiment. A) The DMSO result shows enrichment of 3 targets, which are thought to be outliers belonging to the background as no competition was performed. B-D) Negative controls show no competition R>4.

A



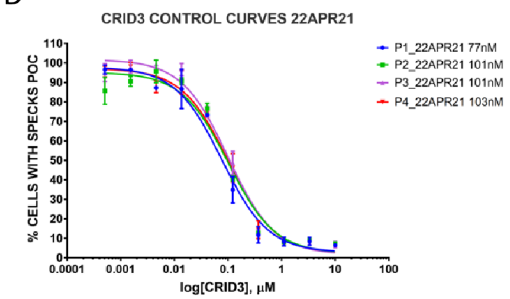
ID	IC50 (µM)
Z1160901943	1.08
Z57984666	1.146
Z1954803958	1.591
Z361892206	1.633
Z2405277079	1.782
Z1532736863	1.828
Z1255505242	5.4
Z316174768	6.592
Z854067046	9.205
Z1937903307	29.11
Z56886635	35.52
Z1937872870	41.91
Z2043306571	87.74

ID	IC50 (µM)
Z2405313977	1.058
Z57984660	2.168
Z905062522	2.247
Z1366922432	2.411
Z56760423	2.517
Z1464091536	3.166
Z2156113832	3.777
Z57032552	6.433
Z57834468	6.67
Z2217316191	9.613
Z2285378028	16.57
Z2285377561	40.7
Z44331517	122.6

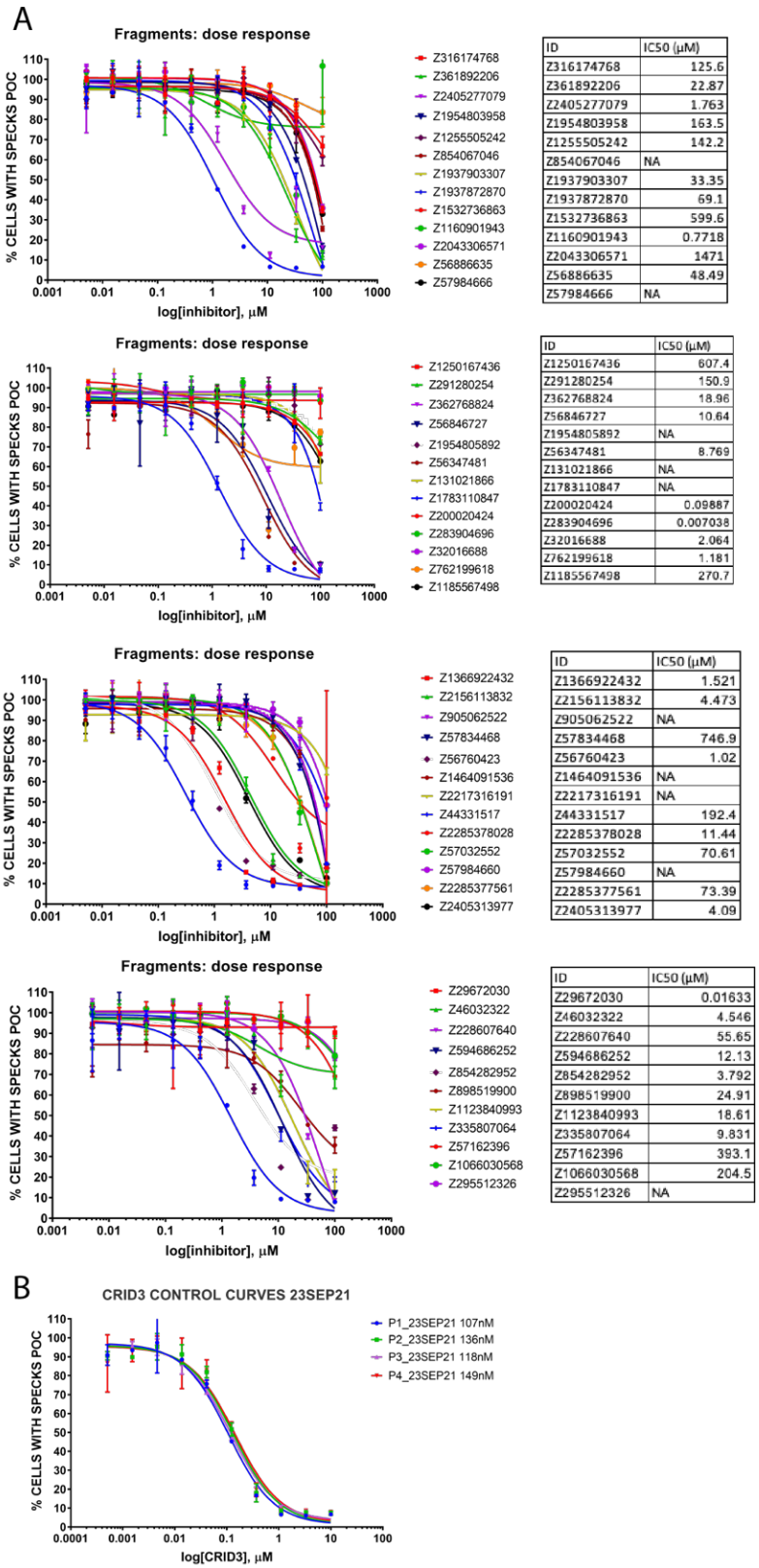
ID	IC50 (µM)
Z32016688	0.8195
Z200020424	0.8226
Z362768824	1.327
Z283904696	1.875
Z291280254	2.218
Z56347481	2.227
Z56846727	3.305
Z1250167436	3.375
Z1783110847	3.749
Z762199618	5.169
Z1954805892	8.317
Z131021866	10.37
Z1185567498	~ 1.162e+015

ID	IC50 (µM)
Z295512326	0.1237
Z29672030	0.2462
Z335807064	5.445
Z854282952	6.322
Z594686252	11.82
Z46032322	12.37
Z1123840993	14.36
Z228607640	75.72
Z898519900	90.79
Z57162396	235.7
Z1066030568	~ 1.751e+015

B



Supplementary Figure S7: Dose-response curves for NLRP3 (DR 1). Cells were primed with LPS for 2 h and triggered with nigericin for 2 h and incubated with respective fragments before speck-readout. IC_{50} values were derived from GraphPad Prism, from plotted dose-response curves (inhibitor vs response, three parameters). Error bars are depicted as SEM. A) Dose-response curves for the fragments on 4 plates. B) CRID3 control for 4 plates.



ID	IC50 (µM)
Z316174768	125.6
Z361892206	22.87
Z2405277079	1.763
Z1954803958	163.5
Z1255505242	142.2
Z854067046	NA
Z1937903307	33.35
Z1937872870	69.1
Z1532736863	599.6
Z1160901943	0.7718
Z2043306571	1471
Z56886635	48.49
Z57984666	NA

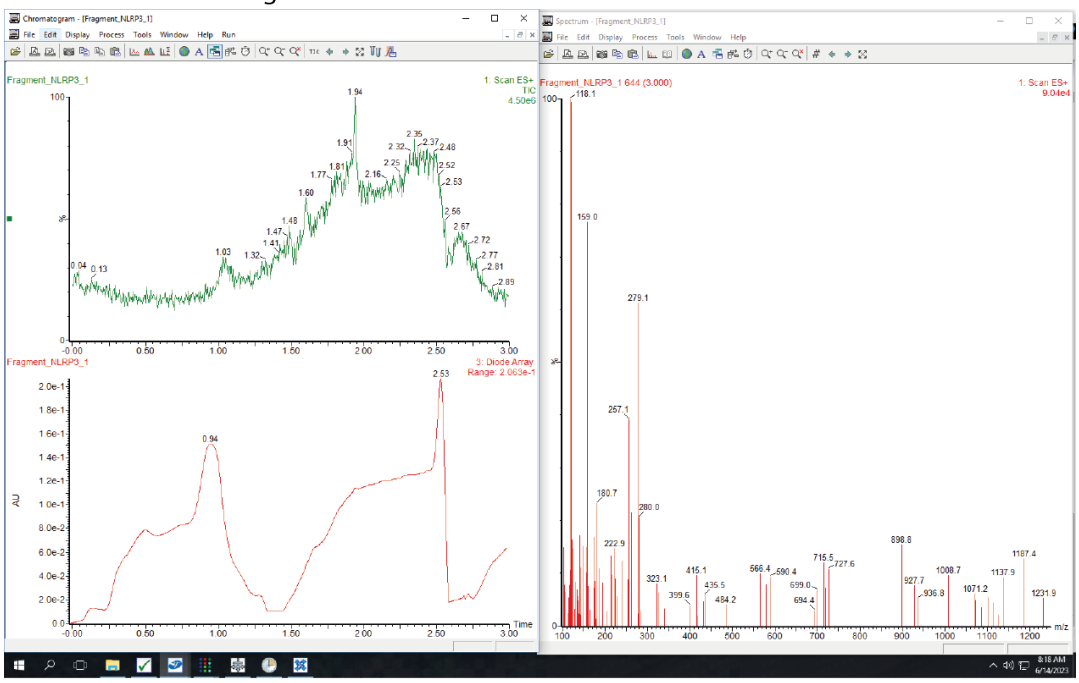
ID	IC50 (µM)
Z1250167436	607.4
Z291280254	150.9
Z362768824	18.96
Z56846727	10.64
Z1954805892	NA
Z56347481	8.769
Z131021866	NA
Z1783110847	NA
Z200020424	0.09887
Z283904696	0.007038
Z32016688	2.064
Z762199618	1.181
Z1185567498	270.7

ID	IC50 (µM)
Z1366922432	1.521
Z2156113832	4.473
Z905062522	NA
Z57834468	746.9
Z56760423	1.02
Z1464091536	NA
Z2217316191	NA
Z44331517	192.4
Z2285378028	11.44
Z57032552	70.61
Z57984660	NA
Z2285377561	73.39
Z2405313977	4.09

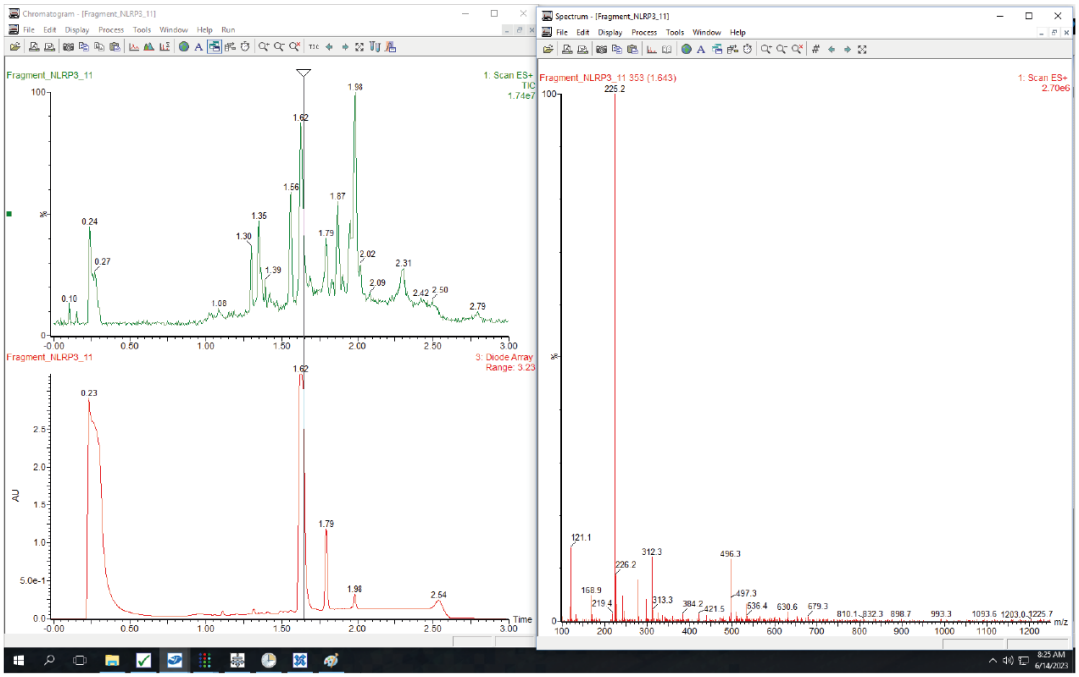
ID	IC50 (µM)
Z29672030	0.01633
Z46032322	4.546
Z228607640	55.65
Z594686252	12.13
Z854282952	3.792
Z898519900	24.91
Z1123840993	18.61
Z335807064	9.831
Z57162396	393.1
Z1066030568	204.5
Z295512326	NA

Supplementary Figure S8: Dose-response curves for NLRP3 (DR 2). Cells were primed with LPS for 2 h and triggered with nigericin for 2 h and incubated with respective fragments before SPECK-readout. IC_{50} values were derived from GraphPad prism, from plotted dose-response curves(inhibitor vs response, three parameters). Error bars are depicted as SEM. A) Dose-response curves for the fragments on 4 plates. B) CRID3 control for 4 plates.

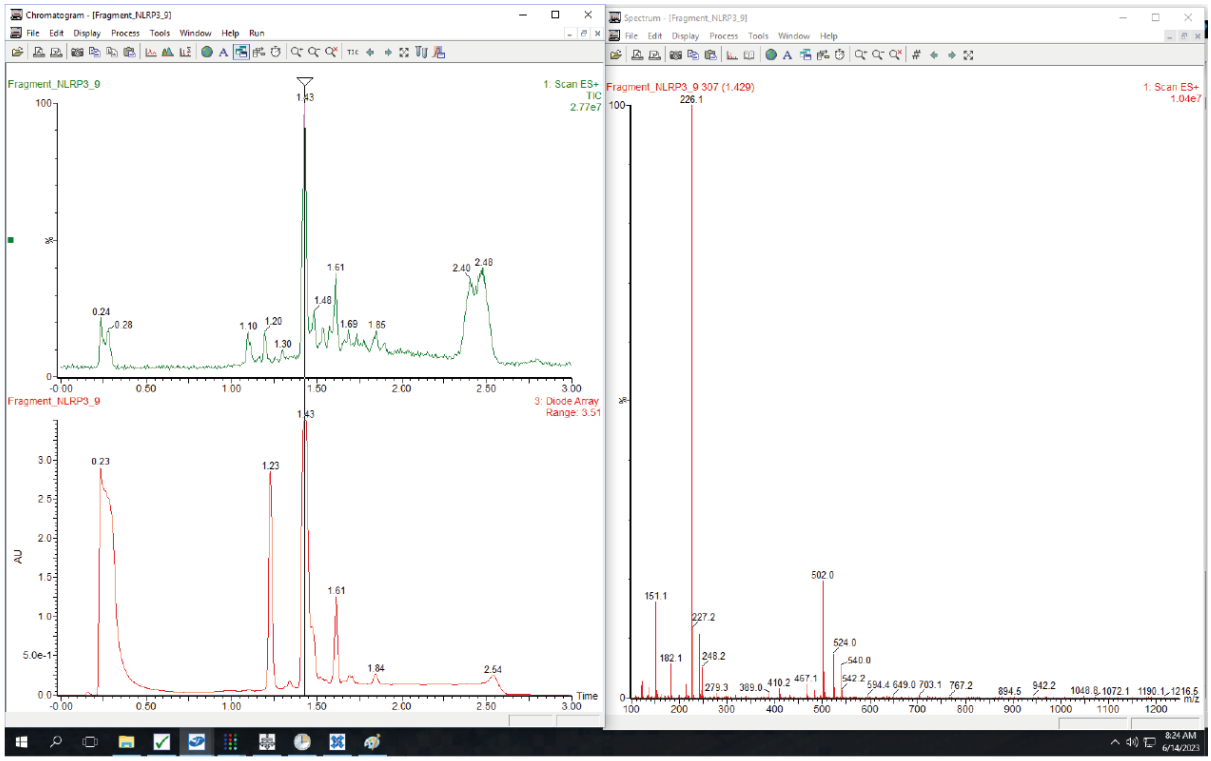
A Z3015818078 MW 278 g/mol



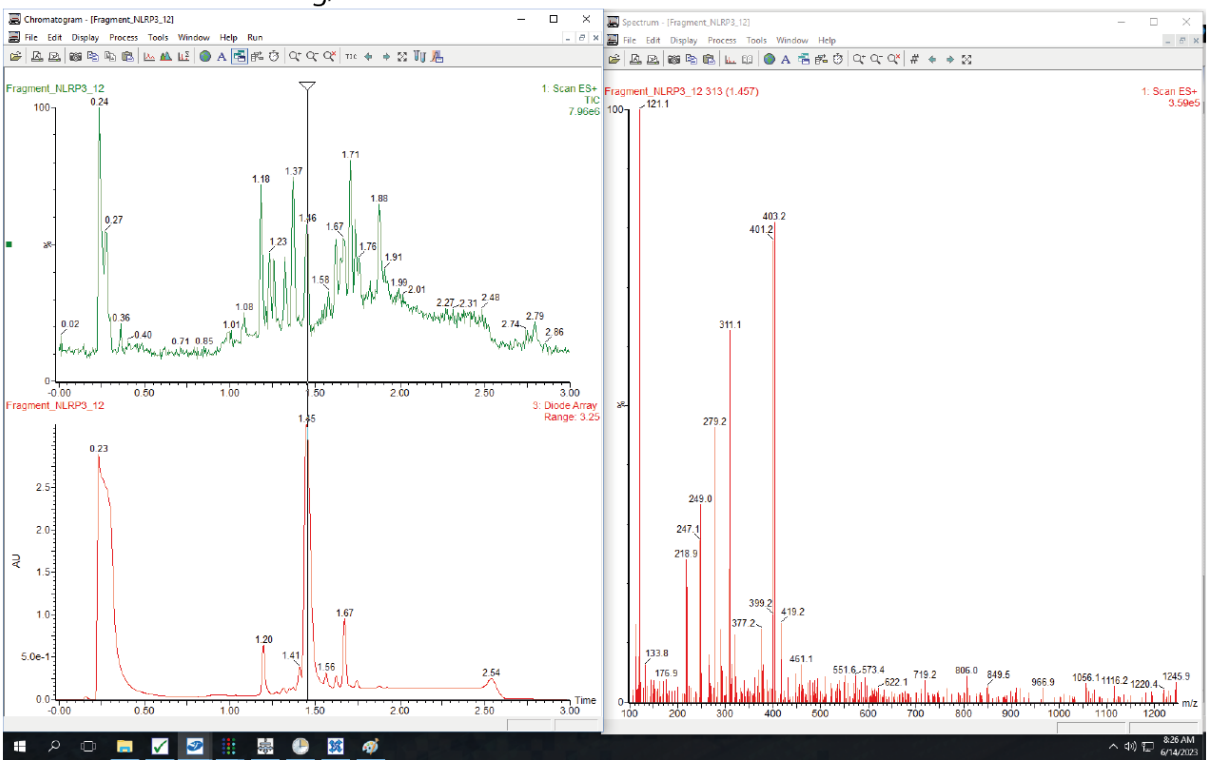
B Z424784962 MW 225 g/mol



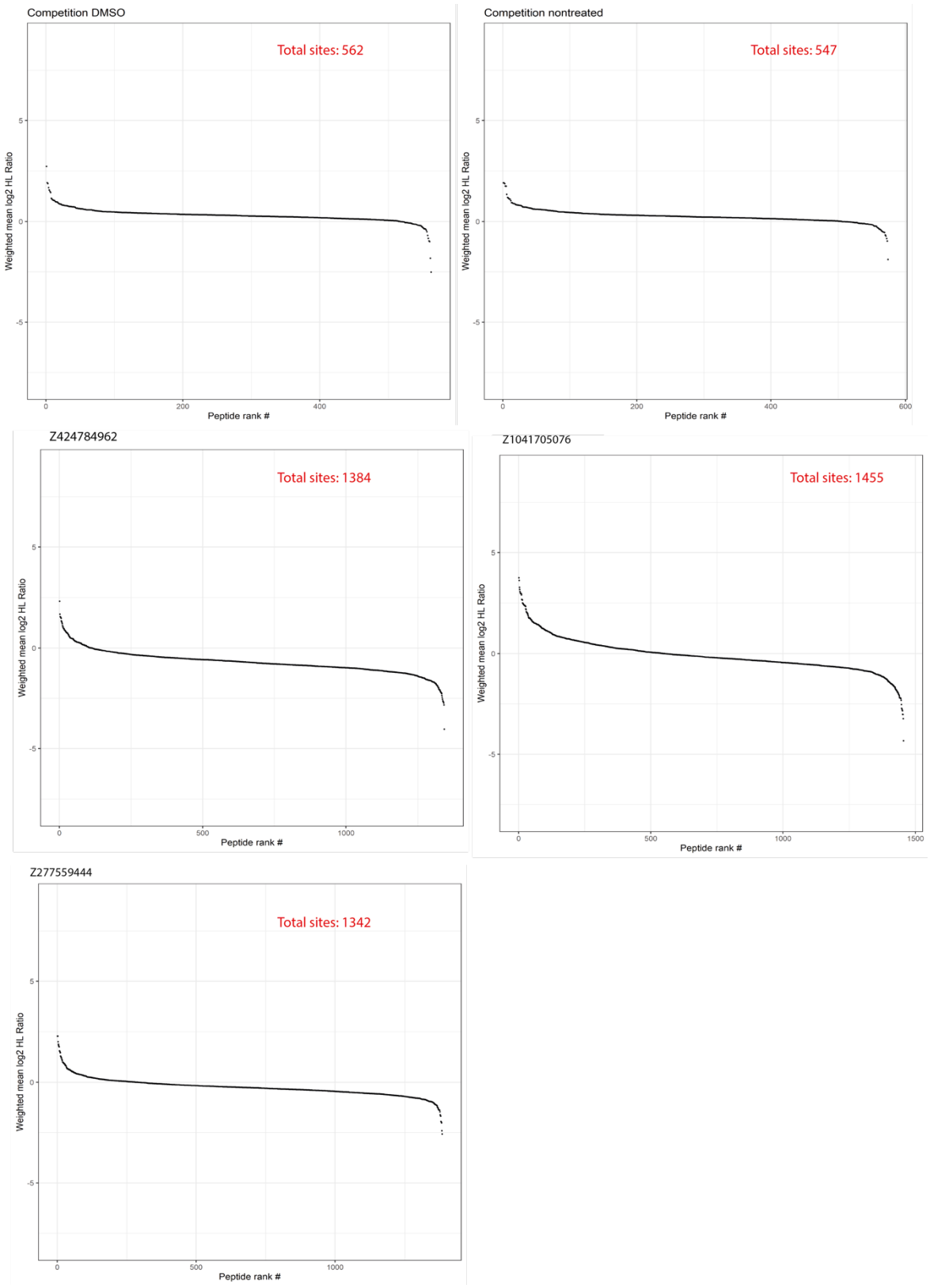
C Z1041705076 MW 224 g/mol



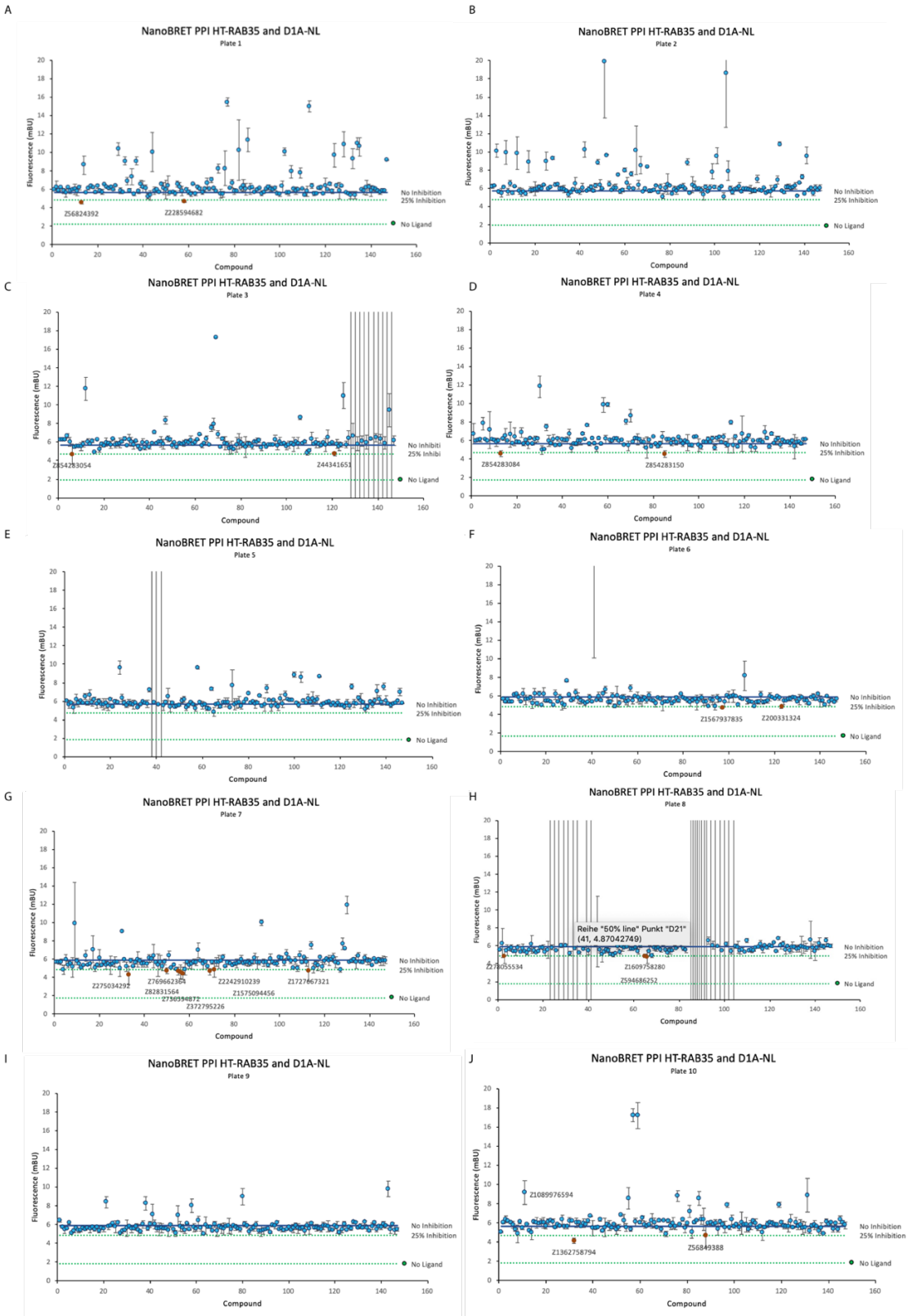
D Z277559444 MW 247 g/mol



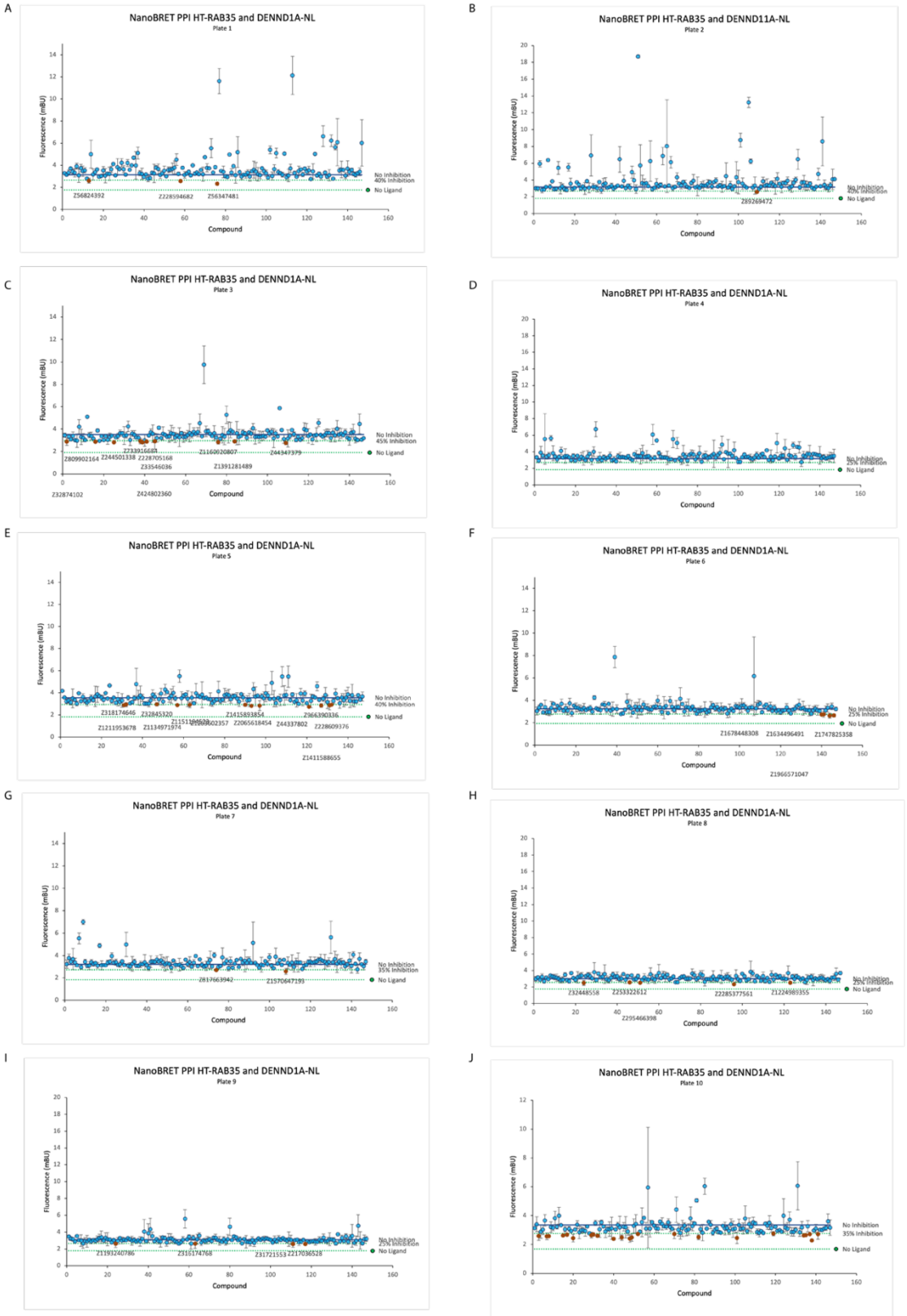
Supplementary Figure S9: LC-MS of fragments for isoTOP ABPP screen, showing ES+ TIC and m/z spectrum for selected peak areas.



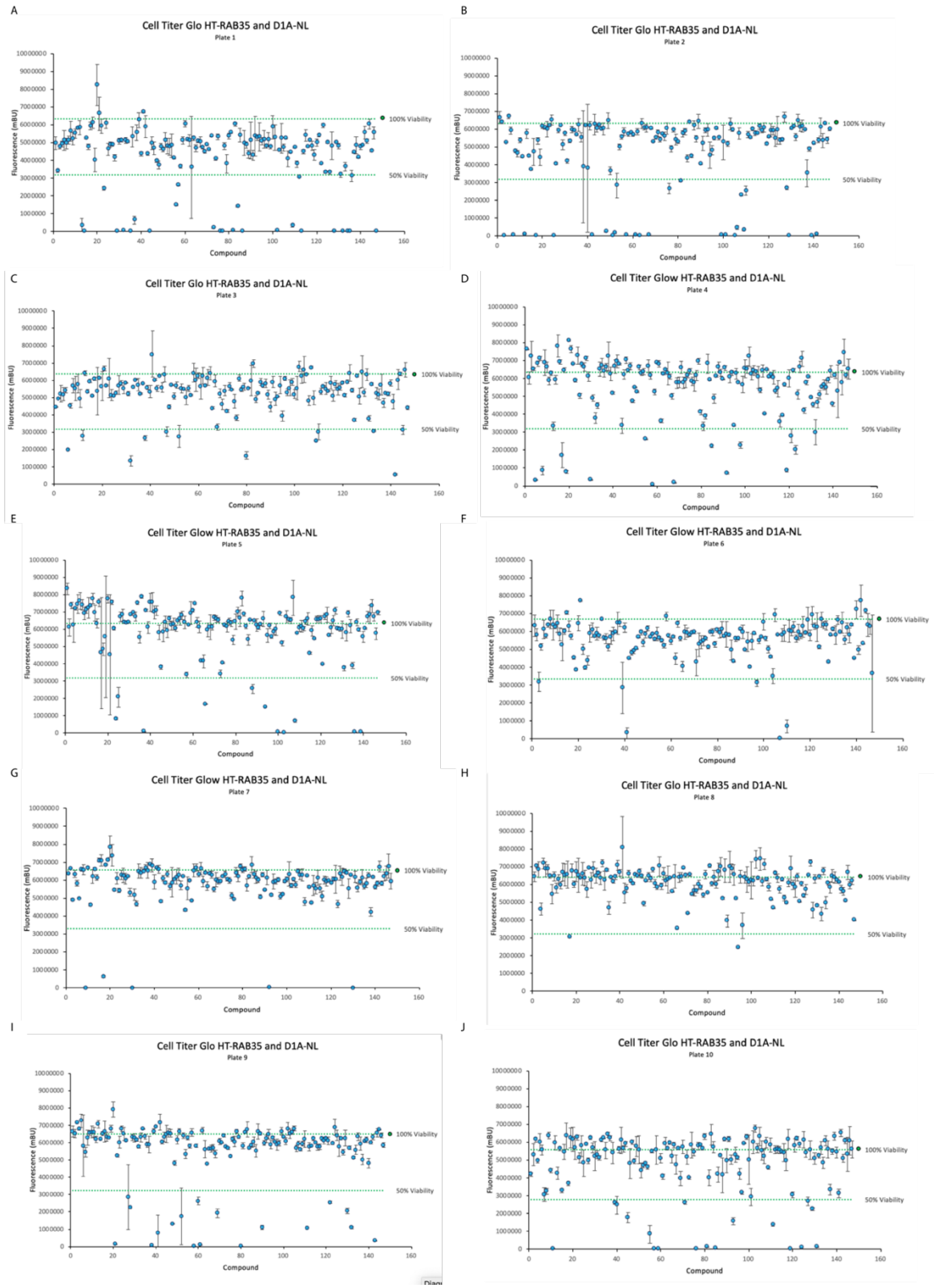
Supplementary Figure 10: IsoTOP ABPP results as waterfall plots for respective fragments and controls in BMDM cells (n=3). The fragments did not yield competed sites with R > 4.



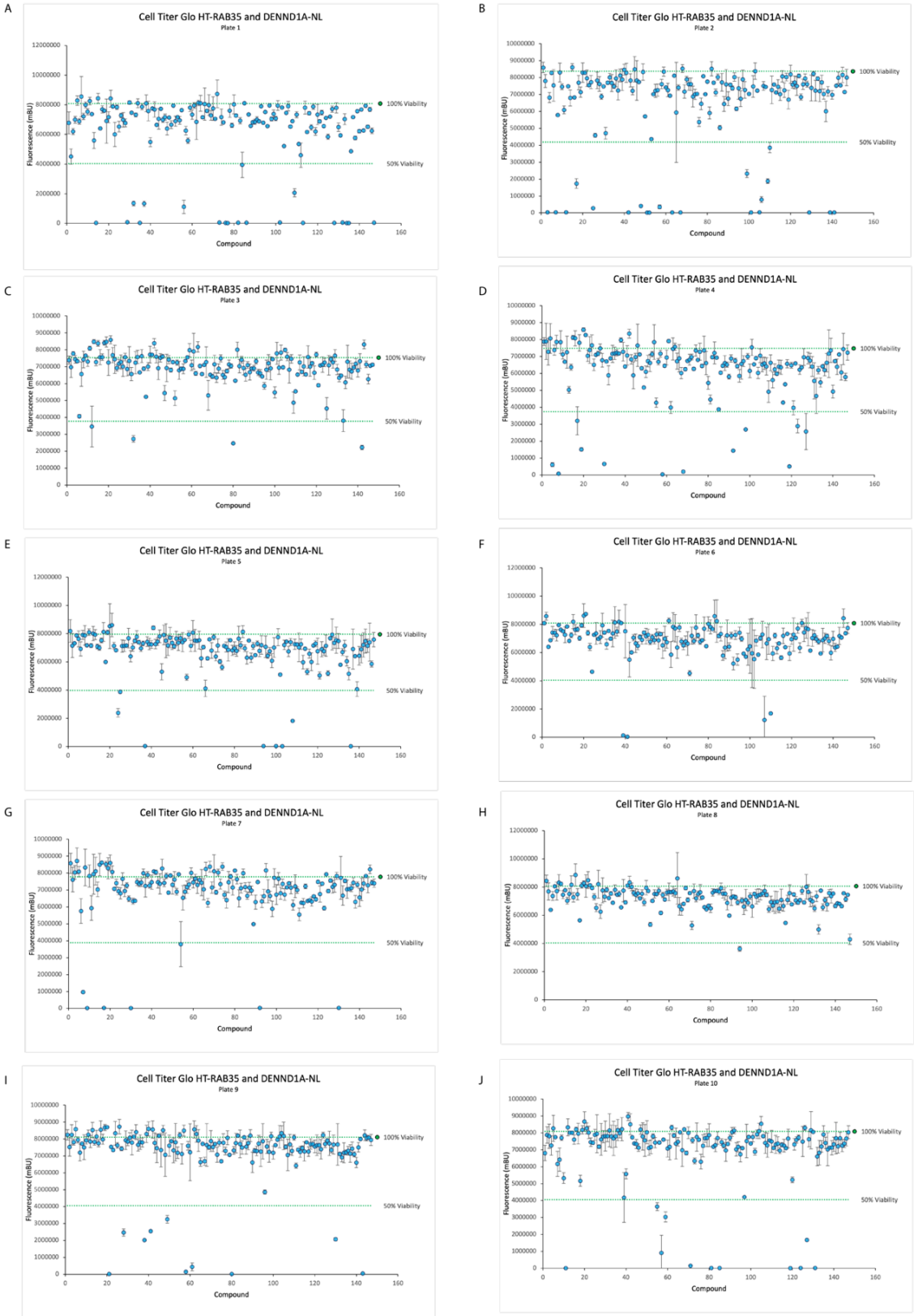
Supplementary Figure S11: DENND1A and RAB35 NanoBRET PPI assay experiment 1, performed on 10 plates using around 1500 fragments in triplicates. A-J) For individual plates the NanoBRET readout mBU is plotted against the compounds. The average mBU of DMSO control with ligand was used to define no inhibition, whereas the DMSO controls without ligand were used to define 100 % inhibition. As a cut-off, a minimum of 25% inhibition was chosen to define a preliminary hit. Error bars are depicted as the STDEV.



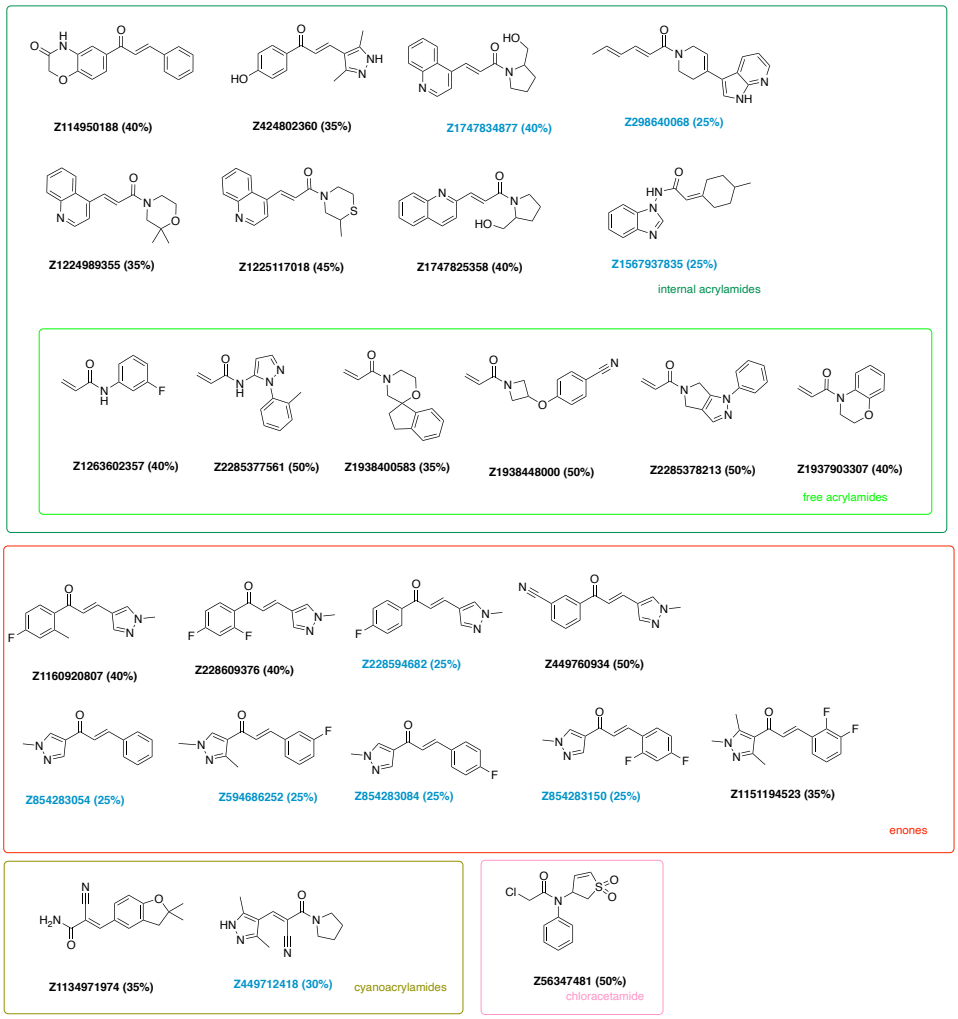
Supplementary Figure S12: DENND1A and Rab35 NanoBRET PPI assay experiment 2, performed on 10 plates using around 1500 fragments in triplicates. A-J) For individual plates the NanoBRET readout mBU is plotted against the compounds. The average mBU of DMSO control with ligand was used to define no inhibition, whereas the DMSO controls without ligand were used to define 100 % inhibition. As a cut-off, a minimum of 25% inhibition was chosen to define a preliminary hit. Error bars are depicted as the STDEV.



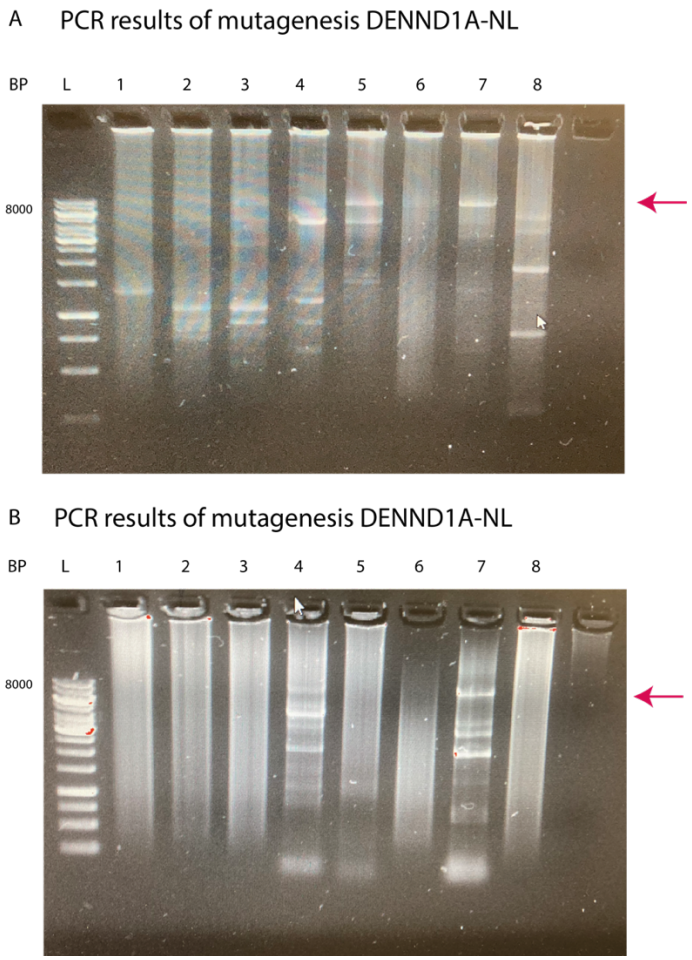
Supplementary Figure S13: DENND1A and RAB35 CTG assay for experiment 1, performed on 10 plates using around 1500 fragments in triplicates. A-J) Results for individual plates, the average fluorescence of DMSO control without ligand were used to define 100% viability. As a cut-off, maximum of 50 % viability was chosen to define a toxic compound. Error bars are depicted as the STDEV.



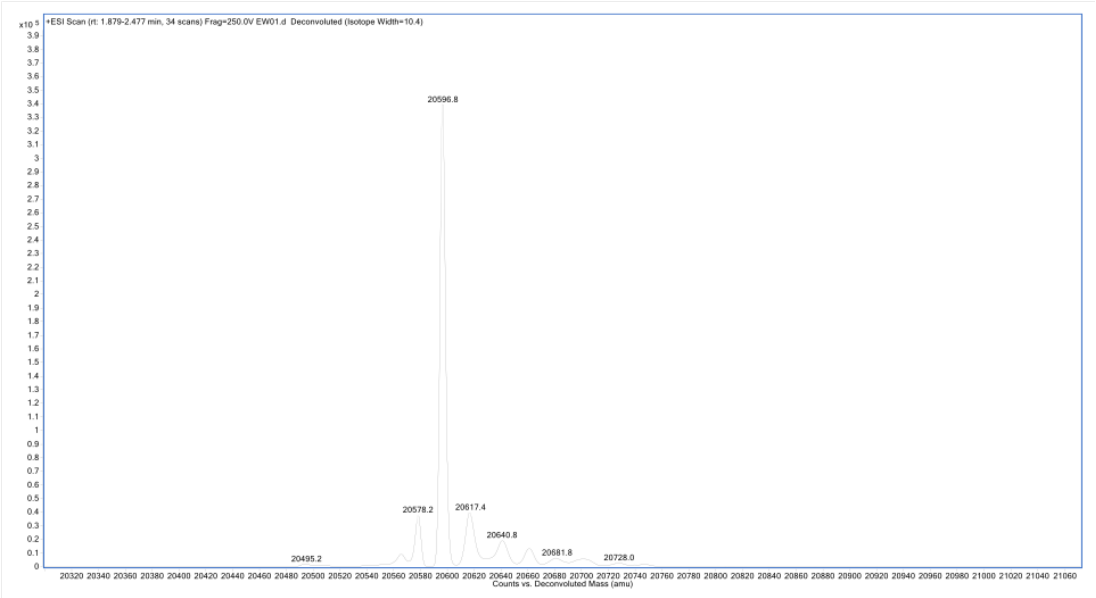
Supplementary Figure S14: DENND1A and RAB35 CTG assay for experiment 2, performed on 10 plates using around 1500 fragments in triplicates. A-J) Results for individual plates, the average fluorescence of DMSO control without ligand were used to define 100% viability. As a cut-off, maximum of 50 % viability was chosen to define a toxic compound. Error bars are depicted as the STDEV.



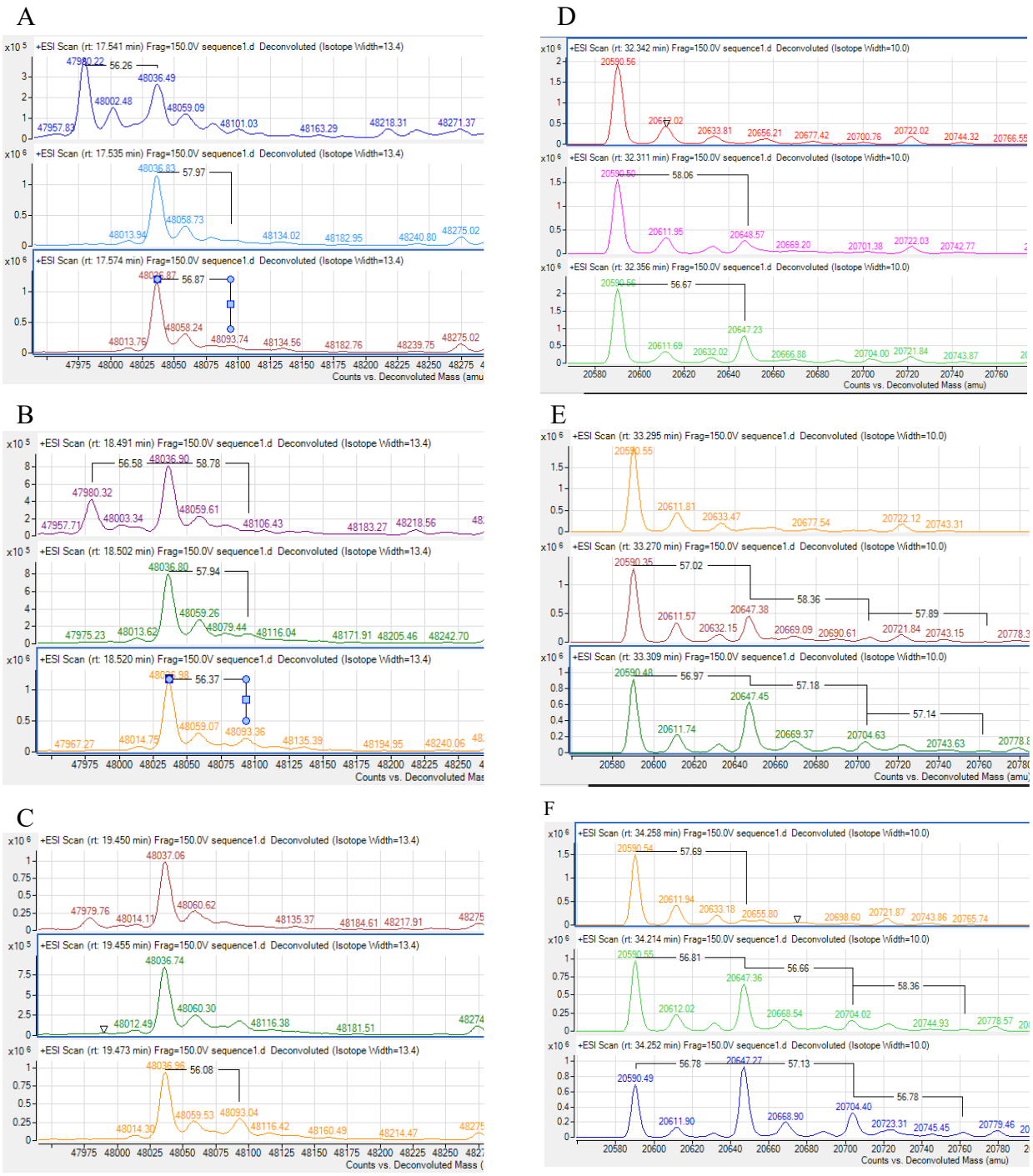
Supplementary Figure S15: Reactive motif-grouped structures of preliminary hit compounds which were selected in the dose-response of DENND1A-RAB35 NanoBRET PPI assays: blue-labelled hits originated from experiment 1, black-labelled hits originated from experiment 2. In brackets, the maximal observed inhibition in % per fragment is stated.



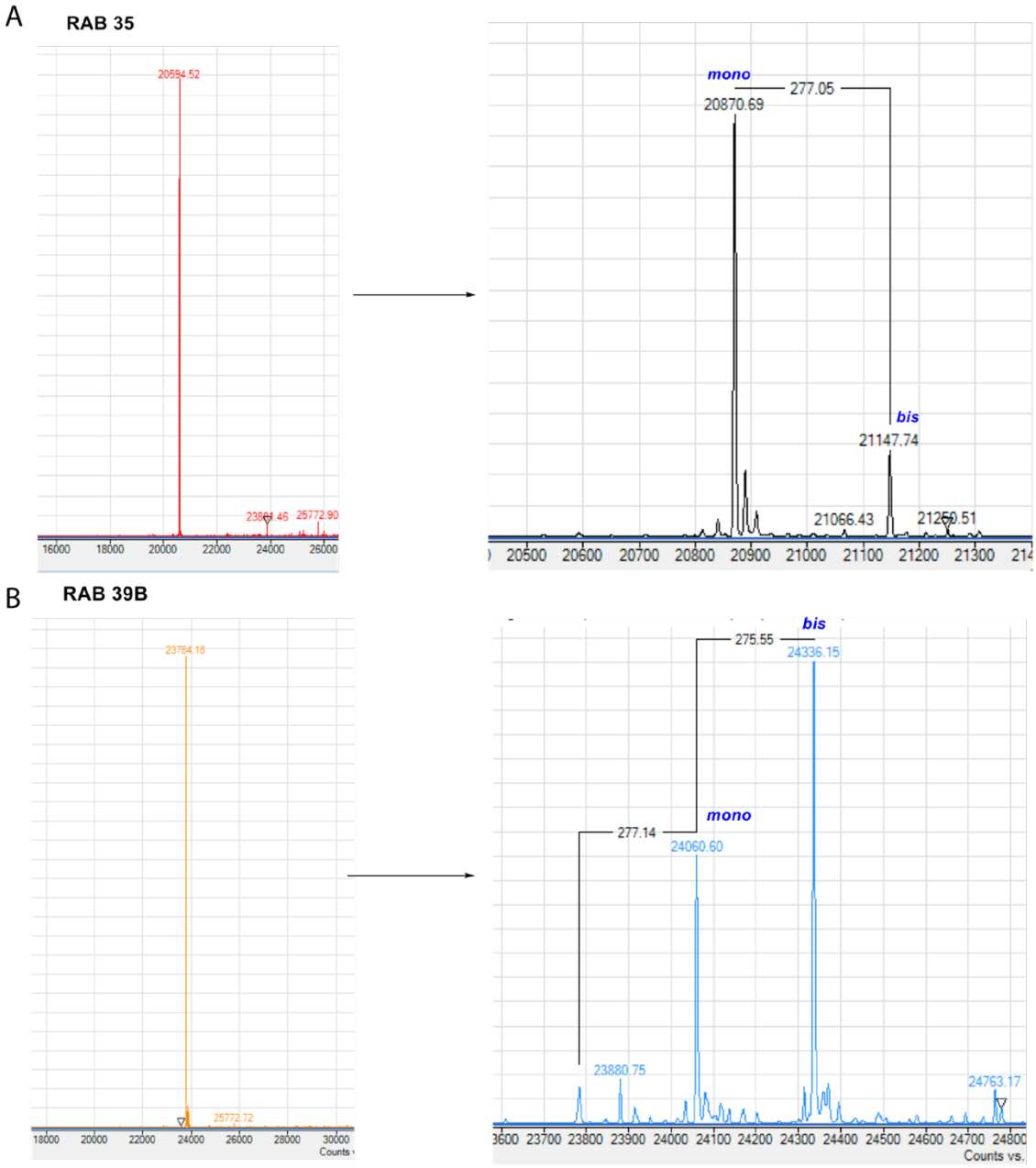
Supplementary Figure S16: Results of two PCR experiments with primers 1-8. Band for DENND1A would be expected at 8921 bp. Bands show smear, multiple bands or bands at different bp.



Supplementary Figure S17: Identity and purity confirmed by intact MS of RAB35a-c002 at 20.5 kDa, experiment performed by Rod Chalk.



Supplementary Figure S18: Recombinant proteins (2 µM) were incubated at room temperature with different concentrations of IA, and mass adduct formation +57 g/mol was measured at different timepoints. A-C depicts mass adduct formation on DENND1A (pure protein at 48 kDa), D-F depicts mass adduct formation on RAB35 (pure protein at 20.5 kDa). A)100 µM IA at 0-3-6h. B) 300 µM IA at 0-3-6h. C) 600 µM IA at 0-3-6h. D) 100 µM IA at 0-3-6h. E) 300 µM IA at 0-3-6h. F) 600 µM IA at 0-3-6h.



Supplementary Figure 19: Modification of RAB family members at 25 °C after 18 h using 20 µM of Z1151194523 in a shaking incubator. A) Mass shifts on RAB35. B) Mass shifts on RAB39B. This experiment was performed by Srinivasa Adusumali.

Supplementary Tables

	Gene IDs	
Cell Line	**inhouse**	**Küster group**
NCIH226	6265	3919
U251	6243	4043
K562	6154	3919
DU145	6532	4016

Supplementary Table T1: Comparison of total proteome gene IDs obtained from selected cancer cell lines. The inhouse data exceeds the data from the literature by > 30 %. Our data was obtained on the Orbitrap Fusion Lumos Tribrid (Thermo Fisher, 2019) with in-solution digest, whereas the Küster group obtained their data from an LTQ Orbitrap XL ETD or Orbitrap Elite mass spectrometer (Thermo Fisher, 2013) using in-gel digestion, which may reduce identified IDs based on rapid MS machine development and loss of material in the in-gel digestion step.

ACO1_C437	CCDC28B_C139	CTSC_C54	FGD6_C370	HOGA1_C258	MACROD2_C104	NNMT_C75	RAP1GAP_C15	SPARC_C273	TUFM_C150
ACTA2_C259	CCDC9B_C157	DCBLD2_C768	FGD6_C405	HROB_C535	MAFF_C74	NOL3_C73	RASSF4_C33	SPHK1_C316	TUFM_C225
ADAT3_C214	CCDC9B_C410	DENND2A_C32	FGD6_C744	HSD3B1_C84	MAGEA2_C10	NPPB_C128	RASSF4_C5	SPRR2D_C32	TUFM_C293
ADD2_C201	CCDC9B_C475	DLK1_C196	FLIP1L_C849	HSPB6_C46	MAGI2_C1378	NRP2_C715	RCSD1_C296	SPRR2D_C63	TUFM_C390
AHDC1_C1446	CCNY1L1_C228	DNM1_C708	FLIP1L_C990	HSPB8_C99	MAP1A_C1983	OLFML1_C111	REM1_C213	SPRR2E_C23	TUFT1_C8
AHNAK2_C1872	CDC16_C367	DPH1_C423	FLNC_C1906	HYLS1_C170	MAP1A_C2437	OLFML1_C74	RENBP_C413	SPRR2E_C32	TWF1_C264
AHNAK2_C4223	CDC25C_C265	DSCC1_C28	FSTL1_C31	ICAM1_C371	MAP1LC3A_C17	PAGE1_C115	RFESD_C19	SPTA1_C799	TWF1_C275
AHNAK2_C4979	CDC42EP3_C211	DST_C2476	FSTL1_C77	ICAM1_C48	MAP2_C1175	PAGE1_C73	RGS10_C74	SSH2_C1332	UBXN2A_C123
AKR1C1_C87	CEP1P_C650	DUSP1_C110	FSTL3_C92	ID1_C145	MAP2_C786	PAGE1_C85	RHPN2P1_C554	STARD13_C347	UPP1_C193
ALB_C500	CFI_C93	DVL3_C92	FSTL3_C95	ID1_C72	MAST4_C1940	PALLD_C1292	RIN1_C438	STC1_C202	UQCRHL_C37
ALDH1L1_C707	CGNL1_C219	ECM1_C151	FYCO1_C318	IGFBP2_C53	MATN2_C51	PALLD_C429	RIPOR1_C710	SYDE1_C459	UQCRHL_C81
ALDOA_C178	CGNL1_C425	EFEMP1_C199	FZD6_C615	IGFBP4_C249	MATN2_C649	PAM_C181	RPAP1_C1199	SYNC_C182	USP27X_C87
ALDOA_C73	CGNL1_C456	EFEMP1_C224	GAGE1_C117	IGFBP5_C219	MBLAC1_C7	PAPSS2_C397	RPAP1_C1272	SYNC_C262	USP9Y_C1238
ANKRD54_C84	CHCHD2P9_C124	EFEMP1_C292	GAGE12B_C117	IGFBP7_C111	MCC_C250	PATJ_C1602	RPL37AP8_C43	SYNJ2_C325	VTN_C430
ANTXR1_C39	CHCHD5_C22	EFEMP1_C298	GALK2_C54	IGFBP7_C156	MCC_C424	PDE1A_C406	SAGE1_C207	SYNM_C1196	WHAMM_C706
APBB2_C148	CIAPIN1_C246	EFEMP1_C48	GATA1_C110	IGFBP7_C81	ME3_C145	PDE1C_C648	SAGE1_C348	SYNPO_C396	WIPF3_C270
ARHGAP29_C1048	CLBA1_C152	EFEMP1_C55	GATA1_C199	IL18_C163	MEIOSIN_C543	PDE4DIP_C136	SAMD4A_C700	SYNPO_C699	WNK4_C499
ARHGAP6_C819	CLIC2_C114	EFEMP1_C61	GATA1_C83	IQCJ-SCHIP1_C250	MICALL2_C676	PDGFRB_C843	SARG_C212	TACC2_C2483	WNT2B_C379
ARHGAP6_C867	CLIC2_C184	EID1_C180	GFAP_C294	IQCJ-SCHIP1_C484	MITF_C209	PDXDC2P_C200	SARG_C22	TARS3_C637	WWC1_C1082
ARHGEF17_C549	CLIC2_C229	EIF2B1_C57	GFPT2_C461	IRS2_C1306	MOCOS_C450	PDZRN3_C906	SARG_C574	TBC1D14_C81	WWC1_C230
ARHGEF35_C251	CLTCL1_C617	EIF4A1_C264	GLUD1_C112	IRS2_C552	MOCS3_C90	PHLDA3_C87	SCLY_C388	TCEAL1_C90	WWC1_C497
ARHGEF35_C98	CLTCL1_C778	ELK1_C207	GLUD1_C172	ITLN1_C48	MRC2_C1153	PHLDB1_C1249	SCP2_C224	TCEAL5_C50	WWC1_C50
ASB9_C216	CNN1_C273	ENY2_C50	GNAL_C346	IVL_C75	MTCL1_C1098	PHLDB1_C621	SCUBE3_C403	TCERG1_C388	WWC1_C617
ASMTL_C592	COBLL1_C630	EPG5_C112	GNAL_C352	KDM5A_C1248	MTCL1_C1581	PHLDB2_C457	SCUBE3_C857	TGFB1_C225	WWC2_C54
ATE1_C413	COBLL1_C678	ERBIN_C843	GORAB_C131	KIAA1217_C1467	MTMR2_C7	PHLDB2_C696	SELENOF_C94	TGFBI_C65	WWC2_C751
ATP7A_C182	COL14A1_C1261	ERF_C492	GORAB_C253	KIAA1217_C1556	MTSS2_C8	PHYHD1_C49	SELENOH_C41	TGIF1_C212	WWC3_C616
BABAM1_C307	COL1A1_C1282	ERICH5_C35	GORAB_C329	KIAA1217_C40	MYC_C85	PI4KB_C657	SELENOW_C10	TGIF1_C303	ZFP36L1_C173
BABAM2_C254	COL1A2_C1186	ESRP2_C411	GSDME_C482	KIF5C_C296	MYH7B_C744	PIPOX_C119	SERPINB2_C161	TGM5_C291	ZNF140_C33
BACH1_C557	COL6A1_C594	ETV1_C22	GSDME_C489	KNL1_C130	MYL3_C76	PKN1_C469	SERPINB2_C79	THBS2_C270	ZNF185_C317
BBC3_C231	COL6A1_C745	ETV1_C416	GSTT1_C14	KRT75_C460	MYL4_C184	PLAU_C62	SERPING1_C205	THSD1_C688	ZPR1_C331
BBIP1_C51	COL6A1_C815	ETV4_C110	GSTT1_C182	KRT81_C427	MYL6_C2	PLAUR_C46	SESN3_C411	TIMM10_C33	
BCL3_C64	COL6A2_C592	ETV4_C422	HBA1_C105	KRT86_C273	MYLK3_C381	PLCL1_C33	SFR1_C125	TIMM44_C319	
BHLHE40_C342	COL6A2_C748	FABP5P3_C53	HBD_C113	L3MBTL4_C558	MYLK3_C462	PLEKHG1_C1316	SFR1_C95	TLN1_C575	
BST2_C9	COL9A3_C529	FAM110A_C114	HBE1_C94	LBHD1_C250	MYPN_C1257	POF1B_C106	SGTB_C142	TNS3_C512	
C14orf119_C94	COLEC11_C170	FAM110C_C70	HBQ1_C90	LBHD1_C271	MYRF_C1084	POTEF_C957	SH2D3A_C381	TRIM2_C254	
C1QBP_C69	CORO1B_C475	FAM114A1_C558	HBZ_C105	LIAT1_C125	MYRF_C167	POTEF_C965	SH3BP4_C17	TRIM47_C551	
C1S_C234	CORO6_C344	FAM117A_C382	HDAC4_C982	LIMA1_C417	NAA16_C82	POU3F3_C361	SH3RF1_C773	TRMT11_C336	
C3_C1513	CORO7_C263	FAM118A_C198	HEATR5A_C641	LIMS3_C10	NAGS_C150	PPDPF_C90	SHROOM1_C557	TROAP_C647	
C3_C662	COX19_C30	FAM120C_C354	HEATR5A_C688	LOX_C412	NAGS_C186	PPIAL4E_C62	SHROOM1_C590	TSC22D2_C201	
C3_C873	CRB2_C1108	FAM13A_C910	HEMGN_C191	LOXL2_C158	NAV1_C1743	PPM1H_C239	SKP2_C345	TSPYL1_C375	
C6orf132_C362	CRB2_C603	FAM13A_C934	HEMGN_C205	LPP_C502	NAV3_C479	PPOX_C382	SLFN13_C571	TSTD1_C79	
CALB1_C219	CRB2_C94	FAM178B_C666	HEMGN_C233	LPP_C524	NAV3_C579	PPP4R1_C905	SLPI_C43	TUBA3C_C20	
CALB1_C257	CSPP1_C400	FAM219A_C32	HEMGN_C244	LRRN4_C559	NAV3_C669	PROS1_C143	SOCS2_C5	TUBA3C_C25	
CALB2_C266	CST6_C113	FAM222B_C322	HEMGN_C256	LRRN4_C650	NCOA4_C462	PRR9_C25	SOX13_C318	TUBA3C_C295	
CAPN9_C367	CT45A10_C109	FAM83A_C356	HEMGN_C329	LRRN4_C72	NFATC3_C219	PSMG3_C17	SOX6_C152	TUBA3C_C347	
CAPS_C152	CT45A6_C22	FAU_C57	HEMGN_C422	LTBP3_C1297	NFATC3_C282	PTAR1_C314	SPAG7_C101	TUBA3C_C376	
CASS4_C741	CTNNA2_C322	FCHO2_C307	HGH1_C199	LTBP3_C71	NFE2_C4	PTPN18_C310	SPARC_C123	TUBA3C_C4	
CBFA2T3_C405	CTNNA2_C792	FDX2_C154	HKDC1_C605	LY96_C105	NFIC_C436	RAB11FIP1_C711	SPARC_C130	TUBAL3_C228	
CCDC115_C68	CTNND2_C1092	FERMT2_C12	HLA-B_C227	LY96_C51	NLE1_C48	RABGGTB_C78	SPARC_C155	TUBB8B_C129	
CCDC120_C196	CTNND2_C127	FEZ1_C73	HMBS_C211	MACF1_C2278	NNMT_C50	RAC3_C81	SPARC_C265	TUFM_C130	

Supplementary Table 2: 480 sites which were not overlapping with the CysDB sites, derived from our non-competition dataset from 8 reactive probes and 4 cell lines with respect to reacted cysteine residues.

APPBP2_C_54	HUWE1_C_1401	PJA1_C_241	RING1_C_69	TRIM28_K_366
ARID1A_C_1827	HUWE1_C_1832	PJA2_C_105	RING1_C_72	TRIM28_K_377
ARID1A_C_1874	HUWE1_C_2721	PJA2_C_224	RNF113A_C_15	TRIM28_K_407
ARID1A_C_1968	HUWE1_C_3239	PJA2_C_48	RNF113A_D_12	TRIM28_K_507
ARID1A_C_336	HUWE1_C_3259	PML_C_338	RNF114_C_110	TRIM28_K_779
ARID1A_M_332	HUWE1_C_3296	PML_C_389	RNF114_C_67	TRIM28_M_423
ARIH1_C_161	HUWE1_C_3361	PML_C_479	RNF114_C_8	TRIM28_R_427
ASB9_C_216	HUWE1_C_3658	PPIL2_C_15	RNF114_Y_113	TRIM28_T_513
ATG16L1_K_179	HUWE1_C_4099	PPIL2_E_17	RNF126_C_15	TRIM28_Y_133
BIRC2_C_45	HUWE1_C_790	PPIL2_K_313	RNF14_C_262	TRIM28_Y_242
BIRC2_C_474	HUWE1_M_2187	PPIL2_K_490	RNF14_C_406	TRIM28_Y_369
BRAP_C_110	IRF2BPL_C_504	PRAME_C_188	RNF14_E_281	TRIM28_Y_755
BRAP_C_306	IRF2BPL_C_63	PRAME_C_80	RNF146_C_354	TRIM33_C_582
BRAP_C_47	IRF2BPL_K_394	PRAME_D_189	RNF166_C_127	TRIM33_C_786
BRAP_C_473	IVNS1ABP_C_143	PRPF19_C_230	RNF169_C_28	TRIM33_C_805
BRCA1_C_712	IVNS1ABP_C_274	PRPF19_K_122	RNF169_C_293	TRIM33_C_943
BTBD10_C_143	IVNS1ABP_C_52	PRPF19_K_179	RNF169_C_337	TRIM33_K_329
CBL_C_508	IVNS1ABP_C_575	PRPF19_K_192	RNF181_M_23	TRIM47_C_347
CBL_C_659	KATNB1_C_344	PRPF19_K_244	RNF2_C_72	TRIM47_C_454
CBL_M_887	KBTBD11_C_421	PRPF19_K_261	RNF20_C_905	TRIM47_C_551
CBLL1_C_73	KCTD12_C_50	PRPF19_K_266	RNF20_C_924	TRIM56_E_229
CIAO1_C_123	KCTD12_Y_106	PRPF19_K_64	RNF213_C_310	TRIM65_C_112
CIAO1_C_212	KCTD16_K_185	PRPF19_T_396	RNF213_C_614	TRIM65_C_174
CIAO1_C_234	KCTD20_C_216	PWP1_C_435	RNF214_C_655	TRIM65_C_320
CIAO1_C_97	KCTD20_C_369	RACK1_C_138	RNF214_C_99	TRIP12_C_332
CISH_C_167	KCTD20_C_82	RACK1_C_153	RNF214_D_219	TRIP12_C_535
CNOT4_C_175	KCTD3_C_599	RACK1_C_168	RNF214_K_582	UBE3A_C_108
CRBN_C_188	KCTD3_C_606	RACK1_C_182	RNF214_M_588	UBE3A_C_198
CRBN_C_287	KCTD3_C_704	RACK1_C_207	RNF220_C_382	UBE3A_C_269
CRBN_C_343	KCTD5_C_28	RACK1_C_240	RNF25_C_316	UBE3A_C_83
DCAF6_C_593	KEAP1_C_319	RACK1_C_249	RNF40_C_890	UBE3A_C_843
DCAF7_C_109	KEAP1_C_613	RACK1_C_286	RNF40_C_950	UBE3C_C_1051
DCAF8_C_272	KLHDC3_C_102	RACK1_K_106	RNF40_D_872	UBE4A_C_79
DDB2_C_322	LMO7_C_261	RACK1_K_139	RNF7_C_61	UBE4B_C_113
DTL_C_544	LRRC42_C_56	RACK1_K_172	RNF7_C_99	UBE4B_C_1164
DTL_C_710	LRRC58_C_296	RACK1_K_185	RNF7_D_59	UBE4B_M_447
DTX2_C_351	LRSAM1_C_397	RACK1_K_225	SH3RF1_C_107	UBR1_C_1603
DTX3L_C_175	LRSAM1_C_75	RACK1_K_264	SH3RF1_C_773	UBR1_C_180
FBXL12_C_212	MED8_C_31	RACK1_K_271	SHKBP1_C_550	UBR1_C_993
FBXL18_C_459	MEX3A_C_328	RACK1_K_38	SKP2_C_205	UBR3_C_288
FBXO2_C_137	MEX3B_C_69	RACK1_K_44	SKP2_C_309	UBR4_C_1458
FBXO2_C_176	MGRN1_C_528	RACK1_M_217	SKP2_C_345	UBR4_C_2222
FBXO2_C_71	MKRN1_C_186	RACK1_M_30	SMURF2_C_151	UBR4_C_2554
FBXO2_K_79	MKRN1_C_305	RACK1_R_118	SMURF2_C_47	UBR4_C_3075
FBXO2_Y_189	MNAT1_C_293	RACK1_R_47	SMURF2_C_706	UBR4_C_3864
FBXO2_Y_217	NEDD4_C_1286	RACK1_T_192	SNRNP40_C_52	UBR4_E_1073
FBXO2_Y_278	NEDD4_K_1172	RACK1_Y_140	SNRNP40_K_18	UBR5_C_2084
FBXO22_C_117	NEDD4_K_874	RACK1_Y_194	SNRNP40_K_275	UBR5_C_2094
FBXO22_C_228	NEDD4_M_1196	RACK1_Y_228	SOCS2_C_111	UBR5_C_2267
FBXO22_C_326	NEDD4_T_626	RACK1_Y_246	SOCS2_C_5	UBR5_C_2314
FBXO22_C_378	NEDD4_Y_530	RACK1_Y_302	STUB1_C_199	UBR5_C_730
FBXO30_C_396	NEDD4_Y_937	RACK1_Y_52	STUB1_C_232	UBR5_E_2096
FBXO30_C_433	NEDD4L_C_874	RAD18_C_63	STUB1_C_48	UBR7_C_260
FBXO30_C_592	NEDD4L_T_209	RBBP4_C_138	STUB1_K_30	UBR7_C_35
FBXO30_C_723	NEDD4L_T_401	RBBP4_C_167	TLE1_C_526	UBR7_C_374
FBXO5_C_95	NLE1_C_280	RBBP4_C_203	TLE3_C_26	UBR7_C_424
GNB2_C_204	NLE1_C_48	RBBP4_E_104	TLE3_C_528	UHRF1_C_170
GNB2_C_25	NLE1_K_224	RBBP4_E_352	TRAF2_C_171	UNK_C_696
GNB2_C_294	NLE1_S_221	RBBP4_K_22	TRAF2_C_287	VHL_C_77
GRWD1_C_11	NOSIP_C_185	RBBP4_T_28	TRAF2_E_120	VPS18_C_22
GRWD1_C_426	NOSIP_C_8	RBBP4_T_54	TRAF2_K_493	WDR61_K_181
GRWD1_C_66	NOSIP_K_172	RBBP4_Y_132	TRIM16_C_178	WDR61_S_137
HECTD1_C_1368	NOSIP_K_21	RBBP4_Y_181	TRIM16_C_286	WDR61_T_179
HECTD1_C_1389	NOSIP_K_289	RBBP4_Y_21	TRIM16_K_202	WDR61_Y_120
HECTD1_C_2071	NOSIP_K_78	RBBP4_Y_32	TRIM16_Y_300	WDR61_Y_213
HECTD1_C_2415	PAFAH1B1_C_168	RBBP5_C_212	TRIM16_Y_371	WDSUB1_C_316
HECTD1_C_254	PAFAH1B1_C_184	RBBP6_C_27	TRIM2_C_254	WWP2_C_186
HECTD1_C_2579	PAFAH1B1_C_226	RBBP7_C_116	TRIM25_C_498	WWP2_C_838
HECTD1_C_436	PAFAH1B1_C_252	RBBP7_C_166	TRIM25_C_70	XIAP_C_12
HECTD1_C_507	PAFAH1B1_K_228	RBBP7_C_97	TRIM25_D_80	XIAP_Y_154
HERC1_C_56	PAFAH1B1_K_76	RBBP7_D_93	TRIM25_E_326	ZNF598_C_456
HERC4_C_1025	PAFAH1B1_K_88	RBBP7_E_103	TRIM25_S_272	
HERC4_C_175	PAFAH1B1_S_304	RBBP7_E_351	TRIM28_C_713	
HERC4_C_60	PAFAH1B1_T_145	RBBP7_K_119	TRIM28_C_717	
HERC4_C_708	PAFAH1B1_T_391	RBBP7_K_219	TRIM28_K_266	
HERC5_C_994	PAFAH1B1_Y_137	RBBP7_T_154	TRIM28_K_272	
HLTF_C_360	PAFAH1B1_Y_394	RBBP7_T_27	TRIM28_K_296	
HLTF_C_442	PDZRN3_C_233	RBX1_C_94	TRIM28_K_304	
HLTF_C_461	PDZRN3_C_764	RC3H1_C_1049	TRIM28_K_319	
HUWE1_C_1133	PDZRN3_C_906	RING1_C_51	TRIM28_K_340	

Supplementary Table S3: 132 unique E3 ligases and 391 unique modified sites identified in non-competition dataset derived from 4 cell lines using 8 reactive probes at 100 μM in lysates for 1 h incubation in isoTOP ABPO workflow.

Site	Weighted.Log2HLRatio.Mean	Weighted.Log2HL.SD
UBR5_C_2267	7.039604522	0.331552426
KCTD20_C_369	6.362049561	0.850533813
CBLL1_C_73	6.345064874	0.564059784
RNF40_C_950	6.1770231	0.832874309
PJA2_C_48	5.721107658	0.443668265
UBE3A_C_108	5.591178757	0.704554388
RNF214_C_655	5.52019503	0.099415762
HUWE1_C_1832	5.513945765	0.854901276
UBE3A_C_108	5.498989528	0.658840977
RAD18_C_64	5.397438578	1.343633673
BRAP_C_47	5.109386304	1.089872531
HLTF_C_360	4.981069529	0.519339732
UBR7_C_374	4.897517407	0.558077606
SOCS2_C_111	4.727265953	0.927912723
PML_C_389	4.704656209	0.181754824
UBR5_C_2314	4.672374316	0.910840306
HUWE1_C_3361	4.650514897	0.722049619
RNF113A_C_15	4.577071247	0.500308224
MKRN1_C_305	4.495560883	0.630432541
MKRN1_C_186	4.482108511	0.576037514
RNF25_C_316	4.481173694	1.389784063
RNF113A_C_15	4.46944337	1.0422536
UBR2_C_1360	4.433634032	0.798785601
NOSIP_C_8	4.418218628	0.147579842
HLTF_C_442	4.323569046	0.72455439
HECTD1_C_1389	4.279672947	0.426779823
RNF214_C_655	4.251617451	0.039227414
ARID1A_C_336	4.24520556	0.829551477
UBR1_C_1603	4.221702326	0.802887589
HUWE1_C_1832	4.213809365	0.439105258
UBR1_C_1603	4.193296145	0.314435156
RAD18_C_63	4.180358553	0.825217002
HECTD1_C_1368	4.154547721	0.595224785
UBR4_C_3864	4.143241025	0.686418373
RNF214_C_655	4.129266329	0.055494846
IVNS1ABP_C_274	4.118038652	0.727063218
SMURF2_C_151	4.089411106	0.830594315
UBE3A_C_83	4.057652112	0.618629806

Supplementary Table S4: Table showing competed E3 ligases with R>4. In total 38 sites were identified. Results were obtained after analysis using the R code written by Jeppe-tranberg Jensen.

Gene Name	Uniprot ID	Index	Amino acid	Result
APPBP2	Q92624	54	C	Exposed
ARID1A	O14497	1007	K	Exposed
		1504	M	Exposed
		1508	Y	Exposed
		1827	C	Exposed
ARIH1	Q9Y4X5	161	C	Buried
		269	C	Exposed
		326	K	Exposed
		327	C	Buried
ARIH2	O95376	280	C	Buried
ASB9	Q96DX5	216	C	Exposed
ATG16L1	Q676U5	179	K	Exposed
BIRC2	Q13490	45	C	Buried
		474	C	Exposed
BRAP	Q7Z569	47	C	Exposed
		306	C	Exposed
		452	C	Exposed
		473	C	Exposed
BTBD10	Q9BSF8	419	C	Exposed
CBL	P22681	353	C	Exposed
		887	M	Exposed
CDC20	Q12834	313	C	Buried
		364	C	Buried
CIAO1	O76071	2	K	Exposed
		52	C	Exposed
		72	C	Exposed
		97	C	Exposed
		123	C	Buried
		212	C	Buried
		234	C	Exposed
		261	C	Buried
		271	C	Buried
CISH	Q9NSE2	167	C	Buried
CNOT4	O95628	175	C	Exposed
CRBN	Q96SW2	188	C	Buried
		205	C	Exposed
		287	C	Exposed
		343	C	Exposed
DCAF1	Q9Y4B6	784	C	Buried
DCAF7	P61962	61	C	Exposed
		109	C	Buried

		256	C	Exposed
DCAF8	Q5TAQ9	195	C	Buried
		272	C	Exposed
		273	C	Buried
		297	C	Buried
		377	C	Exposed
DCAF8L1	A6NGE4	177	C	Buried
DCAF10	Q5QP82	290	C	Buried
DDB2	Q92466	322	C	Exposed
DTL	Q9NZJ0	379	C	Buried
		544	C	Buried
DTX3L	Q8TDB6	159	C	Buried
		175	C	Buried
EED	O75530	182	C	Exposed
FBXL12	Q9NXK8	212	C	Buried
FBXL18	Q96ME1	382	C	Buried
		383	C	Exposed
FBXO2	Q9UK22	71	C	Buried
		79	K	Buried
		92	C	Exposed
		137	C	Buried
		168	Y	Buried
		176	C	Exposed
		189	Y	Buried
		215	C	Buried
		217	Y	Buried
		278	Y	Exposed
FBXO4	Q9UKT5	147	C	Buried
FBXO5	Q9UKT4	202	C	Exposed
FBXO6	Q9NRD1	55	K	Exposed
FBXO7	Q9Y3I1	243	C	Buried
		286	C	Buried
FBXO22	Q8NEZ5	117	C	Buried
		326	C	Exposed
		378	C	Buried
FBXO30	Q8TB52	592	C	Exposed
		687	C	Exposed
		723	C	Exposed
FBXO32	Q969P5	231	C	Exposed
FBXO42	Q6P3S6	89	C	Exposed
		302	C	Buried
FBXO45	P0C2W1	98	C	Exposed
FEM1B	Q9UK73	186	C	Exposed

GNB2	P62879	25	C	Exposed
		149	C	Buried
		204	C	Buried
		271	C	Exposed
		294	C	Exposed
GRWD1	Q9BQ67	66	C	Buried
		235	C	Exposed
		299	C	Exposed
		426	C	Buried
HECTD1	Q9ULT8	436	C	Buried
		487	C	Buried
		878	C	Exposed
		1389	C	Exposed
		2071	C	Exposed
HERC4	Q5GLZ8	60	C	Exposed
		175	C	Buried
		384	C	Exposed
		708	C	Buried
		1025	C	Exposed
HERC5	Q9UII4	994	C	Exposed
IRF2BPL	Q9H1B7	35	C	Buried
		394	K	Exposed
		494	M	Buried
		504	C	Exposed
ITCH	Q96J02	57	C	Buried
IVNS1ABP	Q9Y6Y0	52	C	Exposed
		53	C	Exposed
		143	C	Exposed
		274	C	Exposed
		376	Y	Buried
		575	C	Exposed
KBTBD2	Q8IY47	145	C	Buried
KBTBD11	O94819	257	C	Exposed
		421	C	Exposed
KCTD3	Q9Y597	599	C	Exposed
KCTD9	Q7L273	280	M	Buried
KCTD12	Q96CX2	50	C	Exposed
		106	Y	Exposed
		161	Y	Exposed
		273	K	Exposed
KCTD15	Q96SI1	201	M	Buried
		202	C	Exposed
KCTD16	Q68DU8	185	K	Exposed

KCTD20	Q7Z5Y7	216	C	Exposed
		327	C	Exposed
		369	C	Exposed
KCTD21	Q4G0X4	237	C	Exposed
KEAP1	Q14145	41	E	Exposed
		196	C	Buried
		241	C	Exposed
		288	C	Buried
		317	M	Exposed
		319	C	Exposed
		434	C	Exposed
		613	C	Exposed
		622	C	Exposed
KLHDC3	Q9BQ90	102	C	Exposed
		355	C	Buried
KLHL18	O94889	74	C	Exposed
		232	C	Buried
KLHL26	Q53HC5	603	C	Buried
LRRC41	Q15345	123	C	Exposed
		170	C	Exposed
LRRC42	Q9Y546	242	C	Exposed
LRSAM1	Q6UWE0	75	C	Exposed
		397	C	Exposed
		418	C	Exposed
LZTR1	Q8N653	427	C	Exposed
MED8	Q96G25	31	C	Exposed
		146	M	Exposed
		170	K	Exposed
MEX3B	Q6ZN04	66	M	Exposed
		69	C	Exposed
MID1	O15344	153	K	Exposed
MKRN1	Q9UHC7	179	C	Exposed
		188	E	Buried
		214	C	Buried
MNAT1	P51948	293	C	Buried
NEDD4	P46934	530	Y	Exposed
		626	T	Exposed
		937	Y	Buried
		1172	K	Exposed
		1196	M	Buried
		1286	C	Exposed
NEDD4L	Q96PU5	209	T	Exposed
		401	T	Exposed

		874	C	Exposed
NLE1	Q9NVX2	48	C	Buried
		173	S	Buried
		221	S	Exposed
		224	K	Exposed
		280	C	Buried
NOSIP	Q9Y314	6	K	Exposed
		8	C	Exposed
		20	K	Exposed
		21	K	Exposed
		78	K	Exposed
		172	K	Exposed
		185	C	Exposed
		236	C	Buried
		250	C	Buried
		289	K	Buried
PAFAH1B1	P43034	45	K	Exposed
		70	S	Exposed
		76	K	Exposed
		88	K	Buried
		147	K	Exposed
		168	C	Buried
		184	C	Exposed
		225	Y	Exposed
		226	C	Exposed
		228	K	Buried
		252	C	Buried
		303	K	Exposed
		304	S	Exposed
		329	M	Exposed
		356	C	Exposed
		360	K	Exposed
		391	T	Exposed
		394	Y	Buried
PDZRN3	Q9UPQ7	233	C	Exposed
PDZRN4	Q6ZMN7	419	C	Exposed
PML	P29590	57	C	Buried
		60	C	Exposed
		129	C	Buried
		189	C	Buried
		204	C	Buried
		227	C	Exposed
		338	C	Exposed

		389	C	Exposed
PPIL2	Q13356	15	C	Exposed
		17	E	Exposed
		313	K	Exposed
		387	C	Buried
		490	K	Exposed
PRAME	P78395	80	C	Exposed
		188	C	Exposed
		189	D	Exposed
		332	C	Exposed
		472	C	Buried
PRPF19	Q9UMS4	64	K	Exposed
		86	M	Exposed
		122	K	Exposed
		179	K	Exposed
		192	K	Exposed
		230	C	Buried
		244	K	Exposed
		259	T	Exposed
		261	K	Exposed
		266	K	Exposed
		268	T	Exposed
		298	C	Exposed
		351	C	Buried
		396	T	Exposed
PWP1	Q13610	329	C	Buried
		356	C	Exposed
		400	C	Buried
		435	C	Buried
RACK1	P63244	10	T	Exposed
		19	T	Buried
		30	M	Buried
		38	K	Exposed
		44	K	Exposed
		47	R	Exposed
		50	T	Exposed
		52	Y	Buried
		106	K	Exposed
		118	R	Exposed
		130	K	Exposed
		138	C	Buried
		139	K	Exposed
		140	Y	Buried

		153	C	Exposed
		168	C	Buried
		172	K	Buried
		182	C	Exposed
		183	K	Exposed
		185	K	Exposed
		192	T	Exposed
		194	Y	Buried
		205	S	Buried
		207	C	Exposed
		217	M	Buried
		225	K	Exposed
		228	Y	Exposed
		240	C	Exposed
		246	Y	Exposed
		249	C	Exposed
		252	T	Buried
		264	K	Exposed
		271	K	Buried
		286	C	Buried
		302	Y	Buried
RAD18	Q9NS91	63	C	Exposed
		64	C	Exposed
		223	C	Buried
		289	C	Buried
RBBP4	Q09028	21	Y	Buried
		22	K	Exposed
		25	K	Exposed
		28	T	Exposed
		32	Y	Exposed
		36	M	Buried
		54	T	Exposed
		59	K	Buried
		104	E	Buried
		120	K	Buried
		132	Y	Exposed
		138	C	Exposed
		154	Y	Exposed
		155	T	Exposed
		160	K	Buried
		167	C	Exposed
		178	K	Buried
		181	Y	Exposed

		203	C	Exposed
		212	K	Buried
		220	K	Exposed
		278	C	Exposed
		284	Y	Exposed
		352	E	Exposed
RBBP5	Q15291	202	K	Exposed
		212	C	Buried
		233	C	Exposed
RBBP6	Q7Z6E9	27	C	Exposed
RBBP7	Q16576	27	T	Buried
		59	D	Exposed
		60	Y	Exposed
		88	D	Exposed
		93	D	Exposed
		119	K	Exposed
		131	Y	Buried
		154	T	Exposed
		155	K	Exposed
		159	K	Buried
		166	C	Exposed
		177	K	Exposed
		202	C	Exposed
		219	K	Buried
		277	C	Exposed
		283	Y	Exposed
		351	E	Buried
		356	E	Exposed
RBX1	P62877	94	C	Buried
		105	K	Exposed
RC3H1	Q5TC82	1049	C	Exposed
RING1	Q06587	51	C	Exposed
		69	C	Exposed
		72	C	Buried
		79	S	Buried
		82	K	Buried
		279	C	Exposed
		398	C	Exposed
RNF2	Q99496	72	C	Buried
		133	K	Exposed
		260	S	Buried
RNF7	Q9UBF6	59	D	Buried
		61	C	Exposed

		99	C	Buried
RNF14	Q9UBS8	262	C	Exposed
		281	E	Exposed
		350	C	Exposed
		406	C	Exposed
RNF20	Q5VTR2	905	C	Exposed
		924	C	Exposed
RNF25	Q96BH1	159	C	Buried
RNF34	Q969K3	149	C	Exposed
RNF40	O75150	69	C	Exposed
		872	D	Exposed
		890	C	Exposed
		950	C	Exposed
RNF114	Q9Y508	64	C	Exposed
		67	C	Buried
		85	E	Exposed
		101	S	Exposed
		110	C	Exposed
		111	S	Buried
		113	Y	Exposed
		126	K	Exposed
		139	Y	Exposed
RNF126	Q9BV68	15	C	Exposed
RNF138	Q8WVD3	42	C	Buried
RNF146	Q9NTX7	185	C	Exposed
		354	C	Exposed
RNF166	Q96A37	127	C	Exposed
RNF168	Q8IYW5	190	C	Exposed
RNF169	Q8NCN4	103	C	Buried
RNF181	Q9P0P0	23	M	Exposed
RNF187	Q5TA31	97	C	Buried
RNF214	Q8ND24	215	E	Exposed
		219	D	Exposed
		315	C	Exposed
		366	K	Exposed
		582	K	Exposed
		588	M	Exposed
		655	C	Exposed
RNF220	Q5VTB9	382	C	Exposed
SHKBP1	Q8TBC3	550	C	Buried
SKP2	Q13309	124	C	Exposed
		205	C	Buried
		327	C	Buried

		345	C	Buried
		390	C	Buried
		423	C	Exposed
SMU1	Q2TAY7	107	K	Exposed
		170	K	Exposed
		210	K	Exposed
		219	C	Buried
		298	C	Exposed
		308	K	Exposed
		337	K	Exposed
SMURF2	Q9HAU4	47	C	Exposed
		151	C	Exposed
		706	C	Exposed
SNRNP40	Q96DI7	52	C	Exposed
		99	C	Buried
		148	K	Exposed
		157	C	Buried
		168	C	Buried
		249	Y	Exposed
		270	K	Exposed
		275	K	Exposed
		349	K	Exposed
SOCS2	O14508	111	C	Buried
STUB1	Q9UNE7	30	K	Exposed
		48	C	Buried
		72	K	Exposed
		83	C	Buried
		103	C	Buried
		180	C	Buried
		199	C	Exposed
		232	C	Buried
		244	C	Buried
TLE1	Q04724	526	C	Buried
TLE3	Q04726	26	C	Exposed
		528	C	Buried
TOR1AIP2	Q8NFQ8	310	C	Buried
	Q9H496	86	C	Exposed
TRAF2	Q12933	112	C	Exposed
		120	E	Exposed
		124	C	Exposed
		170	C	Exposed
		171	C	Buried
		287	C	Exposed

		303	C	Exposed
		493	K	Exposed
TRIM2	Q9C040	254	C	Buried
TRIM5	Q9C035	310	C	Exposed
TRIM7	Q9C029	130	C	Buried
		191	C	Exposed
TRIM11	Q96F44	236	C	Exposed
TRIM16	O95361	178	C	Exposed
		202	K	Exposed
		286	C	Exposed
		300	Y	Exposed
		371	Y	Buried
		394	K	Exposed
TRIM24	O15164	246	C	Buried
		882	C	Exposed
TRIM25	Q14258	65	K	Exposed
		70	C	Buried
		80	D	Exposed
		237	K	Exposed
		272	S	Exposed
		273	K	Exposed
		326	E	Buried
		475	C	Exposed
		498	C	Exposed
		602	K	Exposed
TRIM28	Q13263	63	E	Exposed
		68	C	Exposed
		126	S	Exposed
		133	Y	Exposed
		193	R	Exposed
		209	C	Exposed
		232	C	Exposed
		238	K	Exposed
		242	Y	Buried
		254	K	Buried
		261	K	Buried
		266	K	Exposed
		272	K	Exposed
		296	K	Exposed
		304	K	Exposed
		319	K	Exposed
		322	E	Buried
		330	R	Buried

		340	K	Exposed
		366	K	Exposed
		369	Y	Exposed
		377	K	Exposed
		378	M	Exposed
		399	T	Exposed
		407	K	Exposed
		412	R	Buried
		423	M	Exposed
		427	R	Exposed
		443	M	Exposed
		469	K	Exposed
		507	K	Exposed
		513	T	Exposed
		514	T	Buried
		517	Y	Exposed
		628	C	Exposed
		713	C	Exposed
		717	C	Exposed
		750	K	Exposed
		755	Y	Exposed
		776	T	Buried
		815	M	Exposed
TRIM33	Q9UPN9	150	C	Buried
		153	C	Buried
		276	C	Buried
		329	K	Exposed
		447	C	Exposed
		461	C	Exposed
		784	E	Exposed
TRIM38	O00635	58	C	Exposed
TRIM47	Q96LD4	182	C	Buried
		344	E	Exposed
		347	C	Exposed
		454	C	Exposed
		551	C	Buried
TRIM56	Q9BRZ2	229	E	Exposed
TRIM65	Q6PJ69	112	C	Exposed
		174	C	Exposed
		320	C	Exposed
TRIP12	Q14669	535	C	Exposed
		1957	M	Exposed
		1959	C	Exposed

UBE3A	Q05086	83	C	Exposed
		269	C	Exposed
		310	C	Buried
		760	C	Buried
		843	C	Exposed
UBE3C	Q15386	158	C	Buried
		1018	C	Exposed
		1051	C	Buried
UBE3D	Q7Z6J8	52	C	Exposed
UBE4A	Q14139	79	C	Exposed
UBE4B	O95155	447	M	Exposed
		581	C	Exposed
		1164	C	Exposed
UBOX5	O94941	340	C	Buried
UBR1	Q8IWV7	1603	C	Exposed
UBR2	Q8IWV8	1360	C	Exposed
UBR3	Q6ZT12	288	C	Buried
		1858	C	Exposed
UBR7	Q8N806	35	C	Buried
		374	C	Exposed
		424	C	Exposed
UHRF1	Q96T88	410	C	Buried
		497	C	Exposed
UNK	Q9C0B0	696	C	Exposed
VHL	P40337	77	C	Buried
VPS8	Q8N3P4	1371	C	Exposed
VPS11	Q9H270	266	C	Exposed
WDR5	P61964	27	K	Exposed
		205	C	Exposed
		228	Y	Exposed
		250	K	Exposed
WDR12	Q9GZL7	14	K	Exposed
		39	K	Exposed
		97	C	Exposed
		375	C	Exposed
WDR26	Q9H7D7	238	C	Exposed
		316	C	Buried
		338	C	Buried
WDR53	Q7Z5U6	15	C	Buried
		63	C	Exposed
WDR61	Q9GZS3	120	Y	Exposed
		125	T	Exposed
		137	S	Buried

		139	K	Exposed
		140	K	Exposed
		179	T	Exposed
		181	K	Exposed
		213	Y	Buried
		303	C	Exposed
WDR82	Q6UXN9	229	M	Exposed
WSB1	Q9Y6I7	66	C	Buried
WWP2	O00308	838	C	Buried
XIAP	P98170	351	C	Exposed
ZER1	Q7Z7L7	62	C	Exposed
ZNF598	Q86UK7	725	C	Exposed
ZNRF1	Q8ND25	204	C	Buried

Supplementary Table S5: Table showing liganded E3 ligases identified in the non-competition dataset. Out of 571 residues, 385 were classified as exposed and 185 as buried implementing p2rank in the analysis. P2rank is based on the prediction of ligandability of local chemical neighbourhoods, we classified results as either exposed or buried. The analysis was performed by Martin Buttenschön using Tableau.

Plate	*Well*	*Compound name*	*Effect*
6	*I17*	*Z278055534*	*2.786222225*
6	*L17*	*Z594686252*	*3.503605768*
6	*H19*	*Z2285378028*	*3.534841981*
7	*J16*	*Z905062522*	*3.58672413*
8	*N4*	*Z228607640*	*3.713376246*
5	*N17*	*Z1123840993*	*3.745904074*
6	*M9*	*Z56886524*	*3.846145042*
8	*J6*	*Z733916656*	*3.985694765*
7	*G18*	*Z1937872870*	*4.017854111*
6	*N8*	*Z762199618*	*4.027003657*
7	*M17*	*Z1250167436*	*4.190537568*
7	*I15*	*Z1255505242*	*4.202063966*
7	*C15*	*Z1783110847*	*4.218579659*
6	*F8*	*Z2043306571*	*4.28669815*
5	*E6*	*Z854282952*	*4.330008125*
6	*F22*	*Z2285377561*	*4.600281685*
3	*M8*	*Z94598734*	*4.62362186*
4	*K4*	*Z200020424*	*4.738697598*
5	*M12*	*Z1366922432*	*4.739018959*
7	*M19*	*Z1094759230*	*4.827845139*
7	*O21*	*Z1937903307*	*4.908997219*
3	*E9*	*Z56347481*	*4.936345955*
4	*C6*	*Z295512326*	*4.960572676*
7	*B17*	*Z1505641531*	*4.993524684*
3	*D10*	*Z131021866*	*5.015764626*
7	*K14*	*Z1532736863*	*5.032556399*
4	*N5*	*Z44347379*	*5.154506286*
7	*O22*	*Z1269199048*	*5.1620929*
7	*I4*	*Z733916682*	*5.27846816*
3	*C15*	*Z57984666*	*5.332742438*
8	*O4*	*Z1954805892*	*5.423040027*
7	*J19*	*Z2004564056*	*5.449315246*
5	*H9*	*Z1224923409*	*5.529642497*
7	*K15*	*Z854066922*	*5.537774191*
5	*H15*	*Z1203056829*	*5.627068178*
6	*B10*	*Z56846727*	*5.634635767*
3	*I20*	*Z57834468*	*5.721861262*
4	*N13*	*Z898519900*	*5.745281654*
8	*F5*	*Z425636090*	*5.904428725*
7	*O18*	*Z1954803958*	*6.055741556*
5	*C6*	*Z854282962*	*6.111680399*
3	*B18*	*Z56886635*	*6.227402434*
7	*K21*	*Z854067046*	*6.322199897*
5	*I3*	*Z854283122*	*6.356387238*
3	*K17*	*Z235362865*	*6.392852304*
7	*K11*	*Z451452266*	*6.663635688*
4	*G7*	*Z1066030568*	*6.733745638*
4	*F5*	*Z283904696*	*6.810932247*
4	*D11*	*Z226055308*	*6.816655518*

Supplementary Table S6: SPECK-formation assay top 50 hits out of over 200 hits, this analysis was performed by Sohaib Nizami. Effect versus CRID3 control is reported.

Rapidfire data analysis								
Protein	Timep	Concentration (uM)	Compour	Mass predicted	Mass detected	Modifications	Well	File
KEAP1 41	1h	100	1c	134	134	3	E13	Mira E3 1h competitors complet
KEAP1 41	1h	10	1c	134	134	2	E14	Mira E3 1h competitors complet
KEAP1 44	1h	100	1c	134	134	4	E15	Mira E3 1h competitors complet
KEAP1 44	1h	10	1c	134	134	2	E16	Mira E3 1h competitors complet
KEAP1 41	1h	100	9c	168	168	3	F13	Mira E3 1h competitors complet
KEAP1 41	1h	10	9c	168	168	3	F14	Mira E3 1h competitors complet
KEAP1 44	1h	100	9c	168	168	2	F15	Mira E3 1h competitors complet
KEAP1 44	1h	10	9c	168	168	2	F16	Mira E3 1h competitors complet

Supplementary Table S7: Mass shifts observed for competitors 1c and 9c in intact MS using stated constructs. The experiment was conducted at 2 μM protein concentration and varying competitor concentrations. Measurements were taken at 1 h timepoint using the RapidFire.

Name	Sequence	Tm	GC %
DENND1A_NL_N_M243W_r	gtagggccagggagcacagcagtag	62.7	60
DENND1A_NL_N_M243W_f	gtgctccctggccctacctcataggaA	63	55.56
DENND1A_NL_N_Y238A_r	cacagcaggcgtccagcagatgcggCG	66.9	62.96
DENND1A_NL_N_Y238A_f	ctggacgcctgctgtgctcccatGC	63.1	60
DENND1A_NL_N_Y238W_r	cagcaccagtccagcagatgcggcgg	66.9	65.38
DENND1A_NL_N_Y238W_f	gctggactggtgctgtgctcCCA	62.5	60.87
DENND1A_NL_N_Q362A_r	AAGAGCTGCAGCTGTGTGGCGT	67.2	59.2
DENND1A_NL_N_Q362A_f	GCTTGAAGAGGGGCAGCTGTGTG	61.6	44.83
DENND1A_NL_N_Q362W_r	gaagagccacagctgtgtggcgt	64	60.87
DENND1A_NL_N_Q362W_f	cagctgtggctcttcaagcagtttattgat	61.6	43.33
DENND1A_NL_N_Q362A_Q366A_r	caataaacgccttgaagagcgccagctgtgtgg	64.9	48.48
DENND1A_NL_N_Q362A_Q366A_f	cagctggcgctcttcaaggcgtttattgatggtc	64.5	47.06
DENND1A_NL_N_Q362W_Q366W_r	caataaaccacttgaagagccacagctgtgtggcgt	68.3	50
DENND1A_NL_N_Q362W_Q366W_f	cacagctgtggctcttcaagtggtttattgatggtcg	66.7	48.65
DENND1A_NL_N_H225R_r	gtacacgcgctgccagtacatgGGG	63.3	60
DENND1A_NL_N_H225R_f	ggcagcgcgtgtacatccccgT	63.4	63.64

Supplementary Table S8: Primers (pairs, forward and reverse) designed by Laura Dias-Saez for mutating major contributors of DENND1A PPI based on crystal structure PDB: 6EKK.